UNIVERSITY OF SOUTHAMPTON

Faculty of Engineering and Physical Sciences
School of Physics & Astronomy

Error and performance analysis of cold-atom inertial sensors for navigation

by

Nikolaos Dedes

A thesis for the degree of
Doctor of Philosophy

March 2024

University of Southampton

Abstract

Faculty of Engineering and Physical Sciences
School of Physics & Astronomy

Doctor of Philosophy

Error and performance analysis of cold-atom inertial sensors for navigation

by Nikolaos Dedes

Cold-atom inertial (CAI) sensors based on light-pulse atom interferometry show much promise for the next generation of navigation systems thanks to their low scale-factor and bias instability. Despite the high performance demonstrated in laboratory-based experiments, CAI technology is still far from being deployed in real-world navigation applications, and an analysis of the potential errors must be carried out in order to assess their impact on sensor performance.

Within this context, we conduct a theoretical analysis to identify some of the most important error sources, disclose their physical mechanisms, and assess their impact on sensor performance. Through a multidisciplinary approach that combines different methodologies spanning from system engineering to quantum physics modeling, we analyse the response of the CAI sensor to several error sources, including scale-factor, bias, and noise, and establishing clear relations between system parameters and sensor performance. Particular emphasis is given to error sources stemming from the laser-atom interaction during the Raman-pulse sequence and from state detection and imaging.

Moreover, we present a method for optimizing beam-splitter pulses based on time-dependent perturbation theory, demonstrating improvements in the simulated performance of a CAI sensor.

Finally. due to its attractive multi-axial sensitivity and inherent capability to discriminate the acceleration from the rotational signal, we study in more detail errors sources in CAI sensors based on point-source interferometry. We therefore present a read-out method based on Kalman filtering to extract the interferometric phase map from interferograms, along with a compensation scheme for real-time calibration of the rotational scale-factor based on the integration of the CAI sensor with classical inertial sensors.

Contents

List of publications

Journal papers

- N. Dedes, J. Saywell, M. Carey, I. Kuprov, and T. Freegarde, *Optimizing beamsplitter pulses for atom interferometry: A geometric approach*, Physical Review A, 108, 053319 (2023).
- J. Saywell, M. Carey, N. Dedes, I. Kuprov and T. Freegarde, *Efficient state-symmetric beamsplitters and mirrors for atom interferometers using optimized pulses*, Journal of Physics B: Atomic, Molecular and Optical Physics, 55, 205501 (2022).

Conference papers

- N. Dedes, D. Harvey, and T. Freegarde, *Real-time scale-factor calibration for cold-atom gyroscope based on point-source interferometry*, submitted to the The 11th IEEE International Symposium on Inertial Sensors & Systems, (Hiroshima, 2024).
- N. Dedes, D. Harvey, and T. Freegarde, *Error sources in cold atom inertial sensors*, Meeting Proceedings of the 10th Military Sensing Symposium (SET-311, London 2023).
- J. Saywell, M. Carey, N. Dedes, I. Kuprov, T. Freegarde, *Can optimised pulses improve the sensitivity of atom interferometers?*, in Quantum Technology: Driving Commercialisation of an Enabling Science II (SPIE, New York, 2021).

List of Figures

List of Tables

Declaration of Authorship

I declare that this thesis and the work presented in it is my own and has been generated by me as the result of my own original research.

I confirm that:

1. This work was done wholly or mainly while in candidature for a research degree at this University;
2. Where any part of this thesis has previously been submitted for a degree or any other qualification at this University or any other institution, this has been clearly stated;
3. Where I have consulted the published work of others, this is always clearly attributed;
4. Where I have quoted from the work of others, the source is always given. With the exception of such quotations, this thesis is entirely my own work;
5. I have acknowledged all main sources of help;
6. Where the thesis is based on work done by myself jointly with others, I have made clear exactly what was done by others and what I have contributed myself;
7. Parts of this work have been published as:

Signed:..... Date:.....

Acknowledgements

I don't hide that this journey has been arduous, perhaps more than expected. I started this PhD in January 2020, three months before Covid would force the entire world to stop, moving to a different country with high hopes, excitement but also worryings for the unknown. Back then, I was unaware of the challenges that lay ahead. Yet, after four years, I can confidently say that throughout this journey, I've been lucky to find people with unparalleled and exceptional human qualities.

I would like to thank Tim, my academic supervisor, without whom this journey would not have been possible. Thank you for your guidance and the many hot chocolates offered during our meetings.

I would also like to express my gratitude to David Harvey, my industry supervisor, for his support and for arranging many opportunities for me within Thales.

A special thanks goes to the past and present members of the research group. To Joel, who patiently listened to my continuous discussions on quantum navigation and with whom I shared the post-Covid phase of my PhD journey. To Jack and Max, who have proven to be amazing scientists and great colleagues, patiently clarifying my numerous doubts and providing invaluable suggestions.

I would like to thank Tiago and Vim. You were my first flatmates, and I'm certain that without our conversations and laughter, my mental health during the first lockdown would have definitely go south.

A particularly heartfelt thanks goes to Ivan and Hao *Fu-siccome-immobile*. Thank you for the countless laughs, conversations, walks, and hours spent together. Without you, my friends, my journey in Southampton would have felt much emptier.

Un immenso ringraziamento va, come sempre, alla mia famiglia. Il vostro immancabile supporto non conosce confini e distanze. Grazie mamma, babbo, Miriana per esserci sempre e per avere fiducia nei miei mezzi e capacità. Spero mi possiate perdonare per essere andato così lontano da casa, ma come dico sempre: dopo Roma, Italia o Europa che sia, ci metti lo stesso tempo a raggiungerle.

If there is one thing, probably the most important thing, I should acknowledge, it's that without this journey, I would not have had the opportunity to meet the person I love. Alicia, you have been with me for the greatest part of this adventure, providing continuous and tireless support, and always showing wholehearted trust in my capabilities. A great part of the credit goes to you for reaching the end of this journey, and I hope that, regardless of the outcome, you are proud of me.

To my piccolo Gufo

Chapter 1

Introduction

1.1 What is navigation?

The concept of navigation is broad and encompasses various aspects. In its simplest form, navigation refers to the process of determining and following a course or route to reach a destination [1]. However, this definition includes two distinct concepts: firstly, the determination of the position of a vehicle, and secondly, the capability to follow a predetermined set of position points.
A more modern definition of navigation is related to the concept of GNC (guidance, navigation, and control). While guidance involves determining the optimal path or trajectory to reach a destination or achieve a specific objective, and control involves adjusting the vehicle's actuators to achieve the desired trajectory or maintain stability, navigation fundamentally pertains to determining the vehicle's position, velocity, and orientation relative to a reference frame or a desired path [2].
Navigation methods can be broadly divided into two main categories: position fixing and dead reckoning. Position fixing involves the direct determination of the navigation state using external information. This category includes methods such as proximity, ranging and angular positioning, Doppler positioning, and pattern matching [3]. Examples of navigation systems based on position fixing include Global Navigation Satellite Systems (GNSSs), navaids, and visual systems.
In contrast, dead reckoning indirectly determines the navigation state by exploiting measurements of its rate of change. Therefore, estimation of the navigation state is performed via time integration.
Unlike position fixing, dead reckoning does not rely on external information; instead, it depends solely on the vehicle's dynamics. This characteristic ensures robustness against disruptions or corruption of external signals and enhances autonomy. However, the major drawback of dead reckoning lies in the time integration process: errors inherent in the measurements of the rate of change of the navigation state accumulate and propagate during integration leading to inaccuracy and error drifts. This makes

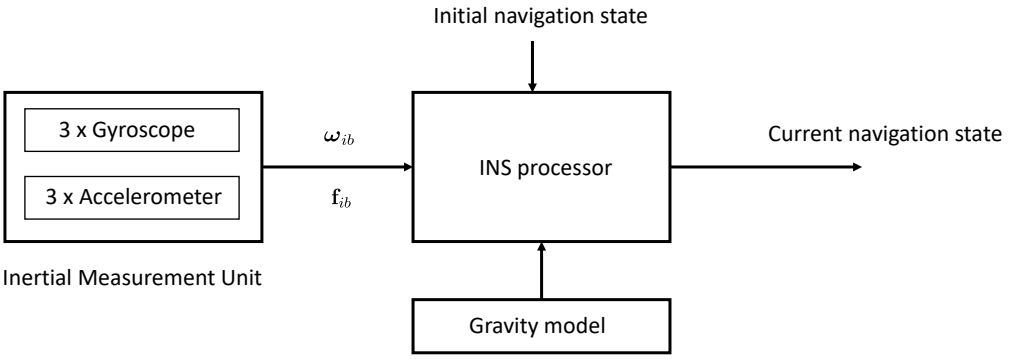

FIGURE 1.1: Block diagram representation of an inertial navigation system.

dead reckoning unsuitable for medium and long-term navigation, requiring combination with position fixing to recover accuracy.

1.2 Inertial navigation systems

The inertial navigation system (INS) is one of the most commonly used dead reckoning navigation systems. In its simplest form, it comprises two main components: an inertial measurement unit (IMU), which includes a triad of orthogonal gyroscopes and a triad of orthogonal accelerometers; and a computer that processes the IMU output to estimate the current navigation state. Gyroscopes measure the angular rate that characterizes the rotation of the body frame with respect to an inertial frame ($\boldsymbol{\omega}_{ib}$). Accelerometers measure the specific force, i.e., the acceleration of the body frame with respect to an inertial frame minus the acceleration due to gravitational force ($\mathbf{f}_{ib} = \mathbf{a}_{ib} - \boldsymbol{\gamma}_{ib}$). As a result, an accelerometer in a static position will measure the reaction to gravity, while in free fall, it will register zero output. Since the accelerometer measures a specific force, a gravity model is needed in order to estimate the navigation state.

INSs can be classified into two categories: gimbaled and strapdown systems. In gimbaled systems, the accelerometer and gyroscope triads are mounted on a platform that is always maintained aligned with the local horizon. In this scheme, gyroscope measurements are used in a closed-loop configuration to provide feedback signals to the gimbal torque motors, which rotate the platform until the gyroscope output is zeroed. Therefore, the orientation of the vehicle is determined by the initial value plus the rotation needed to keep the platform stable. Once the orientation is known, the accelerometer measurements can be used to estimate position and velocity [4].

In strapdown systems, the inertial sensors are rigidly attached to the vehicle's body frame. This greatly simplifies the architecture, reducing cost, size, and weight. However, this simplicity comes at the cost of higher complexity in the algorithms required for estimating the navigation state and increased requirements in terms of dynamic range and bandwidth for the inertial sensors [1]. The possibility to realize compact systems without expensive and complex gimbals makes the strapdown configuration the most diffused and common architecture for INSs.

Nevertheless the type of INS architecture, the estimation of the current navigation state is affected by four main error sources:

- Inertial sensors errors. The estimation of the navigation state is performed integrating in time the specific forces and the angular rates, therefore errors in the measurement process propagate and grow in time [1].
- Alignment (or initialization) errors. In particular, errors in the initial heading estimation are critical and lead to a position error that drifts in time [1].
- Gravity model. The value of the true gravity varies with the position and can differ significantly from the model value. For instance, gravity anomalies of several tenths of nano-g can induce position errors that exceed 100m after 10min of navigation [5].
- Computational errors. These include, the choice of the navigation equation 'mechanization' (i.e. the navigation algorithm) and the computational errors due to processor's finite precision [4].

1.2.1 Inertial sensor errors

Errors in the IMU measurements are the dominant source of error in INSs. Both noise and systematic errors impact the estimation of the current navigation state. In particular, the time-varying nature of systematic errors is critical, as it necessitates additional navigation systems for in-flight calibration.
Inertial sensor errors can be grouped in four categories [3]:

- Bias represents the systematic error component along the sensor's sensitive axis under conditions of zero input. Bias encompasses several categories, including fixed bias, run-to-run bias, and anisoinertia bias. While fixed bias is repeatable, the run-to-run component represents the fraction of bias that changes from one switch-on event to another. Anisoinertia bias describes errors resulting from angular rates and accelerations occurring along axes orthogonal to the sensitive one.

[1] The inertial sensors measure the angular rates and specific forces of the vehicle itself, necessitating sufficient bandwidth and dynamic range to accurately track the vehicle dynamics.

Unfortunately, bias also exhibits a time-varying random component known as in-run bias instability, or simply bias instability, which significantly affects medium and long-term navigation. Bias is usually expressed in degrees per hour for gyroscopes and submultiples of g for accelerometers.

- Scale-factor error represents the deviation of the slope of the input-output sensor's curve from unity. It also includes non-linearity errors, which represent the deviation of the input-output curve from a straight line. Unlike bias, scale-factor error occurs for non-zero input. Additionally, it presents a time-varying stochastic component called scale-factor instability. Scale-factor error is usually expressed in parts per million (ppm).

- Misalignment error is due to the deviation of each sensor' sensitive axis from the orthogonality condition. As a consequence a sensor's measurement is affect by inertial actions along axes orthogonal to its sensitive one. It is usually expressed in ppm.

- Random noise represents the stochastic zero-mean high-frequency error component. It is usually described in terms of white noise spectral density. For the gyroscope, random noise is expressed in terms of angle random walk with dimensions of $\mathrm{deg}/\sqrt{\mathrm{h}}$, while for the accelerometer, it is expressed in terms of velocity random walk ($\mathrm{m/s}/\sqrt{\mathrm{h}}$) or spectral density ($\mu\mathrm{g}/\sqrt{\mathrm{Hz}}$).

The measurement model of an inertial sensor is usually given by [3]

$$\tilde{\boldsymbol{\eta}} = \left(\mathbf{I} + \mathbf{S}_\eta\right)\, \boldsymbol{\eta} + \mathbf{b}_\eta + \mathbf{n}_\eta\,, \tag{1.1}$$

where $\tilde{\boldsymbol{\eta}}$ is a 3x1 vector containing the triad measurements, $\mathbf{I}$ is the 3x3 identity matrix, $\mathbf{S}_\eta$ is a matrix whose diagonal terms contain the scale-factor error and whose off-diagonal terms contain the misalignment errors, $\boldsymbol{\eta}$ represents the vector of the true inertial action (i.e. either the true specif force vector or the angular rate vector), $\mathbf{b}_\eta$ is the bias term, and $\mathbf{n}_\eta$ is the random noise term. The above equation is valid for either a triad of accelerometers or a triad of gyroscopes.

1.2.2 Inertial sensor classification

According to the level of error, inertial sensors can be grouped into different categories. The categorization and their corresponding requirements are not universally determined, as various definitions can be found in the literature [3, 6, 7].
Table 1.1 presents a typical performance-based classification of inertial sensors. Excluding consumer-grade sensors not utilized in navigation applications, tactical-grade

Grade	Strategic	Navigation	Tactical	Consumer
Accelerometer noise $[\mathrm{mg}/\sqrt{\mathrm{Hz}}]$	< 0.001	< 0.1	~ 1	Several
Accelerometer bias inst. [mg]	< 0.001	< 0.1	~ 1	> 5
Gyroscope noise $[\mathrm{deg}/\sqrt{\mathrm{h}}]$	< 0.001	< 0.05	< 0.5	Several
Gyroscope bias inst. [deg/h]	< 0.001	< 0.05	$0.1 - 10$	> 10
Position error [nmi/h]	< 0.05	~ 1	$10 - 20$	Large

TABLE 1.1: Classification of inertial sensors.

sensors offer an accuracy suitable only for short-term navigation (typically less than 5 minutes). In contrast, navigation-grade sensors are suitable for medium-term navigation (up to several hours) but necessitate integration with additional navigation systems, such as GNSS, to correct position drifts. Consequently, a navigation-grade inertial sensor serves as an aid for the GNSS receiver, providing high-data-rate estimation of the navigation state. An INS based on navigation-grade sensors typically exhibits a position error of one nautical mile after one hour of free-inertial navigation[2]. This requirement is crucial for en-route aerial navigation: for instance, within the context of required navigation performance (RNP), RNP-1 mandates aircraft to remain laterally within one nautical mile of a defined path 95% of the time [8].
INSs based on strategic-grade sensors can achieve position errors of less than 100m after one hour of free-inertial navigation. Therefore, they are suitable for navigation applications demanding high levels of autonomy and accuracy, such as space and submarine navigation, as well as for intercontinental ballistic missiles.

1.3 Cold-atom inertial sensors

The need for increasingly high-performance and autonomous navigation systems has been one of the major drivers in the development of cold-atom inertial (CAI) sensors. Since the pioneering experiments led by Kasevich and Chu in the early 1990s [9], the use of cold atoms for probing inertial effects has emerged as a disruptive technology, potentially capable of revolutionizing navigation.

[2]In free-inertial navigation, the position is estimated solely by the INS without aid from GNSS measurements.

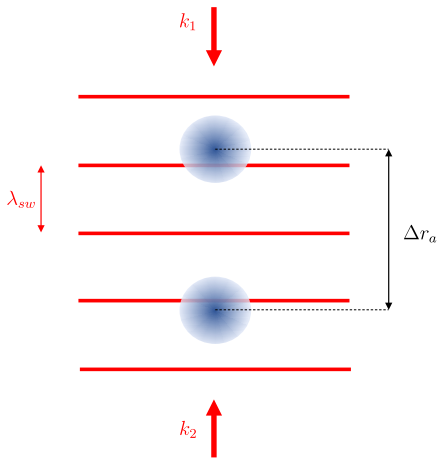

FIGURE 1.2: The laser grating is used as a 'ruler' to measure the atomic displacement during the interferometer's sequence.

When cooled to temperatures on the order of a few micro-Kelvin, atoms behave like waves, forming so-called 'matter-waves.' Similar to the behavior of light, which can be diffracted or reflected by crystals and mirrors, atomic matter-waves can be coherently manipulated by laser fields acting as diffraction gratings and mirrors. The diffracted matter-waves can be combined to form an interferometer that is sensitive to inertial actions, mirroring the same mechanism exploited by classical optical gyroscopes, i.e., the Sagnac effect.

The Sagnac effect can be summarized as follows: under the action of a rotation acting orthogonally to a closed loop, the distance traveled by the diffracted waves along the upper and lower arms of the loop differs. This difference in length manifests as a phase shift in the interference pattern formed by the two waves, which is directly proportional to the area of the loop and inversely proportional to the velocity of the wave. It appears that for a given loop area, the matter-wave interferometer would be characterized by a significantly increased sensitivity, owing to the fact that cold atoms move at a speed approximately ten orders of magnitude slower than the speed of light. For years, this has been the typical way to explain the 'quantum advantage' of CAI sensors [10, 11]. But is this explanation correct and sufficient?

First, the Sagnac effect does not account for accelerations, and it is not immediately clear what the advantage of a cold-atom accelerometer over a classical one would be. Second, the projected increase in sensitivity is based on the assumption that the loop area of the interferometer in a cold-atom gyroscope is the same as that of an optical gyroscope. However, this is not the case, as in fiber optic gyroscopes, coils containing kilometers of fibers can provide extremely large sensitive areas that can be several orders of magnitude higher than those of cold-atom gyroscopes. Therefore, we need another explanation for the quantum advantage.

Research group Sensor (Year)	Short-term sensitivity	Long-term stability	Comments
Sandia Labs IMU (2014)	$3.7\text{mdeg}/\sqrt{\text{h}}$ $0.9\mu\text{g}/\sqrt{\text{Hz}}$	–	Two-axis dual sensor with high data-rate ($f_c = 60\text{Hz}$). Ref. [12]
LNE-SYRTE Gyroscope (2018)	$0.1\text{mdeg}/\sqrt{\text{h}}$	0.06mdeg/h	4-pulse interferometer in zero-dead-time mode. Ref. [13]
Weizmann Institute Gyroscope (2020)	$160\text{mdeg}/\sqrt{\text{h}}$	100mdeg/h	Point-source interferometry. Ref. [14]
State Key Labs Gyroscope (2021)	$0.5\text{mdeg}/\sqrt{\text{h}}$	0.2mdeg/h	Dual sensor with spatially separated Raman beams. Ref. [15]
iXBlue Accelerometer (2022)	$22\mu\text{g}/\sqrt{\text{Hz}}$	60ng	Three-axis sensor. Ref. [16]

TABLE 1.2: Performance of state-of-the-art CAI sensors using different system architectures.

CAI sensors measure specific forces and angular rates by detecting the relative displacement of atoms with respect to a laser standing wave. The relative distance traveled by the atoms can be detected by counting the number of crossings in a standing wave, $\mathcal{N}(t) = \Delta r_a(t)/\lambda_{sw}$, where $\Delta r_a(t)$ is the atomic displacement in time t, and λ_{sw} is the wavelength of the standing wave. Atoms are nearly perfect proof masses, and their motion is highly repeatable in principle. If we use a stable laser to measure their motion, the wavelength λ_{sw} is also highly repeatable. Therefore, the overall measurement of the number of crossings (i.e., the phase) is characterized by high stability. It is indeed this stability in the measurement process that makes CAI sensors so attractive: once calibrated, their measurements remain stable over time and are characterized by minimal drifts.

Table 1.2 shows the state-of-the-art of CAI sensors for different system architectures and configurations. Except for the point-source interferometry architecture, state-of-the-art CAI sensors have demonstrated low-noise and high-stability performance. However, it must be noted that the actual data reported in the table refer to lab-based experiments characterized by benign and controlled environments. So far, only a few field trials have been conducted, showing performance worsening by up to one or more orders of

magnitude in challenging environments [17]. Therefore, the actual performance of CAI sensors in real-world applications is unknown and requires proper investigation.

1.4 Thesis outline

In principle, CAI sensor' measurements are characterized by high stability. However, various error sources, stemming from different physical mechanisms and depending on different system parameters, affect the different sensor's performance. In many cases, these errors could result in non-stable or excessively noisy measurements.
The aim of this thesis work is to establish the performance of CAI sensors for navigation applications by identifying and evaluating their characteristics, sensitivities, and limitations. In order to achieve this, we identify several error sources, disclose the physical mechanisms behind them, and assess their impact on sensor performance both qualitatively and, when possible, quantitatively. Unless otherwise specified, the chosen atomic species in the numerical analysis is ^{85}Rb, primarily due to the fact that our research group has historically adopted this atomic species.
The thesis is organized as follows:

- **Chapter 2**. We introduce the working principles of CAI sensors based on light-pulse atom interferometry. We focus in particular on a three-pulse Mach-Zehnder interferometer scheme using stimulated Raman transitions. Moreover, we explore how CAI sensors can be utilized for navigation.
- **Chapter 3**. We analyze the CAI sensor from a system point of view, identifying the major error sources, their physical mechanisms, and their impact on the sensor's performance.
- **Chapter 4**. We introduce the sensitivity function formalism as a powerful theoretical tool to compute the response of a CAI sensor to both deterministic and stochastic inputs.
- **Chapter 5**. We present a method for designing optimized beam-splitter pulses based on time-dependent perturbation theory, which links the sensitivity function formalism to optimal control in the Bloch sphere picture. We discuss the impact of optimized beam-splitter pulses on scale-factor errors and biases arising from inter-pulse laser intensity variations.
- **Chapter 6**. We address the errors induced by wavefront distortions on CAI sensors operating with both standard and point-source interferometry detection, and highlight possible sources of noise and long-term instability.
- **Chapter 7**. We analyze CAI sensors based on point-source interferometry in more detail. We address the issues of contrast decay and rotational scale-factor errors

arising from the initial atomic distribution. Additionally, we present a readout method that employs an extended Kalman filter for extracting the phase map from interferograms, and a compensation scheme that integrates information from a classical gyroscope to stabilize the rotational scale-factor and limits total contrast loss due to high rotation rates.

- **Chapter 8**. We analyze some of the error sources arising during state detection and imaging, considering different imaging methods.
- **Chapter 9**. We provide a projection for the performance of a CAI sensor, identifying limitations and trends. For a simple case, we compute the projected navigation performance.
- **Chapter 10**. We draw conclusions and offer perspectives on future research.

Chapter 2

Cold-atom inertial sensors for navigation applications

2.1 Light-pulse atom interferometry principles

Light-pulse atom interferometry (LPAI) represents the most common and mature technology for probing inertial effects using cold atoms. In LPAI, atomic matter-waves are diffracted and recombined by means of laser pulses in free-space [18]. Unlike configurations where the atomic wave packets are confined to move within a wave-guide potential [19], free-space propagation ensures the high stability of the atomic trajectories, which do not depend on imperfections in the wave-guide realization [20].

Different diffraction methods have been proposed, each with its pros and cons.
Two-photon Raman diffraction is the most common and widely used method to diffract atomic matter-waves. This technique involves creating a long-lived superposition between the two ground states of an alkali element using a two-photon transition. Two laser beams are precisely tuned so that their frequency difference matches the hyperfine splitting [21]. Arranging the lasers in a counter-propagate configuration ensures Doppler sensitivity and inertial effects probing. In two-photon Raman diffraction the superposition is created between both internal and momentum states. As a result, the phase accumulated by the atomic wavefunction during the interferometer sequence depends on error sources affecting the atomic internal state, such as laser phase noise or stray magnetic fields.
Two-photon Bragg diffraction has gained popularity in recent years as an alternative method. By adjusting the frequencies of two lasers to match the recoil shift, it creates a superposition of only momentum states. While this approach provides immunity to error sources affecting the atomic internal state, it necessitates colder atoms. Additionally, depending on the power of the lasers, Bragg pulses may diffract atomic matter-waves into multiple momentum orders, leading to a reduction in signal-to-noise ratio and the

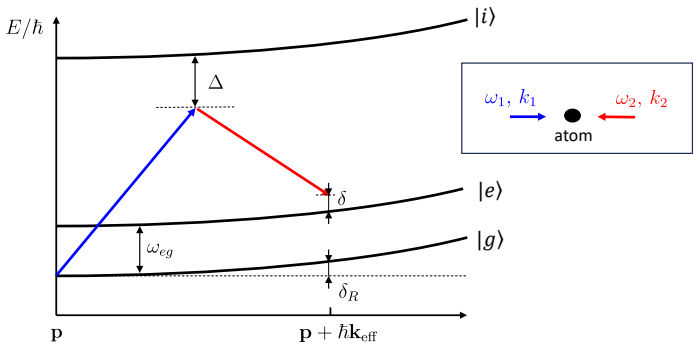

FIGURE 2.1: Energy diagram (not to scale) of the two-photon Raman diffraction. Two lasers couple the state $|g\rangle$ to the state $|e\rangle$ via the far-detuned upper state $|i\rangle$.

emergence of spurious phases due to the interference of these extra states [22].
Only in recent years, the improved stability of laser systems has made possible the implementation of single-photon diffraction using narrow and ultra-narrow clock transitions in alkali-earth elements, such as strontium [23]. Single-photon transitions ensure high transfer efficiency with Rabi frequencies of the order of MHz, thus making possible the realization of large-momentum transfer (LMT) pulse sequences, where multiple laser pulses are concatenated to enlarge the interferometer's area and improve sensitivity [24]. However, the difficulty in realizing agile and robust laser systems characterized by high frequency stability and high powers at different wavelengths [1], and the limitations imposed by spontaneous emissions, are factors that contribute to a less mature technology for the realization of CAI sensors for inertial navigation applications.
Two-photon Raman diffraction operating with rubidium remains the preferred choice in state-of-the-art CAI sensors to this day. Firstly, Raman pulses are more efficient than Bragg pulses, as they do not require atomic ensembles characterized by sub-recoil velocity distributions. Secondly, all laser systems (e.g., for trapping, cooling, interferometry, and detection) share the same wavelength, simplifying the sensor's architecture. Thirdly, robust, efficient, high-power, and cost-effective laser systems can be realized using telecom fiber components via frequency-doubling. The use of fiber components reduces the need for free-space optics, enabling the realization of compact systems, and reducing the sensitivity to optical misalignment in challenging environments [26].

2.1.1 Two-photon Raman diffraction

In two-photon Raman diffraction, two laser beams couple the state $|g,\ \mathbf{p}\rangle$ with the state $|e,\ \mathbf{p}+\hbar\mathbf{k}_{\text{eff}}\rangle$ via the far-detuned upper state $|i,\ \mathbf{p}+\hbar\mathbf{k}_1\rangle$, where $|g\rangle$ and $|e\rangle$ represent the lower and upper ground states, respectively (i.e., the internal degree of freedom).

[1] For example, in the case of ^{88}Sr, the cooling transition necessitates a blue laser, while the clock transition for interferometry requires a red laser [25].

$|\mathbf{p}\rangle$ represents the momentum state (i.e., the external degree of freedom), and $\mathbf{k}_{\text{eff}} = \mathbf{k}_1 - \mathbf{k}_2$ is the Raman effective wave-vector, given by the difference between the wave-vectors associated with the two lasers. During the diffraction process, the atom acquires a momentum $\hbar\mathbf{k}_{\text{eff}}$ as a results of the conservation of momentum.
If the Raman lasers are far-detuned from the upper excited state, the atomic evolution can be described by an effective two-level system. Therefore, for an atom initially in the state $|g,\ \mathbf{p}\rangle$, the probability to be in $|e,\ \mathbf{p} + \hbar\mathbf{k}_{\text{eff}}\rangle$ is given by

$$P_e = \frac{\Omega_{\text{eff}}}{\Omega_R}\ \sin^2\left(\frac{\Omega_R\,\tau}{2}\right), \tag{2.1}$$

where, Ω_{eff} is the effective (or two-photon) Rabi frequency, τ is the laser pulse duration, $\Omega_R = \sqrt{\Omega_{\text{eff}}^2 + \delta^2}$ is the off-resonance Rabi frequency, and δ is the two-photon detuning. The two-photon detuning is given by $\delta = \delta_{12} - \delta_{AC} = \delta_L - (\omega_{eg} + \delta_D + \delta_R + \delta_Z) - \delta_{AC}$, where δ_L is the laser detuning, ω_{eg} is the hyperfine splitting of the ground state, $\delta_D = \mathbf{k}_{\text{eff}} \cdot \mathbf{v}$ is the Doppler detuning, $\delta_R = \hbar k_{\text{eff}}^2/(2\,m)$ is the recoil shift, δ_Z is the Zeeman shift, and δ_{AC} is the AC Stark shift (or one-photon light-shift).
Eq. (2.1) describes the so-called Rabi flopping: the laser pulse interacts with the atomic matter-wave inducing periodic transitions between its energy states. On resonance ($\delta = 0$), the probability P_e is a periodic function depending only on the product $\theta = \Omega_{\text{eff}}\,\tau$, and has a unitary amplitude. We observe that the condition $\theta = \pi$, corresponding to $P_e = 1$, indicates a state inversion, while the condition $\theta = \pi/2$, corresponding to $P_e = 1/2$, places the atomic state in a 50/50 superposition. Therefore, adjusting the pulse duration allows for the inversion and redirection of the atomic state (mirror pulse), or the splitting of the atomic wavefunction into a coherent superposition (beam-splitter pulse).
Eq. (2.1), in its simplicity, highlights two sources of error affecting the efficiency of the diffraction process: pulse-length errors and off-resonance errors. Pulse-length errors result from deviations of the effective Rabi frequency from the nominal resonant value. This occurs, for instance, due to spatial inhomogeneities in the laser intensity experienced by atoms. In contrast, off-resonance errors arise from the frequency difference between the two lasers not precisely matching the hyperfine splitting. For instance, atoms moving in the direction of the effective wave-vector experience Doppler detuning, resulting in sub-optimal diffraction.
Figure 2.2 displays experimental Rabi flopping data. In contrast to the ideal resonant case characterized by a constant and unitary amplitude, the experimental data exhibit damped oscillations. The observed dephasing in the experimental data is likely due to several factors, including Doppler broadening, Zeeman degeneracy, and pulse-length errors resulting from the expansion of the atomic cloud in a Gaussian laser beam. In addition to the collection of the experimental data, we have developed a numerical model based on Monte Carlo simulation that takes as input the measured Zeeman population,

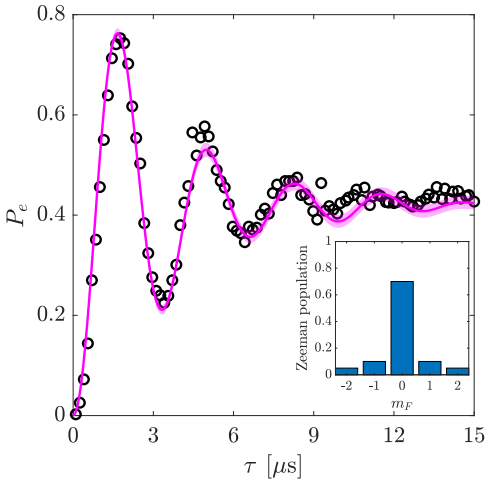

FIGURE 2.2: Rabi flopping of ^{85}Rb. The black circles are experimental data, while the magenta line represents the result of a numerical model based on Monte Carlo simulation. The shaded magenta area individuates the $3-\sigma$ bounds. The inset shows the Zeeman sub-levels population. Experimental parameters: laser power of 110mW and 130mW, lin $\perp$ lin polarization, single-photon detuning $\Delta = 2\,\pi \times 6.8$GHz, beam waist 1.5mm, atomic temperature 10μK, width of the initial cloud 500μm.

the atomic velocity distribution, the initial parameters of the atomic cloud, and the intensity profile of the Raman beam.

2.1.2 Mach-Zehnder interferometer

Mirror and beam-splitter pulses are the cornerstone of LPAI, forming the basis of various types of atom interferometers. Among these, the three-pulse Mach-Zehnder interferometer is the most commonly used for detecting inertial effects.
Initially, the atomic matter-wave is diffracted by a first beam-splitter pulse in a coherent superposition of two states. Subsequently, the atomic wave-packets undergo a first period of free-evolution, during which, they separate in space. A mirror pulse then inverts the atomic states and redirects the wave-packets to close the interferometer's loop. Another period of free evolution follows, during which the spread between the upper and lower wave-packets reduces. Finally, a second beam-splitter pulse allows for interference between the upper and lower wavepackets.
The probability for an atom to be in the $|e,\, \mathbf{p} + \hbar\mathbf{k}_{\text{eff}}\rangle$ state at the output port of the interferometer is (see Appendix A).

$$P_e = P_0 - \frac{C}{2}\cos\left(\Delta\Phi\right), \tag{2.2}$$

where P_0 is the probability offset, C is the fringe's contrast, and $\Delta\Phi$ is the interferometric phase, that contains both the momentum and internal-state dependent phase. A more

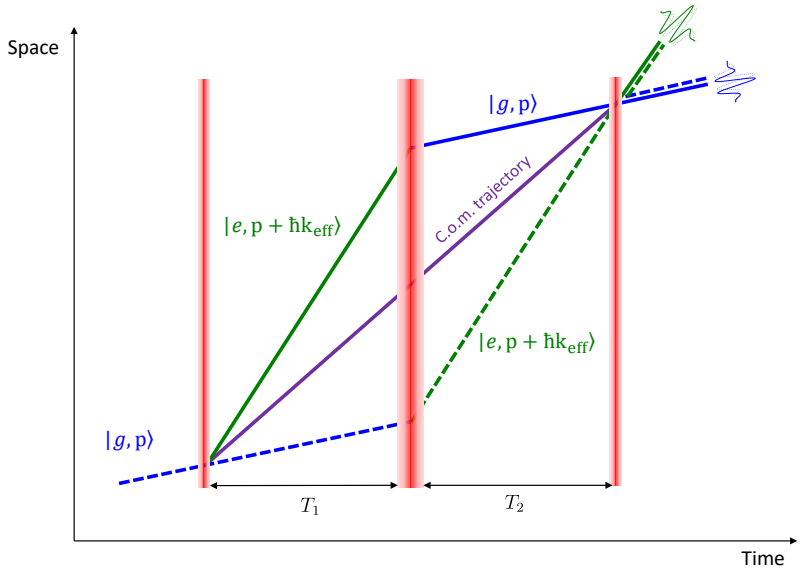

FIGURE 2.3: Recoil diagram of an atom Mach-Zehnder interferometer. The two free-evolution periods are chosen with same duration ($T_1 = T_2 = T$) to suppress initial velocity sensitivity. The continuous and dashed lines represent the upper and lower arm of the interferometer, respectively. The purple line is the centre-of-mass trajectory (or midpoint line).

in-depth analysis of the various phase terms is deferred to Chapter 4.

We anticipate here that the momentum-dependent phase contains the inertial effects, and in the limit of the semi-classical approximation and infinitesimal pulses, it is given by

$$\Delta\Phi_k = \mathbf{k}_{\text{eff}} \cdot \mathbf{r}_{ba}(t_1) - 2\,\mathbf{k}_{\text{eff}} \cdot \mathbf{r}_{ba}(t_2) + \mathbf{k}_{\text{eff}} \cdot \mathbf{r}_{ba}(t_3)\,, \tag{2.3}$$

with $\mathbf{r}_{ba}(t_j)$ relative position of the atomic centre-of-mass' trajectory, represented with a purple line in figure 2.3, with respect to the laser frame at the j-th pulse.

While the expression of the interferometric phase appears to be classical, its origin is purely quantum-mechanical: it arises from the position-dependent phase imparted to the atomic wave-packets by the Raman lasers at each laser pulse.

Assuming for simplicity that the relative motion is described by $\mathbf{r}_{ba}(t) = \mathbf{r}_0 + \mathbf{v}_0\, t + 1/2\,\mathbf{a}\, t^2$, we obtain

$$\Delta\Phi_k = \mathbf{k}_{\text{eff}} \cdot \mathbf{v}_0\,(T_2 - T_1) + \mathbf{k}_{\text{eff}} \cdot \mathbf{a} \left[\frac{(T_1 + T_2)^2}{2} - T_1^2\right], \tag{2.4}$$

where T_1 and T_2 are, respectively, the duration of the first and second free-evolution periods. We observe that selecting a symmetric pulse sequence with respect to the mirror pulse ($T_1 = T_2 = T$) ensures the suppression of the initial velocity dependent term,

causing the above equation to reduce to the well-known result $\Delta\Phi_k = \mathbf{k}_{\text{eff}} \cdot \mathbf{a}\, T^2$. In Chapters 4 and 5, we will see that there can still be a residual sensitivity to the initial velocity when we account for the asymmetries induced by finite-pulse effects.
We observe that the detection of inertial effects through a phase shift limits the sensor's dynamic range. This limitation arises because the cosine function appearing in the interferometric signal expression is periodic, and extracting the term $\Delta\Phi$ from the inversion of Eq. (2.2) results in phase ambiguity.

2.2 Cold-atom inertial sensors for navigation applications

The most intuitive way to use CAI sensors for navigation applications is as an IMU. However, the presence of dead times in the duty cycle, the low bandwidth, and the limited dynamic range prevent the use of CAI sensors as standalone IMUs. Different solutions can be engineered to exploit the 'quantum advantage' of CAI sensors in navigation applications. Here, we report some examples.

2.2.1 IMU in zero-dead-time configuration

The presence of dead times in the sensor's cycle induces both aliasing noise and a reduced capability to capture the vehicle dynamics. Zero-dead-time (ZDT) can be achieved in pulsed interferometers by staggering different interferometers in time. This requires accurate synchronization of atom trapping and cooling, state preparation, Raman pulse timing, and detection [13]. The staggering could occur between different atomic sensors operating in parallel or within one sensor, in which the cooled atomic clouds are launched sequentially in a fountain configuration [27].
Continuous cooled (or thermal) atomic beam interferometers offer an alternative to pulsed counterparts, as they naturally allow for continuous measurements without the need to stagger multiple interferometers in time [28]. Here, atoms are not prepared in a cloud but are focused in a beam propagating in the direction transverse to the Raman beams.
The main drawback of pulsed-ZDT and atomic beam sensors is due to the fact that Raman pulses are delivered by multiple counter-propagating laser pairs that are physically spaced. This poses three main problems. First, the alignment of the multiple Raman pairs requires careful consideration, as eventual misalignments introduce both contrast decay and biases [29]. Second, the Raman light is delivered in the sensor head through independent optics and is retro-reflected by multiple mirrors. Therefore, variations in the optical path and non-common-mode wavefront distortions are potential instability sources. Third, the inertial scale-factor does not depend anymore on the time between the pulses, but on the physical distance between the Raman beams. This can be problematic, since in challenging environments, thermoelastic loads and structural

vibrations could induce variations in the spacing between the beams.
In any case, the ZDT mode does not resolve the issue of dynamic range stemming from phase ambiguity, as an aiding sensor is still necessary to lock the atomic sensor onto the correct fringe. A partial solution to this problem, at least for the gyroscope signal, could be the adoption of point-source interferometry read-out [28].

2.2.2 Hybridization with conventional IMU

Hybridization of CAI sensors with a conventional (or equivalently, classical) IMU combines the high data rate, bandwidth, and dynamic range of conventional inertial sensors with the high stability of atomic ones. The output from a conventional IMU serves essentially three purposes. Firstly, it provides quasi-continuous inertial measurements, enabling the capture of the vehicle's dynamics. Secondly, conventional IMU measurements can be correlated with interferometer measurements to solve phase ambiguity, monitor random phase due to vibrations, and compensate for off-resonance errors resulting from accelerations [17, 16, 30]. In contrast, the high stability and accuracy of the CAI sensor are used to estimate conventional sensor biases, leading to an improvement in long-term stability performance [31]. This type of sensor architecture, initially developed by LNE-SYRTE and then improved and implemented in the realization of a cold-atom accelerometer triad by iXBlue, is suitable for strapdown configurations and does not require bulky and expensive gyro-stabilized platforms. Although it constitutes an elegant solution to multiple problems, the hybridization of CAI sensors with a conventional IMU requires the implementation of complex real-time feedback mechanisms and a careful design of data-fusion algorithms. Moreover, the short-term sensitivity of the hybridized sensor will inevitably be limited by the conventional sensor. This is not necessarily a drawback, as in many cases, the cold-atom sensor may exhibit higher short-term noise than its conventional counterpart.

2.2.3 Gravity gradient based navigation

A gravity gradiometer exploits the simultaneous free-fall of two atomic ensembles to measure gravity gradients, effectively functioning as a differential accelerometer. The differential configuration contributes to the cancellation of several error sources that are common-mode between the two atomic clouds, leading to superior performance compared to cold-atom accelerometers and gyroscopes [32].
The idea of using cold-atom based gravity gradiometry for high-accuracy free-inertial navigation has first been proposed for submarine applications [33, 34]. Two main methods can be found in literature, both requiring the installation of the atomic sensors on stabilized platform in order to limit the error induced by attitude incorrect estimation. The first, called gravity-map matching, is a position-fixing technique that correlates the

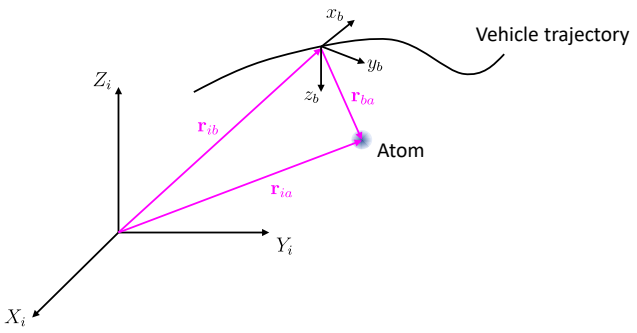

FIGURE 2.4: Cold-atom based local-positioning system exploits the interferometric measurements and the estimated absolute atomic motion to reconstruct the vehicle's position.

gradiometer measurements with predicted values from a gravity database via data-fusion algorithms [35]. The main limitation of this method is due to the resolution of the gravity database [2]. The second is a dead reckoning method, in which the gradiometer measurements are paired with the vehicle's velocity estimates to accurately estimate the gravity vector [36]. Clearly, this second method is suitable for INSs operating with high-performance sensors, where the ultimate navigation performance is limited by errors introduced by the gravity model.

2.2.4 Local positioning system

Specific forces and angular rates are indirect measurements of a CAI sensor. What a CAI sensor truly measures is a linear combination of the relative atomic positions ($\mathbf{r}_{ba}$) at each laser pulse. Knowledge of the gravitational field allows for the estimation of atomic motion with respect to an inertial frame ($\mathbf{r}_{ia}$). Therefore, the vehicle's position with respect to an inertial frame can be reconstructed by subtracting the atomic relative positions from the absolute atomic trajectory ($\mathbf{r}_{ib} = \mathbf{r}_{ia} - \mathbf{r}_{ba}$).
This approach has been termed local positioning system (LPS) as it uses known absolute atomic motion as a reference against which the vehicle's position is estimated [37]. From a certain perspective, the interferometric measurement is comparable to an ultra-accurate ranging measurement, resembling a 'local GPS'. Kasevich and Dubetsky proposed a stabilized platform mechanization to retrieve the position and velocity of a vehicle in the Earth Centred Earth Fixed (ECEF) reference frame using atomic sensors in a zero-dead-time configuration [38]. The major drawback of cold-atom-based LPS is the stringent requirement for precise knowledge of the local gravitational field to accurately determine the atomic absolute motion. Gravity anomalies not reported in databases could lead to significant errors in position estimation.

[2] For instance, the EGM2008 database is characterized by a 1 nautical mile resolution

Chapter 3

Error sources in cold-atom inertial sensors

Although cold-atom inertial (CAI) sensors have demonstrated high long-term stability and low noise in lab-based experiments, their performance in real-world scenarios is still, for the most part, unknown. CAI sensor performance deteriorates in dynamic environments mainly because of a decrease in signal-to-noise ratio due to disturbances such as platform vibrations and rotations, external magnetic fields, and relative motion of the hosting vehicle with respect to the atomic cloud [17]. In many cases, bulky gyro-stabilized platforms, magnetic field shielding, complex feedback mechanisms, and integration with aiding sensors are necessary to limit the impact of several error sources upon CAI sensor performance [39]. In this context, it is crucial to identify and analyze potential error sources in CAI sensors, their dependency on system parameters, and their impact on performance.

It is important to note that with the term 'error source,' we do not only refer to those affecting the sensor's output, i.e., the measured phase shift, but also those affecting the interferometric signal's visibility, i.e., fringe contrast. This is because, among other factors, contrast directly affects the signal-to-noise ratio and the availability of the sensor measurement.

The analysis of the impact of error sources on sensor performance is not an easy task, as it depends on the adopted pulse sequence, diffraction scheme, and overall architecture. For practicality, we focus on a CAI sensor based on a three-pulse Mach-Zehnder interferometer, in which the atomic matter-waves are diffracted by two-photon Raman diffraction.

Our analysis is organized as follows: first, we describe the sensor's system architecture from a functional perspective. Second, we identify and analyze several error sources grouping them on the basis of the affected performance. The analysis aims to disclose the physical mechanisms behind each error source, highlighting mutual interactions and their impact on the sensor's performance.

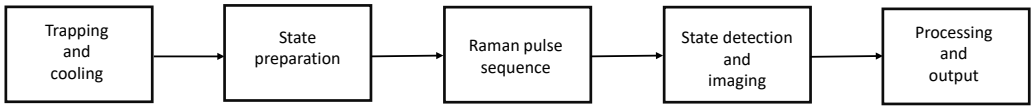

FIGURE 3.1: System architecture of a CAI sensor based on functional components.

3.1 System architecture

In general, five functional components, represented in Figure 3.1, can be identified as the main building blocks of a CAI sensor:

1. **Trapping and cooling**. Atoms are loaded from a background vapour into a magneto-optic trap (MOT). Ultra-high vacuum pressure levels ($< 10^{-9}$mbar) are required to avoid decoherence induced by atomic collisions with the background gas. Atoms are trapped in the zero of a quadrupole magnetic field and slowed by the scattering force of laser light tuned to a closed optical transition. Once the atomic thermal velocity is sufficiently small, the quadrupole field is switched off, and the intensity of the laser is decreased, further reducing the width of the thermal velocity distribution to an equivalent temperature of a few μK.

2. **State preparation**. At the end of the trapping and cooling stage, the atomic cloud is released from the optical molasses, and atoms populate all the Zeeman magnetic sub-levels, m_F, within a hyperfine ground state. Using optical pumping and microwave pulses, atoms are then prepared in the $m_F = 0$ state, which is, at first order, insensitive to magnetic fields. In some cases, additional laser pulses are used to selectively choose atoms from lower velocity classes. This ensures better efficiency in the Raman diffraction process and higher contrast.

3. **Raman pulse sequence**. Atoms prepared in the $m_F = 0$ state interact with three Raman laser pulses. The first pulse acts like a beam-splitter, diffracting the atomic wave-function into a coherent superposition of two states. After the first pulse, the atomic wave-function exists in a coherent superposition of both internal and momentum states and evolves freely for a period T. The second pulse acts like a mirror, inverting the atomic states and redirecting them. The wave-packets propagate for a second free-evolution period of duration T, and at the end of it, a third pulse recombines them, ensuring interference.

4. **State detection and imaging**. The interferometric signal is obtained in the form of a probability by measuring the fraction of atoms in one of the two Mach-Zehnder states. Laser pulses tuned to optical transitions are used to transfer atoms to

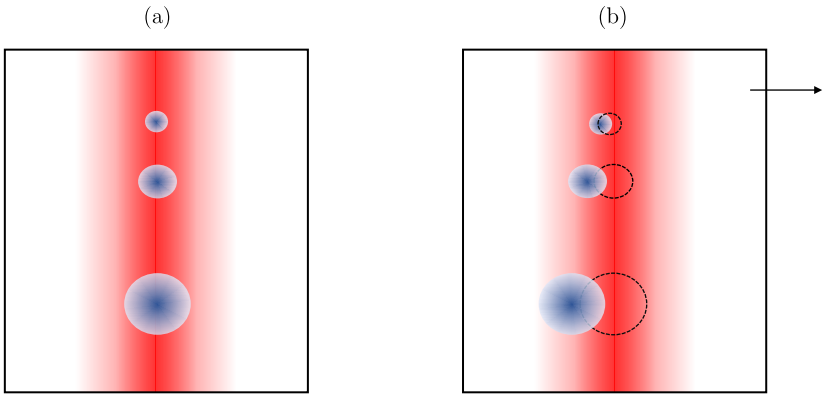

FIGURE 3.2: Coupling between atomic trajectories and spatial inhomogeneities in the intensity profile of the Raman beam. Panel (a): static conditions. Panel (b): dynamic conditions.

excited states, during which photons are emitted. By counting the number of photons with a photodetector, the probability of having the atoms in one of the two states - and thus the interferometric signal - can be determined. Two main read-out techniques are used in CAI sensors: cloud-averaging and point-source interferometry (PSI). In PSI, the interferometric signal is imaged onto a plane in the form of a spatial probability distribution [40]. In cloud-averaging, the interferometric signal is obtained by averaging the probability distribution over the entire atomic cloud, thus requiring scanning of the laser phase to extract inertial information.

5. **Processing and output**. The inertial information is embedded in the phase of the interferometric signal. Depending on the detection scheme, phase extraction requires discriminating the rotation-induced phase (gyroscope signal) from the acceleration-induced phase (accelerometer signal), resolving phase ambiguity, and performing optimal estimation.

3.2 Contrast loss mechanisms

3.2.1 Pulse-length errors

Pulse-length errors arise from the coupling between atomic trajectories and spatial inhomogeneities in the intensity profile of the Raman beam. Typically, Raman laser beams with Gaussian intensity profiles are utilized in light-pulse atom interferometry applications. Gaussian beams are easily achievable experimentally and enable high peak intensities.

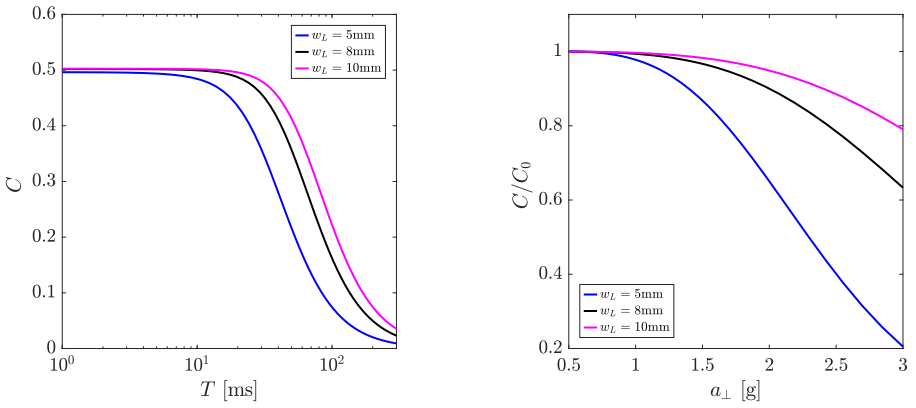

(A) Static (B) Dynamic

FIGURE 3.3: Simulated effect of pulse-length errors on contrast loss. Panel (A): Coupling between the atomic cloud expansion in the plane transverse to the Raman axis and laser intensity inhomogeneity. We assume a beam-splitter pulse duration $\tau = 5\mu$s and cloud temperature $\mathcal{T} = 5\mu$K. Panel (B): fractional contrast decay due to an acceleration transverse to the Raman propagation axis for free-evolution time $T = 10$ms. In both cases we assume a Gaussian intensity profile and ^{85}Rb atoms.

Under static conditions, the spatial inhomogeneity of the intensity profile couples with the expansion of the atomic cloud in the plane orthogonal to the Raman wave-vector direction, thereby inducing a decay in the contrast of the interferometric signal. This decay depends on the width of the atomic space and velocity distributions, as well as on the waist of the intensity profile. In practice, the intensity profile deviates from a Gaussian mode: higher-order Gauss-Laguerre modes and localized inhomogeneities, such as bright spots and intensity rings, further impact the interferometric signal, resulting in reduced contrast [41].

Under dynamic conditions, accelerations acting in the transverse direction to the Raman axis, as shown in Figure 3.2, induce a relative displacement between the center-of-mass of the atomic cloud and the centroid of the Raman beam, leading to further contrast loss.

Figure 3.3 shows the simulated effects of pulse-length errors on interferometer's contrast for both static and dynamic conditions. As expected, the longer the free-evolution time, the more the atomic cloud expands, experiencing intensity variations, and consequently, the more the contrast drops. For the simulation of the dynamic condition case, we assume that the atomic cloud is perfectly centered with the Raman beam at the time of the first pulse. For a free-evolution time of 10ms, a beam waist of 10mm is required to have negligible fractional contrast loss up to 1.5g of transverse acceleration. Clearly, the longer the free-evolution time, the higher the contrast loss for a given acceleration.

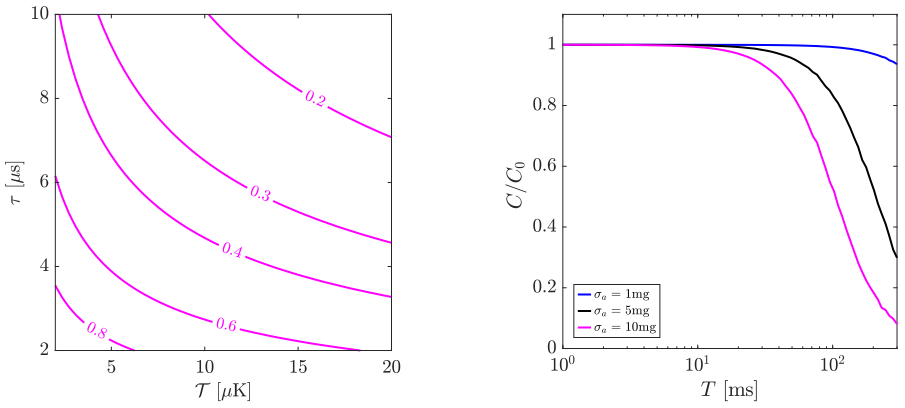

(A) Pulse duration and longitudinal temperature

(B) Longitudinal vibrations

FIGURE 3.4: Effect of off-resonance errors on contrast loss. Panel (A): effect of pulse duration and longitudinal temperature on interferometer contrast for a free-evolution time $T = 10$ms. Panel (B): fraction of contrast decay due to the effect of longitudinal vibrations for beams-splitter duration $\tau = 5\mu$s. In both cases we assume ^{85}Rb atoms.

3.2.2 Off-resonance errors

Off-resonance errors arise from detuning sources. While the light-shift term is typically suppressed by adjusting the intensities of the Raman lasers, the recoil shift is compensated for by shifting the laser frequencies. If the atoms are correctly prepared in the $m_F = 0$ state, the quadratic Zeeman shift is negligible for magnetic fields of the order of a few hundred milli-Gauss. The presence of a residual number of atoms in the $m_F \neq 0$ states could cause contrast decay and magnetic-dependent phases. However, the application of a sufficiently large bias field would render these states off-resonant.

In a counter-propagating arrangement, the primary source of off-resonance errors is the Doppler shift resulting from the component of the relative atomic velocity along the Raman effective wave-vector. The efficiency of the Raman diffraction depends on the convolution between the atomic velocity distribution and the spectral profile of the pulse. The width of the spectral profile is proportional to the effective Rabi frequency; therefore, a high Rabi frequency is required to improve the transfer efficiency.

The presence of an acceleration along the Raman axis is a further source of Doppler detuning. The higher the free-evolution time, the higher the contrast loss induced by a longitudinal accelerations.

Figure 3.4 shows the simulated effect of off-resonance errors on contrast decay. In the simulations, we consider both the influence of the Raman pulse duration and the longitudinal velocity distribution (expressed here as a function of an equivalent temperature). For a given velocity distribution, the shorter the pulse duration (i.e., the higher the Rabi frequency), the less the contrast decay. Furthermore, we analyse the impact of longitudinal vibrations on the contrast. As a rule of thumb, vibrations do not typically constitute a significant source of contrast loss if the induced Doppler shift is much

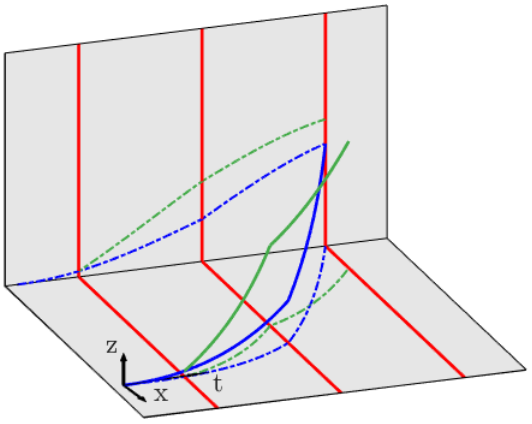

FIGURE 3.5: Effect of the rotation of the Raman beam upon the wave-packets trajectories. The green (blue) colour represents the upper (lower) arm of the interferometer. For completeness, we added also the effect of an acceleration along the z-axis. At the first pulse, the Raman beam is aligned with the z-axis. The red lines indicate the times at which the laser pulses occur. A rotation acting about the y-axis determines an 'open' interferometer configuration.

smaller than the Rabi frequency, i.e., $k_{\text{eff}}\,\sigma_a\,T \ll \Omega_{\text{eff}}$. Therefore, for a given interrogation time, vibrations are less critical for atomic species characterized by a lower value of the effective wave-vector [1].

3.2.3 Rotations of the Raman beam

A rotation of the Raman beam relative to the atomic trajectory leads to contrast loss through two primary mechanisms.
Firstly, when the Raman beam rotates during the pulse sequence, it induces a variation in the momentum kick imparted to the centers of mass of the atomic wave-packets traveling along the upper and lower arms of the Mach-Zehnder interferometer. Consequently, the wave-packets at the time of the final pulse do not perfectly overlap, resulting in reduced interference and contrast reduction [42]. Figure 3.5 shows the upper and lower atomic trajectories in presence of a transverse angular rate and a longitudinal acceleration. The extent of contrast decay depends on the size of the wave-packets at the output port of the interferometer and on the free-evolution time. The wave-packet size is determined by both the atomic momentum distribution and the velocity selectivity of the Raman diffraction process [43].
Secondly, in a CAI sensor with PSI detection, the finite size of the initial atomic cloud couples with angular rates, further reducing the contrast [44]. The initial cloud can be envisioned as an ensemble of point sources that expand over time, accumulating a phase shift proportional to the angular rate via the atomic thermal velocity (Coriolis

[1] For instance, Cs has an effective wave-vector that is 87% of Rb's one.

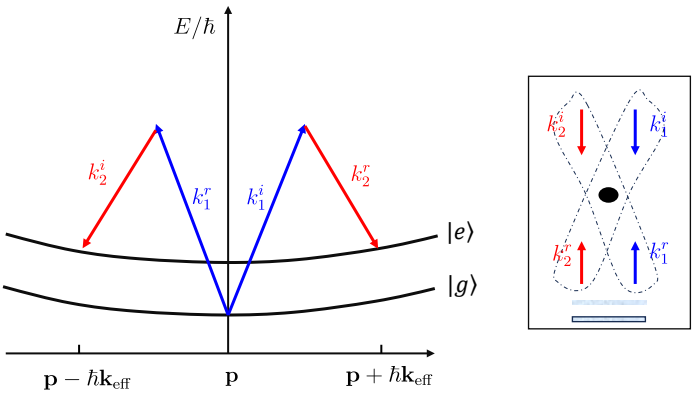

FIGURE 3.6: Energy diagram of Raman diffraction in presence of retro-reflection. The retro-reflecting arrangement induces a double-diffraction scheme that couples multiple momentum states. In the picture, we truncate the momentum ladder to the $\pm\mathbf{k}_{\text{eff}}$ orders.

acceleration). When the cloud is imaged onto a CCD, the averaging process over the velocity distribution results in contrast reduction.

3.2.4 Wavefront distortions

Wavefront distortions couple with atomic trajectories, imprinting position-dependent phases. When averaging over the phase-space distribution, the interference induced by these phases leads to contrast loss.
In most scenarios, wavefront distortions are not the primary source of contrast decay. However, for extended free-evolution times (typically exceeding 100ms) or in sequences involving large momentum transfer, contrast decay resulting from aberrated wavefronts could become significant [45].

3.2.5 Retro-reflection effects

In a retro-reflecting configuration, the incident and reflected wave-vectors generate a momentum ladder, causing Raman transitions to couple multiple momentum states, as shown in Figure 3.6. Consequently, the atomic evolution is no longer described by a single-diffraction process within an effective two-level system. Limiting our attention to the states $|g, \mathbf{p}\rangle$ and $|e, \mathbf{p} \pm \hbar\mathbf{k}_{\text{eff}}\rangle$, a sufficient separation between the $\pm\mathbf{k}_{\text{eff}}$ transitions must be ensured in order to have single-diffraction. However, when this separation is insufficient, a pulse with a high Rabi frequency may excite unwanted transitions, leading to contrast decay [22]. The excitation of unwanted transitions is particularly critical for beam-splitter pulses, which exhibit a higher bandwidth compared to mirror pulses [46].

3.2.6 Detection

PSI detection impacts the contrast of the interferometric signal in the presence of spatial modulation induced by rotations. Firstly, contrast loss occurs due to misalignments between the imaging line-of-sight and the direction orthogonal to the rotation-induced wave-vector. Therefore, to achieve maximum contrast, the imaging line-of-sight should be orthogonal to the spatial modulation. Secondly, long imaging pulses may induce blurring and distortions in the atomic cloud, further reducing contrast [40].
However, PSI detection does not involve averaging over the spatial distribution. Consequently, the contrast decay in the presence of rotations is lower compared to the conventional detection method [40].

3.3 Systematic errors

3.3.1 High-order inertial effects

As stated before, what a CAI sensor really measures is a linear combination of the relative position of the atomic cloud with respect to the laser frame at the different pulses. To find the relative atomic position at the time of each laser pulse, one must solve the equations of motion in the laser rotating frame. For constant specific forces and angular rates, the solution of the equation of motion contains terms that give rise to spurious phase shifts, which depend on the vehicle's dynamics and the duration of the interferometric sequence [47]. These high-order inertial effects are due to couplings between accelerations and angular rates acting along axes orthogonal to the sensitive one and are analogous to anisoinertia bias in classic inertial sensors.
Gravity gradients are another form of high-order inertial effect, as they modify the atomic trajectories, introducing error phases .

3.3.2 Quadratic Zeeman effect

The energy levels of atoms in the $m_F = 0$ Zeeman state exhibit a quadratic magnetic field dependency. A DC field does not affect a CAI sensor because the phase accumulated by the atomic wavefunction is the same in the two halves of the interferometer. However, if the atoms experience time-varying magnetic fields during the interferometric sequence, a phase error arises. Magnetic fields affect a CAI sensor through three main mechanisms [48]:

- Temporal variations. Purely temporal magnetic field variations are mainly due to eddy currents that manifest as transients of the switch-on/off of the magnetic coils during the trapping stage and serve as a bias source.

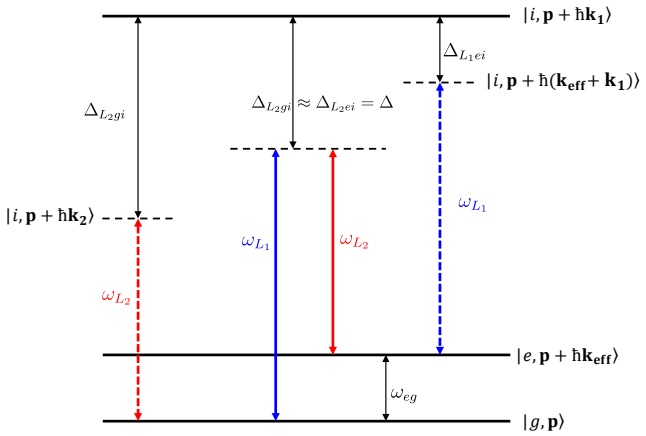

FIGURE 3.7: Internal state energy diagram (not to scale) of the Raman diffraction process. The one-photon light-shifts are due to the self-coupling terms in the effective two-level system.

- Spatial variations along the Raman axis. Spatial inhomogeneities of the magnetic field couple with atomic trajectories along the Raman axis, giving rise to bias and scale-factor errors.
- Magnetic gradient force. A spatial variation of the magnetic field determines a state-dependent force that modifies the atomic trajectories in a Mach-Zehnder interferometer, introducing a further source of bias and scale-factor errors.

3.3.3 Light-shifts

3.3.3.1 One-photon light-shift

Stimulated Raman transitions couple states $|g, \mathbf{p}\rangle$ and $|e, \mathbf{p} + \hbar\mathbf{k}_{\text{eff}}\rangle$ via a far-detuned upper state, as presented in Figure 3.7. One-photon light-shifts (OPLS), or AC Stark shifts, represent self-coupling terms that shift the atomic energy levels according to the laser intensity, polarization, and detuning from the upper state. OPLS is typically suppressed by carefully adjusting laser intensities or frequencies [49]. However, variations in laser intensity from the nominal value can lead to a residual sensitivity to light-shifts, which couples with asymmetries induced by the expansion of the atomic cloud in the presence of spatial intensity inhomogeneities, thus resulting in systematic errors.

3.3.3.2 Two-photon light-shift

Additional light-shifts occur when implementing a laser counter-propagating arrangement with a retro-reflecting mirror. The presence of both momentum states, $|\mathbf{p} \pm \hbar\mathbf{k}_{\text{eff}}\rangle$,

in the Raman diffraction process allows for double transitions in both wave-vector directions. To resolve this Doppler degeneracy and prevent double-diffraction, the Raman transitions in the two wave-vector directions must be sufficiently separated in frequency. This can be achieved through either Doppler detuning [50] or by chirping the laser frequency during the laser pulses [51]. By doing so, the Raman laser can be tuned to one of the two counter-propagating transitions, and the atomic matter-waves undergo standard single-diffraction. However, the presence of an off-resonance transition shifts the atomic energy levels of the resonant one. This detuning is known as two-photon light shift (TPLS) and depends on the Rabi frequency and the detuning between the two momentum transitions [52]. Therefore, TPLS is a systematic error source if there are variations in the Rabi frequency or in the detuning experienced by the atoms during the interferometric sequence.

3.3.4 Wavefront distortions

Non-flatness of the Raman laser wavefront represents one of the major systematic errors in CAI sensors [53]. It can be induced by laser intensity inhomogeneity, collimation errors, or by imperfections in the optical elements through which the laser propagates. The phase error impressed by the distorted wavefront onto the atomic wavefunction depends on the position of the atom within the wavefront itself, in the plane orthogonal to the laser propagation axis. For these reasons it is a function of different parameters such as the sensor configuration, the expansion time of the atomic cloud, the width of the transverse velocity distribution, the type of wavefront distortion, the Raman beam waist, the detection beam radius [53]. Long-term drifts in atomic trajectories are a major source of bias instability when coupled with wavefront distortions.
In CAI sensors with PSI detection, wavefront distortions are particularly critical as they are directly mapped onto the interferometer signal without any averaging process over the space distribution. Consequently, the distribution of phase errors distorts the fringes and severely impacts the extraction of rotational and acceleration signals.

3.3.5 Asymmetry of the interferometer

Variations of the Rabi frequency experienced by the atoms during the first and last pulse or timing errors in the pulse sequence break the temporal symmetry of the interferometer with respect to the central mirror pulse. As a consequence, the CAI sensor becomes sensitive to a steady detuning leading to systematic errors [54]. This occurs because the phase accumulated by the atoms during the first half of the interferometer is no more compensated by the phase shift accumulated during the second half. The major error source is constituted by the asymmetry and/or the offset of the longitudinal atomic velocity distribution entering the pulse sequence.

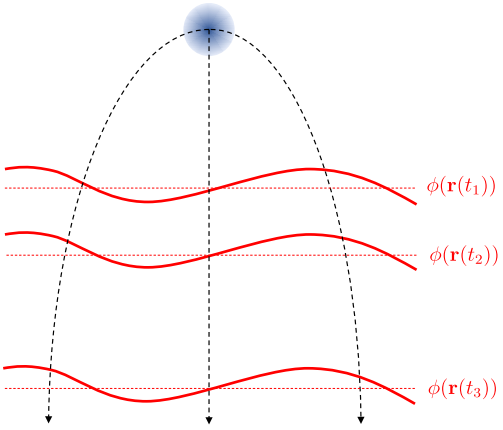

FIGURE 3.8: The interaction between distorted wavefronts and atomic motion occurs in the transverse plane. The phase imposed on the atom at each pulse depends on its position within the distorted wavefront.

3.3.6 Atomic cloud properties: initial size and cloud density

3.3.6.1 Initial size

The finite initial size couples with spatial-dependent phases, such as those caused by rotations and wavefront distortions, leading to systematic errors. Specifically, in a CAI sensor based on PSI detection, the initial size of the cloud affects the rotational scale-factor as a result of the blurred position-velocity correlations in phase-space.

3.3.6.2 Atomic density

The atomic density is a source of systematic errors through two main mechanisms: variations of the refractive index and cold-atom collisions.
The actual momentum imparted to the atom by the Raman laser depends on the refractive index of the medium [55]. The density of the atomic cloud (ρ) modifies the refractive index, and, therefore, the momentum kick imparted to the atomic wave-packets. The momentum imparted to the atom at each pulse is given by $n\,\hbar k_{\text{eff}}$, where the refractive index $n = \sqrt{1 + \text{Re}\{\chi\}}$, and χ is the atomic susceptibility [56]. For a two-level system, with a single-photon detuning (Δ) much larger than the Rabi frequency and the transition natural linewidth (Γ), we get $n = 1 + \delta n$, with $\delta n \approx -(3/2)\,(\pi/k_0^3)\,(\Gamma/\Delta)\,\rho$, and k_0 laser wave-number. The variation of the refractive index, δn, induces systematic errors that depend on the density of the atomic cloud, and the coupling with the atomic trajectory along the Raman axis.
Cold-atom collisions determine a shift of the energy levels that depends on the density of the atomic cloud and on the atomic state [57]. Since, the atomic cloud expands

during the interferometric sequence, its density, and hence, the detuning from Raman transition varies determining a bias that depends on the initial atomic phase-space distribution and on the number of atoms.

3.3.7 Finite pulse duration

The finite duration of Raman pulses affects the scale-factor of a CAI sensor. This can be understood in geometric terms, considering that the scale-factor is proportional to the area enclosed by paths along which the atomic wavepackets travel during the interferometric sequence. A pulse with a finite duration diffracts the center of mass of the wavepacket along paths that differ from the infinitely short duration case [58]. Drifts of the Raman intensity from the nominal value result in a variation of the Rabi frequency, which translates into an effective pulse-length error further affecting the sensor's scale-factor.

3.3.8 Misalignment of the Raman axis

Misalignments of the Raman axis with respect to the vehicle's body frame induce systematic errors in the form of cross-couplings between the different sensitive axes and scale-factor errors. For instance, a tilt of the Raman axis relative to the transverse plane, determined by the x_b and y_b axes, results in a scale-factor error $SF_\epsilon \approx \theta_\perp^2/2$.

3.3.9 Spontaneous emissions

Spontaneous emissions induce decoherence in the interferometric signal, and their probability of occurrence is proportional to the overall time that the Raman laser remains on. Therefore, spontaneous emissions are more critical for atom interferometers operating in large momentum transfer configurations.
A second effect of spontaneous emissions is represented by the so-called coherent population trapping (CPT). The term CPT refers to the phenomenon in which, due to spontaneous emissions, atomic populations become trapped in a dark state, which is a coherent superposition of the two ground states. Because of CPT, the atomic wavefunction accumulates a phase during the first beam-splitter pulse that affects the interferometric phase [59].
Both decoherence and CPT can be mitigated by choosing a large single-photon detuning ($\Delta > 2$GHz).

3.3.10 Multiple Raman lines

The two Raman lasers are typically generated from a common seed through modulation using an electro-optic modulator. When the modulation produces a comb-like spectrum with each electric field line separated by a frequency close to the hyperfine splitting, multiple electric field pairs drive the Raman transition [60]. The presence of parasitic transitions leads to variations in the momentum imparted to the atom, generating a ladder of momentum states. Consequently, the atomic evolution is no longer described by a two-level system. Since each transition imparts a slightly different momentum to the wavepackets, multiple spurious paths originate from each laser pulse, resulting in systematic effects [60].
This effect can be mitigated using optical single-sideband modulation [61].

3.3.11 Detection

The detection process introduces systematic errors due to the convolution of its response function with the atomic distribution.
In conventional cloud-averaging detection, an offset of the atomic distribution relative to the center of the response function results in asymmetric detection of velocity classes. When averaging over space, more atoms from one of the tails of the velocity distribution contribute to the interferometric signal. Consequently, the detected velocity distribution exhibits an apparent offset, leading to systematic effects on the acceleration signal in the presence of angular rates [62].
In PSI detection, systematic errors arise from three main mechanisms: motion blur, optical distortions and misalignments, and finite resolution of the CCD. Motion blur is caused by the relative motion of the atoms with respect to the imaging system, with accelerations in the transverse plane and thermal expansion of the atomic cloud due to recoil heating being the primary sources. Additionally, blurring of the detected atomic distribution is induced by optical distortions of the imaging system. An important effect is represented by the misaligments in the telescope system used to image the atomic cloud, resulting in magnification errors that directly affect the estimation of the spatial frequency modulation. Lastly, the sampling process due to the finite resolution of the CCD leads to aliasing, resulting in detected spatial frequencies differing from the nominal ones.

3.4 Noise

3.4.1 Raman laser

3.4.1.1 Phase noise

Phase noise is due to phase fluctuations in the two Raman frequency components. If these components share the same optical path, phase noise due to perturbations in the path becomes common-mode between them and does not impact the interferometer output. The primary source of phase noise is typically the RF chain utilized for frequency modulation and the generation of Raman components [61].
Phase affects interferometer performance because atoms interact with laser fields for a finite time. The interferometer behaves as a band-pass filter, with its bandwidth determined by the free-evolution time at low frequencies, and by the pulse shape and duration at high frequencies [63]. For a given maximum intensity, a smooth waveform allows for better rejection of high-frequency noise. This can be understood because the high-frequency response of the interferometer is essentially determined by the Fourier transform of the pulse. Therefore, pulses characterized by sharper edges and shorter duration have a larger bandwidth (in the limit of a Dirac pulse, the bandwidth is infinite).

3.4.1.2 Frequency noise

In a retro-reflecting mirror arrangement, the time at which the atomic cloud interacts with the incident laser and the reflected laser differs due to the finite speed at which light propagates. This time delay couples with the Raman frequency noise, inducing a degradation of the signal-to-noise ratio of the interferometer. The degradation is proportional to the time delay and, hence, to the distance between the position at which the atomic cloud interacts with the Raman pulses and the retro-reflecting mirror [64].

3.4.1.3 Intensity noise

Temporal intensity noise affects the interferometric signal via light-shifts. Low-frequency intensity noise affects the interferometer mainly via TPLS, while high-frequency intensity noise is dominated by the OPLS. In particular, in the case of OPLS, the longer the laser-atom interaction, the higher the noise imparted to the atomic wavefunction. Therefore, laser intensity noise is particularly critical for large momentum transfer interferometers.
Spatial intensity noise, resulting from factors such as poor quality optics, induces short-scale phase fluctuations that locally distort the laser wavefronts. This leads to spatial

fluctuations in the momentum imparted to the atomic wavepackets and introduces noise into the interferometric signal. This effect has more impact on PSI sensors, as the conventional detection method significantly suppresses this local effect through averaging over the spatial distribution [65].

3.4.2 Magnetic noise

Temporal and spatial fluctuations of the magnetic field experienced by the atoms during the interferometric sequence affect the noise performance of the CAI sensor via the quadratic Zeeman effect. We anticipate that both the temporal and spatial frequency responses are characterized by a band-pass-like structure, with the bandwidth determined by the duration of the free-evolution time. Specifically, the longer the free-evolution time, the higher the sensitivity of the interferometer to low-frequency temporal noise and long-wavelength spatial noise.

3.4.3 Vibrations

Vibrations are one of the dominant noise sources in CAI sensors [20]. Both linear and angular vibrations cause random fluctuations in the relative position of the laser wavefronts with respect to the atomic position. The frequency response of the interferometer to vibrations exhibits a low-pass filter behavior, with the bandwidth determined by the free-evolution period. Specifically, the longer the free-evolution period, the higher the induced phase noise.
Linear vibrations along the direction of the Raman axis directly affect the acceleration signal, while vibrations in the plane transverse to the Raman axis couple with wavefront distortions, impacting both acceleration and rotational signals [66]. Angular vibrations result from the pointing jitter of the Raman axis and affect both the rotational and acceleration signals.

3.4.4 Dead time effects

Aliasing noise affects the performance of CAI sensors operating in pulse-mode, as dead times associated with trapping, cooling, preparation, and atom detection are unavoidable. During these dead times, no measurements are taken, resulting in uncorrelated noise from different sensor cycles. This directly affects the slope of the Allan deviation of the interferometric signal, which scales as $1/\sqrt{\tau_c}$, with τ_c representing the cluster time. Additionally, the sensor will be affected by noise at multiple integers of the cycling frequency, inducing an aliasing phenomenon similar to that observed in atomic clocks [67].

3.4.5 Detection

3.4.5.1 Atom shot noise

Atom shot noise sets the ultimate theoretical limit of a CAI sensor operating with unentangled atoms and its nature is purely statistical [68]. At the end of the Raman pulse sequence, the Mach-Zehnder interferometer presents two output ports in which the probability to find the atoms in one of the two states follows, in the approximation of central limit theorem, a Gaussian distribution with standard deviation $1/\sqrt{N}$, where N is the total number of detected atoms.

3.4.5.2 Photon shot noise

Atomic populations are detected by measuring the number of emitted or absorbed photons. Photon shot noise is not connected to any quantum phenomenon and arises from the random arrival times of photons in a detection system. Photon shot noise is due to the discrete nature of photon arrivals and can be described by a Poisson distribution with standard deviation $\sqrt{N_p}$, where N_p is the number of detected photons.

3.4.5.3 Technical noise

The laser system used for state detection and imaging is a primary source of technical noise through frequency and intensity fluctuations.
The photodetector is an additional source of technical noise. For instance, random fluctuations in pixel-to-pixel sensitivity, dark current, and thermal noise in the photodetector amplifier circuits (Johnson noise), are noise sources in a CCD.
Finally, stray light scattered by the vacuum chamber walls and fluorescence from background atoms also contribute to technical noise during the detection process.

Chapter 4

The sensitivity function formalism

The output of an atom interferometer is represented by the phase shift resulting from the interference of the wavepackets traveling along its arms. During the time evolution, the wavepackets accumulate a phase that, in general, will depend on the interaction between the laser and the atomic system at each pulse.
Although various formalisms have been proposed in the literature to compute the output of an atom interferometer, none of them exhibit the unique features of the sensitivity function. For instance, the Feynman path integral approach [47] and the density matrix in Wigner representation [69] have been used to obtain analytic expressions of high-order inertial phase shifts, but they neglect the effect of the finite pulse duration. The transfer matrix approach has been employed to take into account finite laser pulse duration effects, but it comes at the cost of great analytic complexity [58, 70, 71]. Moreover, none of the previous formalisms can be extended to describe the phase response of the interferometer to a general time-varying input without adding further complexity. In contrast, the sensitivity function formalism provides the phase response of an atom interferometer to time-varying inputs and accounts for finite pulse effects in an easy and intuitive fashion [72]. Furthermore, its counterpart in the frequency domain allows for the determination of the interferometer response to stochastic inputs, closely resembling the transfer function approach in system engineering [67].

Given a pulse sequence, the sensitivity function formalism provides:

- Scale-factor of the interferometer. This is obtained when the input is represented by the intended quantity to be measured, i.e. angular rates and specific forces.
- Bias of the interferometer. This is obtained when the input is given by an error source (e.g. time-varying magnetic fields, light-shifts, etc.). The capability to describe the phase response to time-varying inputs also allows for the estimation of maneuvering-dependent bias (e.g. response to acceleration jerk, angular acceleration or cross-axis effects).

- Noise performance of the interferometer. The frequency-domain representation of the sensitivity function allows for the determination of the uncertainty of the interferometric phase for a given noise source.

Although, the interferometer phase response can be obtained analytically in the case of conventional rectangular pulses, the sensitivity function formalism can be easily extended to the case of tailored pulses that exhibit time-varying power profiles [63], thus enabling the possibility to study the effects of non-resonant pulses [73].

These features make this formalism suitable for developing an error model for the interferometer and can be utilized in real-time systems to suppress certain error sources [30]. For these reasons, we will extensively employ the sensitivity function throughout this thesis work to quantitatively estimate how the system parameters of the interferometer influence the performance of the cold-atom inertial (CAI) sensor.

The chapter is organized as follows:

1. We introduce and define the phase sensitivity within a general framework, accounting for both cases where the superposed states are in different internal and momentum states ($\pi/2 - \pi - \pi/2$ Raman pulse sequence) or in the same internal state but different momentum states (Bragg or composite alternate pulse sequences).

2. Focusing on the $\pi/2 - \pi - \pi/2$ scheme using rectangular Raman pulses, we present the phase sensitivity function, taking into account finite pulse duration effects and non-resonant conditions. Furthermore, we extend the formalism to analyze the interferometer's response to a general time-varying deterministic or stochastic input.

3. We show how to compute the interferometer's response to inertial effects, encompassing linear accelerations and angular rates, whether they are acting along the sensitive axis or along a direction orthogonal to it.

4. Building on previous works that focused on the interferometer's response to phase noise and longitudinal accelerations, we extend the formalism to encompass time- and space-varying magnetic fields, one- and two-photon light-shifts, and atomic collisions.

5. We show how to combine properly multiple atom interferometers in order to achieve uniform sensitivity in zero-dead-time (ZDT) mode and the effects upon the inertial sensor short-term sensitivity.

4.1 The phase sensitivity function

First introduced by Dick in his seminal paper [74] to study the instabilities caused by local oscillators in atomic clocks, the sensitivity function formalism has been extended to atom interferometry by SYRTE group [67].
The sensitivity function is defined as the response of the interferometric signal to an infinitesimal phase step input [67]. The interferometric signal is represented by the relative number of atoms measured at one of the output ports of the interferometer

$$P_2 = P_0 - \frac{C}{2}\cos(\Delta\Phi)\,, \tag{4.1}$$

where $|1\rangle$ and $|2\rangle$ are the two interferometer's atomic states, P_0 is the interferometric signal offset, C is the contrast, and $\Delta\Phi$ is the interferometric phase. Assuming that $\Delta\Phi = \Delta\Phi_0 + \delta\phi$, where $\Delta\Phi_0$ is a controllable phase offset and $\delta\phi$ is a small perturbation such that $|\delta\phi| \ll 1$, we obtain

$$P_2 = \underbrace{P_0 - \frac{C}{2}\cos(\Delta\Phi_0)}_{P_{2,u}} + \underbrace{\frac{C}{2}\sin(\Delta\Phi_0)\delta\phi}_{\delta P_2}\,, \tag{4.2}$$

with $P_{2,u}$ and δP_2 the unperturbed signal and first-order perturbation term, respectively. Note that the perturbation term δP_2 is maximum when $\Delta\Phi_0 = \pi/2$ and minimum when $\Delta\Phi_0 = 0$; this is in agreement with the fact that the interferometer's maximum (minimum) sensitivity is achieved on the side (bottom) of the central fringe [50].
The sensitivity function is obtained evaluating the variation of the first-order perturbation term with respect to the magnitude of the phase perturbation

$$g(t) \coloneqq \lim_{\delta\phi\to 0} \frac{\delta P_2(t)}{\delta\phi}\,, \tag{4.3}$$

where the perturbation $\delta P_2(t) = P_2(t) - P_{2,u}$ is given by the difference between the perturbed and the unperturbed interferometric signals, and the perturbed signal $P_2(t)$ is computed assuming a phase perturbation $\delta\phi(t) = \delta\phi\,\Theta(t' - t)$, with $\Theta(\dots)$ the Heaviside step function.
In an analogous way, we can define the phase sensitivity function as the variation of the interferometric phase with respect to the magnitude of an infinitesimal perturbation phase

$$g_\phi(t) \coloneqq \lim_{\delta\phi\to 0} \frac{\Delta\Phi(t)}{\delta\phi} = \frac{2}{C\sin(\Delta\Phi_0)} g(t)\,, \tag{4.4}$$

where $\Delta\Phi(t)$ is the interferometric phase accumulated during the pulse sequence. Unlike the sensitivity function that exhibits a dependency on the contrast and the working point of the interferometer [67], the phase sensitivity function is normalized with respect to the contrast and offset phase. This ensures that interferometric phase accumulated by a mono-kinetic atom does not depend on the contrast or phase offset.
The interferometric phase can be computed from Eq. (4.4) as

$$\Delta\Phi = \int_{-\infty}^{+\infty} g_\phi(t)\,\frac{d\phi}{dt}\,dt\,, \tag{4.5}$$

where $\phi(t)$ is the phase of the atomic wavefunction. Eq. (4.5) is the cornerstone of the sensitivity function formalism: the interferometric phase is given by the rate of change of the phase accumulated by the atomic wavefunction, weighed by the phase sensitivity function.

4.1.1 Internal state vs momentum state

Assuming a potential at most quadratic in space, the interferometric phase can be computed using the midpoint theorem [75]

$$\Delta\Phi = \sum_{i=1}^{N} \underbrace{(k_{1,i} - k_{2,i})\,\bar{z}_i}_{\Delta\Phi_k}\ \underbrace{-(\omega_{1,i} - \omega_{2,i})\,t_i + (\varphi_{1,i} - \varphi_{2,i})}_{\Delta\Phi_{\text{int}}} \tag{4.6}$$

where $k_{n,i}\,\bar{z}_i$, $\omega_{n,i}$ and $\varphi_{n,i}$ are, respectively, the position-dependent phase, the effective angular frequency and the effective arbitrary phase acquired by the atomic wavepackets travelling along the n-th arm of the interferometer and at the i-th laser pulse [1]. We note that the interferometric phase exhibits a term that depends on the spatial separation between the arms of the interferometer, i.e. on the atomic momentum state ($\Delta\Phi_k$), and a term that depends only on the internal state ($\Delta\Phi_{\text{int}}$). The terms $k_{n,i}$, $\omega_{n,i}$ and $\varphi_{n,i}$ have a positive (negative) sign if the atom gains (loses) energy; they are zero if no energy variation occurs.

Applying the midpoint theorem to the case of a $\pi/2 - \pi - \pi/2$ interferometer using rectangular Raman pulses, leads to

$$\Delta\Phi_{\text{int}}^{(3P)} = \varphi_{1,1} - (\varphi_{1,2} + \varphi_{2,2}) + \varphi_{1,3} = \varphi_{\text{eff},1} - 2\varphi_{\text{eff},2} + \varphi_{\text{eff},3}\,, \tag{4.7}$$

[1] The quantity $\bar{z}_i = (z_{1,i} - z_{2,i})/2$ is the midpoint trajectory, or, equivalently, the centre-of-mass trajectory described by the atomic wavepackets travelling along the upper and lower arm of the interferometer. The quantity $k_{n,i}$ represents the Raman effective wave-vector.

$$\Delta\Phi_k^{(3P)} = k_1\,\bar{z}_1 - 2\,k_2\,\bar{z}_2 + k_3\,\bar{z}_3\,, \tag{4.8}$$

We note that the momentum and the internal state dependent phase have the same form. This is due to the fact that at each pulse both the internal and momentum state change accordingly. Then we expect that the internal state and momentum state phase sensitivity functions are equivalent.
In contrast, considering the alternate composite sequence of Ref. [76] we obtain

$$\Delta\Phi_{\text{int}}^{(ACP)} = \varphi_{\text{eff},1} - \varphi_{\text{eff},2} - \varphi_{\text{eff},3} + 2\varphi_{\text{eff},4} - \varphi_{\text{eff},5} - \varphi_{\text{eff},6} + \varphi_{\text{eff},7} \tag{4.9}$$

$$\Delta\Phi_k^{(ACP)} = k_1\,\bar{z}_1 + k_2\,\bar{z}_2 - k_3\,\bar{z}_3 - 2\,k_4\,\bar{z}_4 - k_5\,\bar{z}_5 + k_6\,\bar{z}_6 + k_7\,\bar{z}_7\,. \tag{4.10}$$

In this case the momentum state and internal state dependent phases have different forms. As a consequence, we expect that the momentum state and the internal state phase sensitivity functions differ.
Figure 4.1 shows the the recoil diagrams and both the momentum state and the internal state phase sensitivity functions for the conventional $\pi/2 - \pi - \pi/2$ and the alternate composite sequence. In particular, the internal state phase sensitivity function is zero during the free-evolution period, a consequence of the atomic wavefunction being in a superposition of momentum states only. This makes the interferometer robust to momentum-independent error sources such as stray magnetic fields, thus not requiring k-reversal [76].

Although in the following sections we focus on the $\pi/2 - \pi - \pi/2$ interferometer, in which the momentum state phase sensitivity function coincides with the internal state phase sensitivity function, we stress here that in general, the two differ. In particular, the example of the alternate composite pulse highlights the possibility of extending the formalism to compute the phase sensitivity of interferometers that have the atomic wavefunction in a superposition state of momentum states only, such as those adopting Bragg pulses [77] or Raman double diffraction [78].

4.1.2 The phase sensitivity function

The derivation of the phase sensitivity function for a conventional $\pi/2$-π-$\pi/2$ interferometer with rectangular Raman pulses is provided in the Appendix A. In this section, we present only the result

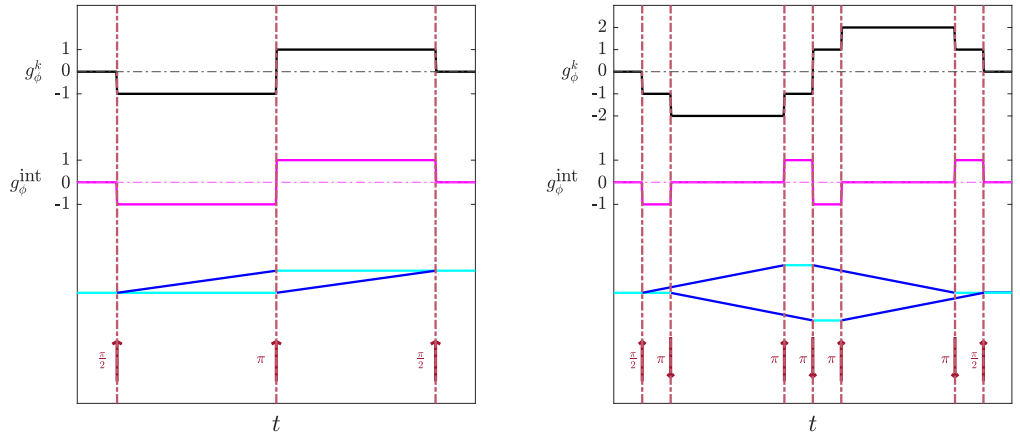

(A) Rectangular pulse sequence (B) Alternate composite sequence

FIGURE 4.1: Momentum state (black) and internal state (purple) dependent sensitivity functions for the rectangular and alternate composite pulse sequence. For completeness, we show the recoil diagrams with blue and cyan colours representing the upper and lower internal states trajectories. The arrows indicate the verse of the effective Raman wave-vector at each laser pulse.

$$g_\phi(t) = \begin{cases} -\frac{\sin(\Omega_1 t)}{\sin(\theta_1)} & 0 \le t \le \tau \\ -1 & \tau \le t \le T+\tau \\ \frac{\sin(\Omega_2(t-T-2\tau))}{\sin(\theta_2/2)} & T+\tau \le t \le T+3\tau \\ +1 & T+3\tau \le t \le 2T+3\tau \\ -\frac{\sin(\Omega_3(t-2T-4\tau))}{\sin(\theta_3)} & 2T+3\tau \le t \le 2T+4\tau \\ 0 & \text{otherwise}\,, \end{cases} \tag{4.11}$$

with τ duration of the $\pi/2$ pulse, T duration of the free-evolution period, Ω_i and θ_i, respectively, the effective Rabi frequency and pulse area of the i-th pulse.
The function $g_\phi(t)$ represents the phase sensitivity of the interferometer under the assumption of a flat laser wavefront and for a mono-kinetic atom. It's important to note that Eq. (4.11) takes into consideration the impact of pulse-length errors; indeed, for resonant pulses ($\theta_1 = \theta_3 = \pi/2$, $\theta_2 = \pi$, and $\Omega_i = \pi/(2\tau)$) Eq. (4.11) reduces to the expression presented in Ref. [67]. As expected, the value of the phase sensitivity function during the free-evolution period remains unaffected by the effective Rabi frequency as shown in Figure 4.2. The sensitivity function's odd parity with respect to the midpoint of the mirror pulse is a result of the pulse sequence's symmetry, which guarantees insensitivity to DC detunings. Therefore, asymmetries observed in the sensitivity function, as experimentally measured by Cheinet *et al.* [67], can be explained by variations in the Rabi frequency experienced by the atoms within the interferometer.

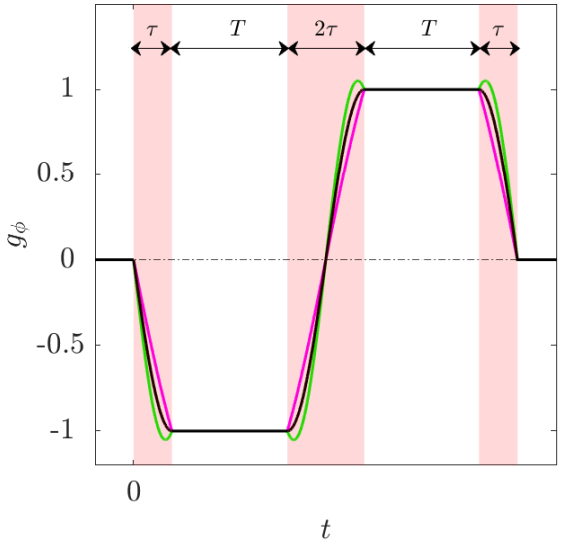

FIGURE 4.2: Phase sensitivity function for a conventional $\pi/2 - \pi - \pi/2$ interferometer. The black line represents the resonant case. The magenta (green) line represents the case in which the effective Rabi frequency is lower (higher) than the resonant case. The red-shaded areas represent the pulses.

4.1.2.1 Link between sensitivity function and atomic trajectories

An intriguing connection between the atomic trajectories and the phase sensitivity function emerges when we examine the dynamics of the wavepackets in momentum space. The rate of change of the mean position of the atomic wavepacket along the Raman effective wave-vector direction is given by [73]

$$\frac{d\langle z\rangle}{dt} = -\int_{-\infty}^{+\infty} |\Psi(k)|^2 \frac{\partial\omega}{\partial k} dk\,, \tag{4.12}$$

where $\Psi(k)$ is the initial momentum-space wavefunction and $\partial\omega/\partial k$ is the group velocity. Assuming that the wavepacket is narrow in momentum space around $k = 0$, we obtain

$$\frac{d\langle z\rangle}{dt} \approx -\hbar \frac{\partial\omega}{\partial p}\bigg|_{p\to 0}\,, \tag{4.13}$$

with $p = \hbar k$, momentum. The angular frequency $\omega(p,t)$ is the time derivative of the phase accumulated by the atomic wavefunction during the interferometric sequence and can be expressed by means of Eq. (4.5) as

$$\omega(p,t) = g_\phi(t)\dot{\phi}(p,t)\,. \tag{4.14}$$

When considering solely the position-dependent phase resulting from the momentum imparted by the Raman laser onto the atomic wavefunction, i.e., $\dot{\phi}(p,t) = k_{\text{eff}}\, v$, we arrive at the following expression

$$\frac{d\,\langle z\rangle}{dt} \approx -v_{\text{rec}}\, g_{\phi}(t)\,, \tag{4.15}$$

where $v_{\text{rec}} = \hbar k_{\text{eff}}/m$ is the recoil velocity, v is the atomic velocity with respect to the laser frame and, we indicated with k_{eff} the Raman effective wave-vector.
Referring to Eq. (4.15), the phase sensitivity function is proportional to the momentum imparted to the centre of mass of the atomic wavepacket. Specifically, the phase sensitivity function quantifies the average velocity difference between the wavepackets traveling along the interferometer arms. Starting from an initial zero-momentum state, the mean velocity difference increases until it reaches the value v_{rec}. During the free-evolution period the upper wavepacket moves with constant velocity v_{rec}, while the lower remains stationary. During the central mirror pulse, state-inversion occurs and the velocity difference changes sign becoming negative. This implies that the separation between the trajectories of the upper and lower wavepackets diminishes during the second half of the interferometric sequence as pictured in Figure (4.1). Due to the sensitivity function's odd parity, the mean velocity of the wavepacket along the upper arm in the first half of the interferometric sequence equals that of the wavepacket along the lower arm in the second half. This ensures that the upper and lower wavepackets overlap at the end of the interferometric sequence. However, when inter-pulse Rabi frequency variations break the symmetry of the phase sensitivity function with respect to the midpoint of the mirror pulse, the upper and lower wavepackets do not perfectly overlap at the output port of the interferometer leading to additional phase shifts and contrast decay [79].

4.1.3 From phase to arbitrary sensitivity

The phase sensitivity function provides the response of the interferometer ($\Delta\Phi$) to the time derivative of the Raman phase (ϕ), i.e. the phase imparted to the atomic wavefunction by the Raman pulse. However, expressing the Raman phase as a function of an arbitrary quantity $\xi(t)$, we can generalize the sensitivity function formalism as

$$g_{\xi}(t) \coloneqq \lim_{\delta\xi\to 0} \frac{\Delta\Phi(t)}{\delta\xi}\,, \tag{4.16}$$

where g_{ξ} is the response of the interferometer to an infinitesimal step input $\xi(t) = \delta\xi\,\Theta(t'-t)$. The interferometric phase is given by

$$\Delta\Phi = \int_{-\infty}^{+\infty} g_{\tilde{\xi}}(t)\,\frac{d\tilde{\xi}}{dt}\,dt\,, \tag{4.17}$$

and integrating by parts we obtain

$$\Delta\Phi = \int_{-\infty}^{+\infty} h_{\tilde{\xi}}(t)\,\tilde{\xi}(t)\,dt\,, \tag{4.18}$$

where $h_{\tilde{\xi}}(t) = -\dot{g}_{\tilde{\xi}}(t)$ is the impulsive response function (IRF).
If we look at the interferometer as a black-box system, the IRF maps a time-varying input ($\tilde{\xi}(t)$) to an output ($\Delta\Phi$), as shown in Figure 4.3. Therefore, the Fourier transform of the IRF, denoted as $H_{\tilde{\xi}}(\omega)$, is the transfer function of the interferometer, and allows for the estimation of the output uncertainty for a given stochastic input. In the presence of coloured noise sources, the Allan variance is the most used uncertainty estimator, and it is given by

$$AVAR_{\Delta\Phi}(\tau_c) = \int_0^{+\infty} F(\omega,\tau_c)\,\underbrace{|H_{\tilde{\xi}}(\omega)|^2\,S_{\tilde{\xi}}(\omega)}_{S_{\Delta\Phi}(\omega)}\,\frac{d\omega}{2\pi}\,, \tag{4.19}$$

where $S_{\tilde{\xi}}(\omega)$ is the power spectral density of the input noise source, and $F(\omega,\tau_c)$ is the filter function that links the power spectral density of the output, $S_{\Delta\Phi}(\omega)$, with the uncertainty estimator and is given by [80]

$$F(\omega,\tau_c) = \frac{1}{2\,m^2}\,\frac{4\,\sin^4\left(\omega\,m\,T_c/2\right)}{\sin^2\left(\omega\,T_c/2\right)} \tag{4.20}$$

with T_c sensor cycling period (i.e., the inverse of the cycling frequency), and $\tau_c = m\,T_c$ the cluster time expressed as multiple integers of the cycling period.
Assuming that the cluster time is much greater than the cycling period leads to

$$AVAR_{\Delta\Phi}(\tau_c) = \frac{1}{\tau_c}\sum_{n=1}^{+\infty} |H_{\tilde{\xi}}(2\pi n f_c)|^2\,S_{\tilde{\xi}}(2\pi n f_c)\,. \tag{4.21}$$

with $f_c = 1/T_c$ cycling frequency (or, equivalently, sensor's sampling rate). Consequently, the Allan variance is only affected by noise at multiple integers of the cycling frequency weighted by the square of the transfer function evaluated at the same harmonics. For a CAI sensor operating in pulse-mode the cycling period is always higher than the interferometer duration because of the dead times associated to atom trapping and cooling, state preparation, and state detection and imaging. As a consequence, noise is uncorrelated between two consecutive measurement cycles and scales as $\sim 1/\sqrt{\tau_c}$.

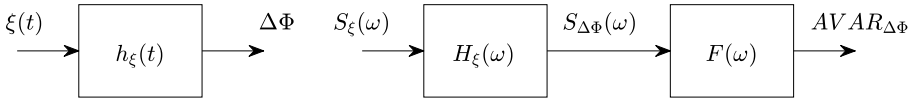

(A) Time domain (B) Frequency domain

FIGURE 4.3: Block diagrams for sensitivity of the interferometer to arbitrary input in time and frequency domain.

4.1.4 The phase impulsive response function

The phase IRF provides the response of the interferometer to a Dirac delta Raman phase and is related to the acceleration imparted to the wavepackets. Taking the time derivative of Eq. (4.11) leads to

$$h_\phi(t) = -\frac{dg_\phi}{dt} = \begin{cases} \frac{\Omega_1 \cos(\Omega_1 t)}{\sin(\theta_1)} & 0 \le t \le \tau \\ 0 & \tau \le t \le T+\tau \\ -\frac{\Omega_2 \cos(\Omega_2(t-T-2\tau))}{\sin(\theta_2/2)} & T+\tau \le t \le T+3\tau \\ 0 & T+3\tau \le t \le 2T+3\tau \\ \frac{\Omega_3 \cos(\Omega_3(t-2T-4\tau))}{\sin(\theta_3)} & 2T+3\tau \le t \le 2T+4\tau \\ 0 & \text{otherwise}\,. \end{cases} \tag{4.22}$$

Figure 4.4 shows the phase IRF in the case of both resonant and off-resonant pulses. We note that in the case of off-resonant pulses the symmetry of the function with respect to the midpoint of the mirror pulse is broken. However, the area underneath the function is independent on the value of the Rabi frequency. Physically this means that the interferometric phase does not depend on the initial phase of the atomic wavefunction.

The phase transfer function, $H_\phi(\omega)$, is the frequency response to a sinusoidal phase input. Recalling the property of the Fourier transform of the derivative of a function, $H_\phi(\omega) = i\,\omega\,G_\phi(\omega)$, where $G_\phi(\omega)$ is the Fourier transform of the phase sensitivity function. Because of the symmetry with respect to the midpoint of the central pulse, it is convenient to take the Fourier transform of the shifted phase sensitivity function, $g_\phi(t-T-2\tau)$. Thus, we obtain

$$H_\phi(\omega) = \mathrm{Re}\{H_\phi(\omega)\} + i\,\mathrm{Im}\{H_\phi(\omega)\} \tag{4.23}$$

where the real and imaginary part of the phase transfer function are given by

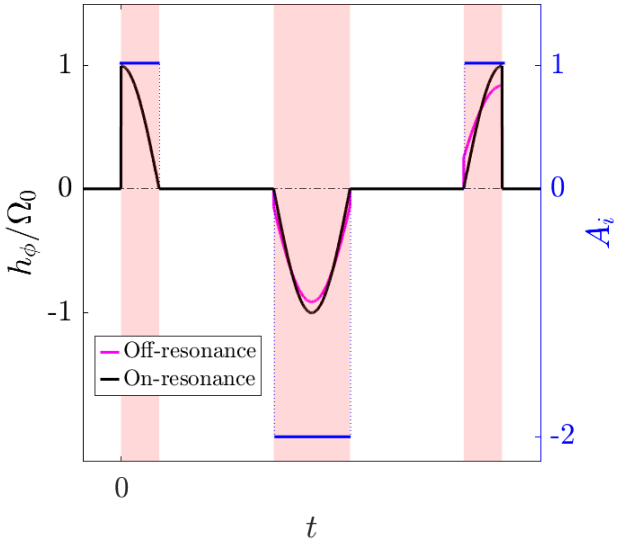

FIGURE 4.4: Phase impulsive response function for a conventional $\pi/2 - \pi - \pi/2$ interferometer normalized with respect to the resonant Rabi frequency, Ω_0. The black and the green line represent, respectively, the resonant case ($\Omega_i = \Omega_0$, with $i = 1, 2, 3$) and off-resonant case ($\Omega_1 = \Omega_0$, $\Omega_2 = 0.9\Omega_0$ and $\Omega_2 = 0.8\Omega_0$). The magenta line represents the area underneath $h_\phi(t)$ for each pulse and it is independent on the Rabi frequency value.

$$\begin{aligned}\mathrm{Re}\{H_\phi(\omega)\} = & 4\sin\left(\frac{2x-y}{2}\right)\sin\left(\frac{y}{2}\right) + \dots \\ & \frac{\hat{\omega}_1}{1-\hat{\omega}_1^2}\left[\frac{\sin(y)}{\sin(\theta_1)} - \cot(\theta_1)\sin(x) - \hat{\omega}_1\cos(x)\right] + \dots \\ & \frac{\hat{\omega}_3}{1-\hat{\omega}_3^2}\left[\frac{\sin(y)}{\sin(\theta_3)} - \cot(\theta_3)\sin(x) - \hat{\omega}_3\cos(x)\right] + \dots \\ & \frac{2\,\hat{\omega}_2}{1-\hat{\omega}_2^2}\left[\hat{\omega}_2\cos(y-x) - \cot\left(\frac{\theta_2}{2}\right)\sin(y-x)\right],\end{aligned} \tag{4.24}$$

$$\begin{aligned}\mathrm{Im}\{H_\phi(\omega)\} = & \frac{\hat{\omega}_1}{1-\hat{\omega}_1^2}\left[\hat{\omega}_1\sin(x) - \cot(\theta_1)\cos(x) + \frac{\cos(y)}{\sin(\theta_1)}\right] - \dots \\ & \frac{\hat{\omega}_3}{1-\hat{\omega}_3^2}\left[\hat{\omega}_3\sin(x) - \cot(\theta_3)\cos(x) + \frac{\cos(y)}{\sin(\theta_3)}\right],\end{aligned} \tag{4.25}$$

with $x = \omega(T+\tau)$, $y = \omega(T+2\tau)$, $\hat{\omega}_i = \omega/\Omega_i$.

The imaginary part of the phase transfer function is non-zero only if the Rabi frequencies during the first and last pulse differ, meaning that the even parity of the phase IRF is broken for a non-symmetric laser intensity configuration. The real part of the transfer function depends on two contributions: at low frequencies the behaviour is dominated by the free-evolution period (first row of Eq. (4.24)), while at high frequencies it mainly depends on the value of the Rabi frequency and on the pulse shape. Focusing on the resonant case ($\Omega_i = \Omega_0$), for $\omega \ll \Omega_0$ the function $|H_\phi(f)| \propto f^2T^2$ behaving like a

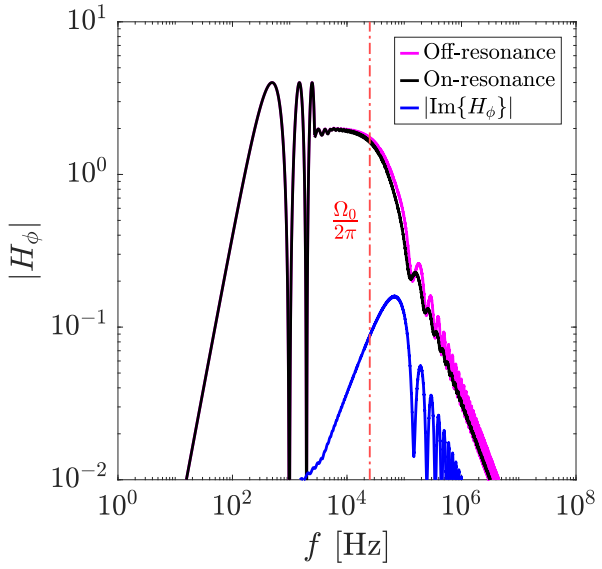

FIGURE 4.5: Phase transfer function for a conventional $\pi/2$-π-$\pi/2$ sequence. For frequencies $f \gtrsim 2000$Hz, only the envelope of the high-frequency oscillations is displayed. The black and the magenta line represent, respectively, the resonant case ($\Omega_i = \Omega_0$, with $i = 1, 2, 3$) and off-resonant case ($\Omega_1 = \Omega_0$, $\Omega_2 = 1.1\Omega_0$ and $\Omega_2 = 1.2\Omega_0$). The blue line represents the imaginary part of transfer function for the off-resonant case. The red dashed line indicates the resonant Rabi frequency. Simulation parameters: $\tau = 10\mu$s, $T = 1$ms.

second-order high-pass filter with a sets of zeros at frequencies $f_n = n/(T + 2\tau)$, where $n = 0, 1, 2, \ldots$. This implies that the CAI sensor is not affected by aliasing noise when operating at a cycling frequency $f_c = 1/(T + 2\tau)$, thereby exploiting the use of multiple staggered interferometers in a zero dead-time mode. For $\omega \gg \Omega_0$, the transfer function $|H_\phi(f)| \propto \Omega_0/(2\pi f)$, thus behaving as a first-order low-pass filter with a cutoff frequency proportional to the Rabi frequency.

Figure 4.5 displays the absolute value of the phase transfer function of a conventional $\pi/2$-π-$\pi/2$ interferometer with a free-evolution time of $T = 1$ms and a pulse duration of $\tau = 10\mu$s. The phase frequency response of the interferometer resembles that of a band-pass filter, with a bandwidth roughly determined by $B_\phi \sim [1/T, \Omega_0/(2\pi)]$. We present both the transfer functions of the interferometer with resonant and off-resonant pulses. As expected, the transfer functions exhibit differences primarily at high frequencies, where the imaginary part of the off-resonant transfer function has an impact.

4.1.4.1 Response to laser phase noise

Following the method reported in Appendix A, we compute the Allan variance of the interferometric phase assuming a white noise model for the laser phase

$$AVAR_{\Delta\Phi}(\tau_c) = \frac{S_\phi^0}{\tau_c}\,\frac{T_c}{2}\left[\frac{\Omega_1(2\,\theta_1+\sin(2\,\theta_1))}{4\sin^2(\theta_1)}+\dots \right.$$
$$\frac{\Omega_3(2\,\theta_3+\sin(2\,\theta_3))}{4\sin^2(\theta_3)}+\dots \tag{4.26}$$
$$\left.\frac{\Omega_2(\theta_2+\sin(\theta_2))}{2\sin^2(\theta_2/2)}\right],$$

with S_ϕ^0 power spectral density of the laser phase noise. Assuming that $\Omega_i = \Omega_0(1+\eta)$, where $\eta = \delta\Omega/\Omega_0$ is the fractional variation in Rabi frequency, we obtain for $|\eta| \ll 1$

$$AVAR_{\Delta\Phi}(\tau_c) \approx \frac{\pi^2}{4}\,\frac{T_c}{\tau_c}\,\frac{S_\phi^0}{\tau}\,(1+\eta)\,. \tag{4.27}$$

The Allan variance of the interferometric phase is inversely proportional to the pulse duration. In particular, a longer pulse (corresponding to a lower Rabi frequency) results in a narrower bandwidth for the phase transfer function, leading to less susceptibility to laser noise. Physically, this phenomenon can be explained by considering that longer pulses result in a more significant averaging of phase noise.

4.2 Inertial sensitivity

In this Section we use the sensitivity function formalism to derive the sensitivity of a conventional $\pi/2-\pi-\pi/2$ interferometer to inertial effects. Specifically, starting from the phase sensitivity function, we derive the sensitivity to rotational and linear motion. The relative motion of a mono-kinetic atom with respect to the laser induces a position-dependent phase given by

$$\phi(t') = \left(\mathbf{C}(t')\,\mathbf{k}\right)\cdot\mathbf{r}_{ba}(t') \tag{4.28}$$

where $\mathbf{k}$ is the effective wave-vector, $\mathbf{r}_{ba}$ is the relative position of the atom with respect to the body-frame (here indicated with the subscript b) to which the laser is attached, and the matrix $\mathbf{C}$ is the direction cosine matrix that describes the orientation of the effective wave-vector with respect to an inertial frame.
The cosine direction matrix at time t' can be obtained as $\mathbf{C}(t') = \mathbf{C}(0)\,\mathbf{C}_{b+}^{b-}(t')$, where $\mathbf{C}(0)$ is the initial cosine direction matrix and can be assumed, for simplicity, equal to the identity matrix. The matrix $\mathbf{C}_{b+}^{b-}$ accounts for attitude variation and can be expressed using the Euler-Rodrigues formula [3]

$$\mathbf{C}_{b+}^{b-}(t') = \mathbf{I} + \frac{\sin|\boldsymbol{\psi}_{ib}(t')|}{|\boldsymbol{\psi}_{ib}(t')|}\,\boldsymbol{\Psi}_{ib}(t') + \frac{1-\cos|\boldsymbol{\psi}_{ib}(t')|}{|\boldsymbol{\psi}_{ib}(t')|^2}\,\boldsymbol{\Psi}_{ib}^2(t') \tag{4.29}$$

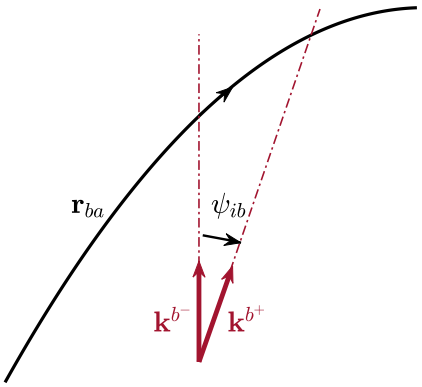

FIGURE 4.6: Rotation of the Raman effective wave-vector with respect to the mean atomic motion.

with the $\mathbf{I}$ 3x3 identity matrix, $\boldsymbol{\psi}_{ib}$ the 3x1 vector that expresses the attitude of the body frame with respect to the inertial frame, and $\boldsymbol{\Psi}_{ib}$ the skew-symmetric matrix of the attitude vector. Assuming an infinitesimal step rotation, $\boldsymbol{\psi}_{ib}(t') = \boldsymbol{\delta\psi}_{ib}\,\Theta(t'-t)$ with $|\boldsymbol{\delta\psi}_{ib}| \ll 1$, we get

$$\phi(t') \approx \left(\mathbf{I} + \boldsymbol{\delta\psi}_{ib}\,\Theta(t'-t)\times\right)\mathbf{k}\cdot\mathbf{r}_{ba}(t')\,, \tag{4.30}$$

and inserting its time derivative in Eq. (4.5) we obtain

$$\Delta\Phi = \Delta\Phi_{\text{trs}} + \Delta\Phi_{\text{rot}} \tag{4.31}$$

with

$$\Delta\Phi_{\text{trs}} = \int_{-\infty}^{+\infty} dt'\, g_\phi(t')\,\mathbf{k}\cdot\dot{\mathbf{r}}_{ba}(t')\,, \tag{4.32}$$

$$\begin{aligned}\Delta\Phi_{\text{rot}} = \int_{-\infty}^{+\infty} dt'\, g_\phi(t') \Big[&\mathbf{k}\times\dot{\mathbf{r}}_{ba}(t')\cdot\boldsymbol{\delta\psi}_{ib}\,\Theta(t'-t) + \ldots \\ &\mathbf{k}\times\mathbf{r}_{ba}(t')\cdot\boldsymbol{\delta\psi}_{ib}\,\delta(t'-t)\Big]\,.\end{aligned} \tag{4.33}$$

The terms $\Delta\Phi_{\text{trs}}$ and $\Delta\Phi_{\text{rot}}$ correspond, respectively, to the interferometric phase shifts arising from translational and rotational motion of the atom with respect to the laser. The decoupling of translational motion from rotational motion is a consequence of the small perturbation approach, in which we neglect contributions of order higher than or equal to $o(\psi_{ib}^2)$.

4.2.1 Rotational dynamics

We start with the definition of the inertial rotation sensitivity function as interferometric phase response to an infinitesimal step rotation

$$\mathbf{g}_{\psi_{ib}}(t) \coloneqq \lim_{\delta\boldsymbol{\psi}_{ib}\to 0} \frac{\Delta\Phi_{\mathrm{rot}}(t)}{\delta\boldsymbol{\psi}_{ib}}\,, \tag{4.34}$$

and by expressing the atomic trajectory as

$$\mathbf{r}_{ba}(t') = \boldsymbol{\ell} + \mathbf{v}_0\, t' + \int_0^{t'} dt'' \int_0^{t''} \ddot{\mathbf{r}}_{ba}(t''')\, dt'''\,, \tag{4.35}$$

where $\boldsymbol{\ell}$ is the initial position offset of the atom with respect to the origin of the body frame (i.e. the lever-arm), and $\mathbf{v}_0$ is the initial velocity.
After substitution of Eq. (4.35) into Eq. (4.33), integration by parts and application of the definition of the rotation sensitivity function we get

$$\begin{aligned}\mathbf{g}_{\psi_{ib}}(t) = {} & g_\phi(t)\,(\mathbf{k}\times\boldsymbol{\ell}) + w(t)\,(\mathbf{k}\times\mathbf{v}_0) + \dots \\ & + h_a(t)\int_0^t dt'\,\left(\mathbf{k}\times\ddot{\mathbf{r}}_{ba}(t')\right) + g_\phi(t)\left(\int_0^t dt'\int_0^{t'}\mathbf{k}\times\ddot{\mathbf{r}}_{ba}(t'')\,dt''\right) + \dots \\ & + \int_t^{+\infty} dt'\, h_a(t')\,(\mathbf{k}\times\ddot{\mathbf{r}}_{ba}(t'))\,,\end{aligned} \tag{4.36}$$

with $w(t) = t\,g_\phi(t) + h_a(t)$, and $h_a(t) = \int_t^{+\infty} g_\phi(t')\,dt'$.
The relative atomic trajectory $\mathbf{r}_{ba}(t)$ can be written as the difference between the atom's absolute motion and body frame's absolute motion. Assuming that the gravitation acting on the body frame is the same of the gravitation acting on the atom we obtain

$$\begin{aligned}\mathbf{g}_{\psi_{ib}}(t) = {} & g_\phi(t)\,(\mathbf{k}^b\times\boldsymbol{\ell}^b) + w(t)\left(\mathbf{k}^b\times\mathbf{v}_0^b\right) + \dots \\ & - h_a(t)\int_0^t dt'\left(\mathbf{k}^b\times\mathbf{f}_{ib}^b(t')\right) - g_\phi(t)\left(\int_0^t dt''\int_0^{t''}\mathbf{k}^b\times\mathbf{f}_{ib}^b(t'')\,dt''\right) + \dots \\ & - \int_t^{+\infty} dt'\, h_a(t')\,(\mathbf{k}^b\times\mathbf{f}_{ib}^b(t'))\,,\end{aligned} \tag{4.37}$$

where the superscript b indicates the reference frame in which the vectors are represented and the term $\mathbf{f}_{ib}^b$ is the specific force, i.e. the difference between the absolute acceleration of the body frame and the gravitation vector [3].
The interferometric phase shift due to the rotational dynamics of the laser frame is given by

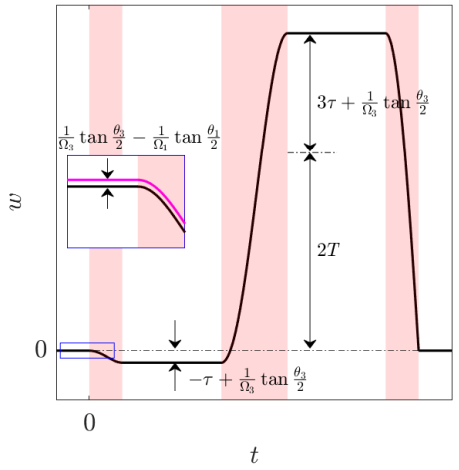

FIGURE 4.7: Coriolis sensitivity for a conventional $\pi/2$-π-$\pi/2$ sequence. The insert shows the detail of the Coriolis sensitivity in the proximity of the first pulse in the case of resonant (black) and off-resonant (magenta) pulse.

$$\Delta\Phi_{\text{rot}} = \int_{-\infty}^{+\infty} \mathbf{g}_{\psi_{ib}}(t) \cdot \dot{\boldsymbol{\psi}}_{ib}^{b}(t)\, dt = \int_{-\infty}^{+\infty} \mathbf{h}_{\omega_{ib}}(t) \cdot \boldsymbol{\omega}_{ib}^{b}(t)\, dt\,, \tag{4.38}$$

where the second equality holds if we neglect high-frequency coning motion [3]. Hence, the rotation sensitivity function is equivalent to the angular rate IRF, i.e. $\mathbf{g}_{\psi_{ib}}(t) \equiv \mathbf{h}_{\omega_{ib}}(t)$.

The angular rate IRF gives the sensitivity of the interferometer to the rotation of the body-frame with respect to the inertial frame. It has three contributions that depend on the relative motion of the atom in the plane transverse to the effective wave-vector:

1. The first term depends on the lever-arm ($\boldsymbol{\ell}^b$) via the phase sensitivity function and is nonzero either in cases of time-varying angular rates or non-resonant pulses.
2. The second term depends on the initial atomic velocity via the function $w(t)$, and represents the sensitivity of the interferometer to the Coriolis acceleration.
3. The third term represents the coupling between angular rate and specific force and gives rise to the so-called anisoinertia bias.

In particular, we observe that the term $\int_t^{+\infty} dt'\, h_a(t')\, (\mathbf{k}^b \times \mathbf{f}_{ib}^b(t'))$ describes the effect of the rotation of the specific force vector. For a geostationary sensor there is no relative rotation of the specific force vector (coincident with the gravity vector) with respect to the body frame and this term is zero [81].

4.2.1.1 Coriolis sensitivity

It is interesting to analyse the Coriolis term, where the angular rate IRF reduces essentially to the function $w(t)$.
Figure 4.7 shows the function $w(t)$, with $t = 0$ being the starting point of the first pulse. Unlike the phase sensitivity function, $w(t)$ is not invariant under temporal translation because the rotational dynamics depends on the choice of the centre of rotation [2]. However, regardless of temporal translation, it retains constancy during the free-evolution periods, and the area beneath it remains independent on the time origin as a consequence of the gauge invariance of the interferometric phase. The constancy of $w(t)$ during the free-evolution periods stems from the fact that a step variation in the tilt angle $\boldsymbol{\psi}_{ib}^{b}$ induces a corresponding step variation in the Raman phase, resembling the behavior observed in the phase sensitivity function $g_{\phi}(t)$.
We observe that the function $w(t)$ is not equal to zero for time intervals preceding the first pulse if there is a discrepancy in the Rabi frequency between the initial and final pulses. Physically this means that the interferometer becomes sensitive to the projection of the atomic velocity along the Raman wave-vector direction due to an initial tilt. From Figure 4.7, we note that,in the limit of infinitesimally short pulses ($\tau \ll T$), the function $w(t)$ tends to the rectangular function $w(t) \to 2\,T$ rect$(t - 3\,T/2)$. This means that, the interferometer detects the angular rate by measuring the difference in the angle that the Raman wave-vector forms with respect to the absolute atomic motion between the last and second pulse, i.e. $\boldsymbol{\Delta\psi}_{ib}^{b} = \boldsymbol{\psi}_{ib}^{b}(2T) - \boldsymbol{\psi}_{ib}^{b}(T)$.

4.2.2 Translational dynamics

The phase shift due to the translational dynamics can be obtained integrating by parts Eq. (4.32)

$$\Delta\Phi_{\text{trs}} = -\int_{-\infty}^{+\infty} h_a(t)\,\mathbf{k}^{b}\cdot\mathbf{f}_{ib}^{b}(t)\,dt\,, \tag{4.39}$$

where the function $h_a(t) = \int_{t}^{+\infty} g_{\phi}(t')\,dt'$ is the acceleration IRF.
Figure 4.8 shows the function $h_a(t)$. We note that the function has a linear dependency on the time during the free-evolution periods. This is due to the fact the acceleration IRF gives the response of the interferometer to a delta-Dirac acceleration or, equivalently, to an infinitesimal step velocity. Therefore a step variation in velocity translates into a ramp in Raman phase. As in the case of $w(t)$, the function $h_a(t)$ becomes non-zero for time intervals preceding the first pulse when the Rabi frequencies during the first and

[2] According to Chasles' theorem, the centre of rotation is defined as the point that satisfies the condition $\boldsymbol{\omega}\times\mathbf{r} = \mathbf{0}$. For a particle moving with constant velocity $\mathbf{r} = \mathbf{v}t$, the time origin defines the centre of rotation. The function $w(t)$ exhibits even parity with respect to the midpoint of the mirror pulse if the time origin coincides with it.

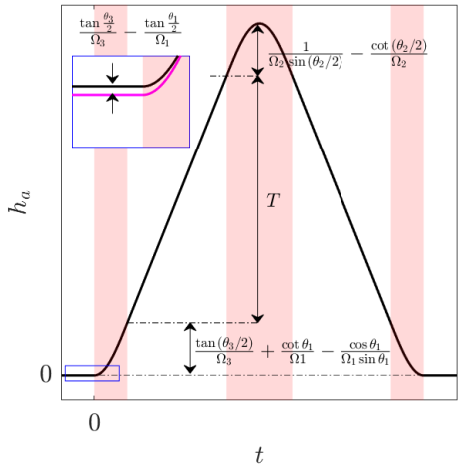

FIGURE 4.8: Acceleration response function for a conventional $\pi/2$-π-$\pi/2$ sequence. The insert shows the detail of the acceleration response function in the proximity of the first pulse in the case of resonant (black) and off-resonant (magenta) pulse.

last pulse differ. Indeed, when the symmetry with respect to the midpoint of the mirror pulse is broken, the interferometer becomes sensitive to an initial velocity [72].
Unlike the function $w(t)$, the acceleration IRF is invariant under temporal translation. This is a consequence of the fact that for a translational motion the centre of rotation is at infinity.

4.2.3 The stationary sensor case

Using Eqs. (4.38) and (4.39) we can compute the inertial phase shift for the simple case of a stationary sensor located on the surface of the Earth and subject to a constant angular rate. The stationary sensor hypothesis implies that

- $\mathbf{f}_{ib}^b = -\mathbf{g}_b^b$, i.e. the specific force equals the reaction to the local gravity. The local gravity is defined as the difference between the gravitation and the centrifugal acceleration [3].
- $\boldsymbol{\omega}_{ib}^b = \boldsymbol{\omega}_{nb}^b + \boldsymbol{\omega}_{ie}^b$, where the first term is the angular rate indicating the rotation of the the body frame with respect the navigation frame and the second term is the angular rate that expresses the rotation of the Earth Centred Earth Fixed frame with respect to the inertial frame [3]. Due to the stationary hypothesis, the so-called 'transport-rate' term, $\boldsymbol{\omega}_{en}^b$, is zero.

[3] A common choice for the navigation frame, here indicated with the subscript n, is the so-called NED frame where the x-axis is aligned with the North direction, the y-axis is aligned with the East direction, and the z-axis is aligned with the local vertical. The ECEF frame, here indicated with the subscript e, rotates about the Earth polar axis with a constant angular rate $\omega_{ie} \approx 15$deg/h.

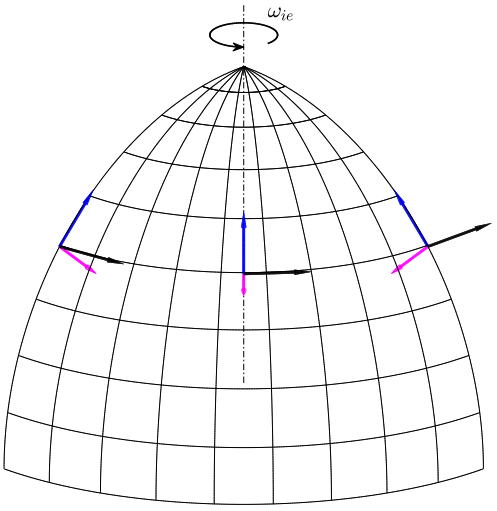

FIGURE 4.9: Sensor in geostationary configuration at three time instants. The local gravity vector points downwards (magenta arrow) and does not change orientation with respect to the projection of the Earth rate, ω_{ie}, on the navigation frame.

Neglecting the effects of the finite pulse duration and summing the rotational and translational phase terms we obtain

$$\begin{aligned}\Delta\Phi = 2\,T^2\,(\mathbf{k}^b \times \mathbf{v}_0^b)\cdot(\boldsymbol{\omega}_{nb}^b + \boldsymbol{\omega}_{ie}^b) + T^2\,(\mathbf{k}^b\cdot\mathbf{g}_b^b) + \ldots \\ + 3\,T^3\,(\mathbf{k}^b \times \mathbf{g}_b^b)\cdot\boldsymbol{\omega}_{nb}^b + 2\,T^3\,(\mathbf{k}^b \times \mathbf{g}_b^b)\cdot\boldsymbol{\omega}_{ie}^b\,.\end{aligned} \tag{4.40}$$

The first row of Eq. (4.40) contains, respectively, the cold-atom gyroscope and the accelerometer scale-factors, while the second row contains the anisoinertia bias terms. In particular, we observe that the phase shift resulting from the coupling of the gravity with Earth rate differs from the phase shift due to the coupling of the gravity with the rotation of the body frame relative to the navigation frame. Physically, if the sensor is geostationary [4], as shown in Figure 4.9, the gravity vector does not change its orientation with respect to the body frame and, consequently, no extra T^3 term arises [47].

4.2.4 Sensor scale-factor

In this section we focus on the CAI sensor scale-factor, i.e. the response to a constant acceleration and rotation acting along the interferometer sensitive axis. For the gyroscope case, the sensitive axis belongs to the plane orthogonal to the Raman effective wave-vector, while for the accelerometer case the sensitive axis is defined by the Raman

[4]The body frame does not rotates with respect to the navigation frame and the only angular rate experienced by the CAI sensor is the Earth rate.

effective wave-vector. In particular, we examine the effects of the finite pulse duration and off-resonance conditions on the interferometer scale-factor.

First, let us consider the accelerometer case, assuming that a constant specific force occurs at a time t_a, while the interferometric sequence starts at time t_1. Using Eq. (4.39) leads to

$$\begin{aligned}\Delta\Phi = -\mathbf{k}^b \cdot \mathbf{f}_{ib}^b \Bigg[(T+2\tau)\left(T + \frac{2}{\Omega_3}\tan\frac{\theta_3}{2}\right) + \epsilon_2 + \dots \\ (t_1 - t_a)\left(\frac{\tan\frac{\theta_3}{2}}{\Omega_3} - \frac{\tan\frac{\theta_1}{2}}{\Omega_1}\right)\Bigg],\end{aligned} \tag{4.41}$$

with

$$\epsilon_2 = -\left(\frac{1}{\Omega_1^2} - \frac{2}{\Omega_2^2} + \frac{1}{\Omega_3^2}\right) + \tau\left(\frac{\cot\theta_1}{\Omega_1} - 2\frac{\cot\frac{\theta_2}{2}}{\Omega_2} + \frac{\cot\theta_3}{\Omega_3}\right). \tag{4.42}$$

The first row in Eq. (4.41) accounts for the interferometric phase due to the constant specific force during the pulse sequence, while the second row is due to the interferometer's sensitivity to the initial velocity. We note that for $t_1 - t_a = -T - 2\tau$ (i.e. the interferometric sequence is considered time symmetric with respect to the midpoint of the mirror pulse and the specific force occurs at the beginning of the pulse sequence), Eq. (4.41) reduces to

$$\Delta\Phi = -\mathbf{k}^b \cdot \mathbf{f}_{ib}^b \left[(T+2\tau)\left(T + \frac{1}{\Omega_1}\tan\frac{\theta_1}{2} + \frac{1}{\Omega_3}\tan\frac{\theta_3}{2}\right) + \epsilon_2 \right] \tag{4.43}$$

which agrees with the expression reported in Ref. [72]. The term ϵ_2 represents a second-order correction and is zero for resonant pulses; therefore, we neglect its contribution in the following analysis.
It is convenient to rewrite the interferometric phase shift in terms of the accelerometer scale-factor ($\mathbf{SF}_a$)

$$\Delta\Phi = \mathbf{SF}_a \cdot \mathbf{f}_{ib}^b\,, \tag{4.44}$$

and assuming that the variations of the Rabi frequency are due to intensity fluctuations of the Raman laser [5]

[5]The value of the Rabi frequency at the i-th pulse is given by $\Omega_i = \Omega_0 + \delta\Omega$, where Ω_0 is the resonant Rabi frequency and $\delta\Omega \ll 1$. Given the proportionality between the Rabi frequency and the square root of the intensity of the j-th Raman laser, we can express $\delta\Omega/\Omega = \delta I_j/(2I_j)$

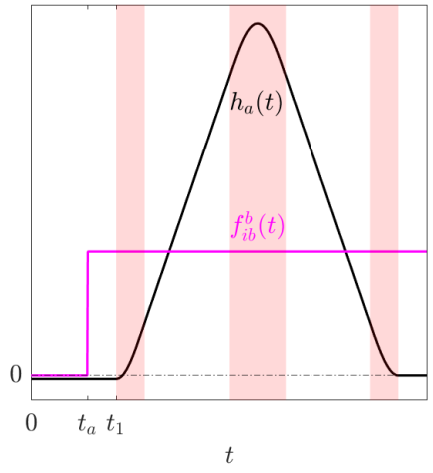

FIGURE 4.10: The accelerometer scale-factor is given by the response of the interferometer to a constant specific force. The time origin coincides with the release of the atom from the MOT.

$$\mathbf{SF}_a = -\mathbf{k}^b T^2 \left[1 + A(\tau) + B(\tau)\frac{\delta I_j}{I_j^0}\right], \tag{4.45}$$

with

$$\begin{aligned} A(\tau) &= \left(2 + \frac{4}{\pi}\right)\frac{\tau}{T} + \frac{8}{\pi}\left(\frac{\tau}{T}\right)^2 \\ B(\tau) &= \left(1 - \frac{2}{\pi}\right)\frac{\tau}{T} + \left(2 - \frac{4}{\pi}\right)\left(\frac{\tau}{T}\right)^2. \end{aligned} \tag{4.46}$$

The finite pulse affects the scale-factor through two mechanisms:

- It induces a calibration error, $A(\tau)$, that depends on the finite duration of the the Raman pulse.
- It induces a scale-factor error that depends on the deviation of the j-th Raman laser intensity from the resonant value, I_j^0. This error is difficult to calibrate because it depends on the long-term drifts of laser intensity and leads to scale-factor instability.

For the gyroscope case we obtain the phase shift from Eq. (4.38) assuming that the atom is characterized by a uniform motion. Following the same steps as for the accelerometer case we obtain the gyroscope scale-factor ($\mathbf{SF}_g$)

$$\mathbf{SF}_g = 2\,(\mathbf{k}^b \times \mathbf{v}_0^b)\,T^2 \left[1 + A(\tau) + B(\tau)\frac{\delta I_j}{I_j^0}\right], \tag{4.47}$$

where the functions $A(\tau)$ and $B(\tau)$ are the same of Eqs. (4.46). We note that the scale-factor of the gyroscope case is perfectly analogous to the accelerometer case, except for the $2\,(\mathbf{k}^b \times \mathbf{v}_0^b)$ term. Indeed, for the gyroscope case, the rotation of the Raman effective wave-vector induces a Coriolis acceleration $\mathbf{a}_c = -2\,(\boldsymbol{\omega}_{ib}^b \times \mathbf{v}_0^b)$ as a consequence of the rotating body frame. Hence, from a classical perspective, a CAI sensor exploits the same working principle as a Coriolis Vibrating Gyroscope (CVG), [1], for detecting angular rates, with the forced linear vibrational motion of the proof mass being replaced by the uniform atomic motion.

4.2.5 Inertial noise

It is interesting to derive the cold-atom accelerometer and gyroscope transfer functions in order to analyse the effect of the interferometer's parameters on the sensor bandwidth and the response to linear and rotational vibrations. For simplicity, we assume that the pulses are all resonant.

The accelerometer transfer function is given by the Fourier transform of the acceleration IRF which is related to the phase sensitivity function by the relation $g_\phi(t) = -\dot{h}_a(t)$. Using the relation between the Fourier transform of a function and its derivative we obtain

$$G_\phi(\omega) = i\,\omega\,H_a(\omega) \implies H_a(\omega) = \frac{G_\phi(\omega)}{i\,\omega} \tag{4.48}$$

Figure 4.11 shows the absolute value of the accelerometer transfer function normalized with respect to T^2. As expected, the response is flat at low frequencies because the interferometer is sensitive to DC acceleration. Indeed, the response at zero frequency represents the accelerometer scale-factor. The function exhibits a set of zeros at frequencies $f_n = n/(T + 2\tau)$, where $n = 0, 1, 2, \ldots$. At high frequencies, the transfer function $|H_a(\omega)|$ is proportional to $1/(2\pi f)^2$, behaving as a second-order low-pass filter with a cutoff frequency proportional to the inverse of the free-evolution period. Hence, the bandwidth of the cold atom accelerometer is roughly given by $B_a \sim [0,\, 1/T]$.

As for the laser phase noise, we compute the Allan variance of the interferometric phase in the case of linear vibrations. Assuming a white noise model and that $\tau \ll T$, we obtain

$$AVAR_{\Delta\Phi}(\tau_c) = \frac{S_a^0}{2\,\tau_c}\,k^2 T^4 \left(\frac{2}{3}\frac{T_c}{T} - 1\right), \tag{4.49}$$

where S_a^0 is the power spectral density of the linear vibration noise. We observe that as the free-evolution period increases, the Allan variance of the interferometric phase also increases. This can be explained by considering that a longer time between the pulses results in a higher accumulation of vibration-induced phase noise in the atomic wavefunction.

We compute the gyroscope transfer function applying the Fourier transform operator to Eq. (4.37) in the hypothesis of zero specific force

$$\mathbf{H}_{\omega_{ib}}(\omega) = (\mathbf{k^b} \times \boldsymbol{\ell}^{\mathbf{b}})\, G_\phi(\omega) - i\,(\mathbf{k}^b \times \mathbf{v}_0^b)\, W(\omega)\,, \tag{4.50}$$

with $W(\omega)$ Fourier transform of the Coriolis sensitivity $w(t)$

$$W(\omega) = \left(\frac{dG_\phi}{d\omega} + \frac{G_\phi}{\omega}\right). \tag{4.51}$$

Figure 4.11 displays both the functions $|G_\phi(\omega)|$ and $|W(\omega)|$, which represent the position-dependent and velocity-dependent frequency responses of the interferometer to a sinusoidal angular rate, respectively. The functions have been appropriately normalized with respect to the square of free-evolution period.
The velocity-dependent frequency response is flat at low frequencies, indicating that the interferometer is sensitive to a DC angular rate. Moreover, it exhibits a series of zeros at frequencies $f_n = n/(2(T + 2\tau))$, where $n = 0, 1, 2, \ldots$, i.e. at half the frequencies of the accelerometer transfer function zeros [6]. At high frequencies, the function $|W(f)|$ behaves as a second-order low-pass filter, with $|W(f)| \propto 1/(2\pi f)^2$. Hence, the bandwidth of the cold atom gyroscope is roughly half of the accelerometer, $B_g \sim [0, 1/2T]$.
The position-dependent frequency response acts as a band-pass filter, with its peak sensitivity occurring at approximately the same frequency as the first zero of the velocity-dependent response function. At higher frequencies, the function scales as $|G_\phi(f)| \propto 1/(2\pi f)^2$. Hence, the lever-arm, $\boldsymbol{\ell}$, affects the gyroscope transfer function only at medium frequencies.

It is interesting to derive the response of the interferometer to angular vibrations, which are linked to the pointing jitter of the Raman effective wave-vector. Assuming a white noise model and neglecting the high-order terms in τ/T, we can express the response of the interferometer both in terms of angular rate noise

[6] Physically, the interferometer detects an acceleration by measuring the increment in velocity between the two halves, i.e. $a \propto (v_{32} - v_{21})/T$, where v_{31} is the atomic velocity between the third and second pulse, and v_{21} is the atomic velocity between the second and half pulse. In contrast, the interferometer detects an angular rate by measuring the increment in the angle that the Raman effective wave-vector forms with respect the atomic trajectory, i.e. $\omega \propto (\psi_3 - \psi_2)/2T$, where ψ_3 is the angle at the third pulse and ψ_2 is the angle at the second pulse. The factor '2' at the denominator explains why the velocity-dependent frequency response to sinusoidal angular rate has zeros at half the frequencies of the acceleration transfer function.

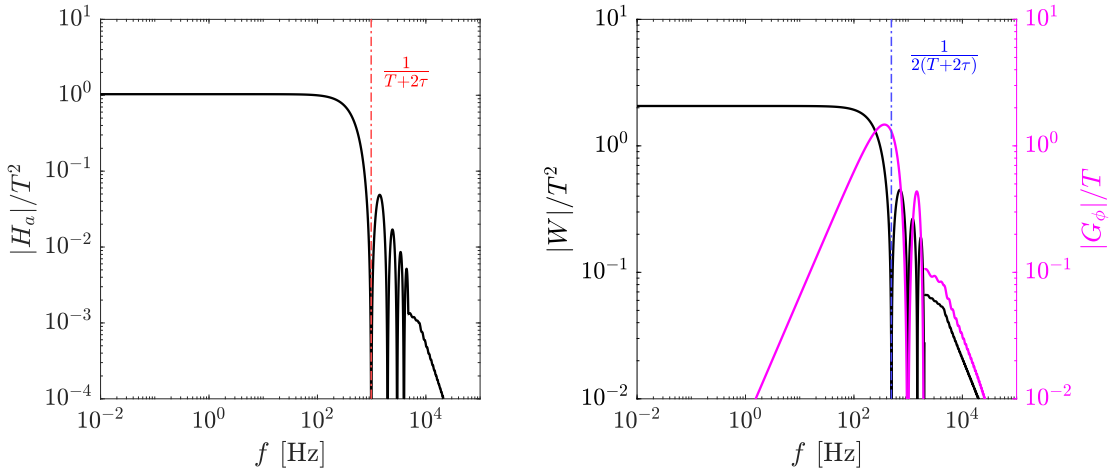

(A) Accelerometer transfer function

(B) Gyroscope transfer function

FIGURE 4.11: CAI sensor transfer functions. For frequencies $f \gtrsim 2000$Hz, only the envelope of the high-frequency oscillations is displayed. Panel (A): Frequency response of the interferometer to linear acceleration. Panel (B): Frequency response of the interferometer to angular rate. The black (magenta) line represents the velocity-dependent (position-dependent) sensitivity. Simulation parameters: $\tau = 10\mu$s, $T = 1$ms.

$$AVAR_{\Delta\Phi}(\tau_c) = \frac{S^0_{\omega_{ib}}\, T^2}{\tau_c}\left[|\mathbf{A}^b|^2\frac{T_c}{T} + 2\,|\mathbf{B}^b|^2\left(\frac{T_c}{T}-1\right)T^2 + 2\,\mathbf{A}^b\cdot\mathbf{B}^b\,T_c\right], \tag{4.52}$$

or pointing noise

$$AVAR_{\Delta\Phi}(\tau_c) = \frac{S^0_{\psi_{ib}}\, T_c}{\tau_c}\left[|\mathbf{A}^b|^2\frac{\pi^2}{4\,\tau} + |\mathbf{B}^b|^2\frac{3\,\pi^2\,T^2}{8\,\tau} + \mathbf{A}^b\cdot\mathbf{B}^b\frac{\pi^2\,T}{2\,\tau}\right], \tag{4.53}$$

where $\mathbf{A}^b = \mathbf{k}^b \times \boldsymbol{\ell}^b$, $\mathbf{B}^b = \mathbf{k}^b \times \mathbf{v}^b_0$, $S^0_{\omega_{ib}}$ is the white noise power spectral density of the angular rate noise in $[(\text{rad/s})^2/\text{Hz}]$, and $S^0_{\psi_{ib}}$ is the white noise power spectral density of the pointing noise in $[\text{rad}^2/\text{Hz}]$.

4.3 Light-shift sensitivity

Light-shifts are one of the mechanisms connected to laser intensity fluctuations that affect the interferometer output. Intensity fluctuations at high frequencies impact the interferometer's noise, while long-term drifts affect the bias stability of the CAI sensor. In the hypothesis of small intensity perturbations, the sensitivity function formalism can be applied to estimate the interferometer's performance in terms of noise and bias stability.

Two fundamental light-shift mechanisms occur within an interferometer: the one-photon light-shift (OPLS) connected to the variation of the atomic energetic levels induced by

laser intensity, and the two-photon light-shift (TPLS) induced by the off-resonant transition in a retro-reflected Raman configuration [52].

4.3.1 One-photon light-shift

The rate of change in Raman phase induced by a small perturbation in laser intensity, $\delta I(t)$, via the OPLS effect is given by

$$\dot{\phi}_{OPLS}(t) = a_1 \, (I_1^0 + \delta I(t)) + a_2 (I_2^0 + \delta I(t)) \, , \tag{4.54}$$

where a_j and I_j^0 are, respectively, the coupling coefficient [7] and the nominal intensity of the i-th laser line. In nominal conditions it is possible to adjust the laser intensities or frequencies in order to suppress the OPLS. Hence, assuming

$$a_1 \, I_1^0 + a_2 \, I_2^0 = 0 \, , \tag{4.55}$$

and $\delta I / I_j^0 \ll 1$, we obtain

$$\dot{\phi}_{OPLS}(t) = a_1 \, (1 - r) \, \delta I(t) \, , \tag{4.56}$$

with $r = I_1^0 / I_2^0$, and inserting it in Eq. (4.5) we obtain

$$\Delta\Phi = \int_{-\infty}^{+\infty} g_\phi^{(0)}(t) \, a_1 \, (1 - r) \, f(t) \, \delta I(t) \, dt \tag{4.57}$$

where $f(t)$ is a function that is 1 during the laser pulse and 0 otherwise. The function $g_\phi^{(0)}(t)$ is the resonant phase sensitivity function [8], i.e. corresponding to the case where the Rabi frequency during each pulse is equal to the resonant one, i.e. $\Omega_i = \Omega_0 = \pi/(2\tau)$ for $i = 1, 2, 3$.
Following Eq. (4.18), we define the OPLS intensity IRF as

$$h_{OPLS}(t) = a_1 \, (1 - r) \, g_\phi^{(0)}(t) \, f(t) \, . \tag{4.58}$$

We note that this function does not define the interferometer's sensitivity to laser intensity but rather its sensitivity to the deviation of the intensity from the nominal value.

[7] The OPLS coupling coefficient depends on the single-photon detuning and on the polarization of the i-th laser line.

[8] We use the resonant phase sensitivity function rather than the general one because we are interested in the effects induced by the deviations of the laser intensity with respect to its nominal value.

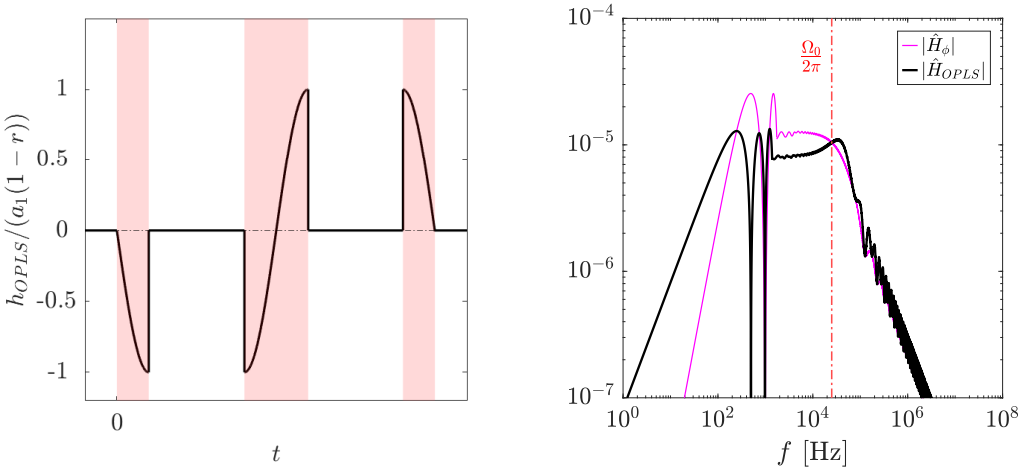

(A) OPLS impulsive response function

(B) OPLS transfer function

FIGURE 4.12: Sensitivity of the interferometer to laser intensity fluctuations. Panel (A): Time response of the interferometer to laser intensity fluctuations. Panel (B): Frequency response of the interferometer to laser intensity fluctuations $\hat{H}_{OPLS} = H_{OPLS}/(a_1(1-r))$ (black line). For comparison we also show the normalized phase transfer function $\hat{H}_\phi = H_\phi/\Omega_0$. For frequencies $f \gtrsim 2000$Hz, only the envelope of the high-frequency oscillations is displayed. Simulation parameters: $\tau = 10\mu$s, $T = 1$ms.

Figure 4.12 shows the OPLS intensity IRF. The odd parity with respect to the midpoint of the mirror pulse reflects the fact that the interferometer is insensitive to a DC laser intensity shift. Moreover, this odd parity suggests that, in the case of long-term intensity drifts, the interferometric phase is mainly affected by the first and last pulses.

Figure 4.12 displays the modulus of the Fourier transform of the OPLS intensity IRF, which represents the frequency response of the interferometer to a sinusoidal laser intensity shift. At low frequencies, the response function behaves like a first-order high-pass filter with an asymptotic trend of $|H_{OPLS}(f)| \propto f\,T/\Omega_0$. It exhibits a set of zeros at frequencies $f_n = n/(2(T+2\tau))$, where $n = 0, 1, 2, \ldots$. At high frequencies, the function behaves as a first-order low-pass filter with a cut-off frequency proportional to the Rabi frequency, resembling the asymptotic trend of the phase transfer function. As illustrated in Figure 4.12, the OPLS transfer function has a wider bandwidth compared to the phase transfer function, resulting in higher sensitivity of the interferometer to low-frequency laser intensity drifts.

It is interesting to compute the response of the interferometer to laser intensity noise. Assuming a white noise model for the intensity fluctuations, we compute the Allan variance of the interferometric phase

$$AVAR_{\Delta\Phi}(\tau_c) = \left[a_1\ I_1^0\,(1-r)\right]^2\ \frac{T_c}{\tau_c}\,S_\eta^0\,\tau\,, \tag{4.59}$$

with S_η^0 power spectral density of the relative intensity noise, i.e. $\delta I/I_1^0$. Unlike the Raman phase noise, the Allan deviation is directly proportional to the pulse duration, meaning that the longer the laser stays on, the more noise is imprinted onto the atomic wavefunction.

4.3.1.1 Bias instability

It is clear that if the atoms experience a time-varying intensity during the interferometric sequence, a bias is produced. However, intensity variations are not only due to the stochastic fluctuations of the Raman laser system, but also to the coupling of the atomic motion in an expanding cloud with laser intensity spatial inhomogeneity.
Assuming a Gaussian beam intensity profile, we obtain

$$\dot{\phi}_{OPLS}(r_\perp, t) = a_1\,(1-r)\,\delta I\,\exp\left(-2\,\frac{r_\perp^2\,(t)}{w_L^2}\right), \tag{4.60}$$

where w_L is the $1/e^2$ beam radius, and $r_\perp(t)$ denotes the atomic position in the transverse plane relative to the centroid of the Raman beam.
Assuming that the initial atomic distribution is Gaussian in phase-space, and averaging over it leads to

$$\dot{\phi}_{OPLS}(t) = a_1\,(1-r)\,\delta I\,\frac{w_L^2}{w_L^2 + 4\,\sigma^2(t)}, \tag{4.61}$$

with $\sigma(t) = \sigma_0 + \sigma_v\,t$ width of the spatial atomic distribution at time t.
The cloud expansion determines a time varying Raman phase rate and hence a bias phase shift. Assuming that laser pulses are short compared to the free-evolution period and, therefore, that the atomic cloud size remains constant during each laser pulse, we obtain

$$\Delta\Phi = \alpha_1\,\delta I\,\frac{16\,\sigma_v^2\,T\,(t_1+T)\,w_L^2}{(w_L^2 + \sigma^2(t_1+2T))(w_L^2+\sigma^2(t_1))}, \tag{4.62}$$

with $\alpha_1 = a_1\,(1-r)\,2\,\tau/\pi$, and t_1 time instant at which the first pulse occurs. A simplified expression can be obtained for $w_L \gg \sigma(t)$

$$\Delta\Phi \approx \alpha_1\,\delta I\,\frac{16\,\sigma_v^2\,T\,(t_1+T)}{w_L^2}, \tag{4.63}$$

As expected, the bias phase shift increases as the degree of asymmetry due to the atomic cloud expansion increases. Physically, the more the cloud expands, the higher the intensity gradient experienced by the atoms during the interferometer sequence.

4.3.2 Two-photon light-shift

When a retro-reflecting mirror is used to create a counter-propagating laser arrangement, two transitions are possible: one associated with the incident effective wave-vector and the other with the reflected one. Assuming that the two transitions are Doppler-detuned and well-resolved, it is possible to tune the Raman laser to be resonant with one transition. The off-resonant transition will, in turn, cause a detuning or, equivalently, a Raman phase rate, [52]

$$\dot{\phi}_{TPLS} = -\frac{\Omega^2}{8\,\delta_D} - \frac{\Omega^2}{8\,\delta_D + 16\,\delta_R} \tag{4.64}$$

where Ω is the Rabi frequency, δ_D and δ_R are, respectively, the Doppler and recoil detuning.
Assuming a small laser intensity fluctuation with respect to the nominal j-th intensity, $|\delta I(t)| \ll I_j^0$, we get

$$\dot{\phi}_{TPLS}(t) = -\beta(t)\,\Omega_0^2 \left[1 + (1+r)\,\frac{\delta I(t)}{I_1^0}\right], \tag{4.65}$$

where $\beta(t) = 1/(8\,\delta_D(t)) + 1/(8\,\delta_D(t) + 16\,\delta_R)$, Ω_0 is the nominal Rabi frequency, and $r = I_1^0/I_2^0$ ratio between the nominal intensities.
Following the same procedure of the OPLS case, we define the TPLS relative intensity IRF as

$$h_{TPLS}(t) = -\Omega_0^2\,(1+r)\,g_\phi^{(0)}(t)\,\beta(t)\,f(t)\,, \tag{4.66}$$

with $g_\phi^{(0)}(t)$ the resonant phase sensitivity function, and $f(t)$ function that is one during the pulses and zero when the laser is off.
Figure 4.13 shows the TPLS intensity IRF. In general the function is asymmetric with respect to the midpoint of the mirror pulse because it depends on the value of the Doppler detuning at each pulse. This implies that even in cases where the intensity fluctuation remains constant over time, it still leads to a bias phase shift. For example, an acceleration along the effective wave-vector direction induces a varying Doppler shift, resulting in a bias phase shift through the TPLS effect.

The modulus of the Fourier transform of the function $h_{TPLS}(t)$ represents the frequency response to intensity fluctuations that impact the interferometer through the TPLS effect, and it is shown in Figure 4.13. At low frequencies, the function is flat, indicating that the interferometer is sensitive to a DC intensity fluctuation. Indeed, a time-varying Doppler detuning breaks the symmetry of the interferometer with respect to the midpoint of the mirror pulse, leading to a bias. At high frequencies, the function behaves

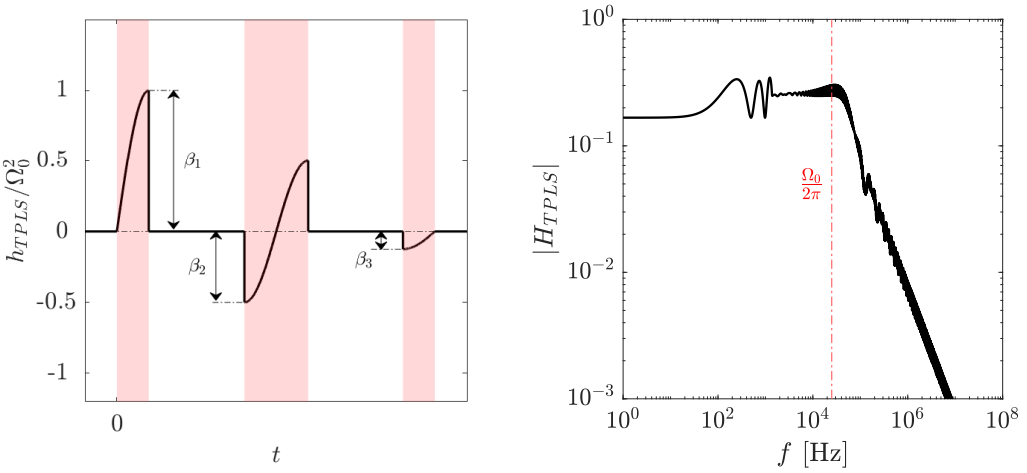

(A) TPLS impulsive response function (B) TPLS transfer function

FIGURE 4.13: Sensitivity of the interferometer to laser intensity fluctuations. Panel (A): Time response of the interferometer to laser intensity fluctuations. Panel (B): Frequency response of the interferometer to laser intensity fluctuations. For frequencies $f \gtrsim 2000$Hz, only the envelope of the high-frequency oscillations is displayed. The red dashed line represents the resonant Rabi frequency. Simulation parameters: $\tau = 10\mu$s, $T = 1$ms, Doppler detuning induced by gravity.

like a first-order low-pass filter with a cut-off frequency proportional to the Rabi frequency.

We compute the response of the interferometer to laser intensity noise assuming a white noise model for the relative intensity fluctuation $\eta_1 = \delta I / I_1^0$. Therefore, the Allan variance of the interferometric phase is given by

$$AVAR_{\Delta\Phi}(\tau_c) = \left(\frac{\pi}{2}\right)^4 \frac{(1+r)^2\, S_{\eta_1}^0}{4\,\tau_c} \frac{1}{\tau^2}\Big[(\beta^2(t_1) + 2\,\beta^2(t_1+T) + \beta^2(t_1+2\,T))\,\frac{T_c}{\tau} - \ldots \\ \frac{8}{\pi^2}\,(\beta(t_1) - \beta(t_1+2\,T))^2\Big]\,, \tag{4.67}$$

and assuming that $T_c \gg \tau$ leads to

$$AVAR_{\Delta\Phi}(\tau_c) \approx \left(\frac{\pi}{2}\right)^4 \frac{(1+r)^2\, S_{\eta_1}^0}{4\,\tau_c} \frac{T_c}{\tau^3}\left[\beta^2(t_1) + 2\,\beta^2(t_1+T) + \beta^2(t_1+2\,T)\right]\,, \tag{4.68}$$

with $S_{\eta_1}^0$ power spectral density of the relative intensity noise. Unlike the OPLS case, the Allan variance decreases as the pulse length increases. This is because longer pulses result in a narrower bandwidth of the Raman pulse and a lower probability of exciting the off-resonant wave-vector transition, thus leading to a weaker TPLS effect.

4.3.2.1 Bias instability

Long-term stochastic fluctuations of the Raman laser intensity lead to bias instability through two main mechanisms:

1. Time-varying Doppler detuning.
2. Coupling between cloud expansion and laser intensity spatial inhomogeneity.

In the first case, we obtain the bias phase shift integrating the area beneath the TPLS relative intensity IRF. Assuming that the Doppler detuning is almost constant during the pulses (short pulse hypothesis):

$$\Delta\Phi = \frac{\pi}{2\,\tau}(1+r)\,\frac{\delta I}{I_1^0}\,(\beta(t_1) - \beta(t_1 + 2\,T))\,, \tag{4.69}$$

with t_1 time at which the first pulse occurs, and T free-evolution time. We note that the phase shift does not depend on the value of the Doppler detuning at the mirror pulse. Therefore, as with the OPLS, the beam-splitting process is the source of the bias phase.

In the second case, a bias phase shift arises as a consequence of the coupling between cloud expansion and laser intensity inhomogeneities. Assuming a Gaussian beam with $1/e^2$ waist w_L, we have

$$\dot{\phi}_{TPLS}(r_\perp, t) = -\beta(t)\,(1+r)\,\frac{\delta I}{I_1^0}\,\Omega_0^2\,\exp\left(-4\,\frac{r_\perp^2(t)}{w_L^2}\right), \tag{4.70}$$

and integrating over an initial Gaussian atomic distribution we obtain

$$\Delta\Phi = \frac{\pi}{2\,\tau}(1+r)\,\frac{\delta I}{I_1^0}\,w_L^2\left[\frac{\beta(t_1)}{w_L^2 + 8\,\sigma^2(t_1)} - \frac{\beta(t_1+2\,T)}{w_L^2 + 8\,\sigma^2(t_1+2T)}\right]. \tag{4.71}$$

Hence, the coupling between cloud expansion and laser intensity inhomogeneity induces a bias even in the case of a constant Doppler shift (where the term $\beta(t)$ is constant). We should note that TPLS calculations are based on the assumption that the two counter-propagating Raman transitions are well-separated in frequency, or, in other words, that the Doppler detuning is sufficiently high to remove the double transition degeneracy. If the Doppler detuning is not high enough, both counter-propagating transitions become resonant, resulting in double Raman diffraction and a complete different interferometer scheme [82].

4.4 Magnetic field sensitivity

Although atoms are prepared in the magnetic $m_F = 0$ state, they still have a sensitivity to magnetic fields via the quadratic Zeeman effect. The time derivative of the Raman phase due to the quadratic Zeeman effect is given by [48]

$$\dot{\phi}_{QZ}(z,t) = 2\,\pi\,K_{QZ}\,B^2(z,t)\,, \tag{4.72}$$

where $B(z,t)$ is the magnetic field along the Raman effective wave-vector axis z. The coupling constant K_{QZ} is inversely proportional to the ground-level hyperfine splitting, so atoms that exhibits a larger splitting are less sensitive to the quadratic Zeeman effect. In order to decouple the temporal and the spatial components we can expand the magnetic field in Taylor series and compute the interferometric phase using the phase sensitivity function

$$\begin{aligned}\Delta\Phi = 2\,\pi\,K_{QZ}\int_{-\infty}^{+\infty} g_\phi(t)\,\Big[B^2(z_0,t) + \ldots \\ 2\,B(z_0,t)\,\frac{\partial B}{\partial z}\,\Delta z(t) + \ldots \\ \left(B(z_0,t)\,\frac{\partial^2 B}{\partial z^2} + \left(\frac{\partial B}{\partial z}\right)^2\right)\Delta z^2(t) + o(\Delta z^3(t))\Big]\,dt\,,\end{aligned} \tag{4.73}$$

Here, $\Delta z(t) = \bar{z}(t) - z_0$ is the displacement of the mean relative atomic trajectory with respect to the location z_0 [9]. The first term in the square brackets represents the purely temporal contribution, while the second and third term depend on the gradient and the curvature of the magnetic field.

4.4.1 Purely temporal sensitivity

Due to the odd parity of the phase sensitivity function with respect to the midpoint of the mirror pulse, a steady magnetic field does not produce any bias phase shift if all the pulses are resonant. However, if the Rabi frequency experienced by the atoms during the first and last pulses differ, the symmetry of the interferometer is broken, and a bias shift is produced as a result of residual sensitivity to steady detunings. Time-varying stray magnetic fields, such as those produced by eddy currents during the switch-off of the MOT quadrupole field, can induce a high bias, which generally depends on their

[9] The trajectories of the centre of mass of the wavepackets travelling along the upper and lower arm of the interferometer can be described by a unique mean trajectory, $\bar{z}(t)$. The choice of the point z_0 in which the Taylor expansion is computed is completely arbitrary. For instance, we can choose $z = z_0$ coinciding with the centre of the quadrupole field in the MOT or with the location at which the first pulse occurs.

amplitude and time constant [83].
During the interferometric sequence, a DC bias magnetic field, B_0, aligned with the direction of the Raman effective wave-vector, is present to define the atomic quantization axis. Therefore, it is interesting to analyze the effect of small deviations in the magnetic field, $\delta B(t)$, from this nominal value, in a similar fashion to what was done for the light-shift effect. Assuming that $|\delta B(t)| \ll B_0$ we can define the magnetic field impulsive response function as

$$h_B(t) = 4\,\pi\,K_{QZ}\,B_0\,g_\phi(t)\,. \tag{4.74}$$

We remark that the function $h_B(t)$ does not represent the sensitivity with respect to the magnetic field overall, but to the fluctuations with respect to the bias field B_0.

Figure 4.14 shows the frequency response to magnetic field fluctuations. The interferometer behaves like a band-pass filter with $|H_B(f)| \propto (2\pi f)^2 T^2$ at low frequencies, $|H_B(f)| \propto 1/(2\pi f)^2$ at high frequencies, and a set of zeros at frequencies $f_n = n/(T+2\tau)$, with n as a positive integer. The magnetic field noise affects the interferometer in a bandwidth which mostly depends on the free-evolution period: the higher the free-evolution period, the more the interferometer is affected by low-frequency magnetic field fluctuations.

The response of the interferometer to white noise magnetic field fluctuations is given in terms of Allan variance as

$$AVAR_{\Delta\Phi} = (4\,\pi\,K_{QZ}\,B_0)^2\,\frac{T_c}{\tau_c}\,S_B^0\,T \tag{4.75}$$

where S_B^0 represents the power spectral density of magnetic field fluctuations, and we have assumed that the pulse duration is significantly shorter than the free-evolution time. It is noteworthy that as the free-evolution time increases, the magnetic noise increasingly impacts the interferometer's performance. This phenomenon can be attributed to the fact that during the free-evolution period, an atom in a superposition of two internal states accumulates a magnetic-field-dependent phase via the quadratic Zeeman effect.

4.4.2 Magnetic field gradient

The bias phase shift due to the magnetic field gradient requires the computation of the relative atomic trajectory. Assuming constant inertial actions and retaining only their linear terms, we compute the mean relative atomic trajectory through Taylor expansion

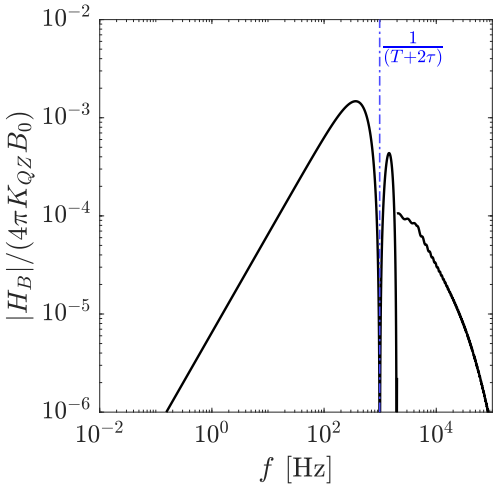

FIGURE 4.14: Frequency response of the interferometer to magnetic field fluctuations. For frequencies $f \gtrsim 2000$Hz, only the envelope of the high-frequency oscillations is displayed. Simulation parameters: $\tau = 10\mu$s, $T = 1$ms.

$$\bar{z}(t) = \bar{z}_0 + \left(v_{z,0} + \frac{v_{\text{rec}}}{2}\right) t - \frac{1}{2}\left[f_z + 2\left(\omega_x\, v_{y,0} - \omega_y\, v_{x,0}\right)\right] t^2 + o(t^3)\,, \tag{4.76}$$

where $\bar{z}_0$ is the initial average position along the Raman axis, $v_{j,0}$, f_j and ω_j are, respectively, the initial position, the initial velocity, the specific force and the angular rate along the j-th direction, and v_{rec} is the recoil velocity. Here $t = 0$ indicates the starting of the interferometric sequence.
Inserting Eq. (4.76) in (4.73) and assuming $\tau \ll T$, leads to

$$\Delta\Phi = 4\,\pi\,K_{QZ}\,B_0\,\frac{\partial B}{\partial z}\left[\Delta z_0\left(\frac{1}{\Omega_3}\tan\frac{\theta_3}{2} - \frac{1}{\Omega_1}\tan\frac{\theta_1}{2}\right) + \Delta v_0\,T^2 + \Delta a_0\,T^3\right]\,, \tag{4.77}$$

with $\Delta z_0 = \bar{z}_0 - z_0$, $\Delta v_0 = v_{z,0} + v_{\text{rec}}/2$, and $\Delta a_0 = -f_z - 2\left(\omega_x\, v_{y,0} - \omega_y\, v_{x,0}\right)$.
The magnetic field gradient induces three distinct errors: firstly, a position-dependent bias arising from differences in the Rabi frequencies experienced by the atoms during the initial and final pulses; secondly, a velocity-dependent bias characterized by a scaling factor of T^2, depending upon the initial velocity along the Raman axis and the recoil velocity; and thirdly, a scale-factor error with a T^3 scaling effect affecting both the accelerometer and gyroscope signals. Long-term fluctuations in the bias magnetic field affect both bias and scale-factor instabilities, while long-term fluctuations in atomic velocity along the Raman axis are a source of bias instability.

4.4.2.1 Magnetic force

The magnetic field gradient induces a state-dependent force perturbing atomic trajectories and consequently resulting in an additional error phase shift [83]. Starting from the expression of the potential induced by the quadratic Zeeman effect

$$U_B(z) = \mp \frac{1}{2} h K_{QZ} B^2(z) , \tag{4.78}$$

where the negative and positive signs are, respectively, for the atoms in the lower and upper ground states of ^{85}Rb [84], and expanding in Taylor series the $B(z)$ term, we obtain the state-dependent acceleration acting on the centre of mass of the atomic wavepacket travelling along each interferometer's arm

$$a_B(t) = \begin{cases} +(\alpha^2 + \beta^2 \Delta z(t)) \operatorname{sgn}(t - T) & \text{for the upper arm} \\ -(\alpha^2 + \beta^2 \Delta z(t)) \operatorname{sgn}(t - T) & \text{for the lower arm} , \end{cases} \tag{4.79}$$

with $\alpha^2 = (h K_{QZ}/m) B_0 \partial B/\partial z$ and $\beta^2 = (h K_{QZ}/m) (\partial B/\partial z)^2$, h Planck constant, and m the atomic mass. Solving the equations of motion to compute the phase accumulated by the wavepackets along the upper and lower arms and neglecting the pulse duration effect, we obtain

$$\Delta\Phi = \frac{2}{3} k_{\text{eff}} \beta^2 T^3 \, (\Delta v_0 + \Delta a_0 \, T) \, . \tag{4.80}$$

where Δv_0 and Δa_0 are the same quantities defined in Eq. (4.77). We note that the term α^2 does not produce any phase shift because the atom spends equal amounts of time in both internal states. The phase shift due to the magnetic force depends on the square of the gradient of the magnetic field via the term β^2: as a result of a time-varying acceleration the phase shift includes terms with scaling higher than T^2. Unlike the phase shift induced by the magnetic field gradient, the phase shift resulting from the magnetic force depends on the Raman effective wave-vector [48].

4.4.3 Complex spatial features

In general, the magnetic field experienced by the atoms during the interferometric sequence may have complex spatial features that cannot be approximated by a Taylor expansion. In this case, it is useful to adopt a transfer function approach that describes the response of the interferometer in the spatial frequency domain [85].
The interferometric phase due to a small magnetic field fluctuation, δB, is given by

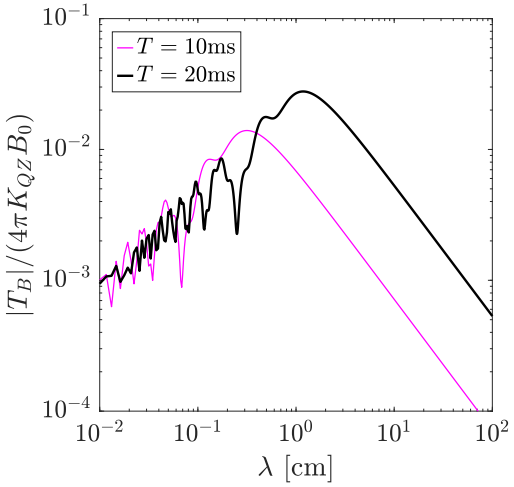

FIGURE 4.15: Spatial frequency response of a gravimeter to magnetic field inhomogeneity for different free-evolution times.

$$\Delta\Phi = 4\,\pi\,K_{QZ}\,B_0 \int_{-\infty}^{+\infty} g_\phi(t)\,\delta B(z,t)\,dt\,. \tag{4.81}$$

If the magnetic field inhomogeneity exhibits complex spatial features, we can express it in function of the frequency component as

$$\delta B(z,t) = \int_{-\infty}^{+\infty} \widehat{\delta B}(k)\,\exp\left(i\,k\,\bar{z}(t)\right)\frac{dk}{2\pi}\,, \tag{4.82}$$

where $\widehat{\delta B}$ is the spatial Fourier transform and $k = 2\pi/\lambda$ is the spatial wave-vector. Substituting Eq. (4.82) in (4.81) we finally obtain

$$\Delta\Phi = 2\int_{0}^{+\infty} \mathrm{Re}\{T_B(k)\,\widehat{\delta B}(k)\}\,\frac{dk}{2\pi}\,, \tag{4.83}$$

where

$$T_B(k) = 4\,\pi\,K_{QZ}\,B_0 \int_{-\infty}^{+\infty} g_\phi(t)\,\exp\left(i\,k\,\bar{z}(t)\right)dt \tag{4.84}$$

is the spatial transfer function of the magnetic field fluctuation.
Figure 4.15 displays the function $|T_B(\lambda)|$ for an interferometer in gravimeter configuration. At short wavelengths, the transfer function scales as $\sim \lambda$, indicating that the interferometer acts as a spatial filter, effectively averaging over high-frequency magnetic field fluctuations. In contrast, at long wavelengths, the transfer function exhibits a scaling $\sim T^2/\lambda$. As expected, this implies that with a longer free-evolution period, the interferometer becomes more sensitive to long-wavelengths magnetic noise.

4.5 Cold-atom collisions

After the molasses stage the atomic source is a diluted cloud of particles that may be assumed to collide elastically. Cold-atom collisions shift the energy of the atomic internal state and induce a detuning [86]

$$\dot{\phi}_{col} = -\frac{4\,\pi\,\hbar}{m}\sum_j \rho_j\,(1+\delta_{gj})(1+\delta_{ej})\mathrm{Re}\{a_{gj}-a_{ej}\}\,, \tag{4.85}$$

where ρ_j is the atomic density associated with the j-th Zeeman sub-level, $|g\rangle$ and $|e\rangle$ are, respectively, the lower and upper hyperfine ground states, a_{ij} is the scattering length resulting from the collision between atoms in the $|i\rangle$ and $|j\rangle$ states, and δ_{ij} is the Kronecker delta accounting for quantum statistics. Assuming that only atoms in the Zeeman $m_F = 0$ state participate in the interferometric pulse sequence we get

$$\dot{\phi}_{col} = -\frac{4\,\pi\,\hbar}{m}\left(2\,\rho_g\,\mathrm{Re}\{a_{gg}-a_{eg}\}+2\,\rho_e\,\mathrm{Re}\{a_{ge}-a_{ee}\}\right)\,. \tag{4.86}$$

During the interferometric sequence, atoms spend equal times in both states, so $\rho_g = \rho_e = \rho/2$. In the hypothesis of elastic collisions $a_{ij} = a_{ji}$, and the the above equation can be written in the compact form

$$\dot{\phi}_{col}(t) = (K_{ee}+K_{gg})\,\rho(t)\,, \tag{4.87}$$

where K_{ii} is the coefficient that determines the frequency shift of the $|i\rangle$ state, and $\rho(t) = N\,n(t)$, with N number of total atoms and $n(t)$ volumetric density. Assuming that the atomic cloud evolves in phase-state starting from an initial spherical symmetric Gaussian distribution, we find an analytic expression for the volumetric density

$$n(t) = \frac{1}{8\,\pi^{3/2}\,\sigma^3(t)}\,, \tag{4.88}$$

with $\sigma(t) = \sigma_0 + \sigma_v\,t$ width of the atomic distribution.
Using the sensitivity function formalism we compute the interferometric phase shift due to cold-atom collisions

$$\begin{aligned}\Delta\Phi = (K_{ee}+K_{gg})\,\frac{N}{8\,\pi^{3/2}\sigma_0^2}\Bigg[\frac{1}{\sigma_0}\left(\frac{1}{\Omega_3}\tan\frac{\theta_3}{2}-\frac{1}{\Omega_1}\tan\frac{\theta_1}{2}\right)+\ldots\\ 2\,T\left(\frac{1}{\sigma(2T)}-\frac{1}{\sigma(T)}\right)\Bigg]\,,\end{aligned} \tag{4.89}$$

with σ_0 the width of the atomic cloud at the beginning of the interferometric sequence. The bias phase shift induced by cold-atom collisions comprises two terms: one dependent solely on the initial atomic density, resulting from the imbalance between the Rabi frequencies experienced by the atoms during the first and last pulse, and the other function of the free-evolution time, stemming from changes in density due to cloud expansion. In any case, the bias phase shift induced by atomic collisions increases with higher atomic density. Consequently, the number of atoms becomes a compromise between the interferometer's signal-to-noise ratio and accuracy.
For temperatures less than 100μK, the coefficient K_{ii} does not depend on the atomic kinetic energy and can be computed via scattering theory [86]. In particular, for ^{85}Rb atoms and a temperature $\mathcal{T} = 1\mu$K the two coefficients are

$$\begin{aligned} K_{gg} &= +\frac{(2\pi)\,5\cdot 10^{-3}}{10^9}, \\ K_{ee} &= -\frac{(2\pi)\,45\cdot 10^{-3}}{10^9}, \end{aligned} \tag{4.90}$$

with K_{ii} in units $[(\mathrm{rad/s})\,\mathrm{cm}^3]$. ^{87}Rb has scattering lengths approximately one order of magnitude smaller than those of ^{85}Rb, resulting in a less significant bias.

4.6 Zero-dead-time mode

Atom interferometers operating in pulse-mode are affected by aliasing noise which severely limits their short-term sensitivity [67]. During the dead time, the Raman phase noise is not monitored, leading to uncorrelated interferometric noise between consecutive measurement cycles.
For an atom interferometer operating in pulse-mode the two-sample Allan variance of the interferometric phase is

$$AVAR_{\Delta\Phi} = \frac{1}{2}\,\langle\left(\overline{\Delta\Phi}_{m+1} - \overline{\Delta\Phi}_m\right)^2\rangle \tag{4.91}$$

where $\langle\ldots\rangle$ is the average operator and $\overline{\Delta\Phi}_m = 1/m\sum_{i=1}^{m}\Delta\Phi_i$ is the average interferometric phase after m measurement cycles. Due to the dead time, two consecutive measurements are uncorrelated, hence in the limit of $m \gg 1$ the Allan deviation is given by

$$ADEV_{\Delta\Phi} = \frac{\sigma_\phi\sqrt{6\,T_c}}{\sqrt{\tau_c}} + \frac{\sigma_m\sqrt{T_c}}{\sqrt{\tau_c}} \tag{4.92}$$

where σ_ϕ and σ_m are, respectively,the rms noise of the Raman phase and the rms measurement noise [10], and the cluster time is a multiple of the cycling period, i.e. $\tau_c = m\,T_c$. The $\sqrt{6}$ factor is due to the fact that each interferometric phase $\Delta\Phi_i = \phi(i\,T_c) - 2\,\phi(i\,T_c + T) + \phi(i\,T_c + 2\,T)$ is the linear combination of three uncorrelated phases and that the two samples $\overline{\Delta\Phi}_m$ and $\overline{\Delta\Phi}_{m+1}$ are uncorrelated. As expected the Allan deviation exhibits a $\sim 1/\sqrt{\tau_c}$ scaling as a consequence of uncorrelated measurements.
In the context of time-domain atom interferometers [11], zero-dead-time (ZDT) mode can be achieved by hybridizing the output of a high-frequency classical inertial sensor with an atom interferometer [16] or by opportunely staggering in time multiple interferometers in a 'juggling' configuration [13, 27].
In the case of a $\pi/2 - \pi - \pi/2$ pulse sequence, ZDT mode can be achieved by staggering three atom interferometers with a time $T_s \approx T$ as shown in Figure 4.17. In this case it is useful to write the term $\overline{\Delta\Phi}_m$ in function of the Raman phases at each pulse

$$\overline{\Delta\Phi}_m = \frac{1}{m}\sum_{i=0}^{m-1} \phi(i\,T) - 2\phi((i+1)\,T) + \phi((i+2)\,T)\,. \tag{4.93}$$

When expanding the sum in Eq. (4.93) consecutive terms cancel out reducing to

$$\overline{\Delta\Phi}_m = \frac{1}{m}\left[\phi(0) - \phi(T) - \phi(m\,T) + \phi((m+2)\,T)\right]\,. \tag{4.94}$$

Combining this term with $\overline{\Delta\Phi}_{m+1}$ and assuming $m \gg 1$ leads to

$$ADEV_{\Delta\Phi} = \frac{2\,\sigma_\phi\,T}{\tau_c} + \frac{\sigma_m\sqrt{T}}{\sqrt{\tau_c}} \tag{4.95}$$

where $\tau_c = m\,T$. The combination of the three atom interferometers creates phase correlations between consecutive pulses. As a consequence, the Allan deviation exhibits a $\sim 1/\tau_c$ scaling, resulting in improved short-term sensitivity compared to the standard single-interferometer case.

In Figure 4.16, we compare the simulated cumulative interferometric phase of three atom interferometers operating in both the standard single mode and the ZDT configuration. While the cumulative phase of the single interferometer exhibits a random walk due to uncorrelated phases between consecutive cycles, the ZDT mode's cumulative phase remains bounded thanks to correlations between consecutive measurement cycles. For completeness, we present the simulated Allan deviation, emphasizing the expected $\sim 1/\tau_c$ scaling in the ZDT case and the enhanced short-term sensitivity

[10] The measurement noise, for instance, is due to the state detection stage and is assumed to be uncorrelated.

[11] Zero-dead time mode is automatically achieved in the space-domain atom interferometers operating with three Raman beams separated in space and with a continuous atomic beam [28].

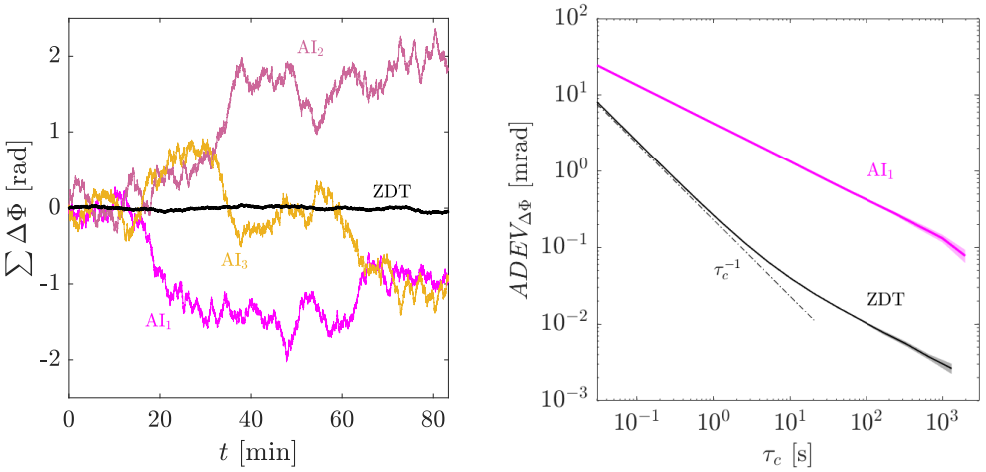

(A) Cumulative interferometric phase (B) Allan deviation

FIGURE 4.16: Comparison of atom interferometer operating in standard and zero-dead-time (ZDT) mode. Panel (A): Simulated cumulative interferometric phase of three atom interferometers (AI_i) operating in standard and ZDT mode. The ZDT cumulative phase is bound at 22mrad rms. Panel (B): Simulated Allan deviations of an atom interferometer operating in standard mode and in ZDT mode. Simulation parameters: free-evolution time $T = 10$ms, cycling period of the i-th atom interferometer $T_c = 3T$, laser phase noise $\sigma_\phi = 10$mrad rms, measurement noise $\sigma_m = 1$mrad rms.

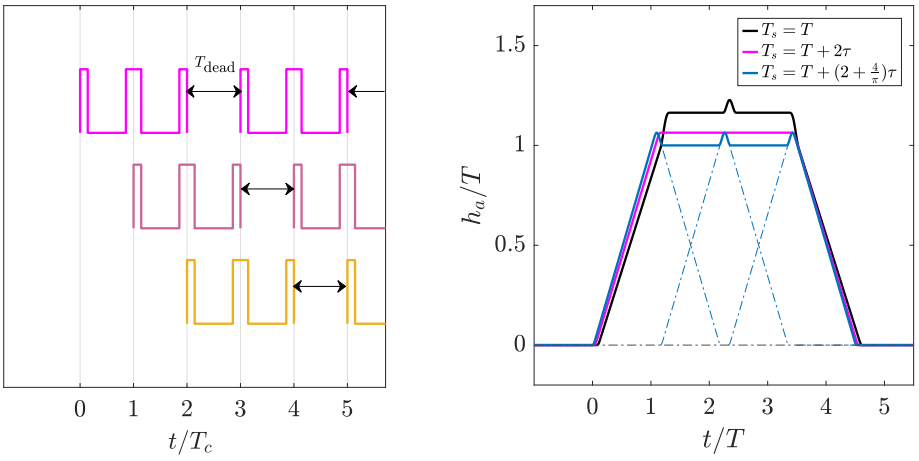

(A) Pulse timing in ZDT mode (B) Combined acceleration IRFs

FIGURE 4.17: Panel (A): Pulse timing diagram of 3 Mach-Zehnder interferometers operating in ZDT mode. The three interferometers are staggered with a time $T_s = T + 2\tau$. Panel (B): Combined acceleration impulsive response functions of three atom interferometers with three different staggering times.

compared to the standard operating mode. However, as atom interferometers are ultimately limited by uncorrelated measurement noise, for longer cluster times, the Allan deviation departs from its $\sim 1/\tau_c$ scaling and instead follows the standard $\sim 1/\sqrt{\tau_c}$ asymptotic behavior.

The combination of three atom interferometers in ZDT mode necessitates a precise selection of the staggering time to achieve uniform sensitivity. In Figure 4.17, we present the combined acceleration IRF for three different staggering time values. Only in the case of $T_s = T + 2\,\tau$ the combined sensitivity is uniform, in line with the Fourier transform of the single acceleration IRF, which has a zero at the frequency $f = 1/(T + 2\,\tau)$. In contrast, the cases of $T_s = T$ and $T_s = T + (2 + 4/\pi)\,\tau$ do not yield uniform sensitivity due to imperfect pulse overlap. Nevertheless, it's worth noting that in the latter case, the combined sensitivity during the free-evolution period remains constant at 1, indicating that the scale-factor of the ZDT accelerometer during these periods is $SF_a = k_{\text{eff}}\,T^2$.

Chapter 5

Optimized beam-splitter pulses

The performance of a cold-atom inertial (CAI) sensor strongly depends on the fidelity of the process with which the laser pulse diffracts the atomic wavefunction. Focusing on the conventional $\pi/2 - \pi - \pi/2$ sequence using rectangular constant-power Raman pulses, the fidelity of the inversion and beam-splitting processes primarily affects the visibility [41, 46] and the phase shift of the interferometric signal [52, 20, 54], respectively. The influence of the inversion process on the contrast fidelity of the interferometer stems from the fact that a rectangular mirror pulse has a narrower bandwidth than the corresponding beam-splitter pulse. On the other hand, the beam-splitting process determines the splitting of the atom in a superposed state during which the wavefunction accumulates the phase impressed by the laser grating.

Composite pulses [87, 88, 89] and optimal control [90, 91] approaches have been used to design tailored pulses that enhance the fidelity of atom interferometers. However, while significant efforts have been invested in designing optimized pulse sequences that demonstrate higher fringe contrast than conventional sequences with constant-power pulses, less attention has been devoted to enhancing interferometric phase fidelity, with a few exceptions [92].
The phase accumulated by the atomic wavefunction at the end of the beam-splitting process (superposition phase) depends on the detuning from the Raman transition. Phase compensation only occurs when the Rabi frequency experienced by the atoms during the first and last pulses is the same [92]. Any asymmetries in the temporal profile of the Rabi frequency relative to the central mirror pulse result in uncompensated superposition phase and, consequently, an error in the interferometric phase. Optimized beam-splitter pulses are characterized by minimized superposition phase across various detunings and Rabi frequency values, thereby ensuring reduced phase dispersion and relaxing the requirement for a symmetric Rabi frequency configuration. Asymmetries in the Rabi frequency experienced by the atomic ensemble can result from various factors, such as couplings between laser spatial intensity inhomogeneities and

atomic motion in the plane transverse to the Raman effective wave-vector, or temporal stochastic fluctuations in laser intensity. Nevertheless, coupling between Rabi frequency asymmetries and phase dispersion induced by a non-optimal beam-splitting process affects the performance of a CAI sensor in terms of bias and scale-factor error [52, 16].

Building upon these premises, this chapter introduces a method for designing optimized beam-splitter pulses characterized by minimized superposition phases across a range of detunings and Rabi frequency values. This method, based on time-dependent perturbation theory (TDPT), links the sensitivity function formalism with optimal control providing a geometric interpretation of the optimization problem in the Bloch sphere picture.

A substantial portion of the material presented here is adapted from Ref. [73]. The structure of the chapter is based as follows

1. We present the motivations and the background theory, showing the link between TDPT and the sensitivity function formalism, and deriving the cost function and the constraints of the optimization problem.

2. After obtaining an optimized beam-splitter waveform that modulates the laser intensity over time while constraining the laser phase to 0 and π values, we proceed to analyze the simulated performance of this standalone optimized pulse, comparing it to a conventional rectangular pulse. In this context, we introduce a novel method for visualizing the evolution of an atomic ensemble on the Bloch sphere and formulate a criterion that attempts to explain how the optimized waveform achieves minimized phase dispersion.

3. We compute the simulated phase fidelity of a Mach-Zehnder interferometer operating with the optimized beam-splitter, showing its impact on the bias of a cold-atom accelerometer in presence of couplings between laser intensity inhomogeneities and atomic motion in the plane transverse to the Raman effective wave-vector. Furthermore, we calculate the scale-factor error caused by inter-pulse laser intensity fluctuations, demonstrating that an atom interferometer operating with optimized beam-splitters offers enhanced performance compared to one operating with conventional rectangular pulses.

4. Finally, we evaluate the possibility to obtain smooth waveforms investigating the effect of high-frequency components upon pulse and interferometer fidelity.

5.1 Background theory

The rotating wave and adiabatic elimination approximations reduce the dynamics of the atom's hyperfine ground states undergoing stimulated Raman transition to an effective two-level system. Starting from the Liouville-von Neumann equation that describe the evolution of the density matrix

$$\boldsymbol{\rho} = \begin{bmatrix} \rho_{gg} & \rho_{ge} \\ \rho_{eg} & \rho_{ee} \end{bmatrix}, \tag{5.1}$$

where the diagonal terms are the atomic populations, $\rho_{ii} = |i\rangle \langle i|$, and the off-diagonal terms are the atomic coherences, $\rho_{ij} = |i\rangle \langle j|$, we define the Bloch vector with the following transformation [93]

$$\begin{pmatrix} b_x \\ b_y \\ b_z \end{pmatrix} = \begin{pmatrix} 2\,\mathrm{Re}\{\rho_{ge}\} \\ 2\,\mathrm{Im}\{\rho_{ge}\} \\ \rho_{gg} - \rho_{ee} \end{pmatrix}. \tag{5.2}$$

Here $|g\rangle$ and $|e\rangle$ are, respectively, the internal lower and upper hyperfine ground states, and the components of the Bloch vector are expressed in the basis defined by the Pauli matrices. With the transformation of Eq. (5.2), the Liouville-von Neumann equation is reduced to a system of real first order ordinary differential equations (Bloch equation)

$$\frac{d}{dt}\begin{pmatrix} b_x \\ b_y \\ b_z \end{pmatrix} = \begin{bmatrix} 0 & -\delta(t) & 0 \\ \delta(t) & 0 & \Omega\, u(t) \\ 0 & -\Omega\, u(t) & 0 \end{bmatrix} \begin{pmatrix} b_x \\ b_y \\ b_z \end{pmatrix}, \tag{5.3}$$

with $\delta(t)$ the two-photon detuning [1], Ω the effective (or two-photon) Rabi frequency, and $u(t)$ a factor that accounts for the time modulation of the effective Rabi frequency. In deriving Eq. (5.3), we made the assumption that the laser phase $\phi_L(t)$ is restricted to take values of 0 and π. This constraint incorporates the laser phase modulation into the sign of the factor $u(t)$. Specifically, $u(t)$ is positive (negative) when the laser phase is $\phi_L = 0$ ($\phi_L = \pi$).

A closer look at Eq. (5.3) reveals that the internal state dynamics is described by the rotation of the Bloch vector in a plane orthogonal to the field vector $\mathbf{F} = (-\Omega\, u(t)\,, 0,\, \delta(t))^T$. To maintain population conservation, the Bloch vector's norm is constrained to unity, which confines its motion to a unitary sphere known as the Bloch sphere.

Eq. (5.3) has an analytical solution when $\delta(t)$ and $u(t)$ are time-invariant. In cases with time-variant parameters one can apply time-dependent perturbation theory (TDPT) to

[1] The two-photon detuning is defined as $\delta = \delta_{12} - \delta_{AC} = \delta_L - (\omega_{eg} + \delta_D + \delta_R) - \delta_{AC}$

obtain an approximate solution in the form of a perturbation expansion series, such as the Magnus [94] and Dyson [95] series, for instance. Although Magnus expansion exhibits some remarkable properties such as the conservation of the unitary character of the time-evolution operator [96], the presence of nested commutators makes it challenging to explicitly construct high-order terms. For this reason and because of its direct link with the sensitivity function formalism, we focus on Dyson expansion.
Approximated solution of Eq. (5.3) can be found in form of Dyson series as

$$\begin{aligned} \mathbf{b}(t) \;=\; & \mathbf{U_0}(t,t_0)\,\mathbf{b}(t_0) + \dots \\ & \mathbf{U_0}(t,t_0)\int_{t_0}^{t} dt' \mathbf{V}(t',t_0)\;\mathbf{b}(t_0) + \dots \\ & \mathbf{U_0}(t,t_0)\int_{t_0}^{t}\int_{t_0}^{t'} dt'dt'' \mathbf{V}(t',t_0)\mathbf{V}(t'',t_0)\;\mathbf{b}(t_0) + \dots \end{aligned} \tag{5.4}$$

where

$$\mathbf{V}(t,t_0) = \mathbf{U_0}^{\dagger}(t,t_0)\mathbf{M}_{\delta}(t)\mathbf{U_0}(t,t_0)\,, \tag{5.5a}$$

$$\mathbf{M}_{\delta}(t) = \begin{bmatrix} 0 & -\delta(t) & 0 \\ \delta(t) & 0 & 0 \\ 0 & 0 & 0 \end{bmatrix}, \tag{5.5b}$$

and $\mathbf{U_0}(t,t_0)$ is the unperturbed time-evolution operator that propagates the atomic state from t_0 to t in the case of zero detuning as it is given by

$$\mathbf{U_0}(t,t_0) = \begin{bmatrix} 1 & 0 & 0 \\ 0 & C(t) & S(t) \\ 0 & -S(t) & C(t) \end{bmatrix}, \tag{5.6}$$

with $S(t) = \sin\theta(t)$ and $C(t) = \cos\theta(t)$. The quantity $\theta(t) = \int_{t_0}^{t} \Omega\, u(t')dt'$ is the angle described by the Bloch vector about the x-axis and is known as pulse area. As expected, in the unperturbed case, the Bloch vector describes a trajectory in the $y-z$ plane.

At the beginning of the Mach-Zehnder sequence, the atom is in one of the ground hyperfine states. Hence, it makes sense to consider as initial condition the basis state $\mathbf{b}(t_0) = (0,\,0,\,1)^T$, i.e. the Bloch vector points at the North pole of the Bloch sphere. This assumption effectively reduces the number of elements in the matrix product $\prod_{\ell=1}^{\infty} \mathbf{V}(t^{\ell},t_0)$ that need to be considered.
Therefore, we report here the Dyson series expansion up to the second order

$$\mathbf{b}(t) = \mathbf{b}^{(0)}(t) + \delta\mathbf{b}^{(1)}(t) + \delta\mathbf{b}^{(2)}(t) + \dots , \tag{5.7}$$

where $\mathbf{b}^{(0)}(t)$ is the unperturbed (zeroth order) solution

$$\mathbf{b}^{(0)}(t) = \begin{pmatrix} 0 \\ S(t) \\ C(t) \end{pmatrix} , \tag{5.8}$$

$\delta\mathbf{b}^{(1)}(t)$ is the first order correction

$$\delta\mathbf{b}^{(1)}(t) = \int_{t_0}^{t} dt' \, \delta(t') \begin{pmatrix} -S(t') \\ 0 \\ 0 \end{pmatrix} , \tag{5.9}$$

and $\delta\mathbf{b}^{(2)}(t)$ is the second order correction

$$\delta\mathbf{b}^{(2)}(t) = \int_{t_0}^{t} dt' \int_{t_0}^{t'} dt'' \, \delta(t') \, \delta(t'') \begin{pmatrix} 0 \\ -S(t'') \, S(t') \\ S(t'') \, C(t') \end{pmatrix} . \tag{5.10}$$

Defining the angles $\delta\Phi$ and $\delta\alpha$, respectively, as the longitude and latitude errors with respect to the unperturbed solution

$$\delta\Phi := \tan^{-1} \frac{b_x}{b_y} , \tag{5.11a}$$

$$\delta\alpha := \sin^{-1} b_z , \tag{5.11b}$$

we can express the terms in the Dyson series in spherical coordinates. In Table 5.1 we reported the longitude and latitude errors up to the second order.

The longitude error, $\delta\Phi$, defines the azimuth deviation of the Bloch vector with respect to the $y - z$ plane and it is connected with the phase error accumulated by the atomic wavefunction. On the other hand, the latitude error, $\delta\alpha$, defines the deviation of the Bloch vector with respect to the equatorial plane and it is connected to the amplitude of the atomic population. The two angles, $\delta\Phi$ and $\delta\alpha$, are positive as shown in Figure 5.1.

We note that, provided as initial condition the basis state $\mathbf{b}(t_0) = (0, 0, 1)^T$, longitude errors are given by odd-order terms of the Dyson expansion, while latitude errors are given by even-order terms of the Dyson expansion. This somehow reflects the parity

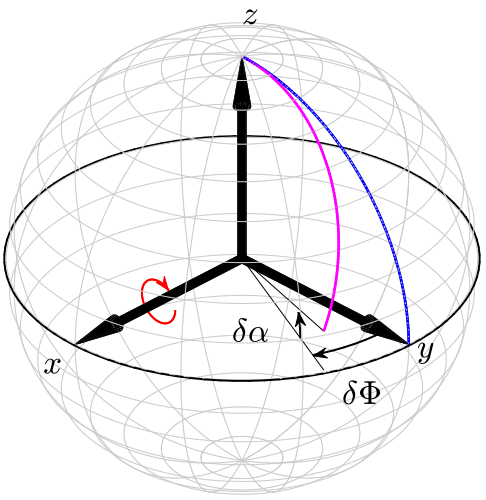

FIGURE 5.1: Bloch sphere representation of the two-level system dynamics. The North and South poles coincide, respectively, with the $|g\rangle$ and $|e\rangle$ basis states. The blue (magenta) curve represents the on-resonance (off-resonance) Bloch vector trajectory obtained for a conventional beam-splitter pulse. The angles $\delta\Phi$ and $\delta\alpha$ are, respectively, the longitude and latitude deviations of the Bloch vector from the on-resonance solution. The red circular arrow indicates the direction of the torque due to the x-component of the field vector.

character of the atomic wavefunction's amplitude and phase as functions of the detuning [92, 97].
For a rectangular constant-power beam-splitter pulse the longitude and latitude errors, up to the second order, are given by

$$\delta\Phi \approx -\frac{\delta}{\Omega}\,\tan\left(\frac{\theta}{2}\right), \tag{5.12a}$$

$$\delta\alpha \approx \left(1-\frac{\pi}{4}\right)\,\frac{\delta^2}{\Omega^2}, \tag{5.12b}$$

where we assumed steady detuning and $\delta \ll \Omega$. In the case of no pulse-length errors ($\Omega = \Omega_0 = \pi/(2\,\tau)$, the results agree with the expressions reported in the Appendix of Ref. [97].

5.1.1 Link with the sensitivity function

Starting from an initial time t_0, let us compute the first-order longitude (phase) error at a final time t_f. For $\delta \ll \Omega$ we get

$$\delta\Phi(t_f) \approx \frac{1}{S(t_f)}\,\int_{t_0}^{t_f} -S(t)\,\delta(t)\,dt\,. \tag{5.13}$$

Order	$\delta\Phi$	$\delta\alpha$
Zeroth	0	$\sin^{-1}[C(t)]$
First	$\tan^{-1}\left[\frac{1}{S(t)}\int_{t_0}^{t} -S(t')\,\delta(t')\,dt'\right]$	0
Second	0	$\sin^{-1}\left[\int_{t_0}^{t} dt' \int_{t_0}^{t'} dt''\,\delta(t')\,\delta(t'')\,S(t'')\,C(t')\right]$

TABLE 5.1: Dyson expansion up to the second order in terms of longitude ($\delta\Phi$) and latitude ($\delta\alpha$) errors.

Comparing Eq. (5.13) with Eq. (4.5), we recognize in the term

$$-\frac{S(t)}{S(t_f)} \equiv g_\phi(t) \tag{5.14}$$

the phase sensitivity function. Hence, Eq. (5.13) not only provides the phase error accumulated by the atomic wavefunction after the beam-splitting process but also yields the interferometric phase[2].
Eq. (5.14) is a generalized expression for the phase sensitivity function valid in the case of time-varying Rabi frequency, where the term $S(t_f)$ at the denominator accounts for pulse-length errors.
For an interferometer operating with conventional constant-power pulses, Eq. (5.14) reduces to Eq. (4.11), and the phase error accumulated by the atomic wavefunction in the case of steady detuning is

$$\delta\Phi \approx \delta\left[\frac{1}{\Omega_3}\tan\left(\frac{\theta_3}{2}\right) - \frac{1}{\Omega_1}\tan\left(\frac{\theta_1}{2}\right)\right]. \tag{5.15}$$

As expected, a steady detuning does not induce any interferometric phase shift when there are no variations in the Rabi frequency experienced by the atoms during the first and last pulse.

5.1.2 Optimization problem

For a resonant beam-splitter pulse, the Bloch vector starting from the basis state $\mathbf{b}(0) = (0,\,0,\,1)^T$ will end up in the state $\mathbf{b}(\tau) = (0,\,1,\,0)^T$, where τ is the beam-splitter duration. Detuning ($\delta \neq 0$) and pulse-length errors ($\Omega \neq \Omega_0 = \pi/(2\,\tau)$) cause deviations of the Bloch vector trajectory from the resonant case. Consequently, the final atomic state

[2]Note that a positive sign of the angle $\delta\Phi$ indicates a negative rotation about the z-axis, while a positive detuning, δ, corresponds to positive rotations about the z-axis. Therefore, when δ in Eq. (5.13) represents either the Doppler detuning (δ_D) or the differential AC Stark shift (δ_{AC}), the angle $\delta\Phi$ is equal to the interferometric phase, $\Delta\Phi$. However, if δ represents the laser detuning (δ_L), then $\Delta\Phi = -\delta\Phi$.

will differ from $(0,\, 1,\, 0)^T$.
Since the deviations of the Bloch sphere trajectory from the resonant case are represented by the angles $\delta\Phi$ and $\delta\alpha$, it is reasonable to assume that a robust beam-splitter pulse should ensure minimized errors for different detuning and Rabi frequency values. Hence, we optimize the beam-splitter pulse solving the following minimization problem

$$\min_{u(t)} \left[\sum_{k,i} w_i^{(k)} \delta\Psi_i^{(k)}(\tau) + \mathcal{P} \right] \qquad \forall\, \delta = \text{const}\,, \tag{5.16}$$

where $\delta\Psi_i^{(k)}$ is the i-th component of the k-th order of the vector $\boldsymbol{\delta\Psi} = (\delta\Phi,\, \delta\alpha)^T$ defining the angular deviation of the Bloch vector for the resonant case. Each term $\delta\Psi_i^{(k)}$ is weighted by a dimensionless coefficient $w_i^{(k)}$ that can be tuned in order to achieve a better optimization. The term $\mathcal{P}$ is a penalty parameter proportional to the second derivative of the Rabi frequency control law, i.e. $\mathcal{P} \propto \partial^2 u/\partial t^2$, and can be tuned in order to enhance the waveform smoothness [98]. Given the pulse duration, τ, the output of the optimization problem is the waveform $u(t)$.
In the solution of the minimization problem described by Eq. (5.16) we impose the following non-linear constraints

$$S(\tau) \leq 1\,, \tag{5.17a}$$

$$|u(t)| \leq 1\,. \tag{5.17b}$$

The first condition ensures that the beam-splitting condition ($\theta(\tau) \leq \pi/2$) is met in the resonant case. The inequality relaxes the constraints, enabling the optimization algorithm to find better waveforms. The second condition sets a constraint on the maximum Rabi frequency, reflecting practical limits on the achievable laser intensity.

5.1.2.1 Dyson series convergence

When using series expansion in TDPT, we need to verify that the convergence criterion is met. In our case, each correction term in the Dyson expansion scales as $(\delta/\Omega)^k$, where k represents the perturbation order. Hence, convergence is achieved if $\delta \ll \Omega$. Even if the detuning is of the same order as the Rabi frequency, convergence can still be achieved splitting the integration of Eq. (5.4) in many time intervals of duration Δt and ensuring that the condition $\|\mathbf{V}(\Delta t)\, \Delta t\|_2 \ll 1$, with $\|\ldots\|_2$ denoting the L^2-norm, is fulfilled [99].
We explicitly verified the convergence of the Dyson series using d'Alembert's criterion. Figure 5.2 shows the norm of the Bloch vector corrections up to the 7th order for $\delta/\Omega =$

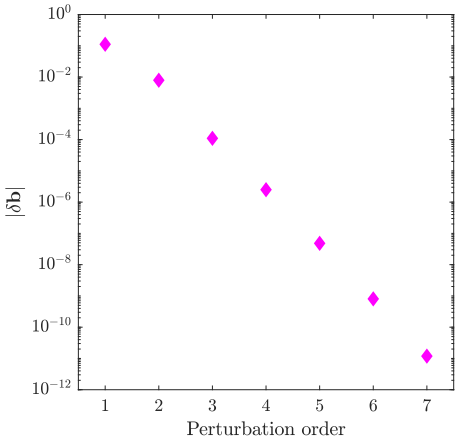

FIGURE 5.2: Norm of the Bloch vector corrections computed for $\delta/\Omega = 1$ and $\Delta t = 100$ns.

1 and $\Delta t = 100$ns. The 7th order term is approximately two orders of magnitude lower than the 6th order term. This monotonic decreasing behavior confirms convergence under our operating conditions.

5.1.3 Features of the optimization method

The choice of an optimization method based on TDPT relies on minimizing errors from off-resonance conditions. The cost function is derived analytically from perturbation expansion terms, eliminating the need for averaging over a specific atomic ensemble, unlike non-perturbative methods such as GRAPE [90] and Krotov-based methods [100]. Instead of aiming to achieve a target state across various detuning values, we seek waveforms that minimize errors caused by off-resonance conditions, adopting an approach similar to early composite pulses design [101]. This error minimization approach helps us avoid the presence of 'wobbles' in pulse fidelity around the resonance condition, a characteristic issue in ensemble-based optimization methods [91, 92, 102]. Formulating the cost function in terms of deviations of the Bloch vector from the resonant case allows for an intuitive geometric interpretation of the optimization problem on the Bloch sphere. Moreover, the optimized method establishes an immediate and direct connection with the sensitivity function formalism, facilitating a clearer understanding of how the beam-splitting process impacts the phase fidelity of the interferometer.

5.2 Results

In this section, we present the results of the optimization, analyzing the impact of the various terms in the cost function. Subsequently, for a given beam-splitter waveform,

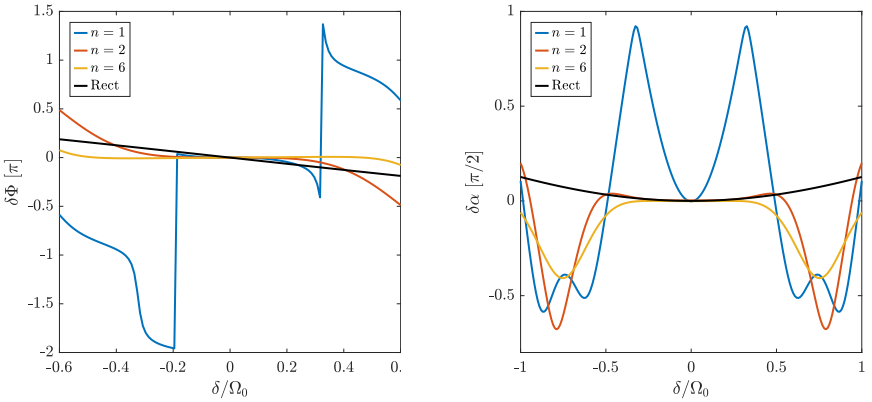

(A) Longitude error (B) Latitude error

FIGURE 5.3: Effect of the number of Dyson expansion orders (n) upon the optimization in terms of longitude and latitude errors. We report, as reference, the longitude and latitude error of a conventional rectangular beam-splitter pulse. The resonant Rabi frequency is $\Omega_0 = 2\pi \times 200$kHz, while the duration of the optimized pulses is $\tau = 8\,t_\pi$.

we conduct a symmetry and stability analysis of the Bloch vector trajectories. Our goal is to explain how the optimized pulse steers an atomic ensemble towards the target error-free state. Finally, we analyze the impact of the optimized beam-splitter pulse on interferometer performance, considering both contrast and phase fidelity. Specifically, we demonstrate that optimizing the beam-splitter pulse enables the interferometer to remain robust against errors induced by asymmetric Rabi frequency configurations relative to the central mirror pulse.

5.2.1 Optimized beam-splitter pulse

Given in input the total duration of the pulse and the maximum Rabi frequency, the output of the optimization is the dimensionless waveform $u(t)$.

Figure 5.3 displays the effects of Dyson series orders on the optimization in terms of longitude (phase) and latitude (population amplitude) fidelity. As expected, the higher the number of orders considered in the cost function, the larger the range of detunings for which the minimization condition is achieved.

Figure 5.4 displays the waveform and pulse area of an optimized beam-splitter pulse. We considered orders up to the 7th in the Dyson expansion. The total pulse duration is $\tau = 8\,t_\pi$, where t_π represents the duration of an equivalent rectangular mirror pulse with a Rabi frequency equal to the maximum Rabi frequency of the optimized waveform. The chosen maximum Rabi frequency is $\Omega_0 = 2\pi \times 200$kHz. We divide the waveform into 200 piecewise segments, each corresponding to a time step of duration $\Delta t = 100$ns, which can be readily handled by the laser modulation system [91, 98, 102].

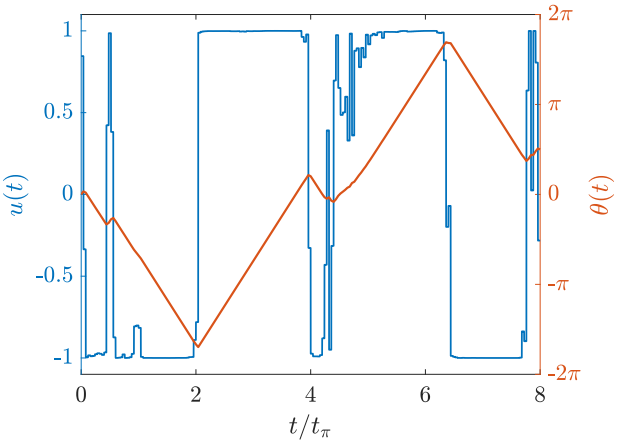

FIGURE 5.4: Dimensionless waveform ($u(t)$) and pulse area ($\theta(t)$) of an optimized beam-splitter pulse. Dyson expansion terms up to the 7th orders have been considered in the cost function. The resonant Rabi frequency is $\Omega_0 = 2\pi \times 200$kHz, while the duration of the optimized pulses is $\tau = 8\,t_\pi$.

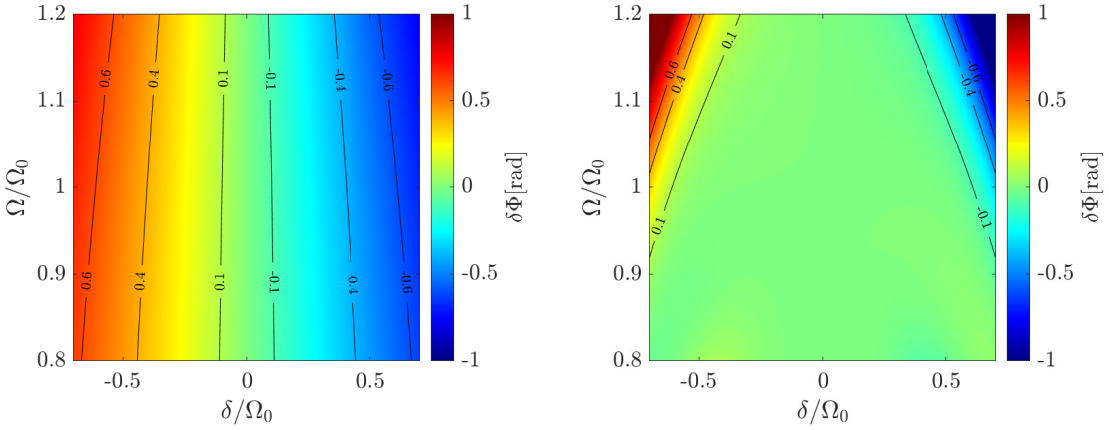

(A) Conventional beam-splitter

(B) Optimized beam-splitter

FIGURE 5.5: Phase map of the conventional and optimized beam-splitter pulse corresponding to the waveform represented in Figure 5.4.

In Figure 5.5, we compare the phase fidelity map of the selected waveform to that of an equivalent beam-splitter pulse with the same maximum Rabi frequency. For $\Omega = \Omega_0$ (no pulse-length errors), the optimized beam-splitter pulse exhibits minimal longitude error (green-shaded area delimited by the ± 0.1rad isolines) over a range of detunings approaching the Rabi frequency. It is worth noting that as the maximum Rabi frequency (Ω) decreases from the design value (Ω_0), the range of detunings over which the minimized longitude error is achieved expands.

5.2.1.1 Symmetry and stability analysis of Bloch vector trajectories

Since the birth of composite pulses and optimal control, the longstanding question of *why* and *how* optimized waveforms work remains open. Although in our case the waveform is quite regular, optimal control could produce very noisy waveforms, making it even more difficult to interpret the results of the optimization [103].

In order to understand how the optimized waveform works, it might be useful, as a first step, to visualize the atomic dynamics on the Bloch sphere. The atomic dynamics is characterized by two parameters, namely the two-photon detuning δ and the maximum Rabi frequency Ω. Therefore, representing the time-evolution of an atomic ensemble on the Bloch sphere under the action of the optimized waveform is not trivial. Although various techniques can be found in literature, such as spectrograms or scalograms, both involving transformations in the frequency domain [103], we propose a method based on the construction of pseudo-probability density functions. Given an ensemble $\mathcal{E} = \{\delta/\Omega_0 \in [\epsilon_{min}, \epsilon_{max}] \text{ and } \Omega/\Omega_0 \in [\eta_{min}, \eta_{max}]\}$ subject to the optimized waveform, we numerically integrate the Bloch equations and construct the time-evolution of the latitude, longitude and latitude-longitude error histograms. We obtain the pseudo-probability density function normalizing the histograms with respect to its maximum value at each time-step. The normalization operation does not alter the pseudo-probability density function shape but provides a better contrast. Figure 5.6 displays the pseudo-probability density function of an atomic ensemble $\mathcal{E} = \{\delta/\Omega_0 \in [-0.8, 0.8] \text{ and } \Omega/\Omega_0 \in [0.8, 1.2]\}$ of 200x200 particles. The top row presents the longitude-latitude error pseudo-probability density function mapped onto the Bloch sphere at three time instants, namely, $t = 2$, 4, and $8\,t_\pi$. The magenta line represents the full time-evolution of the Bloch vector corresponding to $\delta/\Omega_0 = 0.4$ and $\Omega/\Omega_0 = 1$. We note that, given the length of the pulse, the Bloch vector trajectory of a single atom wraps around the sphere multiple times, making it difficult to understand its dynamics on the sphere. The bottom row represents the full time-evolution of the longitude and latitude error pseudo-probability density functions with projections of the aforementioned Bloch vector trajectory. The optimized waveform effectively 'squeezes' the longitude error pseudo-probability density function reducing phase dispersion.

In Figure 5.6, we observe a symmetric pattern of the longitude error distribution with respect to the resonant unperturbed case (i.e. zero-longitude locus), meaning that the Bloch vector trajectories characterized by detunings of opposite signs are steered in opposite directions. As a consequence, negative and positive detuning paths cross each other at multiple times. Nevertheless, at the end of the pulse, the ensemble recombines, converging to the unperturbed target state. This symmetry arises because atomic states are steered on the Bloch sphere solely by controlling the field vector's amplitude (aligned with the x-axis) and restricting the laser phase to values between

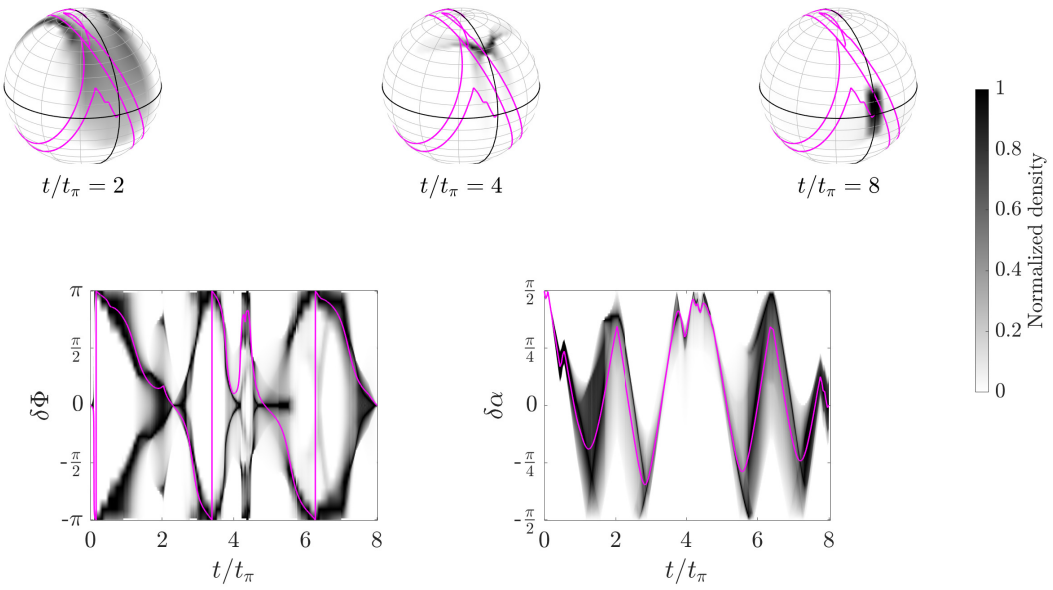

FIGURE 5.6: Time evolution of the distribution representing the atomic ensemble $\mathcal{E}$. The value of the distribution at each time instant has been normalized with respect to the maximum value. Upper panel: latitude-longitude distribution on the Bloch sphere at three different times throughout our optimized pulse: $t/t_\pi = 2$, 4, and 8. The thick meridian is given by the intersection of the Bloch sphere with the y-z plane. The magenta line represents the Bloch vector trajectory and for $\delta/\Omega_0 = 0.4$ and $\Omega/\Omega_0 = 1$. Lower panel: time evolution of the longitude distribution on the left, and latitude distribution on the right. The magenta line represents, respectively, the longitude and latitude projection of the aforementioned Bloch vector trajectory.

0 and π. When the system is on resonance, the Bloch vector trajectory lies in the y-z plane; off-resonance, the plane tilts based on the detuning sign. Consequently, atoms characterized by positive detunings have opposite longitude positions with respect to atoms characterized by negative detunings.

To understand the convergence of the longitude error distribution to the unperturbed case, we present a stability analysis based on the sign of the variation of the longitude error rate with respect to the longitude error itself. Recombination of the ensemble after each crossing point suggests that there must be a condition that forces the different trajectories to converge towards the unperturbed solution, at the end of the pulse, minimizing the longitude error. This stability condition is given by

$$\mathcal{S}(\delta, t) = \frac{\partial \delta\dot{\Phi}}{\partial \delta\Phi} < 0\,, \tag{5.18}$$

where $\delta\Phi$ and $\delta\dot{\Phi}$ are, respectively, the longitude error and the longitude error rate. In Figure 5.7, the stability map $\mathcal{S}(\delta, t)$ is presented for the case of $\Omega = \Omega_0$. Bloch vector trajectories characterized by detunings falling within regions where the stability condition is met converge to the unperturbed solution. By the end of the pulse, atoms with

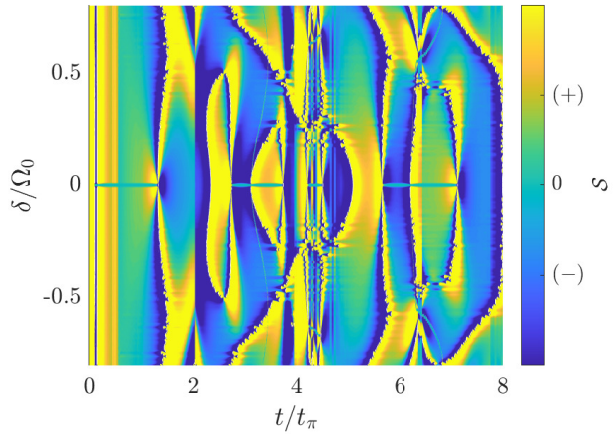

FIGURE 5.7: Stability map of Bloch vector trajectories for the optimized beam-splitter pulse. The Rabi frequency has been considered equal to the design value.

detunings in the range of $\pm 0.5\Omega_0$ satisfy the stability condition. This finding aligns with the phase error map displayed in Figure 5.5, where the optimized beam-splitter exhibits minimal phase error within the same detuning range.
The stability map offers valuable insights into the behavior of Bloch vector trajectories of far-detuned and near-to-resonance atoms. Focusing on the final part of the pulse, particularly when $t/t_\pi \gtrsim 7$, two key observations emerge: first, the Bloch vector trajectories of near-resonance atoms smoothly converge to the unperturbed solution well before the pulse's conclusion. This convergence is clearly illustrated by the presence of a relatively large stability region marked by the blue colour scale on the map. Conversely, trajectories of far-detuned atoms shift from a stable region to an unstable one, represented by a green/yellow colour scale. This transition signifies that they cross the zero-longitude error locus before the pulse's end, resulting in a change in the sign of the phase error. Second, when considering $t/t_\pi < 8$ (i.e. a shorter pulse and, hence, a lower pulse area or a lower effective maximum Rabi frequency), the range of detuning values that meet the stability condition becomes larger. This observation agrees with Figure 5.5, where the detuning range exhibiting minimal phase error expands as the ratio Ω/Ω_0 becomes less than one.

5.2.2 Interferometer performance

In this section, we analyze the performance of an 'optimized' Mach-Zehnder interferometer and compare it to a 'conventional' interferometer operating with rectangular constant-power pulses. The optimized interferometer consists of a beam-splitter with a waveform corresponding to the one shown in Figure 5.4, a rectangular constant-power mirror, and a recombiner pulse obtained by time-reversing the beam-splitter waveform. Time-reversal is necessary in order to guarantee symmetry of the pulse sequence with respect to the mid-point of the mirror pulse and, hence, avoid spurious phase shifts

[91].
Inter-pulse intensity variations break the symmetry of the interferometer, rendering it sensitive to any asymmetry in the velocity distribution or other systematic detuning, and, thus, affecting the bias instability when used as an inertial sensor [54]. Atoms within the interferometer experience inter-pulse intensity variations due to factors such as laser random fluctuations or motion through spatial inhomogeneity. For instance, with a Gaussian Raman beam profile featuring a $1/e^2$ radius of 10mm and a free-evolution time $T = 10$ms, a 1g acceleration of the sensor in the direction transverse to the laser beam axis will cause the atomic cloud to deviate by 2mm from the beam center. As a result, the recombiner pulse intensity that these atoms encounter is only $\sim 92\%$ of the intensity of the beam-splitter.

Figure 5.8 displays the simulated contrast, phase error, and their product for both the conventional and optimized Mach-Zehnder interferometers as functions of the maximum Rabi frequency ratio between the third and first pulse, Ω_3/Ω_1, and the Doppler detuning, $\delta = k_{\text{eff}}v$, where k_{eff} represents the effective wave-vector and v is the atomic velocity. In the simulation, we assume that the maximum Rabi frequencies of the beam-splitter (Ω_1) and mirror (Ω_2) pulses are equal to the resonant value, i.e., $\Omega_1 = \Omega_2 = \Omega_0 = 2\pi \times 200$kHz, while considering different values for the recombiner Rabi frequency (Ω_3).
Unlike the conventional interferometer, which exhibits a monotonically decreasing contrast as $|\delta|$ increases, the contrast map of the optimized interferometer displays a non-trivial behavior with a non-monotonic trend due to the complex features of the optimized waveform.
For a perfectly symmetric pulse sequence, i.e. $\Omega_3 = \Omega_1$, the phase error of the optimized interferometer is zero for every detuning. This is a consequence of the recombiner being the time-reversed version of the beam-splitter. For $\Omega_3 < \Omega_1$, the optimized interferometer exhibits a significant range of detunings over which the minimized phase is achieved. However, outside the minimized phase area, represented by the region enclosed by the $\pm$5mrad isoline, the phase error of the optimized sequence grows more rapidly than the phase error of the conventional one. This behaviour stems from the perturbative approach of our optimization method that minimizes error terms only around the resonance condition.

In order to include the contribution of the different velocity classes, the contrast-weighted interferometric phase has to be averaged over the atomic velocity distribution and normalized with respect the average contrast as reported in [54]. Hence, the average interferometric phase (actual output of the interferometer) is given by

$$\langle \delta\Phi \rangle = \frac{1}{\langle C \rangle} \int_{-\infty}^{+\infty} f(v) C(v) \delta\Phi(v)\, dv\,, \tag{5.19}$$

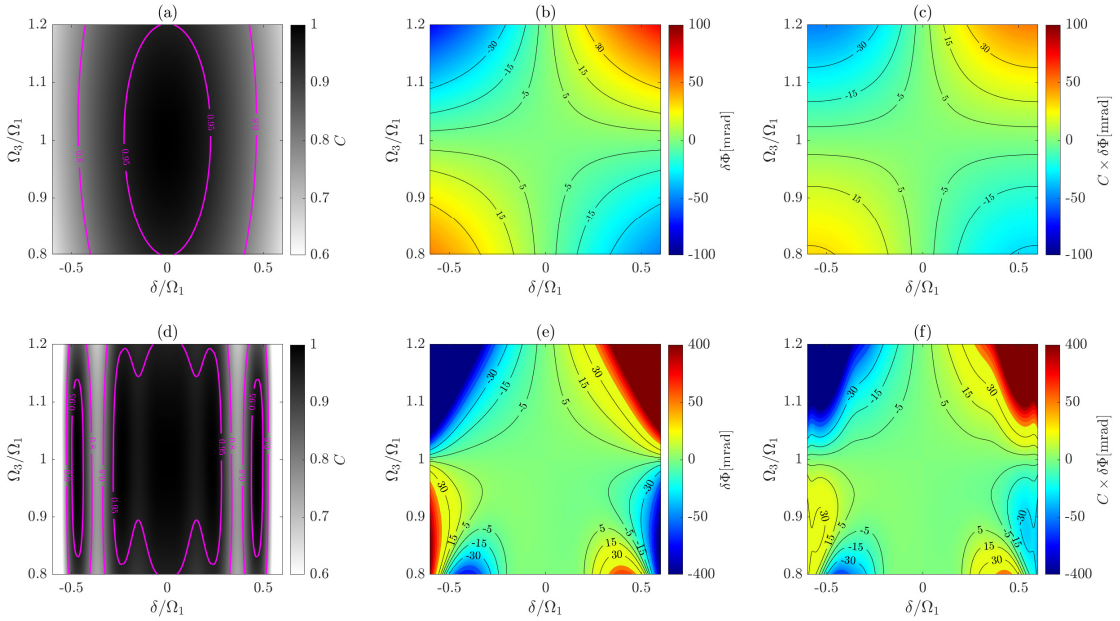

FIGURE 5.8: Upper panel: contrast map (panel (a)), interferometric phase map (panel(b)) and their product (panel (c)) of the conventional interferometer. Lower panel: contrast map (panel (d)), interferometric phase map (panel(e)) and their product (panel (f)) of the optimized interferometer. Simulation parameters: $\Omega_1 = \Omega_2 = \Omega_0 = 2\pi \times 200$kHz.

where $\langle C \rangle = \int_{-\infty}^{+\infty} f(v)C(v)\,dv$ is the average contrast, and $f(v)$ is the velocity distribution of the atomic cloud entering the interferometer.
Because of the odd parity of the contrast-weighted interferometric phase with respect to the detuning, any asymmetry or non-zero mean in the atomic velocity distribution gives rise to a bias. While asymmetries are primarily a result of the velocity selection process [41, 54], non-zero mean may arise from imbalances in counter-propagating laser intensities affecting the release of the atomic cloud from the magneto-optic trap [62], accelerations parallel to the Raman beam propagation axis, or misalignment of the Raman retro-reflecting mirror with respect to the atomic launch trajectory [29].

Figure 5.9 shows the average contrast of the conventional and optimized interferometers. In the simulation we model the velocity distribution along the beam propagation axis as a Gaussian having a standard deviation $\sigma_v = \sqrt{k_B \mathcal{T}/m}$, where k_B, $\mathcal{T}$ and m are, respectively, the Boltzmann constant, the temperature of the atomic cloud and the mass of the atomic species (in our case ^{85}Rb). Although the contrast maps of the optimized and conventional interferometers differ, their average contrasts are nearly similar. This is because for the chosen resonant Rabi frequency, the average contrast primarily depends on the rectangular mirror pulse, which is more velocity selective than the rectangular and optimized beam-splitter pulses.

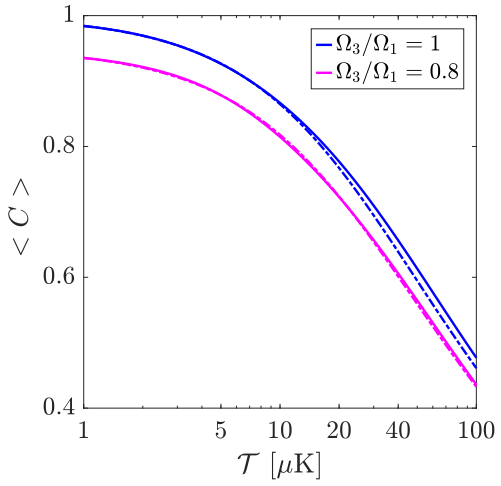

FIGURE 5.9: Average contrast of the conventional (dashed line) and optimized (continuous line) interferometers. The blue color indicates the case $\Omega_3/\Omega_1 = 1$, while the magenta color indicates the case $\Omega_1/\Omega_3 = 0.8$. Simulation parameters: $\Omega_1 = \Omega_2 = \Omega_0 = 2\pi \times 200$kHz.

5.2.2.1 Acceleration-induced bias

As an application case, we report the simulated performance of a cold-atom accelerometer in terms of bias [3] induced by the coupling between inter-pulse laser intensity variations and asymmetry in the velocity distribution. We assume that the laser intensity variations stem from the relative motion of the atomic cloud with respect to the centroid of a Gaussian Raman beam due to an acceleration orthogonal to the laser beam axis. In the simulation, we assume a Gaussian atomic velocity distribution along the beam axis with standard deviation σ_v and mean v_{sel}. The maximum Rabi frequency experienced by the atoms is given by $\Omega(t) = \Omega_0 \exp\left[-2\,\Delta r_\perp(t)^2/w_L^2\right]$, where $\Delta r_\perp(t) = 1/2\,a_\perp\,t^2$ is the transverse displacement of the centre of mass of the atomic cloud with respect to the centroid of the Raman beam, $t = 0$ is the time instant at which the first beam-splitter pulse occurs, and w_L is the $1/e^2$ beam radius.

Figure 5.10 shows the simulated bias of the optimized and conventional cold-atom accelerometers, both operating with a free-evolution time $T = 10$ms, atomic velocity distribution characterized by a temperature $\mathcal{T} = 2.1\mu$K, and beam waist $w_L = 10$mm. In the case of the optimized sequence, a bias less than 0.25μg is achieved for transverse acceleration $a_\perp \leq 1.5$g over a range $|\delta_{sel}| \leq 25$kHz. For $a_\perp \geq 1.6$g, or equivalently $\Omega_3/\Omega_1 \lesssim 0.82$, the conventional pulse sequence outperforms the optimized one in agreement with Figure 5.8.

[3] The bias on the acceleration signal is computed as Bias $= \delta\Phi/SF_a$, where ($SF_a = k_{\text{eff}}T^2$) is the ideal scale-factor of the cold-atom accelerometer.

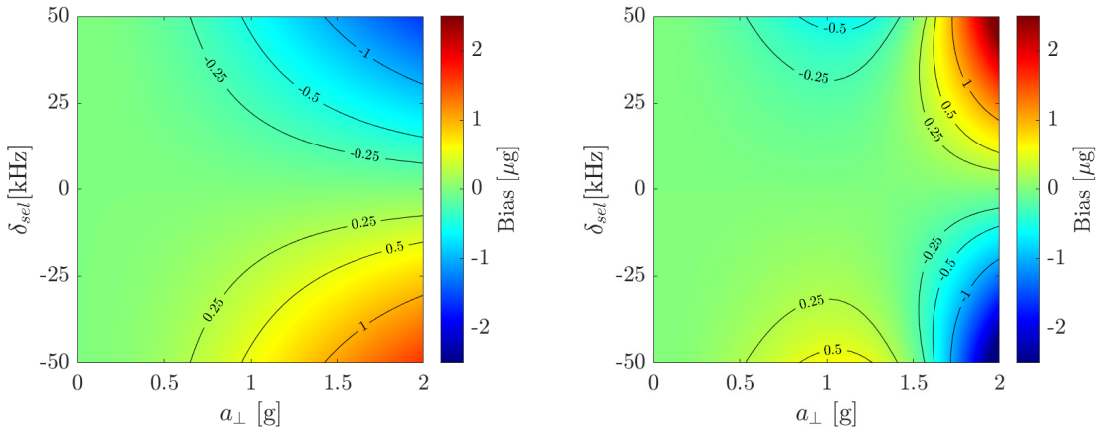

(A) Conventional interferometer (B) Optimized interferometer

FIGURE 5.10: Bias of a cold-atom accelerometer due to the coupling inter-pulse laser intensity variations and asymmetry of the velocity distribution. Panel (A): conventional interferometer. Panel (B): optimized pulse interferometer. Simulation parameters: free-evolution time $T = 10$ms; atomic temperature $\mathcal{T} = 2.1\mu$K; Gaussian beam waist $w = 10$mm; $\Omega_1 = \Omega_0 = 2\pi \times 200$kHz.

5.2.2.2 Sensitivity to laser intensity drifts

One of the key features of the presented optimization method is its connection to the sensitivity function formalism. We recall that, to first order, the phase accumulated by the atomic wavefunction during the interferometric sequence is proportional to the area under the sensitivity function. Consequently, we can readily deduce that the use of optimized beam-splitter pulses significantly reduces the influence of light-shifts upon CAI sensor's performance, as they minimizes the phase accumulated during the beam-splitting process.

Figure 5.11 displays the cumulative interferometric phase induced by light-shifts in units of $[\delta/\Omega_0]$ for both the optimized and conventional interferometers, as determined by Eq. (5.13). The optimized sequence exhibits a minimized cumulative phase value during the free evolution periods, ensuring robustness to intensity fluctuations for pulse sequences in which the free-evolution time T is much greater than the pulse duration. As an application case we compute the bias instability of the optimized and conventional interferometers induced by the coupling between cloud expansion and one-photon light-shift as function of the free-evolution time. Figure 5.11 presents the simulation results, showing that the bias instability is considerably lower than that of the conventional interferometer, ensuring enhanced long-term stability even at short free-evolution times.

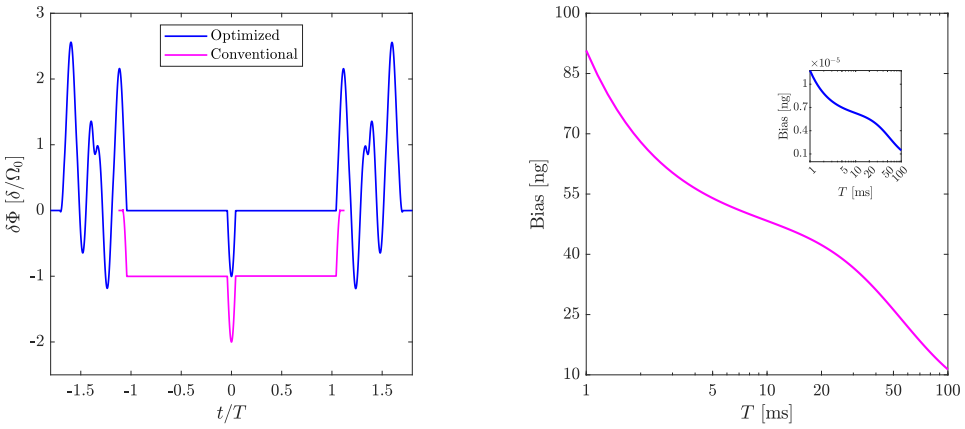

(A) Cumulative phase (B) Bias instability

FIGURE 5.11: Panel (A): response of the interferometer to an infinitesimal δI step input, in units of δ/Ω_0. The plot can equivalently be seen as the cumulative interferometric phase induced by light shifts. Panel (B): bias instability of a cold-atom accelerometer induced by the coupling between cloud expansion and long-term laser intensity drifts via the one-photon light-shift as function of the free-evolution time. The magenta line represents the bias instability of the conventional interferometer. The blue line in the inset is the bias instability of the optimized interferometer. Simulation parameters: atomic temperature $\mathcal{T} = 5\mu$K, initial size cloud $\sigma_0 = 0.5$mm, Gaussian beam with waist $w_L = 5$mm, single photon detuning $\Delta = 2\pi \times 1.5$GHz, nominal Rabi frequency $\Omega_0 = 2\pi \times 200$kHz, polarization configuration $\sigma^+ - \sigma^+$, relative laser intensity drift $\delta I/I_j^0 = 1\%$.

5.2.2.3 Intensity-induced scale-factor errors

Laser intensity fluctuations affect the interferometer scale-factor [16, 72]. Variations in the Rabi frequency experienced by atoms result in a distortion of the temporal profile of the impulse imparted by the laser field onto the atomic wave-function. As a result, the space-time area enclosed by the the atomic states, which defines the interferometer scale-factor, slightly deviates from the nominal value [58]. The sensitivity function formalism offers a geometric interpretation of the interferometer scale-factor in time domain, whereby the scale-factor for a cold-atom inertial sensor can be determined by calculating the area beneath the acceleration or angular rate impulsive response functions.

The sensitivity function formalism determines the interferometer scale-factor as it is inherently linked to the trajectory traced by the centre of mass of the atomic wavepackets that travel along the upper and lower arms of the interferometer. Recalling Eq. (4.15) and integrating in time we obtain

$$\Delta \langle z(t) \rangle = v_{\text{rec}}\, h_a(t)\,, \tag{5.20}$$

where $\Delta \langle z \rangle$ is the spread between the centre of mass of the wavepackets travelling along the upper and lower arms of the interferometer, v_{rec} is the recoil velocity and h_a

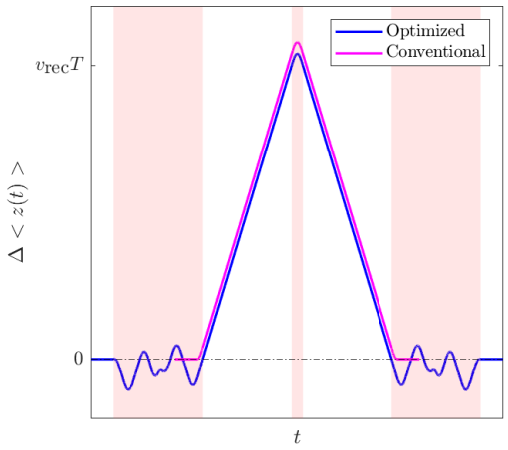

FIGURE 5.12: Spread between the arms of the interferometer for both the optimized and conventional pulse sequences. We assumed same maximum Rabi frequency. The red-shaded areas represent the pulse duration for the optimized interferometer. The spread function of the optimized interferometer crosses zero at the end (start) of the first (last) pulse, ensuring robustness of the scale-factor error to laser intensity variations.

is the acceleration IRF.

The acceleration IRF coincides, modulo the recoil velocity term, with the spread function and, hence, provides the area enclosed by the upper and lower wavepackets. Figure 5.12 shows the spread function $\Delta \langle z \rangle$ for both the conventional and optimized interferometers. As expected, the maximum separation between the arms of the interferometer occurs during the mirror pulse. The optimized interferometer exhibits a zero spread value at the end of the the first pulse. This is a consequence of the optimization condition for which we imposed that the phase accumulated by the wavefunction at the end of the beam-splitter pulse is minimized. Because of the symmetry of the pulse sequence with respect to the midpoint of the mirror pulse, the spread is also zero at the start of the last pulse.

In the case of rectangular constant-power pulses, the relative position of the upper wavepacket with respect to the lower one can be computed analytically. Assuming as initial condition $\langle z(t = -\infty) \rangle = 0$, and considering half of the pulse sequence for symmetry, we obtain

$$\langle z(t = 0) \rangle = v_{\mathrm{rec}} \left(T + \tau + \frac{1}{\Omega_j} \tan \frac{\theta_j}{2} \right) + o(\tau^2) \,, \tag{5.21}$$

where $\langle z(t = 0) \rangle$ is the position of the wavepacket travelling along the upper arm of the interferometer at the midpoint of the mirror pulse, and Ω_j, θ_j and τ are, respectively, the Rabi frequency, the pulse area of the j-th $\pi/2$ pulse and the duration of the $\pi/2$ pulse. We note three contributions:

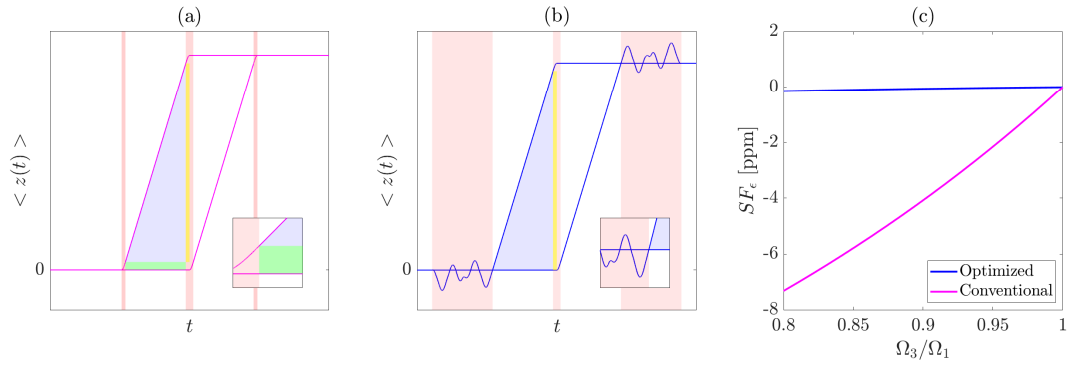

FIGURE 5.13: Panel (a): recoil diagram of the conventional interferometer. The blue, yellow, and green-shaded areas represent half of the scale-factor contribution due to pure free-evolution of the wavepackets, finite mirror duration, and finite beam-splitter duration, respectively. The insets show details in the proximity of the first conventional and optimized beam-splitter pulses. Panel (b): recoil diagram of the optimized interferometer. In this case, there is no contribution due to the beam-splitter. For clarity, only one output port per interferometer is represented. Panel (c): scale-factor error of a cold-atom accelerometer due to the Rabi frequency imbalance between the third and first beam-splitter pulse. We assume: free-evolution time $T = 10$ms; $\Omega_1 = \Omega_2 = \Omega_0 = 2\pi \times 200$kHz.

1. Free-evolution term. The fist term in the round brackets represents the displacement of the wavepacket due to free-evolution duration. Its contribution to the interferometer scale-factor is represented geometrically in Fig. 5.13 with blue.

2. Finite mirror duration. The second term represents the displacement due the finite duration of the mirror pulse. It is represented geometrically with the yellow-shaded area.

3. Finite beam-splitter duration. The third term in the round brackets depends on the beam-splitter Rabi frequency, and its scale-factor geometric representation is given by the green-shaded area. Physically, this term accrues because of the detuning-dependent phase accumulated by the atomic wavepacket during the beam-splitting process. Hence, variations in the nominal Rabi frequency during the beam-splitting process determine scale-factor instability for a conventional interferometer.

In contrast, an interferometer operating with optimized beam-splitter pulses exhibits reduced scale-factor instability due to the fact that at the end of the beam-splitting process, the detuning-dependent phase is minimized. This is shown geometrically in Fig. 5.13, where the optimized interferometer does not exhibit any beam-splitter-dependent contribution to the scale-factor.

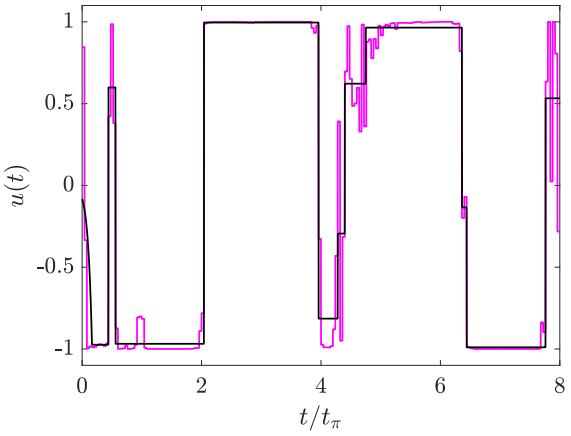

FIGURE 5.14: Comparison between the original dimensionless waveform of Figure 5.4 (magenta line) and the new re-optimized 'smooth' one (black line).

5.2.3 Smooth waveform performance

While the waveform shown in Figure 5.4 can be experimentally implemented with a laser modulation system bandwidth in the range of a few tenths of MHz [4], it is interesting to analyse the optimization results when we increase the penalty parameter in the cost function defined in Eq. (5.16).

Figure 5.14 displays the output of the optimization: the new re-optimized waveform, represented with a black line, is compared to the original waveform from Figure 5.4, depicted here by the magenta line. The re-optimized waveform exhibits enhanced smoothness, making its experimental implementation even more straightforward.

Let us now compare the performance of the re-optimized waveform, here indicated as 'smooth', with the original one. Figure 5.15 shows the latitude error of the standalone pulses and the interferometric phase [5]. While the smoothing operation does not have important effects upon the latitude error (i.e. population transfer), it seems to play a crucial role on the phase fidelity of the interferometer. Panel (B) in Figure 5.15 shows the interferometric phase of Mach-Zehnder interferometers using as beam-splitter/recombiner the original and smooth waveforms. The continuous and dashed lines correspond to cases with $\Omega_3/\Omega_1 = 0.9$ and $\Omega_3/\Omega_1 = 0.85$, respectively. It's worth noting that the performance of the interferometer operating with the original waveform is superior to the one operating with the smoothed waveform, especially as the ratio of the maximum Rabi frequencies between the third and first pulse decreases. This means that the high-frequency components of the original waveform are not artifacts

[4] The limiting factor in our case is the rise time of the acousto-optic modulator which depends on the radius of the input beam. Commercial modulators with rise times less than 100ns are available [104].

[5] The original and smooth waveforms are used as beam-splitters of a Mach-Zehnder interferometer. The recombiner is the time-reversed version of the beam-splitter pulse. In both cases, the mirror is a conventional constant-power pulse.

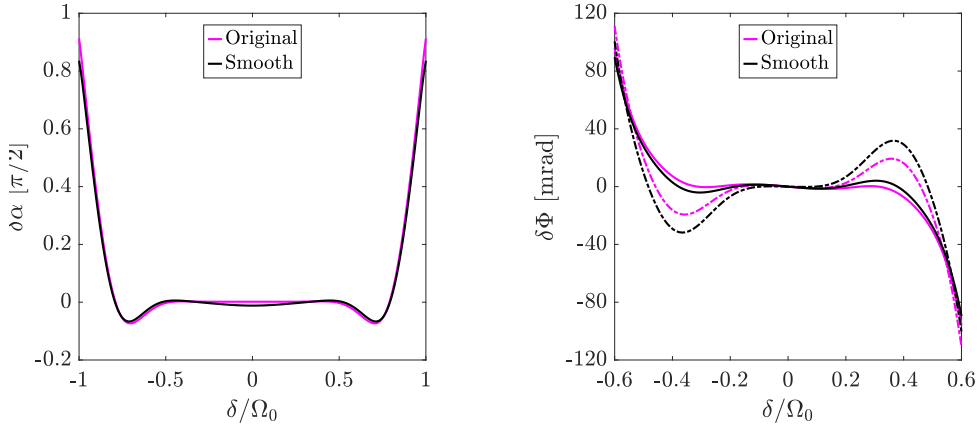

(A) Latitude error (B) Interferometric phase

FIGURE 5.15: Panel (A): latitude error of the standalone beam-splitter pulses for $\Omega = \Omega_0$. The black and magenta line correspond to the smooth and original waveforms, respectively. Panel (B): interferometric phase of Mach-Zehnder interferometer using as beam-splitter/recombiner the smooth and original waveforms. The continuous and dashed lines correspond to cases with $\Omega_3/\Omega_1 = 0.9$ and $\Omega_3/\Omega_1 = 0.85$, respectively.

of the minimum search algorithm, but depend on the cost function and affect the pulse performance.

Chapter 6

Wavefront distortions

The phase imprinted onto the atomic wavefunction by the laser diffraction grating generally depends on the mean position of the atomic wavepacket. When the electric field describing the laser field features a plane wavefront, the imprinted phase depends solely on the atomic position along the beam propagation axis. However, wavefront distortions introduce a dependence of the phase on the atomic motion in the plane orthogonal to the beam propagation axis. As a consequence, coupling between atomic transverse motion and wavefront distortions is an error source for cold-atom inertial (CAI) sensors.

The primary effect of wavefront distortion is bias. However, since the momentum imparted by the laser to the atom depends, in general, on the value of the local electric field's amplitude and phase, severe wavefront distortions may lead to contrast decay. Contrast decay due to wavefront distortion is particularly critical in large momentum transfer configurations where multiple pulses are concatenated to enlarge the area spanned by the wavepackets during the interferometric sequence or in atom interferometers operating with large free-evolution periods [45].

When coupled with vibrations, wavefront distortions become a noise source [66]. Vibrations affect the CAI output through two mechanisms: first, they induce a relative displacement of the laser wavefronts with respect to the atom's mean position; second, they can trigger vibrational modes of the optical elements that induce variations in the wavefronts.

The manner in which wavefront distortions impact the interferometer signal is not trivial and generally depends on the detection scheme. In a conventional cloud-averaging scheme, atomic populations are measured by detecting scattered photons through a photodiode, effectively averaging over the atomic phase-space distribution. On the other hand, the point source interferometry (PSI) technique detects the spatial distribution of the atomic population on a CCD, hence not requiring averaging over the

direction orthogonal to the camera line-of-sight. Therefore, the impact of wavefront distortion on sensors employing cloud-averaging detection is influenced by multiple parameters, including the size of the Raman and detection beams that act as spatial filters [53, 105]. The clipping effect operated by the finite size of the laser beams introduces non-linearity between the cloud temperature and the bias phase, making it difficult to reconstruct the distorted wavefront [106]. In contrast, PSI provides a direct measurement of the distorted phase distribution, making it possible to effectively reconstruct the distorted wavefront in the plane orthogonal to the Raman effective wavevector.

Given these premises, it is crucial to understand the effect of aberrated wavefronts upon interferometer signal. The structure of the chapter is organized as follows:

1. We first examine possible sources of wavefront distortions, with a focus on the Raman laser.
2. For different aberrations, we compute the resulting effect on the interferometric phase in the case of cloud-averaging and PSI sensors.
3. We therefore analyse the coupling between vibrational motion and wavefront distortions as a noise source of the atom interferometer.

6.1 Wavefront distortions sources

6.1.1 Raman beam

The Raman laser beam is one of the main sources of wavefront distortions. In the paraxial approximation, the free propagation of the laser electric field is described by the Helmholtz equation

$$\frac{\partial E(\mathbf{r}_\perp, z)}{\partial z} = \frac{i}{2k_0}\nabla_\perp^2 E(\mathbf{r}_\perp, z)\,, \tag{6.1}$$

where $k_0 = 2\pi/\lambda$ is the electric field wave-number, z is the propagation axis, and $\nabla_\perp^2 = \partial^2/\partial x^2 + \partial^2/\partial y^2$ is the Laplacian operator in the transverse direction to the propagation axis. Assuming that the electric field has the form $E = A\exp\left(i\,\phi\right)$, then Eq. (6.1) can be decomposed into two equations

$$\frac{\partial A}{\partial z} = -\frac{1}{2k_0}\left(2\,\nabla_\perp A\,\nabla_\perp \phi + A\,\nabla_\perp^2\phi\right)\,, \tag{6.2}$$

$$\frac{\partial \phi}{\partial z} = \frac{1}{2k_0}\left(\frac{\nabla_\perp^2 A}{A} - |\nabla_\perp \phi|^2\right)\,. \tag{6.3}$$

The two equations propagate the amplitude, A, and the phase ϕ, of the electric field along the z axis. In particular, Eq. (6.3) represents the wave-vector correction due to the distorted phase and the transverse amplitude distribution. Therefore, the momentum imparted by the laser on the centre of mass of the wavepacket exhibits an additional term $\hbar\,\Delta k$ and it is equal to

$$\hbar\,k = \hbar\,k_0\left(1+\frac{\Delta k}{k_0}\right) = \hbar\,k_0\left[1+\frac{1}{2\,k_0^2}\left(\frac{\nabla_\perp^2 A}{A}-|\nabla_\perp\phi|^2\right)\right]. \tag{6.4}$$

Equation (6.4) agrees with the expression reported in [65] and emphasizes that the interferometer's scale-factor depends on the wavefront and the transverse amplitude distribution that the atoms experience during the pulse sequence. For a Gaussian beam with a waist w_L and an initial phase distribution, ϕ, the relative momentum correction is given by

$$\frac{\Delta k}{k_0} = \frac{2}{k_0^2}\left(\frac{r_\perp^2}{w_L^4}-\frac{1}{w_L^2}\right)-\frac{|\nabla_\perp\phi|^2}{2\,k_0^2}. \tag{6.5}$$

The contribution of the term depending on the amplitude distribution is negligible with respect to other error sources: for instance, assuming a beam with waist $w_L = 5$mm and wavelength $\lambda = 780$nm, we obtain that the scale-factor error is at most $\Delta k/k_0 \approx 4$ppb over a distance $r_\perp \leq 1$cm from the beam centroid. Similarly, the initial wavefront-depending term is negligible. For instance, assuming an initial phase of the form $\phi(\mathbf{r}_\perp, 0) = \alpha\,\mathbf{r}_\perp^2$ and propagating it along the z-axis using the free-propagation operator (see Appendix C) we obtain

$$\phi(\mathbf{r}_\perp, z) = \frac{\alpha\,\mathbf{r}_\perp^2}{1+(2\,\alpha/k_0)\,z}, \tag{6.6}$$

where the term $\alpha = k_0\,a_{\mathrm{wf}}/R^2$, a_{wf} is the peak-to-valley amplitude of the distorted wavefront expressed in units of λ and R is the maximum distance from the centroid of the laser beam. Even for very bad quality optics (i.e. $a_{\mathrm{wf}} \approx \lambda$), we get that $\phi(\mathbf{r}_\perp, z) \approx \phi(\mathbf{r}_\perp, 0)$ for propagation distance $z \leq 1$m. Hence, the scale-factor error of the interferometer is given by $\Delta k/k_0 = -2(\alpha\,\mathbf{r}_\perp)^2/k_0^2$. Therefore, assuming $a_{\mathrm{wf}} = \lambda/5$, the scale-factor error is $\Delta k/k_0 \approx 0.5$ppb over a maximum distance $r_\perp = R = 1$cm.

6.1.1.1 Gaussian beam

Since Eq. (6.2) and (6.3) are coupled, the Helmholtz equation can be solved in the Fourier domain (see Appendix C)

$$\hat{E}(\mathbf{k}_\perp, z) = \exp\left(-i\frac{\mathbf{k}_\perp^2\, z}{2\,k_0}\right)\hat{E}(\mathbf{k}_\perp, 0)\,, \tag{6.7}$$

where the exponential term is the free-space propagator. Assuming as the initial condition at $z = 0$ a Gaussian amplitude profile with a waist w_0 and zero phase distortion, we compute the phase of the electric field

$$\phi(\mathbf{r}_\perp, z) = \underbrace{k_0\, z}_{\text{Flat wavefront}} + \underbrace{\frac{k_0\, \mathbf{r}_\perp^2}{2\,\mathcal{R}(z)}}_{\text{Quadratic term}} \underbrace{- \arctan\frac{z}{z_R}}_{\text{Gouy phase}}, \tag{6.8}$$

where $z_R = k_0\, w_0^2/2$ is the Rayleigh length, $\mathcal{R}(z) = (w(z)\, z_R)^2/(w_0^2\, z)$ is the radius of curvature and $w(z) = w_0\sqrt{1 + (z/z_R)^2}$ is the beam waist. The electric field comprises three phase terms: the primary contribution arising from the flat wavefront, a quadratic term resulting from the amplitude distribution, and an additional term, known as the Gouy phase, attributable to the transverse momentum term in the free-space propagator [107].

While we refer to Section 6.2 for the impact of a quadratic phase term on the interferometric phase, we analyze here the effect of the Gouy phase. For a Raman waist $w_0 \geq$ 5mm and $\lambda = 780$nm, the Rayleigh length $z_R \geq 100$m, hence the Gouy phase term can be linearized $\phi \approx -z/z_R$. The effective Raman phase $\phi_{\text{eff}}(t) = -(z_1(t) - z_2(t))/z_R$, where $z_j(t)$ is the relative trajectory of an atom with respect to the j-th laser and we assumed that the Rayleigh length is the same for the two beams. We compute the interferometric phase using the sensitivity function formalism

$$\Delta\Phi = -\frac{2}{z_R}\left(-\int_{-\infty}^{+\infty} h_a(t)\, f_z(t)\, dt - \int_{-\infty}^{+\infty} w(t)\, \gamma_z(t)\, dt\right), \tag{6.9}$$

where f_z is the z component of the specific force vector $\mathbf{f}_{ib}^b$, γ_z is the z component of the vector $\boldsymbol{\omega}_{ib}^b \times \mathbf{v}_0^b$, and $h_a(t)$ and $w(t)$ are, respectively, the acceleration and angular rate (Coriolis term) impulsive response functions. The factor of 2 arises from the two laser fields composing the Raman pulse being fixed to the hosting vehicle. Consequently, the relative motion of the atom with respect to them is the same.

The Gouy phase gives rise to a scale-factor error. For instance, in the case of a constant specific force, the interferometric phase is given by $\Delta\Phi = -2\, f_z\, T^2/z_R$, corresponding to a scale-factor error of $\leq$ 1ppb for a beam waist $w_0 \geq$ 5mm. Therefore, for typical values of the Raman beam waist, the effect of the Gouy phase is negligible with respect to other error sources.

6.1.1.2 Intensity noise

Let us analyze the impact of noise sources upon the momentum imparted to the atoms. According to Eq. (6.4), both amplitude and phase spatial distributions in the transverse plane affect the recoil kick. Following [65], it is possible to evaluate the effect of amplitude and phase noise upon the interferometric phase. From Eq. (6.4), we observe that the amplitude noise has a dominant effect [1]. Assuming for simplicity a Gaussian auto-correlation function for the relative electric field amplitude $\bar{A} = A/\langle A \rangle$

$$R_{\bar{A}}(\mathbf{r}_\perp) = \sigma_{\bar{A}}^2 \, \exp\left(-\frac{\mathbf{r}_\perp^2}{L_c^2}\right) \tag{6.10}$$

with L_c the coherence length, it is possible to compute the power spectral density associated with the amplitude noise computing the Fourier transform of the auto-correlation function $S_{\bar{A}}(\mathbf{k}_\perp) = \mathcal{F}\{R_{\bar{A}}\}$. At this point, we compute the mean square of the relative wave-vector correction $\epsilon = \Delta k/k_0$ as

$$\sigma_\epsilon^2 = \int_{-\infty}^{+\infty} \underbrace{\left(\frac{-\mathbf{k}_\perp^2}{2\,k_0^2}\right)^2 S_{\bar{A}}(\mathbf{k}_\perp)}_{S_\epsilon(\mathbf{k}_\perp)} \frac{d^2\mathbf{k}_\perp}{(2\,\pi)^2} = \left(\frac{\sigma_{\bar{I}}}{2}\right)^2 \frac{8}{(k_0\,L_c)^4}\,, \tag{6.11}$$

where we have expressed the relative amplitude noise as a function of the relative intensity noise (i.e. $\sigma_{\bar{A}} = \sigma_{\bar{I}}/2$). The term $S_\epsilon(\mathbf{k}_\perp)$ is the power spectral density of the relative wave-vector correction.

Due to laser intensity noise, there exists an uncertainty in the value of the recoil momentum imparted to the atoms. This uncertainty increases as the local intensity or the coherence length decreases. It should be noted that the effect described by Eq. (6.11) is local, therefore for a cloud-averaging sensor, its contribution upon the uncertainty of the scale-factor error is mitigated because atoms average over high- and low-intensity spots during the thermal expansion [65, 108]. In contrast, for PSI sensors, this effect should lead to noise in the spatial phase map, as no averaging is performed in the transverse plane by the detection system.

Figure 6.1 displays the computed power spectral density of the spatial intensity noise for our top-hat Raman beam with a diameter of 6mm. The inset shows the relative noise profile along the horizontal axis, with an amplitude of approximately $\pm 10\%$. To mitigate edge effects, we process the data from the central portion of the beam. As expected, the power spectral density of the relative intensity noise exhibits an exponential decay. Peaks in the frequency range $[40,\, 100]\,\mathrm{cm}^{-1}$ are attributed to diffraction induced by dust particles on the lens system. The fit of the power spectral density with

[1] The relative wave-vector correction noise scales linearly with respect to the amplitude noise, i.e. σ_A/A, and quadratically with respect to the phase noise, i.e. σ_ϕ^2.

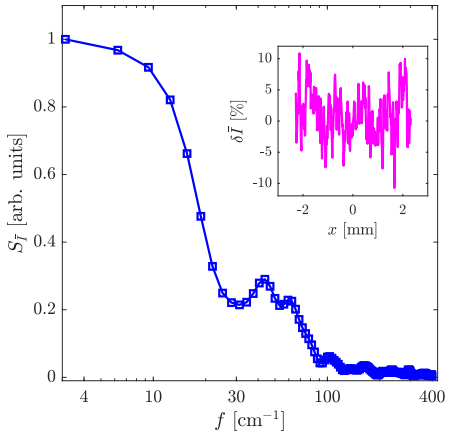

FIGURE 6.1: Power spectral density of the spatial intensity noise of our Raman beam. The inset shows the portion of relative intensity noise considered for the analysis. Fit of the power spectral density with a Gaussian function gives $L_c = 110\mu$m.

a Gaussian function reveals a coherence length of $L_c = 110\mu$m, corresponding to an uncertainty in the relative wave-vector correction of $\sigma_\epsilon \approx 180$ppb.

6.1.2 Collimation error effect

Raman light passes through a collimator before being injected into the vacuum chamber. Collimation errors cause the beam to change its waist along the propagation axis, thereby introducing distortion in the wavefront. Assuming for simplicity that the collimation is achieved through a focusing lens with focal length f and numerical aperture NA, using the ABCD matrix method we obtain the collimation angle error due to a misfocus error Δf

$$\Delta\theta = -\frac{\Delta f}{f} NA\,. \tag{6.12}$$

The same method can be used to compute the properties of a Gaussian laser beam as propagating along its axis. The complex curvature of the laser beam after the collimator is given by [109]

$$Q_2 = \frac{A\,Q_1 + B}{C\,Q_1 + D} \tag{6.13}$$

where Q_1 is the complex curvature before the optics and A, B, C, and D are the propagation matrix elements. The radius of curvature at the j-th location, $\mathcal{R}_j$, is proportional to the real part of the complex curvature element, i.e. $1/\mathcal{R}_j = \mathrm{Re}\{1/Q_j\}$. Therefore, assuming a point source we compute the curvature of the laser beam after the collimator

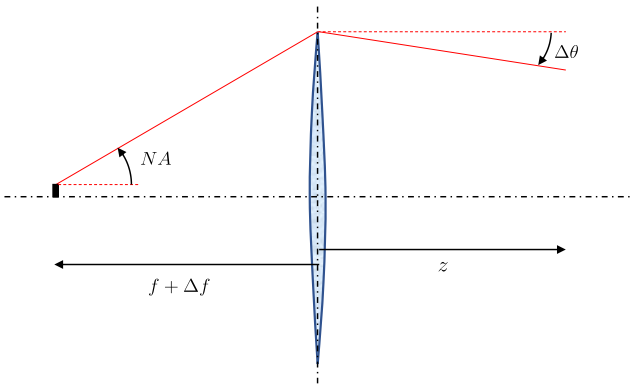

FIGURE 6.2: Simple collimation system formed by a focusing lens with focus f and numerical aperture NA.

$$\frac{1}{\mathcal{R}(z)} = \frac{\Delta\theta/NA}{(\Delta\theta/NA)(f-z)-f}, \tag{6.14}$$

where z is the longitudinal distance from the focusing length. We note that as $\Delta\theta \to 0$, the flat wavefront condition is recovered, i.e., $1/\mathcal{R}(z) \to 0$. As the collimation error $\Delta\theta$ or the longitudinal distance increases, the radius of curvature also increases accordingly.

6.1.3 Optical elements

Optical elements are an unavoidable source of wavefront distortions. While the wavefront distortions of incoming laser beams can be suppressed using a retro-reflecting mirror arrangement, this does not eliminate the distortions induced by optical elements. These elements include glass windows, quarter-wave plates, and the retro-reflecting mirror [20]. In many cases, to minimize the impact of wavefront distortions, the number of optical elements is kept to a minimum by adopting design solutions that involve placing the optics in a vacuum chamber , thus avoiding the distortions induced by glass windows or air turbulence [106].
In the retro-reflecting configuration, the mirror is the most crucial element, as it represents the reference for measuring the relative atomic motion. Therefore, we analyze the impact of thermoelastic effect and structural vibrations upon wavefront distortions.

6.1.3.1 Thermoelastic effects

Thermoelastic effects induce deformation of the optical elements and are a prominent source of wavefront distortion. In order to evaluate their impact we assume that the mirror can be modelled as an isotropic circular plate of radius R and thickness h, subject

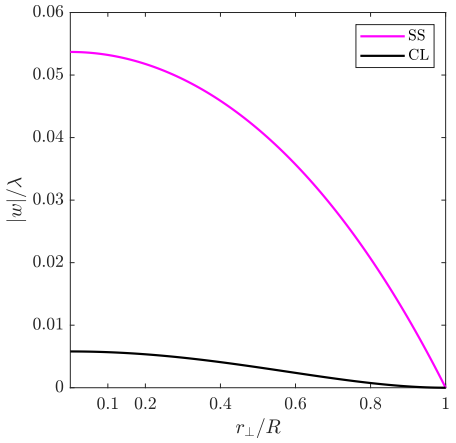

FIGURE 6.3: Longitudinal displacement in fraction of wavelength ($\lambda = 780$nm) induced by a parabolic temperature distribution. Simulation parameters: substrate in silica with thermal expansion coefficient $\alpha = 0.55$ppm/K and Poisson ratio $\nu = 0.17$, $\mathcal{T}_0 = 290$K, $\beta = 1/\mathcal{T}_0$, $R = 1.5$cm, $h = 6$mm.

to an axisymmetric temperature profile $\mathcal{T}(r_\perp) = \mathcal{T}_0 \left(1 + \beta\, \bar{r}_\perp^{\,m}\right)$. Following the method reported in [110] we compute the vertical displacement for both simply supported (SS) and clamped (CL) boundary conditions

$$w(r_\perp) = \begin{cases} \frac{\mathcal{D}\,R^2}{2\,(1+\nu)} \left[\frac{(m+3-\nu)}{(m+2)} \left(1 - \bar{r}_\perp^2\right) + \frac{2\,(1+\nu)}{(m+2)^2} \left(1 - \bar{r}_\perp^{m+2}\right) \right] & \text{, for SS} \\ \frac{\mathcal{D}\,R^2}{(2+m)^2} \left[\frac{m}{2} - \frac{(m+2)}{2}\, \bar{r}_\perp^2 + \bar{r}_\perp^{2+m} \right] & \text{, for CL ,} \end{cases} \tag{6.15}$$

where $\bar{r}_\perp = r_\perp/R$ is the dimensionless radial position, ν is the Poisson ratio, $\mathcal{D} = \left[3\,(1+\nu)\,\alpha\,\beta\,\mathcal{T}_0\right]/h$ is the thermal bending stiffness, and α is the thermal expansion coefficient.

In Figure 6.3 we show the longitudinal displacement in fraction of wavelength of a plate subject to a parabolic temperature distribution. As expected, the maximum displacement in the clamped case is significantly smaller than the simply supported because of higher bending stiffness induced by the constraints. The mirror's deformation is influenced by the temperature gradient, the substrate material, and its geometric features. For the geometric parameters assumed in Figure 6.3 and material properties in Ref. [111], the peak-to-valley deformation is $\sim \lambda/20$ for the simply supported case and $\sim \lambda/150$ for the clamped case.

Time fluctuations of the environment temperature $\mathcal{T}_0$ or of the radial temperature gradient induce variations in the wavefront distortion and are a source of bias instability. Referring to the simply supported case, for $r_\perp \ll R$ the mirror deformation can be described by a parabolic function $w(r_\perp) \approx \mathcal{A} - \mathcal{B}\, r_\perp^2$, where $\mathcal{A}$ is a constant offset, and $\mathcal{B} = \mathcal{D}\,(m+3-\nu)/\left[2\,(1+\nu)\,(m+2)\right]$. Assuming that the atomic motion in the transverse plane is induced by thermal expansion, the interferometric phase is expressed

as $\Delta\Phi = k_{\text{eff}} \mathcal{B}\, v_0^2\, T^2$. For a cloud-averaging sensor and assuming a Gaussian velocity distribution with variance σ_v, we obtain a bias on the acceleration signal given by $B_a = 2\,\mathcal{B}\,\sigma_v^2$. As an example, we calculate the bias induced by the coupling between wavefront distortion and the motion of an expanding cloud of ^{85}Rb atoms with a velocity distribution corresponding to a temperature of 5μK. Under the same conditions as those in Figure 6.3, the bias instability is $\sim$ 1.6ng for environment temperature fluctuations of 10%.

6.1.3.2 Structural vibrations

External stochastic inputs can induce structural vibrations in the optical mirror, leading to deformation of the reflective surface and distortion of the wavefronts. When modelling the mirror as an isotropic circular plate subject to axisymmetric boundary conditions, the longitudinal displacement is a linear combination of n mode shapes [112]

$$w(\bar{r}_\perp,\, t) = \sum_{n=0}^{+\infty} A_n \left[J_n(\Lambda_{mn}\bar{r}_\perp) - \frac{J_n(\Lambda_{mn})}{I_n(\Lambda_{mn})}\, I_n(\Lambda_{mn}\bar{r}_\perp) \right] \cos(n\,\theta)\, \exp(i\,\omega\,t) \tag{6.16}$$

where $J_n(\ldots)$ and $I_n(\ldots)$ are, respectively, the Bessel and modified Bessel functions of first kind, Λ_{mn} is the m-th dimensionless natural frequency associated to the n-th shape mode. The constants A_n and θ are, respectively, the amplitude of the vibrational mode and the nodal line angle and are uniquely determined once the external input is known (forced vibration problem).
The dimensionless natural frequencies can be computed by solving an eigenvalue problem for the associated boundary condition. In particular the solution of the following equation

$$J_0(\Lambda_{mn})\, I_1(\Lambda_{mn}) + I_0(\Lambda_{mn})\, J_1(\Lambda_{mn}) = \frac{2\,\Lambda_{mn}}{1-\nu}\, J_0(\Lambda_{mn})\, I_0(\Lambda_{mn})\,, \tag{6.17}$$

leads to the determination of the natural frequencies for the simply supported case. For the clamped case the equation to be solved is given by

$$J_0(\Lambda_{mn})\, I_1(\Lambda_{mn}) + I_0(\Lambda_{mn})\, J_1(\Lambda_{mn}) = 0\,. \tag{6.18}$$

The relation between the natural frequency (ω_{mn}) and the dimensionless natural frequency is given by

$$\omega_{mn} = \Lambda_{mn}^2 \left(\frac{h}{R}\right)^2 \sqrt{\frac{E}{12\,(1-\nu^2)\,\rho\,h^2}} \tag{6.19}$$

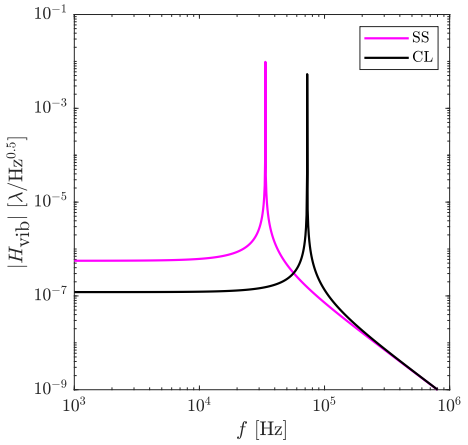

FIGURE 6.4: Vibration transfer function in fraction of wavelength ($\lambda = 780$nm) induced by a white noise acceleration noise. Simulation parameters: $S_a = (2\mathrm{mg}/\sqrt{\mathrm{Hz}})^2$, quality factor $Q = 1/(2\,\zeta) = 10^6$.

with E Young modulus and ρ density of the material.
Because the low-frequency mode shapes carries the higher energy content we limit our analysis to the first axisymmetric mode shape ($m = n = 0$). Numerical solution of Eq. (6.17) and (6.18) in the case of a fused silica plate with the same geometric properties of Figure 6.3 leads to $\omega_{00} \approx 2\pi \times 33$kHz for the simply supported case and $\omega_{00} \approx 2\pi \times 72$kHz for the clamped case.
The vibration response of the mirror can be described by a Lorentzian-like function centred in the natural frequency with a width that depends on the structural damping

$$|H_{\mathrm{vib}}(\omega)|^2 = \frac{S_a}{(2\,\zeta_{mn}\,\omega_{mn}\,\omega)^2 + (\omega^2 - \omega_{mn}^2)^2} \tag{6.20}$$

where S_a is the white power spectral density associated to the external acceleration noise and ζ_{mn} is the structural damping of the m-th natural frequency associated to the n-th mode shape.
In Figure 6.4, we display the vibration response of the optical mirror corresponding to the first axisymmetric mode shape for both the simply supported and clamped cases. Due to the high quality factor ($Q = 1/(2\,\zeta)$) of bulk fused silica [113], the frequency response is nearly flat at low frequencies and exhibits a narrow peak at the resonant frequency. Even with a relatively large acceleration noise of $2\mathrm{mg}/\sqrt{\mathrm{Hz}}$, the maximum sensitivity at resonance corresponds to a distorted wavefront with a peak-to-valley amplitude less than $\lambda/100$. As acceleration noise predominantly affects low frequencies, we calculate the root mean square (rms) value of the amplitude for the simply supported case in the range $0 \leq f \leq 10$kHz to be $\sigma_{A_0} \approx \lambda/4500$. Therefore, wavefront distortions induced by structural vibrations are negligible for the usual materials and geometric parameters of optical mirrors used in atom interferometry applications.

6.2 Bias phase

Wavefront distortions couple with atomic motion in the plane orthogonal to the Raman beam propagation axis, giving rise to a position-dependent phase. This phase primarily leads to bias. The actual bias on the CAI sensor signal depends on the adopted detection scheme. Therefore, we will report the impact of wavefront distortions for both cloud-averaging and PSI sensors.

6.2.1 Cloud-averaging sensor

In cloud-averaging detection a photodiode collects the fluorescence emitted by a cloud of atoms. Hence, the interferometric signal is obtained operating an effective integration over the entire phase-space.
Although the finite size of both the Raman and detection beams acts as a spatial filter, limiting the impact of atoms belonging to higher velocity classes upon the bias phase [105], we develop a simple analytical model that assumes the atomic cloud has a size much smaller than the Raman and detection beam waists. This provides a quick quantitative estimate of how the cloud parameters affect the bias phase.
We analyze the impact of different wavefront distortions modelling them with Zernike polynomials [114]. Assuming a constant velocity motion in the transverse plane, for a given aberrated phase, $\phi(\mathbf{r}_\perp)$, we first compute the space-dependent interferometric phase, $\Delta\Phi(\mathbf{r}_\perp)$, and then we average over the cloud distribution, $f(\mathbf{r}_\perp)$, to obtain its average value, $\langle\Delta\Phi\rangle = \int_{-\infty}^{+\infty} f(\mathbf{r}_\perp)\,\Delta\Phi(r_\perp)\,d^2\mathbf{r}_\perp$.
In Table 6.1 we report the results for different Zernike polynomials Z_n^m, up to the fourth order ($n \leq 4$). For each transverse direction, we assume that that the atomic trajectories are of the type $x(t) = x_0 + v_0\,t$, where v_0 is distributed as a Gaussian with zero mean and standard deviation σ_v. We observe that:

- The defocus, corresponding to an axisymmetric distortion with a constant curvature, gives rise to a bias that depends only on the expansion rate of the cloud.
- Low-order non-axisymmetric aberrations do not give rise to a bias in the case of isotropic expansion ($\sigma_{v,x} = \sigma_{v,y}$).
- Coma induces a bias that depends on the initial atomic position. Indeed, this type of aberration could be used to align the center of the atomic cloud with the centroid of the Raman beam, as experimentally demonstrated by Trimeche et al. [115].
- For high-order aberrations, the bias no longer depends on T^2 but on a combination of factors, including the time at which the first pulse occurs t_1, the initial position (x_0, y_0), the maximum radial distance R, and the expansion rate.

TABLE 6.1: Bias induced by distorted wavefronts on a cloud-averaging CAI sensor. The distorted wavefronts are modelled with Zernike polynomials Z_n^m. For the j-th aberration of order n, the parameter $\alpha_j = k_0\, a_{wf}/R^n$, where $k_0 = 2\pi/\lambda$ is the laser nominal wave-vector, R is maximum radial distance and a_{wf} is the peak-to-valley amplitude of the aberrations in units of λ.

Aberration type	**Distorted phase ϕ**	**Bias phase $\langle\Delta\Phi\rangle$**
Astigmatism y (Z_2^{-2})	$\alpha_A\,(2\,x\,y)$	0
Defocus (Z_2^0)	$\alpha_D\,\left[2\,(x^2+y^2)-R^2\right]$	$4\,\alpha_D\,T^2\,(\sigma_{v,x}^2+\sigma_{v,y}^2)$
Astigmatism x (Z_2^{+2})	$\alpha_A\,(y^2-x^2)$	$2\,\alpha_A\,T^2\,(\sigma_{v,y}^2-\sigma_{v,x}^2)$
Trefoil y (Z_3^{-3})	$\alpha_T\,(3\,x\,y^2-x^3)$	$6\,\alpha_T\,T^2\,x_0\,(\sigma_{v,y}^2-\sigma_{v,x}^2)$
Coma y (Z_3^{-1})	$\alpha_C\,[-2\,x\,R^2+3\,x\,(x^2+y^2)]$	$6\,\alpha_C\,T^2\,x_0\,(\sigma_{v,y}^2+3\,\sigma_{v,x}^2)$
Coma x (Z_3^{-1})	$\alpha_C\,[-2\,y\,R^2+3\,y\,(x^2+y^2)]$	$6\,\alpha_C\,T^2\,y_0\,(\sigma_{v,x}^2+3\,\sigma_{v,y}^2)$
Trefoil x (Z_3^{-3})	$\alpha_T\,(y^3-3\,y\,x^2)$	$6\,\alpha_T\,T^2\,y_0\,(\sigma_{v,y}^2-\sigma_{v,x}^2)$
Tetrafoil y (Z_4^{-4})	$\alpha_{2T}\,(-4\,x^3\,y+4\,x\,y^3)$	$24\,\alpha_{2T}\,T^2\,x_0\,y_0\,(\sigma_{v,y}^2-\sigma_{v,x}^2)$
2nd astigmatism y (Z_4^{-2})	$\alpha_{2A}\,\left(-6\,x\,y\,R^2+8\,x^3\,y+8\,x\,y^3\right)$	$48\,\alpha_{2A}\,T^2\,x_0\,y_0\,(\sigma_{v,x}^2+\sigma_{v,y}^2)$
Primary sph. (Z_4^0)	$\alpha_{PS}\,\left[R^4-6\,(x^2+y^2)^2-6\,R^2\,(x^2+y^2)\right]$	$12\,\alpha_{PS}\,T^2 A_{PS}$ [(1)]
2nd astigmatism x (Z_4^{+2})	$\alpha_{2A}\,\left[3\,R^2\,(x^2-y^2)-4\,(x^4+y^4)\right]$	$6\,\alpha_{2A}\,T^2 A_{2A}$ [(2)]
Tetrafoil x (Z_4^{+4})	$\alpha_{2T}\,(x^4-6\,x^2\,y^2+y^4)$	$6\,\alpha_{2T}\,T^2\,(\sigma_{v,y}^2-\sigma_{v,x}^2)\,A_{2T}$ [(3)]

[(1)] $A_{PS} = 3\,\eta\,(\sigma_{v,x}^4+\sigma_{v,y}^4)+2\,\eta\,\sigma_{v,x}^2\,\sigma_{v,y}^2+\sigma_{v,x}^2\,(6\,x_0^2+2\,y_0^2-R^2)+\sigma_{v,y}^2\,(2\,x_0^2+6\,y_0^2-R^2)$
[(2)] $A_{2A} = 4\,\eta\,(\sigma_{v,y}^4-\sigma_{v,x}^4)+\sigma_{v,y}^2\,(8\,y_0^2-R^2)-\sigma_{v,x}^2\,(8\,x_0^2-R^2)$
[(3)] $A_{2T} = 2\,(x_0^2-y_0^2)+\eta\,(\sigma_{v,x}^2-\sigma_{v,y}^2)$
[(4)] $\eta = 6\,t_1\,(t_1+2\,T)+7\,T^2$

6.2.2 Point source interferometry sensor

Point source interferometry (PSI) enables spatial mapping of atomic populations by imaging them onto a CCD. Consequently, it is possible to reconstruct the transverse space-dependent phase map by appropriately combining different images [116]. The PSI scheme does not average atomic populations in the transverse plane; hence, the reconstruction of the distorted wavefronts is unambiguous because each aberration has unique spatial features.

Complication in evaluating the interferometric phase map due to the aberrated wavefront is represented by the finite size of the initial atomic cloud. Following the semi-classical model developed by Hoth *et al.* [44], the probability density function describing how the atomic population at the output port of the interferometer is distributed in space is given by the convolution of the initial space distribution, $n_0(\mathbf{r}_\perp)$, with an ideal point source, $n_{PS}(\mathbf{r}_\perp)$. Using the semi-classical model, we compute analytic expressions of the interferometric phase map for different aberrations. First, we derive the atomic population distribution at the detection evaluating the convolution integral

$$\begin{aligned} n(\mathbf{r}_\perp, \phi_L) =& n_0(\mathbf{r}_\perp) \circledast n_{PS}(\mathbf{r}_\perp, \phi_L) \dots \\ =& \mathcal{N}(\mathbf{r}_\perp, \sigma_0) \circledast \mathcal{N}(\mathbf{r}_\perp, \sigma_{PS}) \left[P_0 + C/2 \cos\left(\Delta\Phi(\mathbf{r}_\perp) + \phi_L\right)\right], \end{aligned} \tag{6.21}$$

where $\mathcal{N}(\mathbf{r}_\perp, \sigma)$ denotes a Gaussian distribution with zero mean and standard deviation σ, and σ_0 and σ_{PS} are, respectively, the standard deviation of the initial cloud and of the ideal expanded point source. The term ϕ_L is a constant arbitrary offset induced by the laser system, while the term $\Delta\Phi(\mathbf{r}_\perp)$ contains the space-dependent interferometric phase due to an angular rate acting along the y direction and the aberrated wavefront. Second, we obtain the PSI phase map by combining four signals [116]

$$\Phi_{PSI}(\mathbf{r}_\perp) = \arctan\left[\frac{n(\mathbf{r}_\perp, \pi/2) - n(\mathbf{r}_\perp, 3\pi/2)}{n(\mathbf{r}_\perp, \pi) - n(\mathbf{r}_\perp, 0)}\right]. \tag{6.22}$$

In order to have analytic expressions that are easy to interpret, we assume that the phase induced by the distorted wavefront is much smaller than the angular-rate's contribution. We report the results in Table 6.2 by modeling the wavefront aberrations as Zernike polynomials and limiting our analysis to the third order.
We observe that:

- Due to blurred position-velocity correlations resulting from the finite size of the initial cloud, the actual local phase map gradient is less than that in the ideal point source case. This generalization extends the result obtained by Hoth *et al.* for a constant gradient [44].
- For the ideal point source case ($\sigma_0 = 0$), the reported expressions reduce to the interferometric phase $\Delta\Phi(x, y)$ computed from the distorted wavefront $\phi(x, y)$.
- In general, distorted wavefronts induce non-linearity in the phase map. However, we note that couplings between the initial size of the cloud and aberrations give rise to errors in the acceleration (phase offset of the phase map) and rotational signal (phase gradient of the phase map).

The coupling between initial size of the cloud and wavefront distortions induces two types of errors: a bias and a scale-factor non-linearity.

TABLE 6.2: Bias phase map induced by distorted wavefronts on a PSI CAI sensor. The distorted wavefronts are modelled with Zernike polynomials Z_n^m. For the j-th aberration of order n, the parameter $\alpha_j = k_0\, a_{wf}/R^n$, where $k_0 = 2\pi/\lambda$ is the laser nominal wave-number, R is maximum radial distance and a_{wf} is the peak-to-valley amplitude of the aberrations in units of λ. The initial phase-space atomic distribution is assumed to be Gaussian with widths σ_0 and σ_v. At detection the size of the cloud is $\sigma_f = \sqrt{\sigma_0^2 + (\sigma_v\, T_{ex})^2}$.

Aberration type	**Distorted phase ϕ**	**Bias phase map $\Phi_{PSI}(x,y)$**
Astigmatism y (Z_2^{-2})	$\alpha_A\,(2\,x\,y)$	$4\,A_A\,F^2\,x\,y$
Defocus (Z_2^0)	$\alpha_D\,\left[2\,(x^2+y^2) - R^2\right]$	$4\,A_D\,F\,[2\,\sigma_0^2 + \ldots$ $F\,(x^2+y^2) + F\,k_{\omega,x}^2\,\sigma_0^4]$
Astigmatism x (Z_2^{+2})	$\alpha_A\,(y^2 - x^2)$	$2\,A_A\,F^2\,[k_{\omega,x}^2\,\sigma_0^4 + \ldots$ $(y^2 - x^2)]$
Trefoil y (Z_3^{-3})	$\alpha_T\,(3\,x\,y^2 - x^3)$	$6\,A_T\,\eta\,F^3\,[3\,k_{\omega,x}^2\,\sigma_0^4\,x + \ldots$ $x\,(3\,y^2 - x^2)]$
Coma y (Z_3^{-1})	$\alpha_C\,[-2\,x\,R^2 + 3\,x\,(x^2+y^2)]$	$18\,A_C\,\eta\,F^2\,[F\,x\,(x^2+y^2) + \ldots$ $4\,\sigma_0^2\,x - 3\,k_{\omega,x}^2\,F\,\sigma_0^4\,x]$
Coma x (Z_3^{-1})	$\alpha_C\,[-2\,y\,R^2 + 3\,y\,(x^2+y^2)]$	$18\,A_C\,\eta\,F^2\,[F\,y\,(x^2+y^2) + \ldots$ $4\,\sigma_0^2\,y - k_{\omega,x}^2\,F\,\sigma_0^4\,y]$
Trefoil x (Z_3^{-3})	$\alpha_T\,(y^3 - 3\,y\,x^2)$	$6\,A_T\,\eta\,F^3\,[3\,k_{\omega,x}^2\,\sigma_0^4\,y + \ldots$ $y\,(y^2 - 3\,x^2)]$

(1) $F = 1 - \sigma_0^2/\sigma_f^2$
(2) $k_{\omega,x} = 2\,k_{\text{eff}}\,T^2\,\omega_y/T_{ex}$
(3) $A_j = \alpha_j\,(T/T_{ex})^2$
(4) $\eta = (t_1 + T)/T_{ex}$

Figure 6.5 illustrates the bias introduced by defocus and coma aberrations on the acceleration and rotation signals, respectively. As expected, the bias diminishes with an increasing ratio between the sizes of the final and initial clouds, σ_0/σ_f. This reduction is attributed to the fact that, for longer expansion times, position-velocity correlations build up, approaching the ideal point source case in the limit $\sigma_f/\sigma_0 \to \infty$. As σ_f/σ_0 increases, requirements on the flatness of the wavefronts can be relaxed. For compact sensors, where the expansion time is constrained by the dimensions of the vacuum chamber (for example, Ref. [117]), the defocus-induced bias on the acceleration signal can reach magnitudes on the order of tenths of ng. Conversely, the bias induced by coma aberration on the rotation signal remains below 1deg/h for $\sigma_0/\sigma_f > 1.7$.
It is interesting to note that long-term drifts of the cloud size are a source of bias instability. For instance applying propagation error we can estimate the bias instability for both the acceleration

$$\Delta f = \left| \frac{16\, A_D\, \sigma_0^2\, F^2}{SF_a} \right| \frac{\Delta\sigma_0}{\sigma_0}\,, \tag{6.23}$$

and the rotation signal

$$\Delta\omega = \left| \frac{144\, A_C\, \eta\, \sigma_0^2\, F^2\, [1 - 2\,(\sigma_0/\sigma_f)^2]}{SF_g} \right| \frac{\Delta\sigma_0}{\sigma_0}\,, \tag{6.24}$$

where the term $SF_a = k_{\text{eff}}\, T^2$ and $SF_g = 2\, k_{\text{eff}}\, T^2/T_{ex}$ are, respectively, the acceleration and rotation signal scale-factors.
We report in Figure 6.5 the impact of long-term drifts in the size of the atomic cloud on the long-term stability of the PSI sensor. With a 1% fluctuation in the initial cloud size, the bias instability on the acceleration signal remains below 1ng for $\sigma_f/\sigma_0 \geq 2$. On the other hand, achieving a bias instability of less than 1mdeg/h in a strategic-grade gyroscope necessitates high-quality optics with a wavefront flatness better than $\lambda/50$ and an high expansion time, characterized by a ratio $\sigma_f/\sigma_0 \geq 4$.

The coupling between the initial size of the cloud and wavefront distortions introduces errors such as anisoinertia bias and scale-factor non-linearity. In Figure 6.5, we present the results for different ratios of σ_f/σ_0 and wavefront peak-to-valley amplitudes. To maintain anisoinertia bias below 1ng/deg/s in the acceleration signal and scale-factor non-linearity below 2ppm in the rotational signal, a ratio of $\sigma_f/\sigma_0 \geq 3$ and a wavefront flatness better than $\lambda/30$ are required.

6.3 Coupling with vibrational motion

Wavefront distortions are a noise source when coupled with platform vibrations in both the longitudinal and transverse direction with respect to the Raman beam axis.
For instance in the case of a Gaussian beam, longitudinal vibrations affect the interferometer signal via the Gouy phase. For a white noise vibration noise, the Allan variance of the accelerometer signal is given by

$$AVAR_a(\tau_c) = \frac{4\, S_a^2}{\tau_c} \frac{1}{z_R^2\, k_{\text{eff}}^2} \left(\frac{2}{3} \frac{T_c}{T} - 1 \right) \tag{6.25}$$

where τ_c is the cluster time, T_c is the cycling time, and S_a^0 is the linear vibration power spectral density. Even in harsh environments characterized by an acceleration noise of $1\text{mg}/\sqrt{\text{Hz}}$, the short-term sensitivity of the sensor is $\sim 0.007\text{ng}/\sqrt{\text{Hz}}$ for a beam waist of 0.5mm, a cycling frequency of 1Hz and a free evolution time of $T = 10$ms. Therefore,

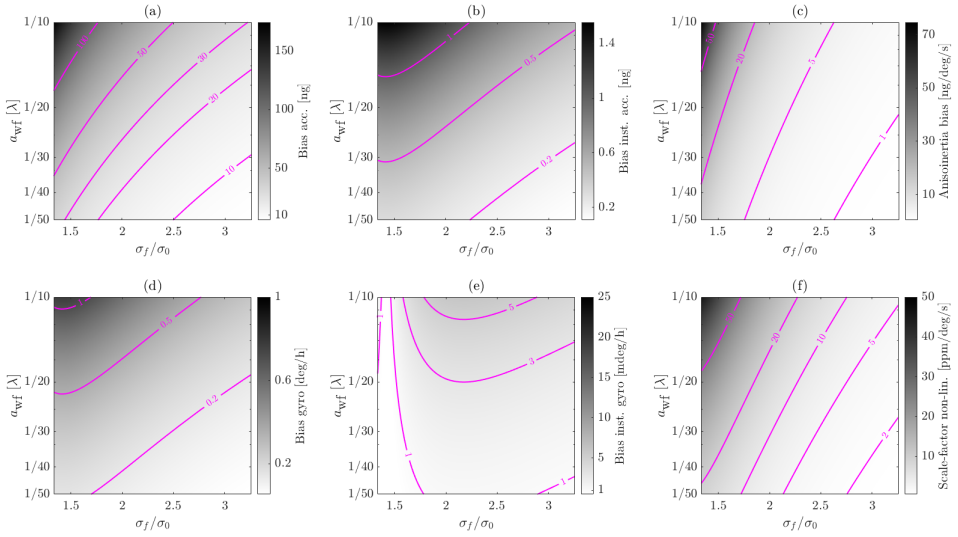

FIGURE 6.5: Errors induced by defocus and coma aberrations on PSI sensor. Upper panel: bias (panel (a)), bias instability (panel(b)) and anisoinertia bias (panel (c)) of the acceleration signal. Lower panel: bias (panel (d)), bias instability (panel(e)) and scale-factor non-linearity (panel (f)) of the rotational signal. The calculations have been performed for fixed free-evolution time.

we can conclude that wavefront distortions in a Gaussian beam have a negligible effect on interferometer performance when coupled with longitudinal vibrations.

The coupling of transverse vibrations with wavefront distortions depends on the aberration type. For a quadratic aberration, such as defocus, the phase noise imparted by the laser to the atomic wavefunction is given by

$$\delta\phi(t) \approx 2\,\alpha_D\,[2\,r_\perp(t)\,\delta r_\perp(t)]\,, \tag{6.26}$$

where $r_\perp(t)$ represents the mean motion of a mono-kinetic atom in the transverse plane and we neglect high-order terms of the vibration-induced displacements $\delta r_\perp(t)$. Assuming a uniform motion and infinitesimal pulses we obtain the vibration-induced interferometric phase

$$\begin{aligned}\Delta\Phi =& 4\,\alpha_D\,\{r_0\,[\delta\,r_\perp(0) - 2\,\delta\,r_\perp(T) + \delta\,r_\perp(2\,T)] + \ldots \\ & (2\,v_0\,T)\,[\delta r_\perp(2\,T) - \delta r_\perp(T)]\}\,,\end{aligned} \tag{6.27}$$

where $t = 0$ coincides with the time at which the first pulse occurs.
In Eq. (6.27), we observe a first term dependent on the initial atomic position, which affects the acceleration signal, and another term dependent on the initial velocity, affecting the rotational signal. The mathematical form of the position and velocity-dependent

terms resembles, respectively, the phase and Coriolis sensitivity functions in the limit of infinitesimal pulses. Therefore, we can apply the sensitivity function formalism to compute the Allan variance

$$AVAR_{\Delta\Phi}(\tau_c) = \frac{S^0_{a_\perp}\,(4\,\alpha_D\,T^2)^2}{2\,\tau_c}\left[r_0^2\,\left(\frac{2}{3}\frac{T_c}{T}-1\right)+\ldots\right.$$
$$\left.(6\,v_0\,T)^2\left(\frac{16}{27}\frac{T_c}{T}-1\right)\right], \tag{6.28}$$

where $S^0_{a_\perp}$ is the power spectral density of the white noise transverse acceleration. As expected, the longer the free-evolution time, the higher the noise induced by the transverse vibrations.

Chapter 7

Point-source interferometry

Cold-atom inertial (CAI) sensors based on point-source interferometry (PSI) exploit the imaging of atomic population's spatial distribution to infer angular rates and specific forces. Firstly demonstrated experimentally at Stanford within Kasevich's group, PSI was essentially developed as a detection technique allowing for multi-axial inertial sensing with a single magneto-optic trap (MOT) [40].

The use of a single MOT and a charge-coupled device (CCD) greatly simplifies the sensor architecture compared to dual-atom interferometers. In dual-atom interferometers, two atomic clouds are launched in a counter-propagating arrangement to discriminate the inertial phase shift induced by specific force from the phase shift induced by angular rate. PSI leverages position-velocity correlations within an expanding atomic cloud to deduce angular rates. Unlike specific forces that result in a phase offset, angular rates introduce a spatially varying phase that modulates the atomic populations in the plane transverse to the Raman beam. Consequently, PSI enables the simultaneous measurement of two angular rates in the plane orthogonal to the Raman beam and one acceleration along the Raman beam axis.

Rotations of the Raman beam with respect to atomic trajectories imprint a phase on the wavefunction that linearly depends on the initial velocity. Therefore, this results in a linear phase variation across the imaged atomic population with a gradient proportional to the applied angular rate. The measurement of a spatial gradient, as opposed to a phase shift as in cloud-averaging sensors, presents three main advantages: first, it circumvents the phase ambiguity problem, effectively extending the dynamic range; second, by combining multiple images and scanning the phase offset, it becomes possible to determine the sign of the applied angular rate; third, the interference fringes align with the direction of the applied angular rate, offering the potential for gyrocompassing operations.
Moreover, PSI enables the measurement of high-order phase distributions induced by wavefront distortions, thus facilitating bias calibration in cloud-averaging CAI sensors.

Given the evident advantages that PSI offers, this chapter investigates some of the error sources with a specific focus on contrast decay mechanisms, scale-factor, and read-out errors affecting the rotational signal. First, when coupled with a rotation, the initial atomic distribution has a significant impact on PSI gyroscope contrast and scale-factor error, as the phase distribution truly depends on the dynamics of the wavefunction in phase-space. Second, the estimation of the rotation-induced phase gradient is not a trivial problem, especially in the partial-fringe regime characterized by low angular rates or in the presence of low signal-to-noise ratio (SNR). Third, the use of PSI sensor for inertial navigation application requires the stabilization of its scale-factor, therefore attention should be paied to this fundamental aspect.

The structure of the chapter is organized as follows:

1. We analyze the impact of the initial atomic distribution on the contrast decay and scale-factor error. First, we explain the underlying physical mechanism using a phase-space evolution model based on the Wigner function formalism. Second, we analyze quantitatively the impact of system parameters on PSI performance.
2. We present a read-out protocol based on extended Kalman filter for the estimation of the interferometric phase map from PSI images, analyze the impact of SNR and wavefront aberrations on the estimated phase gradient.
3. We present a compensation protocol for stabilizing the PSI rotational scale factor, which involves data-fusion with a classical inertial sensor. The protocol, based on Kalman filtering, can be applied in real-time and estimates the PSI rotational scale-factor tracking eventual drifts.

7.1 Effect of the initial atomic distribution

The initial atomic phase-space distribution plays a crucial role in the reduction of SNR and introduces errors in the sensor's scale-factor. Hoth *et al.* developed a semi-classical model based on the assumption that atomic distributions can be described by classical probability density functions. The initial atomic spatial distribution, characterized by a probability density function $n_0(\mathbf{r})$, expands due to thermal motion and interacts with the laser diffraction gratings. At detection, a single atom will end up in a position $\mathbf{r} + \mathbf{r}_{PS}$, where $\mathbf{r}_{PS}$ denotes the atomic displacement caused by thermal expansion. Therefore, the probability density function describing the final atomic distribution is given by the convolution of the initial cloud with the expanded one [1]. For an initial

[1] We recall the following classical result of probability theory: given two probability density functions, $f(x)$ and $g(y)$, the probability density function describing the sum of the two random variables, $h(x+y)$, is obtained by convoluting $f(x)$ with $g(y)$, i.e., $h(x+y) = f(x) \circledast g(y)$.

Gaussian phase-space distribution, the convolution integral has an analytic solution, and the final atomic distribution is given by [44]

$$n(\mathbf{r}_\perp) = \mathcal{N}(\mathbf{r}_\perp, \sigma_f)\ \left[P_0 + (C_0/2)\ \exp\left(-\sigma_0^2\, \mathbf{k}_\omega^2\, F/2\right)\ \cos\left(F\, \mathbf{k}_\omega \cdot \mathbf{r}_\perp + \Delta\Phi_{\text{off}}\right)\right] \tag{7.1}$$

where $\mathcal{N}(\ldots)$ is a normal distribution with standard deviation $\sigma_f = \sqrt{\sigma_0^2 + \sigma_{PS}^2}$, σ_0 is the standard deviation of the initial space distribution, $\sigma_{PS} = \sigma_v\, T_{ex}$ is the standard deviation of the expanded cloud due to thermal motion (i.e., the ideal point source), P_0 is the fringe offset, and C_0 is the contrast in absence of angular rate. The term $\mathbf{k}_\omega$ is the spatial phase gradient induced by an angular rate in the case of ideal point source, F is the scale-factor term that accounts for scale-factor dependency on the initial size of the atomic cloud and $\Delta\Phi_{\text{off}}$ is the phase offset (e.g., acceleration-induced phase, laser phase etc.).
The rotation-induced phase gradient can be generalized to the time-varying case using the Coriolis sensitivity function

$$\mathbf{k}_\omega = \frac{1}{T_{ex}} \int_{-\infty}^{+\infty} -w(t) \left(\mathbf{k}^b \times \boldsymbol{\omega}_{ib}^b(t)\right)\, dt\,, \tag{7.2}$$

and for infinitesimal pulses we get

$$\mathbf{k}_\omega = -\frac{2\,T}{T_{ex}} \left(\mathbf{k}^b \times \Delta\boldsymbol{\psi}_{ib}^b\right) \tag{7.3}$$

where T_{ex} is the total expansion time, and $\Delta\boldsymbol{\psi}_{ib}^b = \int_T^{2\,T} \boldsymbol{\omega}_{ib}^b(t)\, dt$ is the integrated angular rate.
Eq. (7.3) has a strong physical interpretation: what a PSI gyroscope really measures is not an angular rate, but the integrated angular rate, i.e., the so-called 'delta-theta'. We observe that in the case of a constant angular rate we recover the well-known expression for the phase gradient $\mathbf{k}_\omega = -2\,(T^2/T_{ex})\,\mathbf{k}^b \times \boldsymbol{\omega}_{ib}^b$.

7.1.1 Scale-factor error

The first effect of the initial space distribution is related to deviations of the rotational scale-factor from the ideal point source case. For a Gaussian distribution the scale-factor correction factor is given by

$$F = 1 - \left(\frac{\sigma_0}{\sigma_f}\right)^2\,. \tag{7.4}$$

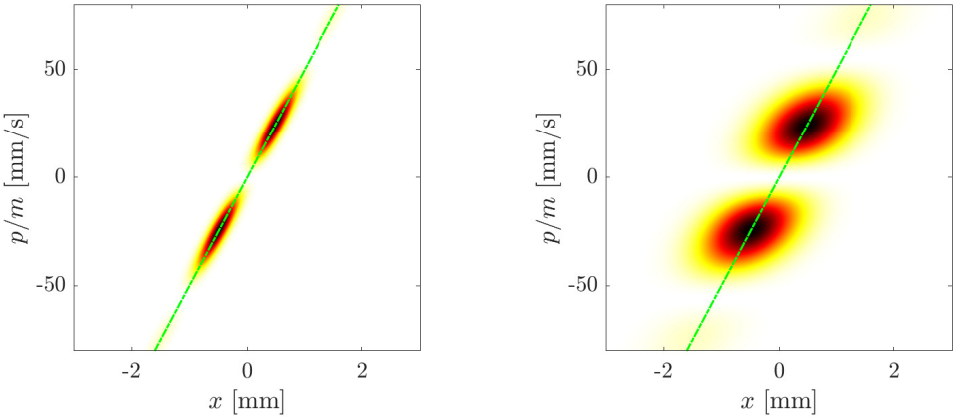

(A) $\sigma_0 = 0.1$mm (B) $\sigma_0 = 0.5$mm

FIGURE 7.1: Simulated phase-space distribution of the upper ground state population of ^{85}Rb at the output port of a Mach-Zehnder interferometer for different initial cloud sizes. The dashed green line, $p/m = x/T_{ex}$, indicates the ideal point source limit. Simulation parameters: initial Gaussian distribution, $T_{ex} = 20$ms, $\mathcal{T} = 10\mu$K, $\omega = 2$deg/s.

We observe that for $\sigma_0 = 0$, the correction factor is unitary and we recover the point source phase gradient.

The physical origin of the scale-factor variation due to the finite size of the initial cloud can be understood by examining the atomic population distribution in phase-space. The time-evolution of the atomic phase-space distribution has been modelled using Wigner function formalism (for more details refer to Appendix B).

Figure 7.1 shows the phase-space distributions of the upper ground state of ^{85}Rb at the output port of a Mach-Zehnder interferometer in the presence of an angular rate and for two initial cloud dimensions. In the simulation we assume that the initial initial atomic cloud has a Gaussian phase-space distribution with a position standard deviation σ_0 and a momentum standard deviation $\sigma_p = \sqrt{k_B \mathcal{T} m}$. In both cases, we observe interference fringes due to the action of an external angular rate. The finite size of the initial cloud blurs the momentum-position correlations, as illustrated by the 'blobs' around the ideal point source limit, here represented by a dashed green line. For a fixed expansion time, the smaller the initial cloud size, the more the blobs appear to stretch along the point source limit line, and, therefore, the more the momentum-position correlations build up. Since the PSI signal is obtained by marginalizing the phase-space distribution along momentum space, blurred momentum-position correlations translate, for a given position, into interference among different velocity classes. This interference modifies the modulation of the PSI signal in real space and, therefore, the spatial phase gradient. From this point of view, the factor F represents a sort of correlation factor. While in the point source limit, momentum and position are perfectly correlated and $F = 1$, in the case of a finite initial size, these correlations are not perfect, and $F \leq 1$.

Long-term drifts of the initial cloud size or of the expansion rate are sources of scale-factor instability for the PSI gyroscope. Applying error propagation to Eq. (7.4) we obtain

$$\frac{\Delta F}{F} = \left(\frac{\sigma_0}{\sigma_f}\right)^2 \sqrt{4\left(\frac{\Delta\sigma_0}{\sigma_0}\right)^2 + \left(\frac{\Delta\mathcal{T}}{\mathcal{T}}\right)^2}, \tag{7.5}$$

that implies fluctuations of the initial cloud size and temperature at ppm levels to guarantee scale-factor instability of the same order of magnitude. Achieving such a level of control over the dimensions of the initial cloud is extremely challenging experimentally; therefore, scale-factor instability represents a major issue for a PSI gyroscope.

Eq. (7.4) is valid only in the case the initial space distribution is Gaussian. For a general distribution the correction factor F could be modified as follows

$$F = 1 - \left(\frac{\sigma_0}{\sigma_f}\right)^{\mu} \tag{7.6}$$

where the free parameters μ depends on the actual initial distribution. As an example, we study the effect of the initial cloud shape, modelling it as a generalized Gaussian distribution [118]

$$n_0(r_\perp) = \frac{\beta}{2^{(\beta+1)/\beta}\,\sigma_0\,\Gamma(1/\beta)}\,\exp\left(-0.5\left|\frac{r_\perp}{\sigma_0}\right|^{\beta}\right) \tag{7.7}$$

with β shape factor, and $\Gamma(\ldots)$ is the Gamma function. Note that the standard Gaussian distribution correspond to the case $\beta = 2$.
For different values of β, we numerically evaluate the time evolution of the atomic distribution and extract the parameter F for various ratios of σ_f/σ_0. Fitting the numerical results with Eq. (7.6) enables the extraction of the parameter μ, as presented in Table 7.1. For a fixed initial width σ_0, an initial distribution with higher tail values (e.g., $\beta < 2$) is characterized by greater scale-factor deviations from the ideal point source case. This is intuitive as, in the frequency domain, the distribution has a lower cut-off frequency, thereby modifying the Fourier transform of the ideal point source at angular frequencies $k_\perp = \pm k_\omega$ more significantly [2].

Nevertheless, in the high-expansion regime ($\sigma_f \gg \sigma_0$), the scale factor tends toward the point source limit, i.e., $F \to 1$. An increase in the expansion time leads to the rotation and 'stretching' of the atomic distribution in phase-space. This stretching reduces the spread in momentum for a given position and, consequently, diminishes the interference of different velocity classes responsible for the scale-factor error.

[2] The Fourier transform of the ideal point source is characterized by three peaks: one at zero frequency and the other two at $k_\perp = \pm k_\omega$.

TABLE 7.1: Effect of the shape parameter, β, on the scale-factor error and contrast of the PSI gyroscope. The scale-factor correction factor is modelled as $F = 1 - (\sigma_0/\sigma_f)^{\mu}$. The contrast decay is modelled as $\exp(-\bar{\sigma}_0^2\,\mathbf{k}_\omega^2\,F/2)$, with $\bar{\sigma}_0 = \nu\,\sigma_0$.

Shape parameter β	**S.F. parameter μ**	**Contrast parameter ν**
1.6	1.73	1.18
2	2	1
2.4	2.20	0.89

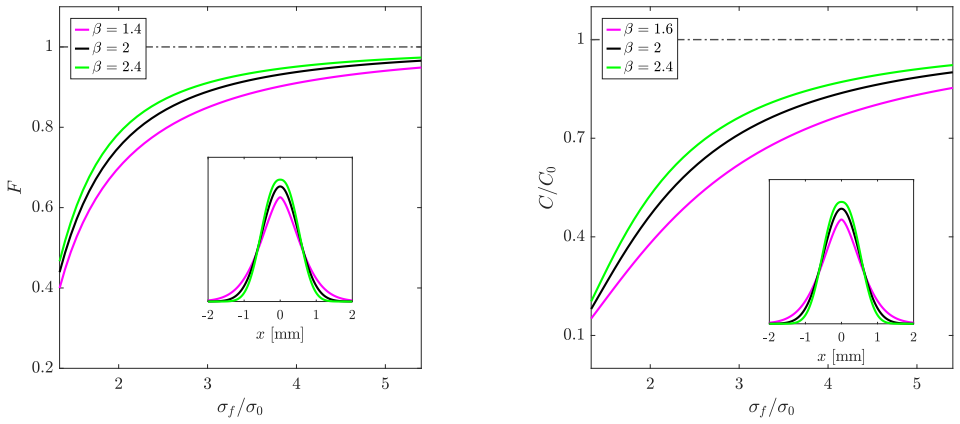

(A) Scale-factor variation (B) Contrast variation

FIGURE 7.2: Effect of the shape of the initial space distribution on the scale-factor and contrast of a PSI gyroscope. We model the initial cloud as a generalized Gaussian distribution described by the parameter β. The inset shows the correspondent space distributions of the initial cloud for a fixed σ_0. The dashed black lines indicate the point source limit. Simulation parameters: $\omega = 1\text{deg/s}$.

7.1.2 Contrast decay

The second effect related to the finite size of the initial cloud is the contrast decay in the presence of an external angular rate. Referring again to Figure 7.1, we observe that a higher value of the initial cloud size leads to blurred position-momentum correlations. Therefore, averaging over different velocity classes results in a wash-out of the rotation-induced fringes in real space. On the contrary, in the point source limit, position and momentum are perfectly correlated or, in other words, there is a one-to-one correspondence between position and momentum. Hence, for each position, there is only the contribution carried by a single velocity class, and no wash-out of the interference fringes occurs.

In order to take into account the effect of the shape of the initial cloud we model the contrast decay as

$$C = C_0\,\exp\left(-\,\mathbf{k}_\omega^2\,\bar{\sigma}_0^2\,F/2\right) \tag{7.8}$$

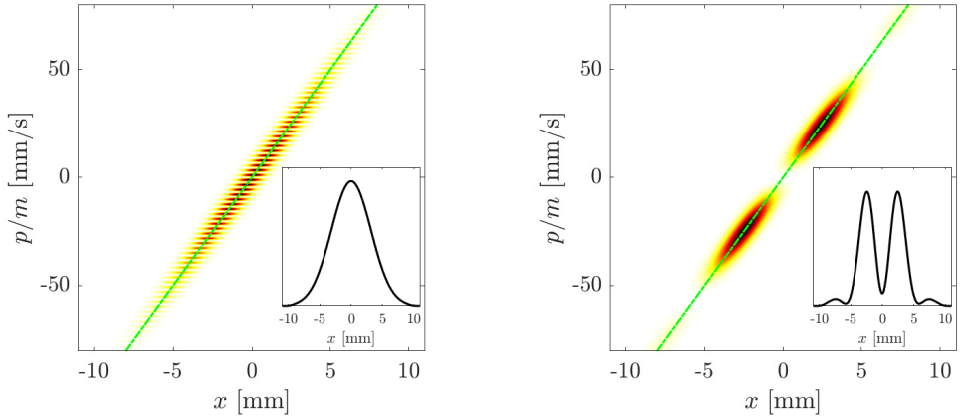

(A) $T_{ex} = 2\,T$ (B) $T_{ex} = 5\,T$

FIGURE 7.3: Simulated phase-space distributions in high-expansion regime. The dashed green line, $p/m = x/T_{ex}$, indicates the ideal point source limit. Simulation parameters: initial Gaussian distribution with $\sigma_0 = 0.5$mm, $T_{ex} = 100$ms, $\mathcal{T} = 10\mu$K, $\omega = 2$deg/s.

where the scale-factor correction parameter F is given by Eq. (7.6), and $\bar{\sigma}_0 = \nu\,\sigma_0$ is the initial size of an effective Gaussian distribution.
Modeling the initial cloud as a generalized Gaussian distribution, we determine the free parameter ν by fitting the results of the numerical simulation with Eq. (7.8). The retrieved values of ν are reported in Table 7.1. As expected, a distribution characterized by higher tail values compared to the Gaussian distribution behaves like a Gaussian distribution with an equivalent larger initial size.

In the case of contrast, what happens in the high-expansion regime is not trivial, and it depends on how the cloud expansion is achieved. Figure 7.3 illustrates two scenarios where the high-expansion regime is attained by either increasing or keeping constant the free-evolution time, respectively. In the first case, the term $F \to 1$, but the rotation-induced wave-vector $|\mathbf{k}_\omega| \to \infty$, leading to contrast decay. Physically, the longer the free-evolution time, the greater the modulation of the distribution in momentum. This high-frequency modulation results in a rapid wash-out of the fringes when the phase-space distribution is marginalized. In the second case, an increase in the expansion time while keeping the free-evolution time constant leads to $F \to 1$ and $|\mathbf{k}_\omega| \to 0$. Consequently, $C \to C_0$, recovering the point source limit case. Physically, this is because, for a fixed free-evolution time, the cloud expansion induces rotation and stretching of the atomic distribution in phase-space, thereby reducing the spread in the momentum direction for a given position. This reduction results in less interference between different velocity classes and less fringes wash-out when averaging over the momentum distribution.

7.2 Additional error sources

7.2.1 Spatial scale-factor variation

In Chapter 4, we discussed how the sensor scale-factor is influenced by the Rabi frequency encountered by the atoms. In the presence of laser spatial inhomogeneity, atoms undergo varying intensity levels, resulting in a spatial variation of the scale-factor.
We compute the scale-factor error for the point source case, assuming a Gaussian intensity profile, and that the distance traveled by the atoms during the interferometric sequence is much smaller than the Raman beam waist. To the first order in τ/T, the scale-factor error is given by

$$F_\epsilon(r_\perp) \approx \left[\left(-2+\frac{4}{\pi}\right)\left(\frac{r_\perp}{w_L}\right)^2+\left(-2+\pi+\frac{4}{\pi}\right)\left(\frac{r_\perp}{w_L}\right)^4\right]\frac{\tau}{T}\,. \tag{7.9}$$

For instance, assuming a laser beam waist of $w_L = 1$ cm, $\tau/T = 0.1\%$, and $T_{ex} = 2\,T$, the scale factor varies at most by 45 ppm over a radius of 3 mm. We observe that, for a given free-evolution time, the spatial scale-factor error can be reduced by increasing the expansion time.

7.2.2 Contrast decay due to imperfect wavepacket overlap

The rotation of the Raman beam during the pulse sequence determines a variation in the momentum kick imparted to the center of mass of the atomic wavepackets traveling along the upper and lower arm of the interferometer. As a consequence, the centers of mass at the time of the final pulse are not perfectly overlapped in phase-space, resulting in contrast decay.
For a Gaussian wavepacket, the contrast decay due to the imperfect wavepacket overlap is given by [43]

$$C = \exp\left[-\frac{1}{4\,\hbar^2}\mathbf{\Delta R}^T\,\mathbf{\Sigma}_p\,\mathbf{\Delta R}\right] \tag{7.10}$$

where $\mathbf{\Delta R}$ is the centre of mass' space displacements at the time of the final pulse, and $\mathbf{\Sigma}_p = \mathrm{diag}(\sigma_{p,x}^2,\,\sigma_{p,y}^2,\,\sigma_{p,z}^2)$ is the momentum covariance matrix associated to the atomic wavepacket. The quantity $\hbar/\sigma_{p,i}$ has the units of a length and represents the extension of the wavepacket.
The space displacement can be obtained solving the classical equations of motion of the centres of mass traveling along the upper and lower arm of the interferometer. For

a constant angular rate, we compute the space displacement at the final pulse up to the third order in T

$$\mathbf{\Delta r} \approx 2\,T^2\,\boldsymbol{\omega}_{ib}^{b} \times \mathbf{v}_r - 3T^3\,\left(\boldsymbol{\omega}_{ib}^{b} \times \boldsymbol{\omega}_{ib}^{b} \times \mathbf{v}_r\right)\,, \tag{7.11}$$

Equation (7.11) generalizes the result reported in Ref. [42] and highlights that only to the first order in $\boldsymbol{\omega}_{ib}^{b}$, the contrast decay is determined by angular rates orthogonal to the recoil velocity direction. However, for $T < 10$ ms, the T^3 term is less than 0.02%/deg/s of the T^2 term, and therefore, negligible for a first approximation analysis.
Neglecting the T^3 term in Eq.(7.11) we obtain

$$C = \exp\left(-|\mathbf{k}_\omega|^2\,\bar{\sigma}_{PS}^2/4\right). \tag{7.12}$$

where $\bar{\sigma}_{PS} = \bar{\sigma}_v\,T_{ex}$ is the size of an equivalent point-source characterized by a velocity width $\bar{\sigma}_v$. We remark that the quantity $\bar{\sigma}_v$ is not necessarily equal to the initial atomic velocity width. Therefore, it is not proportional to the temperature of the atomic ensemble. Instead, it depends on the velocity selection process operated by the Raman diffraction on the atomic ensemble. Hence, $\bar{\sigma}_v$ coincides with the wavepacket's velocity width at the output port of the interferometer and is a function of both the initial velocity distribution and the efficiency of the Raman pulses. The velocity selection reduces the wavepacket's momentum width ensuring a higher de Broglie wavelength, and, hence, a better overlap with less contrast decay [43].

The contrast loss *de facto* determines the upper bound of the maximum angular rate detectable by a PSI gyroscope. Assuming that the upper bound of the sensor dynamic range is equivalent to the angular rate that induces a 90% contrast decay compared to the case with zero angular rate, we obtain, for a Gaussian wavepacket,

$$|\mathbf{k}_{\omega,\,max}| = \sqrt{\frac{2\,\ln(10)}{\sigma_0^2\,F + \bar{\sigma}_{PS}^2/2}}\,. \tag{7.13}$$

Figure 7.4 shows the ratio, η, between the maximum angular rate due to the initial cloud size and the imperfect wavepacket overlap as a function of the free-evolution time, T, and the time-of-flight, $T_d = T_{ex} - 2T$. The initial size of the cloud limits the PSI dynamic range at low-expansion regimes in agreement with the experimental results in Ref. [44]. With an increase in the free-evolution time or time-of-flight, imperfect wavepacket overlap becomes the dominant limiting effect. In any case, the free-evolution time is the primary limiting factor for the dynamic range of a PSI gyroscope. For instance, assuming a temperature $\mathcal{T} = 5\mu$K, a free-evolution time less than 10ms is required to detect angular rates higher than 2deg/s. Therefore, a sensor operating in

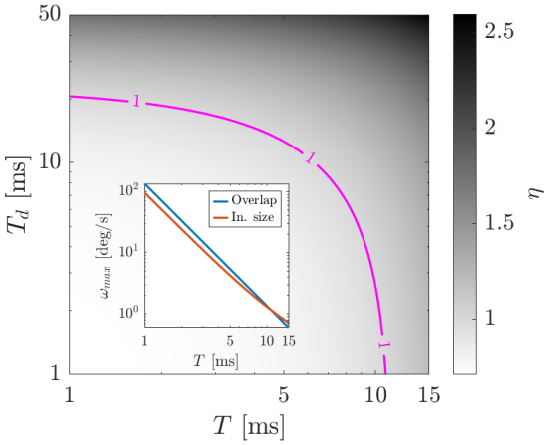

FIGURE 7.4: Ratio, η, between the maximum angular rate due to the initial cloud size and the maximum angular rate due to the imperfect wavepacket overlap as function of the free-evolution time and the flight-of-time after the interferometer pulse sequence. The inset shows the maximum angular rate as function of the free-evolution time for the case $T_d = 1$ms. We neglect the Raman velocity selectivity. Simulation parameters: temperature $\mathcal{T} = 5\mu$K, initial size $\sigma_0 = 0.5$mm.

a closed-loop configuration would be necessary to overcome contrast loss due to high angular rates.

7.2.3 High-order phase shifts

Eq.(7.3) is obtained neglecting the higher-order terms in the variable $\boldsymbol{\omega}_{ib}^b$. A solution of the classical equation of motion in the rotating frame can be obtained in terms of a power series $\mathbf{r}_{ba}^b(t) = \sum_{n=0}^{\infty} \mathbf{a}_n\, t^n$, where the coefficients $\mathbf{a}_n$ can be computed via recursive substitution starting from known initial conditions $\mathbf{r}_{ba}^b(0) = \boldsymbol{\ell}^b$, and $\dot{\mathbf{r}}_{ba}^b(0) = \mathbf{v}_0^b$. For constant specific force and angular rate, the relative atomic trajectory, up to the third order in t, is given by

$$\begin{aligned}\mathbf{r}_{ba}^b(t) = \boldsymbol{\ell}^b &+ \left(\mathbf{v}_0^b + \frac{\mathbf{v}_{\text{rec}}^b}{2}\right) t + \dots \\ &- \left(\boldsymbol{\Omega}_{ib}^b \boldsymbol{\Omega}_{ib}^b\, \boldsymbol{\ell}^b + 2\,\boldsymbol{\Omega}_{ib}^b\, \mathbf{v}_0^b + \mathbf{f}_{ib}^b\right) \frac{t^2}{2} + \dots \\ &+ \left[\frac{1}{2}\,\boldsymbol{\Omega}_{ib}^b \boldsymbol{\Omega}_{ib}^b \left(\mathbf{v}_0^b + \frac{\mathbf{v}_{\text{rec}}^b}{2}\right) + \frac{1}{3}\,\boldsymbol{\Omega}_{ib}^b \left(\boldsymbol{\Omega}_{ib}^b \boldsymbol{\Omega}_{ib}^b\, \boldsymbol{\ell}^b + \mathbf{f}_{ib}^b\right)\right] t^3 + o(t^4)\,,\end{aligned} \tag{7.14}$$

where we indicated the vector product by means of the skew-symmetric matrix $\boldsymbol{\Omega}_{ib}^b$. Assuming infinitesimal resonant pulses we obtain the following interferometric phase shift

$$\begin{aligned}\Delta\Phi = &- \mathbf{k}^b \cdot \left(\mathbf{\Omega}^b_{ib}\mathbf{\Omega}^b_{ib}\,\boldsymbol{\ell}^b + 2\,\mathbf{\Omega}^b_{ib}\,\mathbf{v}^b_0 + \mathbf{f}^b_{ib}\right)\,T^2 + \dots \\ &+ \mathbf{k}^b \cdot \mathbf{\Omega}^b_{ib}\mathbf{\Omega}^b_{ib}\left(\mathbf{v}^b_0 + \frac{v^b_{\text{rec}}}{2}\,\widehat{\mathbf{k}}^b\right)\,3\,T^3 + \dots \\ &+ \mathbf{k}^b \cdot \mathbf{\Omega}^b_{ib}\left(\mathbf{\Omega}^b_{ib}\mathbf{\Omega}^b_{ib}\,\boldsymbol{\ell}^b + \mathbf{f}^b_{ib}\right)\,2\,T^3\,.\end{aligned} \tag{7.15}$$

Therefore, the rotational signal of a PSI sensor is affected by a bias

$$\mathbf{\Delta k}_\omega = \frac{3\,T^3}{T_{ex}}\,\mathbf{k}^b \times \boldsymbol{\omega}^b_{ib} \times \boldsymbol{\omega}^b_{ib} \tag{7.16}$$

This error source represents a cross-coupling between angular rates in the longitudinal and transverse direction to the Raman effective wave-vector. Assuming angular rates with a magnitude of 1deg/s and a free-evolution time of 10ms, we obtain a bias of 0.94deg/h per axis.

In presence of angular accelerations, the derivative of the attitude angle is not equal to the angular rate but is described by the so-called Bortz equation. To second order accuracy, the Bortz equation can be approximated as [119]

$$\dot{\boldsymbol{\psi}}^b_{ib} \approx \boldsymbol{\omega}^b_{ib} + \frac{1}{2}\boldsymbol{\alpha}^b_{ib} \times \boldsymbol{\omega}^b_{ib}\,, \tag{7.17}$$

with $\boldsymbol{\alpha}^b_{ib} = \int_{-\infty}^{t} \boldsymbol{\omega}^b_{ib}(t')\,dt'$. The second term on the right hand side represents the so-called 'coning' correction and accounts for non-commutativity of rotations due to change in the direction of the vector $\boldsymbol{\psi}^b_{ib}$ during the interferometer pulse sequence. Assuming a linearly varying angular rate, we compute the bias of the PSI gyro

$$\mathbf{\Delta k}_\omega = -\frac{2\,T^2}{T_{ex}}\,\boldsymbol{k}^b \times \left[\frac{3\,T}{2}\,\dot{\boldsymbol{\omega}}^b_{ib} + \frac{7\,T^2}{12}\left(\boldsymbol{\omega}^b_{ib,0} \times \dot{\boldsymbol{\omega}}^b_{ib}\right)\right]\,, \tag{7.18}$$

where the first term on the right-hand side is due to the angular acceleration and the second term represents the coning correction. For instance an angular rate of 1deg/s, with a free-evolution time 10ms and an angular acceleration of 0.1deg/s^2 gives rise to an acceleration-induced bias of 5.4deg/h and a coning error of 0.4deg/h.

7.3 Read-out protocol

An angular rate orthogonal to the Raman beam propagation axis induces a spatial modulation of atomic populations, with a frequency proportional to the applied rotation. Retrieving the spatial frequency by fitting a signal, as described by Eq. (7.1), to the

atomic distribution is critical, especially in cases of low angular rates that result in less than one fringe.
Several techniques have been developed to extract information in the low angular rate regime. For instance, Sugarbaker *et al.* applied a large bias rotation to the Raman retro-reflecting mirror to induce multiple fringes across the cloud [120] and retrieve the unknown angular rate by parametric fitting. Chen *et al.* used principal component analysis on multiple interferograms to reconstruct the spatial modulation [117]. NIST developed a method, called 'Simple, High dynamic range, and Efficient Extraction of Phase map' (SHEEP), in which four interferograms in quadrature were combined to reconstruct the interferometer phase map [116].
The SHEEP method has demonstrated superior capabilities with respect to principal component analysis in the low angular rate regime and requires a significantly lower number of interferograms. However, it is based on the inverse tangent function, arctan, which is periodic in the interval $(-\pi,\ \pi]$ and requires additional unwrapping, noise filtering, and phase-stitching operations [121].
Therefore, we propose a read-out protocol based on an extended Kalman filter (EKF), that estimates the phase map using as measurements four interferograms in quadrature and avoiding the use of the arctan function. The application of Kalman-based filters to phase unwrapping is not new and has been previously proposed in several fields such as digital holography and synthetic aperture radar applications [122, 123, 124].

7.3.1 Filter mathematical model

The EKF algorithm is based on two equations. A state-space model that estimates the desired state and a measurement model that links the actual observation and the desired state.
We write the state-space equation as

$$\mathbf{x}_k = \boldsymbol{A}\,\mathbf{x}_{k-1} + \boldsymbol{\eta}_{k-1}\,, \tag{7.19}$$

with $\mathbf{x}_k$ state vector evaluated at the k-th pixel location, and $\mathbf{A}$ the state transition matrix, given by

$$\mathbf{x}_k = \begin{pmatrix} s_k & C_k & \Phi_k & \Phi_k^{(1)} & \Phi_k^{(2)} \end{pmatrix}^T\,, \tag{7.20a}$$

$$\mathbf{A} = \begin{bmatrix} 1 & 0 & 0 & 0 & 0 \\ 0 & 1 & 0 & 0 & 0 \\ 0 & 0 & 1 & \frac{\Delta\zeta}{1!} & \frac{\Delta\zeta^2}{2!} \\ 0 & 0 & 0 & 1 & \frac{\Delta\zeta}{(2-1)!} \\ 0 & 0 & 0 & 0 & 1 \end{bmatrix}, \tag{7.20b}$$

where we denote $\Phi^{(j)}$ as the j-th derivative of the phase distribution, and s as the square of the final atomic distribution width σ_f. We assume that the phase map is described by a second order polynomial in the generic direction ξ, however, in the case of high phase variations, we can extend the model including more terms in the Taylor expansion. The term $\boldsymbol{\eta}$ is the stochastic part of the state-space model and is assumed to be Gaussian with covariance matrix $\mathbf{Q}$.
The measurement model is given by

$$\mathbf{z}_k = \mathbf{h}(\mathbf{x}_k) + \boldsymbol{\nu}_k\,, \tag{7.21}$$

with $\mathbf{z}_k$ the observations vector

$$\mathbf{z}_k = (I_S \quad I_C \quad s)^T = \left(n\left(\mathbf{r}_\perp, \frac{\pi}{2}\right) - n\left(\mathbf{r}_\perp, \frac{3\pi}{2}\right) \quad n(\mathbf{r}_\perp, \pi) - n(\mathbf{r}_\perp, 0) \quad s\right)^T. \tag{7.22}$$

As usual the notation $n(\mathbf{r}_\perp, \phi_L)$ indicates the atomic distribution in the plane orthogonal to the Raman propagation axis with a laser phase offset ϕ_L. The stochastic term $\boldsymbol{\nu}$ is assumed to be Gaussian with covariance matrix $\mathbf{R}$.
The function $\mathbf{h}(\ldots)$ is non linear as we assume that the observations are linked to the state vector parameters via Eq. (7.1). Therefore we need to linearize the measurement model computing at each estimation step the Jacobian

$$\mathbf{H}_k = \frac{G(s_k)}{2\pi s_k}\begin{bmatrix} \frac{C_k(\mathbf{r}_\perp^2 - 2s_k)}{2s_k^2}\sin\Phi_k & \sin\Phi_k & C_k\cos\Phi_k & 0 & 0 \\ \frac{C_k(\mathbf{r}_\perp^2 - 2s_k)}{2s_k^2}\cos\Phi_k & \cos\Phi_k & -C_k\sin\Phi_k & 0 & 0 \\ 1 & 0 & 0 & 0 & 0 \end{bmatrix}, \tag{7.23}$$

with $G(s) = \exp\left[-\mathbf{r}_\perp^2/(2\,s)\right]$.

7.3.2 Implementation

Beginning with an initial condition, the filter estimates, pixel-by-pixel, the size of the final cloud, the contrast, the interferometric phase, its gradient, and curvature. We assume as initial condition

$$\mathbf{x}_0 = \begin{pmatrix}\sigma_0^2 & C_0 & \arctan\left(I_S/I_C\right) & 0 & 0\end{pmatrix}^T \tag{7.24}$$

with σ_0 size of the initial atomic cloud and $C_0 = 0.5$.
At each step the filter uses the measurement model to correct the *a priori* estimation

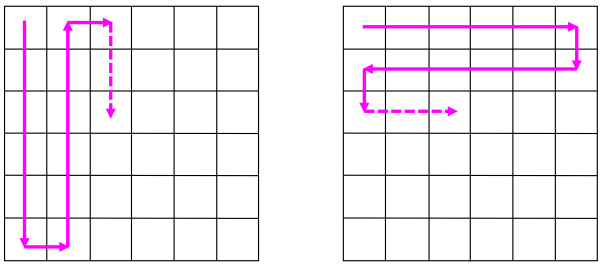

FIGURE 7.5: Path-following strategy implemented in the EKF for the phase map estimation.

given by the state-space model. The correction depends on the covariance matrix associated to the estimation uncertainty, that is propagated as

$$\mathbf{P}_k = \mathbf{A}\,\mathbf{P}_{k-1}\,\mathbf{A}^T + \mathbf{Q}\,, \tag{7.25}$$

and on the covariance matrix associated to the measurement noise $\mathbf{R}$. For an assigned measurement noise, the quantities $\mathbf{P}_0$ and $\mathbf{Q}$ can be tuned to guarantee optimal convergence of the filter. We found that the most critical parameter is the driving noise of the state-space model, chosen to be a diagonal matrix $\mathbf{Q} = \mathrm{diag}[\sigma_s^2\ \sigma_C^2\ 0\ \sigma_{\Phi^{(1)}}^2\ \sigma_{\Phi^{(2)}}^2]$. This choice results from assuming that the state vector terms are independent stochastic variables. Moreover, setting $\sigma_\Phi = 0$ allows for optimal tracking of a varying phase without lag errors.

Once the quantity Φ is estimated for all the pixels, we determine the phase gradient and phase curvature by fitting a second-order surface to the estimated phase map, instead of relying on the output of the filter. This approach ensures robustness, as the filter's measurement model is directly dependent on the phase and not on the gradient and curvature.

As the filter estimates the phase map pixel-by-pixel in a cascade sequential mode, crucial aspects are represented by both the initial pixel and the path-following strategy. In order to not add further complexity to the algorithm we implement a double path-following strategy as shown in Figure 7.5.
We found better results in the phase gradient estimation when running the filter along a 'serpentine' path that propagates in the direction orthogonal to the intended gradient to be estimated. Therefore, to estimate the horizontal (vertical) phase gradient we adopt a serpentine path that advances column-by-column (row-by-row). This because the starting point of each serpentine leg is characterized by the lowest SNR and, then, the worst estimation.

7.3.3 Simulation results

We run the EKF filter over a set of PSI images, adding pixel and shot-to-shot phase noise. The pixel noise depends on the detection process and technical sources, such as the CCD. The shot-to-shot phase noise depends, for instance, on laser phase noise in the RF chain or linear vibrations. Moreover, we add non-linearities in the nominal phase map in the form of second order wavefront distortions of the type $\Phi_{\mathrm{WF}} = \alpha_{xx}\, x^2 + \alpha_{yy}\, y^2 + \alpha_{xy}\, x\, y$.

Figure 7.6 shows an example of simulated measurements, I_S and I_C, and the Extended Kalman Filter (EKF) phase estimate, assuming an input angular rate of 1deg/s directed along the vertical direction. For comparison, we show the phase map computed via the arctan function. The EKF filters out the noise and outputs a continuous, unwrapped phase map. We observe that the estimated phase map differs from the true map by an offset; this is because the phase at the initial pixel is estimated using the arctan function. Nevertheless, the algorithm effectively tracks the phase gradient with a final error of 350ppm. The residuals between the estimated and true phase maps reveal a periodic structure that is attributed to the shot-to-shot phase noise, in agreement with experimental results reported in Ref. [116].

Assuming a shot-to-shot phase variation, we can compute, in the hypothesis of small perturbations, the PSI phase map at the j-th image

$$\Phi_j \approx \phi_\omega + \cos(2\,\phi_\omega)\frac{\delta\varphi_j + \delta\varphi_{j-2}}{2} \tag{7.26}$$

where ϕ_ω is the rotation induced phase, and $\delta\varphi_j = \varphi_j - \varphi_{j-1}$. Here, the quantity ϕ_j denotes the difference between the actual offset phase and the intended laser offset phase, ϕ_L, at the j-th image. The shot-to-shot phase variation, $\delta\varphi$, introduces an error in the PSI phase map, which contains a sinusoidal term with a spatial frequency twice that of the rotation-induced term and an amplitude that depends on the phase noise. For the parameters assumed in Figure 7.6, the input angular rate corresponds to a phase gradient of $k_\omega \sim 1.4\mathrm{rad/mm}$. According to the simple model of Eq. (7.26), in presence of phase noise, the phase gradient induces a modulation of wavelength $\sim 2.2\mathrm{mm}$, consistent with the residuals shown in Figure 7.6.

Phase noise significantly impacts the performance of the EKF scheme. To assess the filter's performance, we conducted a Monte Carlo simulation, considering atom shot noise and phase noise as noise sources. The phase noise is assumed to follow a Gaussian distribution with a standard deviation of σ_ϕ. Additionally, we introduced second-order phase distortions corresponding to a peak-to-valley amplitude of $\lambda/10$ over a circle with a radius of 1 cm.
Figure 7.7 presents the simulation results in terms of scale-factor error as a function of

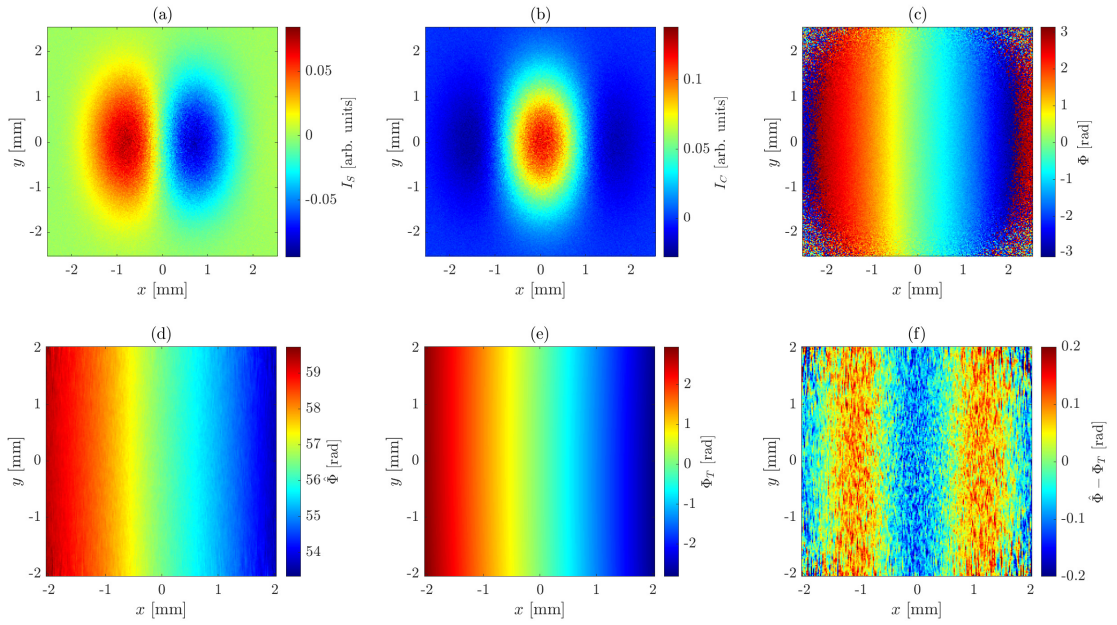

FIGURE 7.6: Noisy simulated PSI interferograms and EKF estimation. Panel (a): I_S signal. Panel (b): I_C signal. Panel (c): phase map estimated with the arctan function. Panel (d): phase map estimated by the EKF. Panel (e): true phase map. Panel (f): residuals between the estimated phase map and the true phase map, subtracted by a constant phase offset. Simulation parameters: pixel dimension 20μm,input angular rate $\omega = 1$deg/s, shot-to-shot phase noise $\sigma_\phi = 100$mrad.

the input angular rate. We observe that the scale-factor error remains nearly independent of the angular rate value for $\omega < 0.3$ deg/s and decreases rapidly as the magnitude of the angular rate increases. This behavior is expected, as the state observability is enhanced with higher rotational-induced phase.

At low angular rates, the EKF tracking error is significantly affected by the phase noise. This is due to the fact that we used the same filter tuning parameters for all three different σ_ϕ values considered. In real-world applications, the filter should be tuned based on the appropriate sensor characteristics, or it could be tuned in an adaptive fashion to account for variations in measurement noise during operating conditions [3].

The major source of phase noise is represented by linear vibrations in the Raman wavevector direction, and its impact increases with the free-evolution time. A possible solution to limit the impact of linear vibrations is to employ a scheme in which a classical accelerometer is used to estimate the vibration-induced phase at each shot in a similar fashion as done in cloud-averaging sensors [31].

Further improvements in phase map estimation could be achieved by using more advanced Kalman filtering algorithms, such as the unscented Kalman filter or particle filter, which can remove possible errors introduced by the linearization of the measurement model and non-Gaussian noise. Additionally, machine learning represents

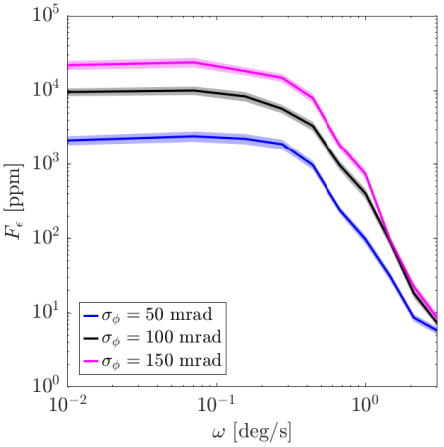

FIGURE 7.7: Performance of the EKF is evaluated in terms of scale-factor error for various input angular rates and phase noise. We assume that the angular rate vector forms an angle of $\theta = 20$ deg with respect to the vertical axis. The shaded area represents the 1-σ bound, while the thick line denotes the average value over 50 samples. Simulation parameters: pixel dimension 12μm, atom-shot noise corresponding to 10^6 atoms, quadratic phase distortion with a peak-to-valley amplitude of $\lambda/10$ over a 1 cm circle, shot-to-shot phase noise.

another obvious alternative, particularly suitable when high non-linearities and low signal-to-noise ratios prevent an accurate estimation of the interferometric phase map.

7.4 PSI scale-factor instability compensation

The long-term drift of the initial phase-space atomic distribution is the primary cause of scale-factor instability in the PSI rotational signal.
Avinadav *et al.* proposed two techniques to stabilize the PSI scale-factor [14]. The first is a contrast-based method relying on the analytical model expressed by Eq. (7.1). This method utilizes the zero-rotation contrast and the effective size of the detected atomic cloud as calibration parameters. The second method, independent of any assumed model, involves applying an additional known rotation to calibrate the scale factor, albeit at the cost of halving the sensor sampling frequency.

Following the approach of modeling-independent calibration, we develop a scale-factor error compensation scheme based on data-fusion between a PSI sensor and a conventional gyroscope (CG). A Kalman filter (KF) protocol is employed to track the PSI scale-factor in real-time by exploiting two consecutive measurements. We anticipate that the halving of the PSI sampling frequency does not pose a problem since the PSI is treated as an aiding sensor that stabilizes the bias drift of the CG in a similar manner to what has been proposed for cold-atom accelerometers [31].

7.4.1 Filter mathematical model and implementation

The state vector and the state transition matrix are given, respectively by

$$\mathbf{x}_j = \begin{pmatrix} F_j^{PSI} & \dot{F}_j^{PSI} \end{pmatrix}^T , \tag{7.27a}$$

$$\mathbf{A} = \begin{bmatrix} 1 & \Delta t \\ 0 & 1 \end{bmatrix}, \tag{7.27b}$$

where F_j^{PSI} and $\dot{F}_j^{PSI}$ are respectively the PSI scale-factor and its first derivative at the j-th time instant, and Δt is the duration of the filter update step. As usual, we assume that the state vector is a random variable whose stochastic part is determined by the covariance matrix $\mathbf{Q}$.
The measurement model is given by

$$z_j = F_j^{PSI} , \tag{7.28}$$

Therefore, at each time-step the filter estimates the state vector using the PSI scale-factor as a measurement.
The compensation schemes through which the filter measures the PSI scale-factor is represented in Figure 7.8 and it is resumed as follows:

1. Every two PSI shots, a piezo stage tilts the Raman retro-reflecting mirror by a quantity opposite to the corresponding CG measurement, $\mathbf{\Omega}_j^{CG} = \begin{pmatrix} \omega_{i,j}^{CG} & \omega_{2,j}^{CG} \end{pmatrix}^T$, plus a known bias rotation $\mathbf{\Omega}_j^T = (0 \;\; \omega_T)^T$.
2. Neglecting the bias and noise terms, the PSI output is given by the two-shot phase gradient $\mathbf{K}_j = F_j^{PSI}\left(\mathbf{\Omega}_j + \mathbf{\Omega}_T - \mathbf{\Omega}_j^{CG}\right)$, where $\mathbf{\Omega}_j$ is the vector containing the two-shot true angular rates.
3. Assuming that the error terms in the CG measurements are small compared to the true angular rate and to the known bias rotation, we can infer the PSI scale factor as $F_j^{PSI} \approx (k_{2,j} - k_{1,j})/\omega_T$, where $k_{i,j}$ is the i-th element of the vector $\mathbf{K}_j$.
4. The measurement F_j^{PSI} is given as input to the KF that filters out the noise and tracks the time-varying PSI scale-factor.

The adopted solution of tilting the retro-reflecting mirror at every PSI shot by an amount equal to the CG output is intended to render the compensation scheme independent of vehicle rotational dynamics, ensuring the robustness of the compensation scheme with respect to shot-to-shot variations in the true angular rate. Furthermore, this feedback

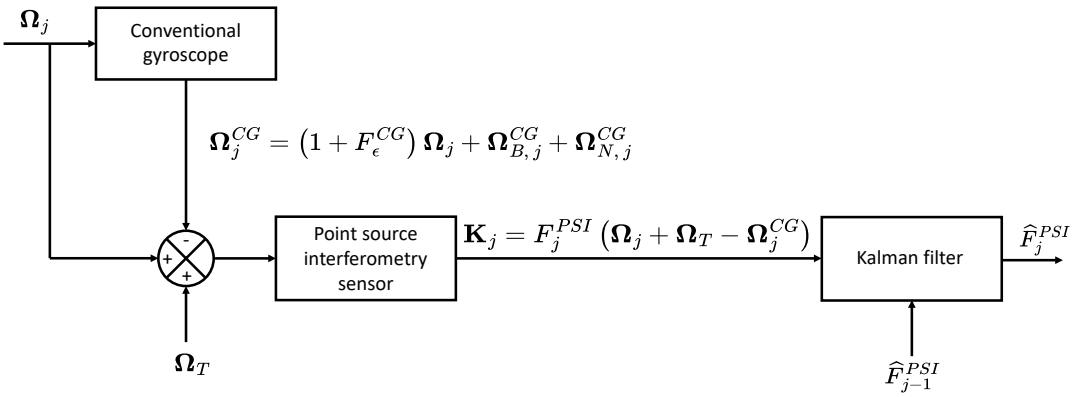

FIGURE 7.8: Compensation scheme for the real-time estimation of the PSI rotational scale-factor.

configuration enables PSI sensor operations in the high angular rate regime, where a complete loss of contrast would otherwise make retrieving the interferometric signal impossible. Another drawback is represented by the noise and stability of the piezo stage, which directly affects the measurement of the PSI rotational scale-factor. Any potential long-term drifts can be suppressed by alternating the sign of the applied bias rotation, while achieving nrad precision would ensure noise levels comparable to those of a navigation-grade CG [40].

The use of CG read-out as input for the mirror counter-rotation affects the measurement of the PSI scale-factor by introducing CG-dependent errors. In particular, assuming that the CG is affected by scale-factor error, bias and noise, we obtain

$$k_{2,j} - k_{1,j} = F_j^{PSI}\left[\omega_T - F_\epsilon^{CG}\left(\omega_{2,j} - \omega_{1,j}\right) - \left(\omega_{N,2,j} - \omega_{N,1,j}\right)\right], \tag{7.29}$$

where we assume that the bias and scale-factor variations of the CG occur at time-scales longer than the PSI cycling period. While, strictly speaking, the measurement of the PSI scale-factor is affected by the CG scale-factor error and noise, in practical terms, the dominant error source is the CG noise[3]. Therefore, a low-noise CG, such as a navigation-grade sensor, should be used in the compensation scheme.

We point out that in our modeling, we did not account for a potential misalignment between the CG and PSI sensor sensitive axes. However, for misalignment errors up to 0.1 mrad and angular accelerations up to 0.1 deg/s^2, the predominant source of error

[3]The amplitude of the noise of a navigation-grade CG is a few tenths of a degree per hour, while even for a typical scale-factor error of 50ppm and angular accelerations of 0.1deg/s^2, the error term in PSI scale-factor measurement is only 18mdeg/h.

is still represented by the CG noise.
An important aspect is represented by the feedback mechanism that translates the CG read-out into the Raman mirror rotation. In the case of a high free-evolution period, the low bandwidth of the PSI sensor introduces lag errors. Therefore, the rotation to be imposed on the Raman mirror should be computed using the sensitivity function formalism, similar to the approach taken with cold-atom accelerometers [30].

Finally, let us now make a few comments on the KF tuning parameters. The measurement covariance matrix $\mathbf{R}$ depends on the noise level of the CG and PSI sensor, and the precision of the piezo stage. The covariance matrix of the driving noise is assumed to be $\mathbf{Q} = \text{diag}[0\ \sigma_{\dot{F}}^2]$, where the tuning parameter $\sigma_{\dot{F}}$ is chosen such that it minimizes the variance of the KF innovation. For simplicity, we choose as initial condition $\mathbf{x}_0 = \begin{pmatrix} F_0^{PSI} & 0 \end{pmatrix}^T$, where F_0^{PSI} is the true value of the PSI scale-factor at the initial time.

7.4.2 Simulation results

To test the compensation scheme, we generate synthetic data for both the CG and the PSI sensor. The CG errors include white noise, with an rms value proportional to the sensor's angle random walk, bias and scale-factor instability, modeled as a first-order Gauss-Markov process [125]. The PSI scale-factor instability is due to the variation in the initial size of the atomic cloud and is modeled as a random walk process. We assume a quite large drift of $\sim 6\%$ per hour in the initial cloud size.
Synthetic data for a navigation-grade CG, characterized by an angle random walk of $5\text{mdeg}/\sqrt{\text{h}}$, a bias instability of 10mdeg/h, and a scale-factor instability of 50ppm, are generated at a sampling frequency of 200Hz. PSI data are generated at a realistic sampling frequency of 1Hz; therefore, the update frequency of the KF is 0.5Hz.
We assume that the true angular rate oscillates around a mean value of 1deg/s with a period of $\sim$ 30min, and that known bias rotation applied to the retro-reflecting mirror is equivalent to an angular velocity of 4deg/s .

Figure 7.9 displays the results of the simulations. The KF effectively tracks the PSI scale-factor error over a time span of 5h without introducing further instabilities, as demonstrated by the moving average of the residuals between the filter estimate and the ground truth. The histogram of the residuals is comparable to a normal distribution with a standard deviation of 230ppm and a mean of 2ppm. For completeness, we compare the angular rate tracking error with and without PSI scale-factor compensation. The compensation scheme effectively stabilizes the PSI scale-factor, preventing errors that could otherwise reach magnitudes as large as 0.5deg/s.

The stabilization of the rotational scale-factor is a necessary step towards integrating the PSI sensor into strapdown inertial navigation systems. Although the tilting of the

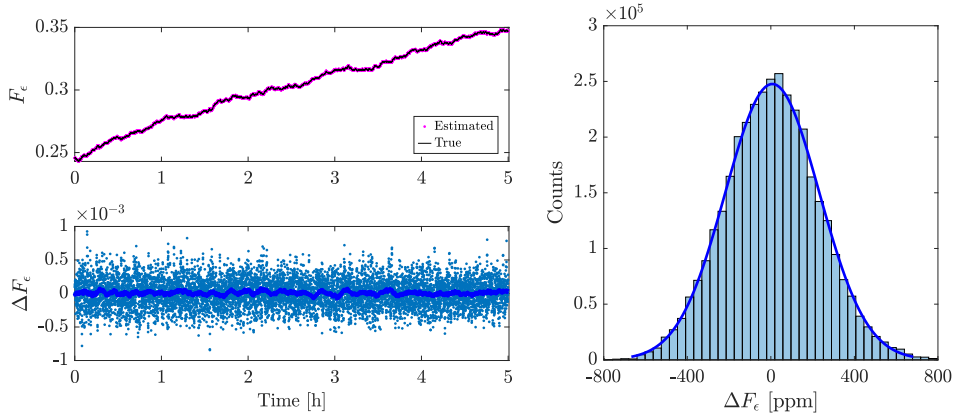

(A) KF tracking and tracking error

(B) Tracking error histogram

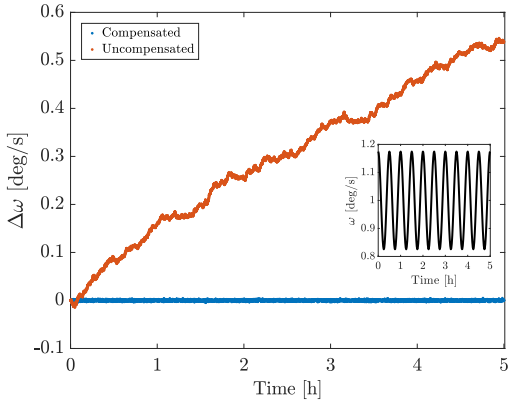

(C) Angular rate error

FIGURE 7.9: Simulated KF performance. Panel (A): KF tracking of the PSI rotational scale-factor error and tracking error. The thick blue line represents a 5min moving average. Panel(B): Histogram of the scale-factor tracking error and relative fitting. Panel (C): Angular rate error for the compensated and uncompensated PSI scale-factor error. The inset shows the true angular rate. Simulation parameters: navigation-grade CG with sampling frequency 200Hz, PSI sensor with sampling frequency 1Hz.

retro-reflecting mirror introduces errors that depend on the precision and accuracy of the piezo-stage, it is necessary to overcome total contrast loss in high-dynamic environments. We note that the presented scale-factor calibration scheme is based on a 'loosely-coupled' data-fusion architecture, in which an indirect quantity (i.e., the inferred angular rate) is used in the measurement model. However, we could envision a 'tightly-coupled' architecture that utilizes the PSI raw signal, i.e., the spatial atomic population distribution, as a filter observable. In this way, additional errors due to time-correlated noise are further suppressed, and fringe parameters are estimated in real-time.

Chapter 8

State detection and imaging system errors

At the end of the interferometer pulse sequence, the presence of atoms in one of the output ports is detected. The resulting interferometric signal is derived as a probability, determined by measuring the relative fraction of atoms occupying one of the Mach-Zehnder states. This probabilistic nature sets the ultimate uncertainty on phase estimation, and fluctuations in the number of detected atoms from shot to shot represent the performance limit of cold atom inertial (CAI) sensors [11].

Cloud-averaging and point source interferometry (PSI) are the two prevailing techniques employed for read-out in light-pulse atom interferometry. Cloud-averaging involves acquiring the signal by averaging the atomic probability distribution over space using a photodetector or a charge-coupled device (CCD). Consequently, scanning of the interferometric phase becomes necessary to extract the inertial measurement. In contrast, PSI directly captures the atomic distribution onto a CCD, enabling the extraction and analysis of spatial features.

According to the CAI sensor architecture, various state detection and imaging techniques can be implemented to obtain the interferometric signal. The most widely employed techniques include absorption imaging and fluorescence imaging, both of which are destructive methods [126]. Absorption imaging exploits variations in the intensity profile of the probe beam induced by the atomic distribution and represents the standard for imaging cold and ultra-cold atoms. On the other hand, fluorescence imaging allows the detection of atomic ensembles by means of the emission of scattered photons triggered by optical transitions. Far off-resonance methods, such as dark-ground imaging [127] and phase contrast imaging [128], offer quasi non-destructive detection and are widely used in the context of ultra-cold atoms where imaging low numbers of atoms requires a high signal-to-noise ratio [129].

Absorption imaging and fluorescence imaging are mostly used in atom interferometry applications with thermal ensembles, where the high number of atoms and low optical depths ensure robustness and easy experimental implementations [126]. For this reason, we will focus on these two imaging methods in the remaining part of the chapter.

Regardless of the chosen method, atomic clouds are imaged through the detection of emitted or missing photons. Fluctuations in the number of detected photons from shot to shot introduce a further noise source in the retrieval of the inertial-induced phase. Unlike atom shot noise, photon shot noise is classical and is not correlated to the probabilistic nature of the quantum measurement.

As observed in previous chapters, angular rates orthogonal to the Raman effective wave-vector induce a spatial modulation of the atomic distribution within the plane containing the angular rate vector. The spatial frequency of the atomic distribution is proportional to the applied angular rate, hence any distortions induced by the imaging system directly affect the inertial measurement. Moreover, motion of the atoms during the imaging causes blurring of the interferometric signal, further modifying the detected spatial frequency.

At the end of the imaging process, the photons detected by the CCD are converted into electrons, and the resulting signal undergoes amplification. This conversion and amplification process can introduce noise, which in turn leads to fluctuations in the effective number of detected atoms. Additionally, it's important to consider the finite number of pixels in the CCD that samples the atomic distribution, as this limits the maximum detectable spatial frequency and affects the uncertainty of the inertial measurement estimation.

The structure of the chapter is organized as follows:

1. We examine the influence of atom and photon shot noise, elucidating their physical origins and their effects upon the performance of a CAI sensor.

2. We introduce absorption imaging highlighting the working principles, the relation between the detected signal and the atomic distribution, and noise performance.

3. We describe fluorescence imaging with particular emphasis on the so-called "blue fluorescence" detection in which two probe beams in a ladder scheme trigger spontaneous emission of 420nm "blue" photons ensuring background-free images. We derive a multi-level atomic system in order to model the fluorescence signal and extract requirements on the stability of the imaging laser beams.

4. We investigate the influence of aberrations and distortions in the imaging system on the detected interferometric signal. This analysis encompasses the consequences arising from the finite size of the atomic cloud along the imaging beam

axis, as well as the misalignment between the CCD line-of-sight and the imaging beam axis.

5. We present and quantify the impact of motion blur that occurs during the imaging phase, resulting from factors such as the expansion of the atomic cloud, recoil heating, linear displacements, and vibrations.

6. We analyze the impact of the CCD on the performance of a CAI sensor in terms of finite number of pixels, non uniform response and noise.

8.1 Shot noise

8.1.1 Atom shot noise

The interferometric signal is obtained measuring the relative fraction of atoms in one of the two output ports of the interferometer. Hence, the detection of a single atom in the generic $|j\rangle$ state can be considered as a Bernoulli experiment characterized by a certain occurrence probability P_j. Assuming an ensemble of N total uncorrelated atoms, the probability to detect N_j atoms is a binomial distribution

$$P_{N_j} = \frac{N!}{N_j!(N-N_j)!} P_j^{N_j} (1-P_J)^{N-N_j}\,, \tag{8.1}$$

where the mean and the variance are, respectively, NP_j and $NP_j(1-P_j)$. If $N \to \infty$, the central limit theorem can be applied and the binomial tends to a Gaussian distribution with same mean and same variance

$$P_{N_j} \to \exp\left(-\frac{\left(P_j - \frac{N_j}{N}\right)^2}{2\frac{P_j(1-P_j)}{N}} \right), \tag{8.2}$$

where we rearranged the terms in a more suitable way. From Eq. (8.2) two conclusions can be drawn: first, the quantity N_j/N represents an unbiased estimator for P_j; second, the uncertainty on P_j estimation is characterized by a standard deviation

$$\sigma_{P_j} = \sqrt{\frac{P_j(1-P_j)}{N}}\,. \tag{8.3}$$

This result represents the atom shot noise, or quantum projection noise, and sets the ultimate performance of an atom interferometer operating with uncorrelated atoms [68]. The $1/\sqrt{N}$ scaling, known as standard quantum limit, could be further improved using

correlated atoms by means of squeezed states, thus approaching the $1/N$ Heisenberg limit [130].

8.1.2 Photon shot noise

Atomic distributions are imaged by means of coherent laser radiations though photon detection. The number of detected photons can be described by a Poisson distribution characterized by a standard deviation $\sqrt{N_P}$, where N_P is the average number of detected photons. Fluctuations in the number of detected photons from shot to shot constitute a noise source that, especially in the case of absorption imaging of atomic clouds characterized by low density, could overcome the atom shot noise levels [126].

8.2 Absorption imaging

Absorption imaging has garnered significant utilization over the years in ultra-cold atom imaging [131, 132], atomic clocks using ultra-narrow optical transitions [133], as well as CAI sensor applications [14, 44].
The interferometric signal is retrieved measuring the light absorbed by the atomic ensemble. In the paraxial approximation, the electric field propagating along the z-axis and passing through a medium of susceptibility χ is given by (see Appendix C)

$$E(\mathbf{r}_\perp, z_+) = \exp\left(i\frac{k_0}{2}\int_{z_-}^{z_+}\chi\left(\mathbf{r}_\perp, z\right)dz\right)E\left(\mathbf{r}_\perp, z_-\right), \tag{8.4}$$

where k_0 is the wave-number of the electric field and $\mathbf{r}_\perp$ defines the coordinates in the plane orthogonal to the propagation axis. For a two-level system atom interacting with a circularly polarized field, the susceptibility is given by [56]

$$\chi(\mathbf{r}_\perp, z) = \frac{\sigma_{sc}}{k_0}\left(\frac{i-2\bar{\delta}}{1+s+4\bar{\delta}^2}\right)n(\mathbf{r}_\perp, z), \tag{8.5}$$

with $\sigma_{sc} = 6\pi/k_0^2$ is the resonant scattering cross-section, $s = I/I_s$ is the saturation parameter (i.e. ratio between laser intensity and saturation intensity), $\bar{\delta} = \delta/\Gamma$ is the ratio between the laser detuning and the optical transition linewidth, and $n(r_\perp, z)$ is the atomic density. Assuming that the variations of the amplitude of the incident electric field in the transverse plane are negligible over the atomic cloud extension, we obtain the value of the electric field after the medium as

$$E(\mathbf{r}_\perp, z_+) = \exp\left(-\alpha(\mathbf{r}_\perp) + i\beta(\mathbf{r}_\perp)\right)E\left(\mathbf{r}_\perp, z_-\right), \tag{8.6}$$

with $\alpha(r_\perp) = (\sigma_{sc}\, n(\mathbf{r}_\perp)/2)/(1+s+4\bar{\delta}^2)$ attenuation factor, $\beta(\mathbf{r}_\perp) = -2\alpha(\mathbf{r}_\perp)\bar{\delta}$ phase factor, and $n(\mathbf{r}_\perp) = \int_{z_-}^{z_+} n(\mathbf{r}_\perp, z)dz$ column density. Hence, the atomic ensemble modifies both the amplitude and phase of the laser radiation.
In terms of intensity, the differential equation that describes the propagation of the light through a medium is given by the Beer-Lambert law (see Appendix C)

$$\frac{\partial I}{\partial z} = -k_0\, \mathrm{Im}\{\chi(\mathbf{r}_\perp, z)\}\, I\,, \tag{8.7}$$

and integrating the above equation from z_- and z_+ we obtain

$$(1+4\,\bar{\delta}^2)\, OD(\mathbf{r}_\perp) + s_0\left(1 - e^{-OD(r_\perp)}\right) = \sigma_{sc}\, n(\mathbf{r}_\perp)\,, \tag{8.8}$$

where $OD = -\ln\left(I_{obj}/I_0\right)$ is the optical depth, $s_0 = I_0/I_s$, and we rename $I_- \to I_0$ and $I_+ \to I_{obj}$, respectively, the intensity of the laser field before and after the atomic medium, i.e. the object intended to be imaged. Eq. (8.8) shows that measurement of the optical depth is needed in order to retrieve the spatial atomic distribution, and that in general the relation between the two quantities is not linear. Solution of the transcendental Eq. (8.8) can be obtained in terms of the Lambert $\mathcal{W}$-function [134]

$$OD(\mathbf{r}_\perp) = \frac{\sigma_{sc}\, n(\mathbf{r}_\perp) - s_0}{1+4\,\bar{\delta}^2} + \mathcal{W}\left(\frac{s_0}{1+4\,\bar{\delta}^2}\exp\left(\frac{s_0 - \sigma_{sc}\, n(\mathbf{r}_\perp)}{1+4\,\bar{\delta}^2}\right)\right). \tag{8.9}$$

This equation has a general validity regardless the atomic density value and the saturation parameter. For weakly absorbing medium, Eq. (8.8) can be linearized

$$OD(\mathbf{r}_\perp) \approx \frac{\sigma_{sc}\, n(\mathbf{r}_\perp)}{1+s_0+4\,\bar{\delta}^2}\,. \tag{8.10}$$

On-resonance and for a weak probe beam intensity, $OD(\mathbf{r}_\perp) \approx \sigma_{sc}\, n(\mathbf{r}_\perp)$. Figure 8.1 shows the error in the estimation of the atomic density when using the linearized expression of Eq. (8.10) for different optical depths and saturation parameters. In light pulse atom interferometry applications, it is common to detect clouds of $N = 10^6$ atoms with a size of 1-5mm. Consequently, the maximum optical density is in the range 0.042-0.017 for $s_0 = 0.1$, leading to errors below the 1% level in the estimation of the atomic density when using the linearized expression of Eq. (8.10).

8.2.1 Laser noise requirements

In order to reconstruct the atomic distribution using absorption imaging, a minimum of two images is necessary: one capturing the laser beam without the presence of atoms,

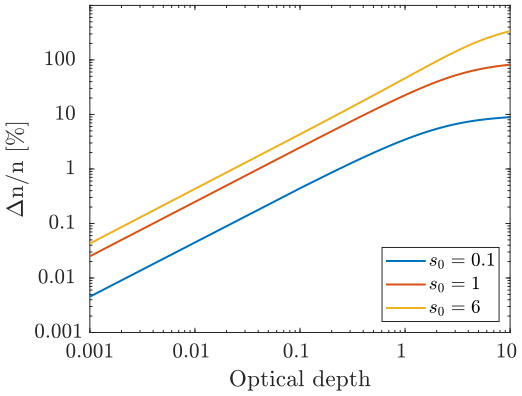

FIGURE 8.1: Percentage error in the estimation of the atomic density when using the linearized model of Eq. (8.10) instead of the complete model of Eq. (8.8), for different saturation parameters and on-resonance ($\bar{\delta} = 0$).

and another with the atoms included. Hence, any fluctuations in the laser intensity or frequency leads to errors in the estimated column density. Assuming that the laser intensity and frequency noise are uncorrelated and described by normal distributions with standard deviations σ_{I_0} and σ_δ, the uncertainty of the optical depth is given by

$$\sigma_{OD}^2 = \left(\frac{\partial OD}{\partial I_0}\right)^2 \sigma_{I_0}^2 + \left(\frac{\partial OD}{\partial \bar{\delta}}\right)^2 \sigma_{\bar{\delta}}^2 + \frac{1}{2}\left(\frac{\partial^2 OD}{\partial \bar{\delta}^2}\right)^2 \sigma_{\bar{\delta}}^4 , \tag{8.11}$$

where the second order term in $\bar{\delta}$ is dominant near resonance. In the case of Gaussian atomic density, the optical depth uncertainty can be related to interferometric signal uncertainty via Eq. (8.10)

$$\sigma_{P_j} = \left(\frac{1 + s_0 + 4\bar{\delta}^2}{\sigma_{sc}}\right)\left(\frac{2\,\pi\,\sigma_{cl}^2}{N}\right)\sigma_{OD} , \tag{8.12}$$

where P_j is the probability to detect the atom in the $|j\rangle$ state of the interferometer, and σ_{cl} is the width of the atomic cloud. Using Eq. (8.11) we get

$$\sigma_{P_j}^2 \approx \frac{P_j^2}{(1 + s_0 + 4\,\bar{\delta}^2)^2}\left[s_0^2\,\frac{\sigma_{I_0}^2}{I_0^2} + 64\,\sigma_{\bar{\delta}}^2\left(\bar{\delta}^2 + \frac{\sigma_{\bar{\delta}}^2}{2}\right)\right] , \tag{8.13}$$

where we neglected terms of order higher than $o(1/\bar{\delta}^4)$.
Figure 8.2 shows the requirements for laser intensity and frequency noise necessary to achieve uncertainty of the interferometric signal at the atom shot noise level. In the low saturation regime ($s_0 = 0.1$) and close to resonance, a relative intensity noise $\sigma_{I_0}/I_0 <$ 1% and a frequency noise $\sigma_\delta <$ 100kHz are required to achieve atom shot noise level uncertainty. Unlike intensity noise, meeting the frequency noise requirement could be

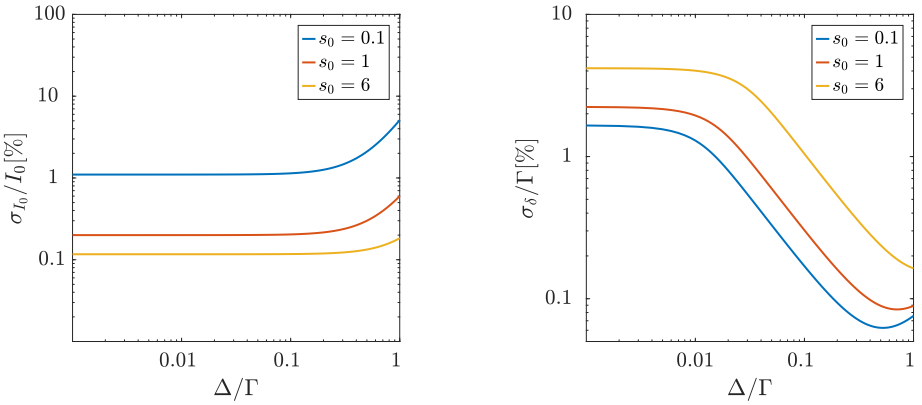

(A) Intensity noise requirement

(B) Frequency noise requirement

FIGURE 8.2: Requirements for the laser noise parameters in order to achieve below atom shot noise level uncertainty. Simulation parameters: total number of detected atoms $N = 10^6$, interferometric signal $P_j = 1/2$.

challenging due to the necessity of employing laser systems with narrow linewidths [135].

In the previous analysis a number of simplifications have been adopted. First, the Beer-Lambert law describes the atomic response to the imaging beam as an ensemble of uncorrelated single particles. In the context of light pulse atom interferometry operating with thermal clouds, this assumption is reasonable because the atomic density is such that the absorption/emission of photons from nearby atoms can be neglected [136]. Second, the decrease in the absorption signal due to atomic fluorescence has been neglected because absorption signal prevails over fluorescence signal at low atomic densities[127]. Third, a simple two-level system model has been assumed, thus neglecting the multi-level structure due the hyperfine splitting. In reality, the presence of multiple levels induces losses that determine a reduction of the effective scattering cross-section and, hence, of the absorption imaging signal [137]. A further reduction of the scattering cross-section is due to variations in the saturation intensity induced by fluctuations of the laser polarisation and stray magnetic fields [131].

8.2.2 Photon shot noise requirement

The intensity of the imaged beam is proportional to the number of incident photons. Therefore, the optical depth can be expressed as $OD = -\ln(N_{P,obj}/N_{P,0})$, where $N_{P,obj}$ and $N_{P,0}$ are, respectively, the number of detected photons with and without the atomic medium. Recalling that photon shot noise follows Poisson statistics, we can express the optical depth uncertainty as

$$\sigma_{OD} = \sqrt{\frac{1}{N_{P,obj}} + \frac{1}{N_{P,0}}}, \tag{8.14}$$

and using the definition of optical depth, $N_{P,0} = N_{P,obj}\, e^{OD}$, in combination with Eq. (8.12), we obtain the uncertainty over the interferometric signal

$$\sigma_{P_j} = \left(\frac{1 + s_0 + 4\bar{\delta}^2}{\sigma_{sc}}\right)\left(\frac{2\,\pi\,\sigma_{cl}^2}{N}\right)\frac{\sqrt{1 + e^{-OD}}}{\sqrt{N_{P,obj}}}\,. \tag{8.15}$$

At this point we can compute number of photons that have to be detected in order to achieve the atom shot noise limit. For an average probability $P_j \approx 1/2$ the atom shot noise is $\sigma_{P_j} = 1/(2\sqrt{N})$, and

$$N_{P,obj} \geq \left(\frac{1 + s_0 + 4\bar{\delta}^2}{\sigma_{sc}/2}\right)^2 \frac{(2\,\pi\,\sigma_{cl}^2)^2}{N}\left(1 + e^{-OD}\right)\,. \tag{8.16}$$

We observe that as the atomic density decreases, the number of photons needed to reach the atom shot noise limit increases. Therefore, for atomic clouds characterized by low atomic densities, we may need to detect a number of photons that exceeds the capability of the CCD. For a cloud of size $\sigma_{cl} = 2.5$mm containing $N = 10^6$ atoms of ^{85}Rb and imaged by a resonant pulse with a saturation parameter $s_0 = 0.1$, we need to detect $N_{P,obj} \approx 1.7 \times 10^{11}$ photons in order to achieve the atom shot noise limit. Assuming a pixel well depth of 5×10^4 photons per pixel, the CCD must have a number of pixels $N_{pix} \geq 3.5 \times 10^6$ in the area covered by the atomic cloud. With a detection area equal to a circle with radius $3\,\sigma_{cl}$, the pixel dimension should be $d_{pix} \leq 7\mu$m. The limit on the maximum number of detectable photons imposed by the pixel well depth translates into a constraint on the minimum number of pixels required. Therefore, achieving noise performance below the atom shot noise limit could be challenging for cold-atom sensors operating with absorption imaging because the number of required pixels could be too high.

8.3 Fluorescence imaging

Fluorescence detection has proven to be the main detection technique in light-pulse atom interferometry applications due to its simplicity of implementation and high signal-to-noise ratio. Two main detection methods have been developed: sequential detection and simultaneous detection.

In sequential detection, atomic states at the output port of the interferometer are not separated in space, and their detection occurs one after the other through a temporal sequence of three laser pulses tuned to different optical transitions [20]. Briefly, a first pulse tuned to the cooling transition detects atoms in the upper ground state. Normalization of the atomic populations is achieved by a second repump pulse followed by a third cooling pulse.

In contrast, simultaneous detection uses a relatively long pusher pulse, resonant with one of the atomic states, to operate spatial separation between the two output ports of the interferometer [138]. Subsequently, a repump pulse followed by a cooling pulse is used to simultaneously image both atomic states. Detecting both output ports with a single pulse allows for the rejection of common-mode noise, thereby relaxing the stability requirements of the lasers. However, the use of simultaneous detection in PSI applications is limited by the contrast loss and blurring induced by the long pusher pulse that deforms one of the two atomic clouds via recoil heating.
While fluorescence detection is the most common technique in cloud-averaging configurations, absorption imaging is preferred for detecting the spatial distribution of atomic populations. In conventional methods based on infrared transitions, the detection beam shares the same wavelength as the fluorescence signal, and spurious light scattered from surfaces results in extremely noisy images [139]. In this context, background-free fluorescence detection represents a promising method for imaging atomic ensembles, combining high-signal features with virtually zero background noise [140].

8.3.1 Background-free fluorescence imaging

In background-free fluorescence detection, the fluorescence signal is at a different wavelength compared to the detection beam. Consequently, by filtering the optical signal, it is possible to isolate the atoms' contribution from the background. For this reason, achieving background-free imaging requires a multi-photon transition process that pumps the atoms into an excited state characterized by a transition line different from that of the pumping fields.
A step-wise two-photon ladder transition is necessary to achieve background-free fluorescence with ^{85}Rb atoms. Referring to the fine structure depicted in Figure 8.3, a first 780nm laser beam couples the $5S_{1/2}$ ground state with the $5P_{3/2}$ intermediate state. Subsequently, a second 776nm laser couples the $5P_{3/2}$ state with the $5D_{5/2}$ state, where a fraction of the atoms decay back emitting 'red' photons. Another fraction of atoms decays to the $5S_{1/2}$ state via the $6P_{3/2}$ intermediate state, emitting 'blue' photons at 420nm.

In a similar manner to what we have done in the case of absorption imaging, we compute the noise requirements of the imaging lasers to reach the atom shot noise level. Due to the multi-level structure involved in the generation of blue photons, we develop a numerical model based on optical Bloch equations (OBEs) to compute the fluorescence signal.
The model accounts for the hyperfine structure, including the effect of losses in dark

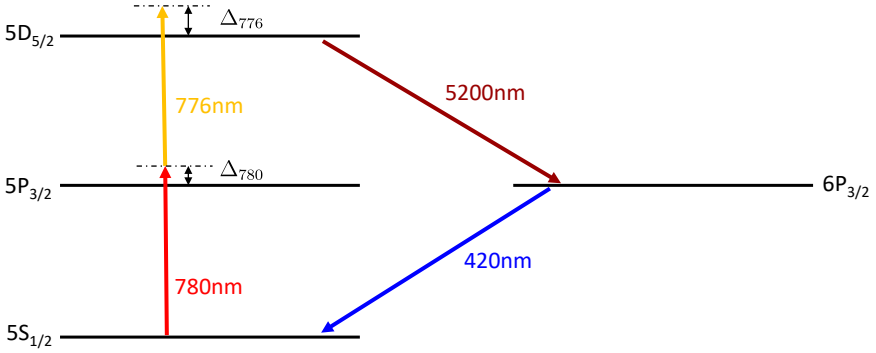

FIGURE 8.3: Laser scheme to generate 420nm photons in ^{85}Rb. We represented only the fine structure manifold for simplicity.

states, which are not negligible. In our analysis, we neglect the magnetic Zeeman substructure and the Doppler broadening due to the relative velocity of the atoms with respect to the laser frame. Additionally, we assume that the intensity experienced by the atoms across the cloud is constant. Further details of the numerical model are provided in Appendix D. Briefly, we integrate the optical Bloch equations (OBEs) over time and calculate the number of blue scattered photons per atom as $N_{420} = \int_0^{t_p} \Gamma_{420}\, \rho_{6P_{3/2}}(t)\, dt$, where Γ_{420} is the natural linewidth of the $5S_{1/2} \rightarrow 6P_{3/2}$ transition, $\rho_{6P_{3/2}}$ is the overall atomic population in the $6P_{3/2}$ level, and t_p is the pulse duration. Clearly, N_{420} is a function of the laser parameters $\mathbf{p}_L = [s_{780}\ s_{776}\ \Delta_{780}\ \Delta_{776}]^T$, where s_j and Δ_j are, respectively, the saturation parameter and the detuning of the j-th closed transition.
Requiring that the contribution of laser noise to the fluorescence signal be less than or equal to the atom shot noise is equivalent to the condition $(\sigma_F)_{\sigma_{\mathbf{p}_L}} \leq (\sigma_F)_{\sigma_N}$, where $F = N_{420}\, N$ represents the total blue fluorescence signal and N denotes the number of detected atoms. Recalling that $\sigma_N = \sqrt{N}$ [126], we compute the requirements on the laser noise solving numerically the condition

$$\sqrt{\left(\frac{\partial N_{420}}{\partial \mathbf{p}_L}\right)^2 \sigma^2_{\mathbf{p}_L} + \frac{1}{2}\left(\frac{\partial^2 N_{420}}{\partial \mathbf{p}_L^2}\right)^2 \sigma^4_{\mathbf{p}_L}} \leq \frac{N_{420}}{\sqrt{N}}\,, \tag{8.17}$$

where we assumed that the laser noise parameters are uncorrelated and follow a normal distribution.
Figure 8.4 displays the results of the numerical simulations for a pulse duration of $t_p = 100\mu$s and a total number of atoms $N = 10^6$. The plots depict isolines representing the 1% relative intensity noise and the 5% normalized frequency noise, at which performance at the atom shot noise level is achieved [1]. These isolines delineate boundaries in the parameter space within which atom shot noise level performance

[1] The intensity noise plot is obtained in resonant conditions, while the frequency noise plot is obtained for fixed saturation parameters.

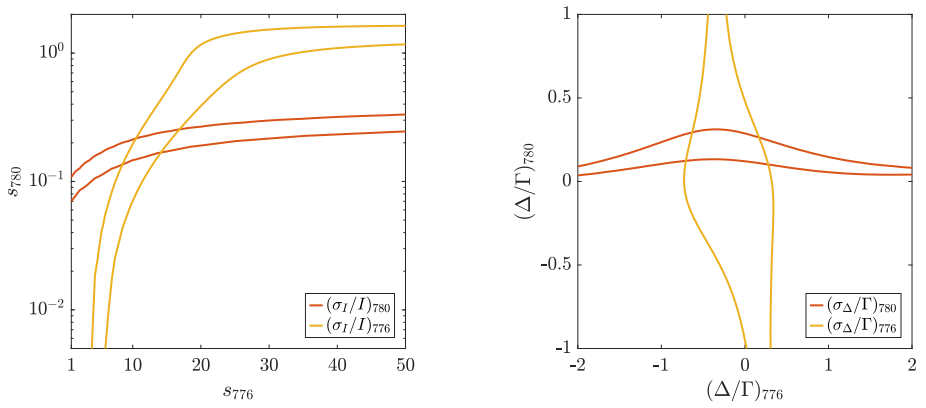

(A) Intensity noise (B) Frequency noise

FIGURE 8.4: Requirements on the noise parameters of the detection laser system to achieve atom shot noise limit for blue fluorescence imaging. We assume a pulse duration of 100μs and a number of detected atoms $N = 10^6$. Panel (A): the isolines represent the 1% relative intensity noise for the 780nm and 776nm lasers in resonant conditions. Panel (B): the isoline represent the 5% normalized detuning noise for the 780nm and 776nm lasers for $s_{780} = 0.15$ and $s_{776} = 10$.

can be achieved with relative intensity noise higher than 1% and normalized frequency noise higher than 5%. The 1% relative intensity noise bounds delineate an area centered at (12.4, 0.2) with dimensions 5.9×0.1. In contrast, the 5% normalized frequency noise bounds (corresponding to $\sigma_{\Delta_{776}} = 21$kHz, and $\sigma_{\Delta_{780}} = 300$kHz) delineate an area centered at $(-0.2, 0.2)$ (corresponding to (86, 1200) kHz) with dimensions 0.92×0.20 (corresponding to 397×1200 kHz).

For the conditions analyzed, our analysis highlights two results: firstly, due to losses in dark states, the maximum signal-to-noise ratio is achieved when the 780nm and 776nm lasers are slightly blue-detuned and red-detuned, respectively. Secondly, achieving atom shot noise level performance requires the use of a 776nm laser with a narrower linewidth compared to the 780nm laser. This result was somewhat expected, as the 780nm transition is 14 times wider than the 776nm transition.

8.4 Imaging aberrations and distortions

Aberrations and distortions of the interferometric signal induced by imperfection of the imaging system are inevitable. In this context, Fourier optics is a great theoretical tool to analyse the impact of optical elements, reducing the problem to the formulation of response functions in spatial frequency domain.

The light scattered by the object (i.e. the atomic distribution) can be described by a scalar field $u_{obj}(\mathbf{r}_\perp, z)$, where z represents, as usual, the propagation axis and $\mathbf{r}_\perp$ the coordinates in the transverse plane. The imaged field $u_{img}(\mathbf{r}_\perp, z)$ is the result of the action of the optical system on the object field

$$\hat{u}_{img}(\mathbf{k}_\perp, k_0) = H_{sys}(\mathbf{k}_\perp, k_0)\, \hat{u}_{obj}(\mathbf{k}_\perp, k_0)\,, \tag{8.18}$$

where the hat symbol indicates the Fourier transform, and $H_{sys}(\mathbf{k}_\perp, k_0)$ is the transfer function that describes the optical system. The linearity in the frequency domain is a direct consequence of the fact that the object, consisting of many point sources, is imaged using a coherent light source. The resulting image is a superposition of the spherical wavefronts originating from these point sources, and, therefore, the convolution between the object field and the optical system [141].
Most of the optical elements can be described by the combination of four fundamental operators. In paraxial approximation [142]

1. Scaling operator $\longrightarrow V[m]u(\mathbf{r}_\perp, z) = u(m\mathbf{r}_\perp, z)$.
2. Fourier transform operator $\longrightarrow \mathcal{F}u(\mathbf{r}_\perp, z) = \int_{-\infty}^{+\infty} u(\mathbf{r}_\perp, z)\, e^{-i\mathbf{k}_\perp \mathbf{r}_\perp} d\mathbf{k}_\perp$.
3. Quadratic phase operator $\longrightarrow Q[-\frac{1}{f}]u(\mathbf{r}_\perp, z) = \exp\left(-\frac{ik_0\mathbf{r}_\perp^2}{2f}\right)u(\mathbf{r}_\perp, z)$.
4. Free-propagation operator $\longrightarrow R[\Delta z]u(\mathbf{r}_\perp, z) = \frac{\exp(ik_0\Delta z)}{i\lambda\Delta z} \exp\left(i\frac{k_0\mathbf{r}_\perp^2}{2\Delta z}\right) \circledast u(\mathbf{r}_\perp, z)$.

Each operator corresponds to distinct fundamental properties. The scaling operator characterizes the magnification imparted by the optical system, while the quadratic phase and free-propagation operators describe, respectively, the propagation through a thin lens of focal length f and over a distance Δz. Note that in absence of optical elements, the object field acquires a quadratic phase due to free-space propagation.

8.4.1 Defocus and magnification

The atomic distribution is usually imaged by means of a system of two relay lenses. Calling d_1, d_2, and d_3, respectively, the distances between the object and the first lens, the two lenses, and the last lens and the imaging plane

$$u_{img}(\mathbf{r}_\perp) = R[d_3]\, Q[-1/f_2]\, R[d_2]\, Q[-1/f_1]\, R[d_1]\, u_{obj}(\mathbf{r}_\perp)\,, \tag{8.19}$$

with f_1 and f_2 are, respectively, the focal length of the first and second lens. Assuming $d_2 = f_1 + f_2$, and using algebra operator properties [142], we obtain

$$u_{img}(\mathbf{r}_\perp) = V[-f_2/f_1]\, R[\Delta z_{def}]\, u_{obj}(\mathbf{r}_\perp)\,, \tag{8.20}$$

with $\Delta z_{def} = d_3 + d_1 - (f_1 + f_2)$. The first term in the right-hand-side of Eq. (8.20) indicates that the image is a scaled inverted version of the object with a magnification

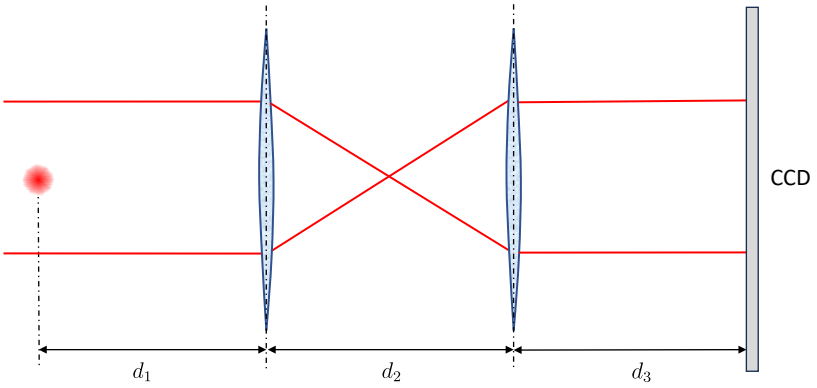

FIGURE 8.5: Relay lens system used to image the atomic cloud onto a CCD.

$m = -f_2/f_1$. When the absolute value of the magnification differs from one, the frequency modulation of the imaged atomic distribution differs from the original, leading to a scale-factor error in the angular rate signal of the PSI sensor. As a result, calibration becomes necessary. The second term in the right-hand-side of Eq. (8.20) indicates that when the atomic cloud is out of focus, a quadratic phase proportional to Δz_{def} arises. Using the definition of free-propagation operator and assuming for simplicity that $f_1 = f_2$, we obtain the imaged field in the frequency domain

$$\hat{u}_{img}(\mathbf{k}_\perp) = \underbrace{\exp\left(ik_0\Delta z_{def}\right)\exp\left(-i\frac{\mathbf{k}_\perp^2\,\Delta z_{def}}{2k_0}\right)}_{H_{def}(\mathbf{k}_\perp,\,\Delta z_{def})}\hat{u}_{obj}(\mathbf{k}_\perp)\,, \tag{8.21}$$

with $H_{def}(\mathbf{k}_\perp, \Delta z_{def})$ the defocus transfer function.
Since the atomic distribution is proportional to the scattered field, we can express the imaged column density as

$$\hat{n}_{img}(\mathbf{k}_\perp) = H_{def}(\mathbf{k}_\perp, \Delta z_{def})\hat{n}_{obj}(\mathbf{k}_\perp)\,. \tag{8.22}$$

By considering an initial Gaussian atomic distribution in phase-space, along with modulation of the atomic in the x direction caused by an angular rate, we are able to calculate the PSI phase map as follows:

$$\Phi_{PSI}(x,y) = k_{\omega,x}x\left[1 - \frac{\Delta z_{def}^2}{2\,k_0^2\,\sigma_f^6}\left(2\sigma_f^2 + k_{\omega,x}^2\sigma_f^4 - x^2 - y^2\right)\right] + o(\Delta z_{def}^3)\,, \tag{8.23}$$

with σ_f size of the atomic distribution in the transverse plane at the detection stage and $k_{\omega,x}$ rotation-induced wave-vector. A defocus results in three distinct effects: scale-factor error, scale-factor non-linearity, and spatial non-linearity within the phase map. For $\lambda = 780\text{nm}$, $\sigma_f = 3\text{mm}$, $\Delta z_{def} = 1\text{mm}$, and $k_{\omega,x} = 6000\text{rad/m}$, the scale-factor and scale-factor non linearity are, respectively, -0.4ppb and -30.8ppb.

8.4.2 Thickness effect

The lens system collects the light scattered by an object that has a finite extension along the imaging axis. This induces a defocus effect even if the centroid of the object is perfectly focused. The 3-D transfer function for a lens system with a finite numerical aperture $NA = \sin\theta$ is given by [143]

$$H_{3D}(f_\perp, f_z) = \Theta\left(-f_\perp + \frac{\sin\theta}{\lambda}\right)\delta\left(\frac{f_z\lambda}{4\sin^2\frac{\theta}{2}} + \frac{1}{4\sin^2\frac{\theta}{2}} + \frac{f_\perp^2\lambda^2}{2\sin^2\theta}\right), \tag{8.24}$$

with f_z spatial frequency along the imaging axis, $f_\perp = \sqrt{f_x^2 + f_y^2}$ spatial frequency in the transverse plane, λ the wavelength of the scattered light, θ the maximum half-angle of the cone of light entering or leaving the lens system, $\Theta(\dots)$ and $\delta(\dots)$, respectively, the Heaviside and Dirac functions.
The light scattered by an object characterized by a Gaussian density distribution along the z-axis with a standard deviation σ_z is given by

$$\hat{u}_{obj}(f_\perp, f_z) \propto \exp\left(-2\pi^2\sigma_z^2 f_z^2\right)\hat{n}_{obj}(f_\perp). \tag{8.25}$$

The imaged scalar field in real space can be obtained using the inverse Fourier transform

$$u_{img}(\mathbf{r}_\perp, z) = \mathcal{F}^{-1}\{H_{3D}(f_\perp, f_z)\hat{u}_{obj}(f_\perp, f_z)\} \propto \mathcal{F}^{-1}\{H_{thick}(f_\perp)\hat{n}_{obj}(f_\perp)\}, \tag{8.26}$$

with

$$\begin{aligned} H_{thick}(f_\perp) = \frac{\sin^2\frac{\theta}{2}}{4\pi}\Theta\left(-f_\perp + \frac{\sin\theta}{\lambda}\right)\exp\left[\frac{iz\sin^2\frac{\theta}{2}}{\lambda}\left(\frac{f_\perp^2\lambda^2}{2\sin^2\theta} - \frac{1}{4\sin^2\frac{\theta}{2}}\right)\right]\dots \\ \exp\left[-\frac{32\pi^2\sigma_z^2\sin^4\frac{\theta}{2}}{\lambda^2}\left(\frac{f_\perp^2\lambda^2}{2\sin^2\theta} - \frac{1}{4\sin^2\frac{\theta}{2}}\right)^2\right], \end{aligned} \tag{8.27}$$

and considering the leading term in $f_\perp$, we obtain

$$H_{thick}(\mathbf{k}_\perp) \approx \hat{\Omega}\,\Theta(-|\mathbf{k}_\perp| + k_0 NA) \exp\left(-\frac{\mathbf{k}_\perp^4 \sigma_z^2}{8\, k_0^2\, \gamma(\hat{\Omega})}\right), \tag{8.28}$$

where $\hat{\Omega} = \frac{\sin^2 \frac{\theta}{2}}{4\pi}$ is the fraction of solid angle intercepted by the lens system and $\gamma(\hat{\Omega}) = 1 - 2\hat{\Omega}^2 + 4\hat{\Omega}^4$ is a corrective factor for large numerical apertures. The Heaviside term in Eq. (8.28) represents the diffraction limit of a lens system with numerical aperture NA, while the exponential term accounts for the blurring due to the thickness of the atomic cloud along the imaging axis.
The maximum spatial frequency induced by an angular rate is three orders of magnitude smaller than the diffraction limit , hence we can consider the Heaviside function equal to one. We compute the PSI phase map assuming a rotation-induced modulation of the atomic distribution along the x-axis

$$\Phi_{PSI}(x, y) = k_{\omega,x} x \left[1 - \frac{\sigma_z^2}{2\, k_0^2\, \gamma(\hat{\Omega})\, \sigma_f^6} \left(2\,\sigma_f^2 + k_{\omega,x}^2 \sigma_f^4 - x^2 - y^2\right)\right] + o(\sigma_z^3)\,. \tag{8.29}$$

This result shows that an atomic cloud with a finite size along the imaging axis induces a defocus error with an equivalent defocus length $(\Delta z_{def})_{eq} = \sigma_z \gamma(\hat{\Omega})^{-\frac{1}{2}}$. For $\lambda = 780\text{nm}$, $\sigma_z = \sigma_f = 3\text{mm}$, $NA = 0.45$, and $k_{\omega,x} = 6000\text{rad/m}$, the scale-factor and scale-factor non linearity are, respectively, -2ppb and -305ppb.

8.4.3 Misalignment of the CCD line-of-sight

Regardless of the technique used, the imaging process is equivalent to an effective integration of the atomic distribution along the CCD line-of-sight. A misalignment between the CCD line-of-sight and the Raman effective wave-vector can induce contrast decays in the imaged atomic distribution when coupled with an angular rate [40].
Assuming an initial Gaussian phase-space distribution, the imaged atomic distribution in the rotated CCD frame is

$$n_{img}(x_r, y_r, z_r) = \frac{1}{(2\,\pi)^{\frac{3}{2}}\, \sigma_f^3} \exp\left[-\frac{x_r^2 + y_r^2 + z_r^2}{2\sigma_f^2}\right] \left[P_0 + \frac{C_0}{2} \cos\left(k_{\omega,y}\, y_r\right)\right], \tag{8.30}$$

with x_r and y_r axes orthogonal to CCD line-of-sight z_r, σ_f size of the atomic cloud at the detection stage $k_{\omega,y}$ rotation-induced phase gradient due to an angular rate. The wave-vector $k_{\omega,y}$ is orthogonal to the Raman effective wave-vector acting along the z-axis. Assuming a small misalignment $\theta_x \ll 1$ between the CCD line-of-sight and the Raman effective wave-vector, and integrating along it leads to an interferometric signal with contrast

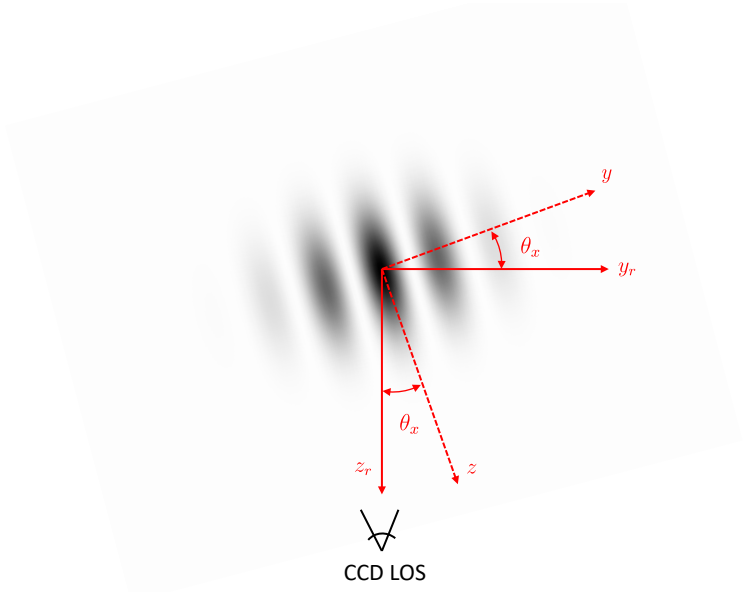

FIGURE 8.6: Misalignment between the line-of-sight of the CCD (z_r) and the Raman effective wave-vector direction (z).

$$C = C_0 \exp(-k_{\omega,y}^2 \sigma_f^2 \theta_x^2)\,. \tag{8.31}$$

For $k_{\omega,y} = 6000\text{rad/m}$, $\sigma_f = 3\text{mm}$ and $\theta_x = 10\text{mrad}$, the contrast of the imaged interferometric signal is $\sim 3\%$ less than the case with no misalignment; hence, alignment at a level better than 1mrad is necessary to achieve contrast decay of less than 1%.

8.4.4 Aberrations

Optical aberrations in imaging systems are due to the fact that the wavefront of the scalar field describing light propagation is not spherical at the exit pupil [143, 144]. Aberrations can be due to defects and imperfections in the optics as well as to geometric misalignment (e.g. object not in focus).
The transfer function that models optical aberrations is given by [144]

$$H_{ab}(k_x, k_y) = \exp\left[i\, k_0\, W\left(\frac{k_x}{k_0}\, z,\, \frac{k_y}{k_0}\, z\right)\right] \tag{8.32}$$

with $W(x, y)$ the aberration function that describes the deviation of the wavefront from the ideal sphere in the transverse plane, z is the distance of the imaging plane from the exit pupil, k_0 is the wave-number associated to the light field. The aberration function is commonly expressed as a series expansion in the form of Zernike polynomials.

As an example we compute the effect of a tilt aberration over the imaged interferometric signal in presence of a rotation-induced modulation of the atomic density. The tilt aberration function is given by

$$W(x,y) = \alpha_x \frac{x}{R} + \alpha_y \frac{y}{R}\,, \tag{8.33}$$

with α_j the peak-to-valley deviation of the actual wavefront from the ideal spherical one, in the generic j-th direction and in units of λ, and R maximum distance over which the phase map is evaluated.
Given the tilt transfer function $H_{tilt}(k_x,k_y) = \exp\left[i\,z\,(\alpha_x k_x + \alpha_y k_y)/R\right]$, and a Gaussian atomic distribution modulated in space along the x-axis by a rotation-induced wavevector $k_{\omega,x}$, we compute the imaged atomic distribution

$$\begin{aligned} n_{img}(x,y) = \frac{1}{2\pi\sigma_f^2} \exp\left[-\frac{\left(x+\alpha_x z/R\right)^2 + \left(y+\alpha_y z/R\right)^2}{2\sigma_f^2}\right] \dots \\ \left[P_0 + \frac{C}{2}\cos\left(k_{\omega,x}x + \frac{k_{\omega,x}\alpha_x z}{R}\right)\right]\,. \end{aligned} \tag{8.34}$$

A tilt aberration has two effects: it causes an apparent shift of the centre of the atomic cloud and induces an anisoinertia bias on the acceleration signal. For instance, assuming $k_{\omega,x} = 6000\text{rad/m}$, $z = 5\text{cm}$, $R = 1\text{cm}$, $\alpha_x = \lambda/10$, with $\lambda = 780\text{nm}$, a bias phase shift of $\sim 2\text{mrad}$ is produced.

To provide comprehensive information, we present in Table 8.1 the transfer function and the bias PSI phase map for optical aberrations modeled using Zernike polynomials up to the third order. Assuming small aberrations, the bias phase map can be approximated through a Taylor expansion. Consequently, we include in the Table only the leading order from the series expansion. The defocus term is not reported in the Table because it has been treated separately in the previous subsection.

8.4.5 Distortions

While optical aberrations are the result of imperfections in the optical system and occur, for example, when light rays passing through the system are not perfectly focused, resulting in blurred image or loss of image sharpness, optical distortions result from non-uniform magnification of an image across its field of view. Optical distortion manifest as geometric distortions of an image. They can be caused, for instance, by the shape of the system's lens or by the curvature of the image plane.
Optical distortions can be described as geometric transformations of the object according to [145]

Aberration type	Transfer function	Bias phase map
Tilt	$\exp\left[i\frac{z\,(\alpha_x\,k_x+\alpha_y\,k_y)}{R}\right]$	$\frac{k_{\omega,x}\,\alpha_x\,z}{R}$
Astigmatism y	$\exp\left[i\frac{2\,z^2\,\alpha_y\,k_x\,k_y}{k_0\,R^2}\right]$	$\frac{4\,k_{\omega,x}\,\alpha_y^2\,z^2}{k_0^2\,R^4\,\sigma_f^6}x(y^2-\sigma_f^2)$
Astigmatism x	$\exp\left[i\frac{z^2\,\alpha_x\,(k_y^2-k_x^2)}{k_0\,R^2}\right]$	$-\frac{2\,k_{\omega,x}\,\alpha_x^2\,z^4}{k_0^2\,R^4\,\sigma_f^6}x(2\sigma_f^2+k_{\omega,x}^2\sigma_f^4+y^2-x^2)$
Trefoil y	$\exp\left[i\frac{z^3\,\alpha_y\,k_x(-k_x^2+3k_y^2)}{k_0^2\,R^3}\right]$	$-\frac{k_{\omega,x}\,\alpha_y\,z^3}{k_0^2\,R^3\,\sigma_f^4}(k_{\omega,x}^2\sigma_f^4+3y^2-3x^2)$
Coma y	$\exp\left[i\frac{z\,\alpha_y\,k_x(-2\,k_0^2\,R^2+3\,z^2\,(k_x^2+k_y^2))}{k_0^2\,R^3}\right]$	$\frac{\alpha_y\,z\,k_{\omega,x}}{k_0^2\,R^3\,\sigma_f^4}A_{c,x}(x,y)$
Coma x	$\exp\left[i\frac{z\,\alpha_x\,k_y(-2\,k_0^2\,R^2+3\,z^2\,(k_x^2+k_y^2))}{k_0^2\,R^3}\right]$	$-\frac{6\,\alpha_x k_{\omega,x}\,z^3}{k_0^2\,R^3\,\sigma_f^4}xy$
Trefoil x	$\exp\left[i\frac{z^3\,\alpha_x\,k_y(k_y^2-3k_x^2)}{k_0^2\,R^3}\right]$	$\frac{6\,\alpha_x k_{\omega,x}\,z^3}{k_0^2\,R^3\,\sigma_f^4}xy$

TABLE 8.1: Transfer function and bias phase map induced by optical aberrations in the imaging system modelled as Zernike polynomials with $A_{c,x} = -2\,k_0^2\,R^2\,\sigma_f^4 + 3\,z^2(4\sigma_f^2+k_{\omega,x}^2\sigma_f^4-y^2-3x^2)$.

$$\mathbf{r}_{img} = f(\mathbf{r})\,\mathbf{r}_{obj}\,, \tag{8.35}$$

with $f(\mathbf{r})$ distortion function, that is usually modelled as a polynomial expansion. For instance, the first order radial distortion is modelled by $f(x,y) = 1 + a(x^2+y^2)$, with $a > 0$ in the case of barrel distortion and $a < 0$ in the case of pincushion distortion.

8.5 Motion blur effect

Relative motion between the atomic distribution and the imaging system results in blurring effects with consequent loss of contrast and variations of the PSI phase map with respect to the stationary case.

8.5.1 Cloud expansion

A first source of motion blur is represented by the expansion of the atomic cloud, which can be attributed to either its finite velocity width or recoil heating. During the imaging process an atom at an initial position $\mathbf{r}_\perp$ is displaced by a quantity $\mathbf{\Delta r}_\perp(t)$. As a consequence, the final atomic distribution is given by the convolution between the initial

distribution, $n_{obj}(\mathbf{r}_\perp)$, and the displacement one, $\Delta n_{obj}(\mathbf{r}_\perp(t))$. In reality, the imaging system detects an average between the initial and final distribution given by

$$\langle n_{img}(\mathbf{r}_\perp)\rangle = \frac{1}{t_{det}}\int_0^{t_{det}} n_{img}(\mathbf{r}_\perp, t)dt\,, \tag{8.36}$$

with $n_{img}(\mathbf{r}_\perp, t) = n_{obj}(\mathbf{r}_\perp) \circledast \Delta n_{obj}(\mathbf{r}_\perp(t))$, and t_{det} total duration of the detection time. Assuming as initial and displaced distributions, respectively, a Gaussian with standard deviation σ_f modulated by a rotation-induced wave-vector, $k_{\omega,\perp}$, and a Gaussian with standard deviation $\Delta\sigma(t)$, we can compute the final distribution

$$n_{img}(\mathbf{r}_\perp, t) = \frac{e^{-\frac{\mathbf{r}_\perp^2}{2\bar{\sigma}_f^2(t)}}}{2\,\pi\,\bar{\sigma}_f^2(t)}\left[P_0 + \frac{C(t)}{2}\cos\left(\bar{F}(t)\,\mathbf{k}_{\omega,\perp}\cdot\mathbf{r}_\perp\right)\right]\,, \tag{8.37}$$

with

$$\begin{aligned}\bar{\sigma}_f^2(t) &= \sigma_f^2 + \Delta\sigma_f^2(t)\,,\\ C(t) &= C_0\,\exp\left(-\frac{k_{\omega,\perp}^2\,\bar{F}(t)\,\Delta\sigma_f^2(t)}{2}\right),\\ \bar{F}(t) &= 1 - \frac{\Delta\sigma_f^2(t)}{\bar{\sigma}_f^2(t)}\,.\end{aligned} \tag{8.38}$$

The expansion of the atomic cloud during the imaging induces a contrast decay and a reduction of the rotation-induced phase gradient. However, for detection times of the order of hundreds of microseconds and angular rates of the order of thousands of radians/meter the contrast decay is negligible and $\bar{\sigma}_f \approx \sigma_f$. Hence, cloud expansion mainly affects the PSI phase map.

Two mechanisms, finite temperature associated with velocity width and recoil heating, govern the expansion of the atomic distribution. In the former case, the expansion is characterized by $\Delta\sigma_f^2(t) = \Delta\sigma_{exp}^2(t) = \sigma_v^2\,t^2$, where σ_v represents the width of the Maxwell-Boltzmann velocity distribution. In the latter case, the expansion can be correlated with the photon scattering rate. Specifically, atoms undergo a random walk due to the recoil induced by spontaneous emission of photons when interacting with a resonant laser field [132].
Following [146], the mean square of the transverse velocity component due to photon scattering is given by

$$\Delta\sigma_{v,H}^2(t) = \frac{2}{3}v_{rec}^2 N_P(t)\,, \tag{8.39}$$

where the factor $2/3$ accounts for the motion in the two direction x and y, v_{rec} is the recoil velocity and $N_P(t)$ is the number of scattered photons in the time t that can be expressed in function of the scattering rate $N_P(t) = \int_0^t R_{sc}(t')dt'$. For a two-level system atom $R_{sc} = \frac{\Gamma}{2}\frac{s_0}{1+s_0+4\bar{\delta}^2}$, and therefore the increase in the size of the atomic cloud due to recoil heating is given by

$$\Delta\sigma_H^2(t_p) = \left(\int_0^{t_p} \Delta\sigma_{v,H}(t)dt\right)^2 = \frac{8}{27} R_{sc}\, v_{rec}^2\, t_p^3\,, \tag{8.40}$$

with t_p duration of the imaging pulse. Unlike the free-expansion case, the increase in cloud width resulting from photon emission is proportional to the cube of the time, providing clear evidence of the random walk process.
Combining Eqs. (8.37) and (8.36), and assuming negligible contrast decay, we obtain the detected PSI phase map

$$\Phi_{PSI}(\mathbf{r}_\perp) = \mathbf{k}_{\omega,\perp} \cdot \mathbf{r}_\perp \left[1 - \frac{1}{\sigma_f^2}\left(\frac{\Delta\sigma_{exp}^2(t_{det})}{3} + \frac{\Delta\sigma_H^2(t_p)}{4}\right)\right], \tag{8.41}$$

where the $1/3$ and $1/4$ factors account for the average process of the imaging system. The increase in cloud size due to free-expansion is dependent on the total detection time t_{det}, whereas the expansion resulting from recoil heating depends only on the fraction of detection time in which the laser is on.
Figure 8.7 shows the scale-factor error of the angular rate signal of a PSI sensor operating with a cloud of ^{85}Rb atoms with a size of $\sigma_f = 3$mm at the beginning of the detection stage, and a temperature $\mathcal{T} = 10\mu$K. Both the total scale-factor error and the individual contributions resulting from free expansion and recoil heating are reported. Specifically, for recoil heating, we examine the scattering of 780nm 'red' photons caused by a resonant laser beam with a saturation parameter of $s_0 = 0.1$. We consider both a two-level system and a simple multi-level model that incorporates losses due to the hyperfine structure [126]. In the low saturation regime and for the given pulse lengths, assuming a two-level system results in an overestimation of the scale-factor error $\lesssim 17\%$ compared to the multi-level model.
The error model of Eq. (8.40) highlights the dependency of the scale-factor error on the intensity and detuning of the imaging beam. Consequently, any drift in the laser intensity and frequency induces a scale-factor instability. Assuming a two-level system atom and applying error propagation we obtain a simple approximation for the gyroscope scale-factor instability given by

$$\sigma_{SF,g} \approx \frac{2}{27}\frac{v_{rec}^2\, t_p^3}{\sigma_f^2}\frac{\Gamma/2}{(1+s_0+4\bar{\delta}^2)^2}\left[s_0^2\frac{\sigma_{I_0}^2}{I_0^2} + 64\,\sigma_{\bar{\delta}}^2\left(\bar{\delta}^2 + \frac{\sigma_{\bar{\delta}}^2}{2}\right)\right]^{1/2}, \tag{8.42}$$

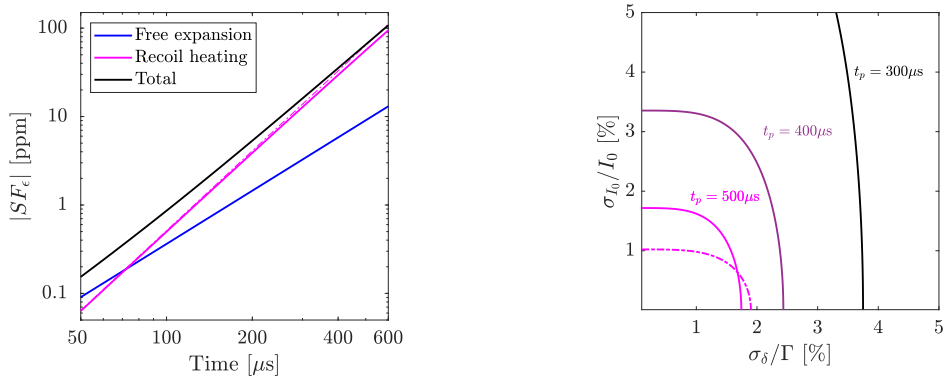

(A) Scale-factor error (B) Scale-factor instability

FIGURE 8.7: Effect of the cloud expansion on the gyroscope scale-factor. Panel (A): Scale-factor error of the angular rate signal induced by the expansion of the cloud during the detection. The dashed magenta line assumes a two-level system, while the continuous magenta line takes into account the losses due to the hyperfine structure. Panel (B): Scale-factor instability due to intensity and frequency drift of the imaging beam. The continuous curves represent the 1ppm isolines for $s_0 = 0.1$ and different pulse duration. The dashed magenta curve represents the 1ppm isoline for $t_p = 500\mu$s and saturation parameter $s_0 = 0.2$.

where we neglected terms higher than $1/\bar{\delta}^4$. Figure 8.7 shows the 1ppm scale-factor instability isolines for pulse length $t_p = 300$, 400, 500μs, saturation parameter $s_0 = 0.1$, resonant laser, and cloud dimension at the beginning of the detection $\sigma_f = 3$mm. As expected, the longer the pulse and the higher the beam intensity the more stringent is the requirement on laser intensity and frequency stability in order to achieve scale-factor instability below the 1ppm level. Hence, the imaging beam intensity and the pulse duration is a trade-off between the scale-factor and photon shot noise requirement.

8.5.2 Mean motion

So far we analyzed blur due to cloud expansion. In this Subsection we are interested in the effect of the mean motion of the atomic cloud during the imaging. Displacement of the cloud in the plane orthogonal to the imaging axis determines blurring of the detected atomic distribution.
Using the method of moments reported in Ref. [147], the mean motion blur transfer function can be obtained as

$$H_{mmb}(k_j) = \sum_{n=0}^{\infty} \left(\frac{1}{t_{det}} \int_0^{t_{det}} x_j^n(t) dt \right) \frac{(-ik_j)^n}{n!}, \tag{8.43}$$

where $x_j(t)$ indicates the relative motion of the object with respect to the imaging system in the transverse plane along the generic jth direction, k_j is the associated spatial angular frequency, t_{det} id the total detection time.

Assuming a linear constant-velocity motion $x_j(t) = v_j\, t$, the transfer function can be found to be [147]

$$H_{mmb}(k_j) = \mathrm{sinc}\left(k_j \frac{v_j\, t_{det}}{2}\right) \exp\left(-i\, k_j\, v_j \frac{t_{det}}{2}\right). \tag{8.44}$$

For a Gaussian atomic distribution modulated by a rotation-induced phase gradient along the same direction of the constant-velocity motion we obtain a PSI phase map

$$\Phi_{PSI}(x_j) = k_{\omega,j} x_j \left(1 - \frac{\pi^2\, v_j^2\, t_{det}^2}{12\, \sigma_f^2}\right) - k_{\omega,j}\, v_j\, \frac{t_{det}}{2} + o(v_j^3). \tag{8.45}$$

Motion in the transverse plane induces both a scale-factor error on the angular rate signal and an anisoinertia bias on the acceleration signal. The induced error is maximum when the motion occurs along the same direction of the rotation-induced phase gradient and zero when orthogonal to it.

8.5.3 Classical fringes

Interference patterns resulting from the scattering of the imaging beam due, for instance, to the presence of dust on optical elements can further distort the detected atomic distribution [132, 148]. In absorption imaging these classical fringes are common mode between the reference image and the image with the atoms and, resulting in their cancellation. However, in presence of a relative motion in the transverse plane due, for instance, to mechanical vibrations or air turbulence, the fringes may not completely cancel out, leading to errors. Nevertheless, fringe-removal algorithms can be applied to reduce this source of error [148, 149]. On the other hand, classical fringes do not affect background-free fluorescence imaging since the resulting signal is at a different wavelength with respect to the probe beams.

8.6 CCD error sources

The CCD represents the final component in the imaging system chain and it impacts the performance of a CAI sensor through two main mechanisms: the finite number of pixels and noise sources.

8.6.1 Finite number of pixels

The CCD is an array of photosensitive elements, known as pixels, which acts as an image sampler. As a result, the detected atomic distribution is discrete and generally

depends on factors such as the size, shape, and number of pixels.
A reduced pixel count in an image leads to undersampling increasing the likelihood of encountering aliasing artifacts, particularly when capturing or displaying high-frequency details. Application of the Whittaker-Shannon sampling theorem leads to determination of the upper bound of the pixel dimension [144]

$$d_{pix,j} \leq \frac{1}{2\, f_{j,max}}\,, \tag{8.46}$$

where, $f_{j,max}$ is the maximum spatial frequency of the atomic distribution modulation in the j-th direction and we assumed that the pixel pitch (i.e., the distance between the centroid of two consecutive pixels) is equal to the pixel size. In the hypothesis of spatial domain extending in the range $-L_x \leq x \leq L_x$, $-L_y \leq y \leq L_y$, and maximum frequency proportional to the maximum rotation-induced phase gradient, we obtain

$$N_{pix} \geq \frac{4}{\pi^2}\, L_x\, L_y\, (k_{\omega,x})_{max} (k_{\omega,y})_{max}\,, \tag{8.47}$$

with N_{pix} the number of pixels required to sample the atomic distribution without significant distortions. For instance, with $L_x = L_y = 10\text{mm}$, $(k_{\omega,x})_{max} = (k_{\omega,y})_{max} = 6000\text{rad/m}$, at least $N_{pix} = 1460$ pixels are required, corresponding to a pixel size $d_{pix} \leq 260\mu\text{m}$.
Nevertheless, shape and pixel size directly affect the imaged atomic distribution introducing distortions. For a rectangular pixel of dimension $d_{pix,x}$ and $d_{pix,y}$, the transfer function is given by [150]

$$H_{pix}(k_x, k_y) = \frac{d_{pix,x}\, d_{pix,y}}{\Delta_{pix,x}\, \Delta_{pix,y}}\, \text{sinc}\left(\frac{k_x\, d_{pix,x}}{2}\right) \text{sinc}\left(\frac{k_y\, d_{pix,y}}{2}\right), \tag{8.48}$$

with $\Delta_{pix,x}$ and $\Delta_{pix,y}$, respectively, the pixel pitch in the x and y direction. We compute the PSI phase map assuming a square pixel with pitch equal to the size and Gaussian atomic distribution modulated by a rotation-induced phase gradient along the x direction

$$\Phi_{PSI}(x, y) = k_{\omega,x} x \left(1 - \frac{\pi^2 d_{pix}^2}{12\sigma_f^2}\right) + o(d_{pix}^3)\,. \tag{8.49}$$

We observe that the finite resolution of the CCD introduces blurring in the PSI signal, which leads to a scale-factor error in the gyroscope signal similar to the mean motion in the transverse plane. To achieve a scale-factor error of less than 10ppm with an atomic cloud of size $\sigma_f = 3\text{mm}$, a pixel dimension $d_{pix} \leq 10\mu\text{m}$ is required. Hence, the

constraint on pixel size imposed by the scale-factor error requirement is more stringent than the Whittaker-Shannon criterion.

8.6.1.1 Fitting error

The detected angular rate and acceleration in CAI sensors with PSI read-out are obtained by fitting the phase map with a plane. The angular rate and acceleration are inferred, respectively, from the fitted phase gradient and offset.
Given a signal of the form

$$S(x_j) = \theta_0 + \theta_1 x_j + \delta S_j \,, \tag{8.50}$$

where θ_0 and θ_1 are the parameters that we want to estimate and δS_j is the noise, it is possible to compute the uncertainty of the least-square fitting of the signal with a straight line as [151]

$$\sigma_S^2(x_j) = \frac{\sigma^2}{N}\left[1 + \frac{1}{\sigma_x^2}(x_j - \bar{x})^2\right] , \tag{8.51}$$

with N number of data-points in which the signal $S(x_j)$ is known, σ is the standard deviation of the noise, here assumed as Gaussian, $\bar{x} = \frac{1}{N}\sum_{j=1}^{N} x_j$ is the data-point average, and σ_x the uncertainty on the data-point distribution. Assuming a uniform data-point distribution in the interval $[-L/2,\, L/2]$, we obtain

$$\sigma_x^2 = \frac{(N^2-1)\Delta x^2}{12} \,, \tag{8.52}$$

with Δx spacing between the x_j points. Substitution of Eq. (8.52) in (8.51) and assuming that $N \gg 1$ leads to

$$\sigma_S^2 = \frac{\sigma^2}{N} + \frac{\sigma^2}{N^3}\,\frac{12}{\Delta x^2}\, x_j^2 \,. \tag{8.53}$$

Renaming $N \to N_{pix}$, $\sigma_S \to \sigma_{pix}$ and considering equal spacing between data-points, i.e. $\Delta x = L/N_{pix}$ we obtain

$$\sigma_S^2 = \underbrace{\frac{\sigma_{pix}^2}{N_{pix}}}_{\text{Phase offset fitting uncertainty}} + \underbrace{\frac{\sigma_{pix}^2}{N_{pix}}\,\frac{12}{L^2}}_{\text{Phase gradient fitting uncertainty}} x_j^2 \,, \tag{8.54}$$

with N_{pix} number of pixels, and σ_{pix} phase map noise at pixel level. Hence, the phase offset and phase gradient fitting uncertainties are given respectively by

$$\sigma_{\theta_0} = \frac{\sigma_{pix}}{\sqrt{N_{pix}}}\,, \tag{8.55}$$

$$\sigma_{\theta_1} = \frac{\sqrt{12}}{L}\,\frac{\sigma_{pix}}{\sqrt{N_{pix}}}\,, \tag{8.56}$$

As expected, in the hypothesis of uncorrelated pixel noise, the phase offset and phase gradient uncertainties scale as $1/\sqrt{N_{pix}}$.

8.6.2 Pixel cross-talk

In an ideal scenario, photo-electrons produced within the silicon material should remain confined within the designated pixel. However, due to thermal diffusion and the presence of weak electric fields within the active region of a pixel, these signal electrons tend to diffuse into adjacent pixels, resulting in undesired cross-talk [152]. The modelling of this effect is complex and depends on the particular CCD architecture. For a front-illuminated CCD, the cross-talk transfer function can be obtained modelling charge diffusion in the silicon substrate [153, 154]

$$H_{ct}(k) = \frac{1 - \left(\frac{\exp\left(-\alpha\, d\right)}{1+\alpha\, L_0\,(1+k^2\, L_0^2)^{-1/2}}\right)}{1 - \left(\frac{\exp\left(-\alpha\, d\right)}{1+\alpha\, L_0}\right)}\,, \tag{8.57}$$

with α absorption coefficient of the substrate, L_0 the diffusion length, and d the CCD depletion depth [2]. A typical value for the diffusion length of electrons in silicon is around of the order of tenths of microns, while the rotation induced wave-vector is at most thousands of radians per meter. As a consequence, the term $k^2 L_0^2 \ll 1$ and convolutions of the cross-talk transfer function with the atomic distribution at the end of the interferometer sequence leads to the following PSI phase map

$$\Phi_{PSI}(x) = k_{\omega,x} x \left(1 - \frac{\alpha\, L_0^3\,/(\exp\left(\alpha\, d\right) - 1)}{\sigma_f^2}\right) + o(L_0^4)\,, \tag{8.58}$$

where we assumed a Gaussian atomic distribution modulated by a rotation induced wave-vector along the x-axis. As expected, the cross-talk induces blurring of the atomic

[2] The depletion depth refers to the region near the surface of the CCD where the majority of the charge carriers are depleted due to the applied voltage. This depletion region forms a potential barrier that collects the generated charge carriers and prevents them from spreading to neighboring pixels.

distribution with a consequent scale-factor error on the gyroscope signal proportional to the diffusion length. The scale-factor error depends strongly on the absorption coefficient which, for silicon, is a monotonic decreasing function of the light wavelength - for instance, at $\lambda = 780$nm, the absorption coefficient at room temperatures is $\alpha = 1030\text{cm}^{-1}$ [155]. Assuming a diffusion length $L_0 = 100\mu$m and a cloud size $\sigma_f = 3$mm, a thick layer with a depletion depth of $d = 50\mu$m would be required to achieve a scale-factor error of $\sim$ 66ppm. In contrast, using blue-fluorescence signal at $\lambda = 420$nm ($\alpha = 52700\text{cm}^{-1}$), a negligible scale-factor error would be produced even for thin silicon layers with depletion depth below 10μm. The criticality of cross-talk at near infrared wavelengths is strictly connected to the lower absorption. When light penetrates deeper into the CCD material, it increases the probability of charge carriers being generated outside the depletion region and, thus, spreading into adjacent pixels. However, increasing the depletion depth leads to higher diffusion lengths, thus worsening electron diffusion. Consequently, there exists an optimal thickness that maximizes absorption while minimizing the diffusion length.
The variations in temperature determine changes in the optical properties of silicon, resulting in scale-factor drifts. Figure 8.8 shows the scale-factor error of the gyroscope for various temperature variations ΔT when exposed to radiation with a wavelength of $\lambda = 780$nm. In this analysis, a reference temperature $\mathcal{T}_0 = 300\mu$K is assumed, and the absorption coefficient is modeled with a temperature dependent power law of the type $\alpha(\mathcal{T}) = \alpha(\mathcal{T}_0)(\mathcal{T}/\mathcal{T}_0)^b$, where the coefficient b depends on the wavelength of the radiation [155].
To limit scale-factor errors at near-infrared wavelengths caused by pixel cross-talk, a possible solution is to adopt back-illuminated CCDs or insert an epitaxial layer above the silicon substrate [154]. With a back-illuminated architecture, the incident light passes directly through the silicon substrate, thereby avoiding reflections and scattering due to the metal electrode layer (i.e., pixel layer) and reducing the probability of charge generation in neighboring pixels. Additionally, the electron flux in the silicon substrate is lower compared to the front-illuminated architecture due to absorption in the undepleted region, further reducing the likelihood of charge diffusion and pixel cross-talk [153]. The addition of an epitaxial layer to front-illuminated CCDs mimics the back-illumination process, leading to a reduction of the electron flux and, consequently, of the effective diffusion length.

8.6.3 CCD noise

Three main noise sources can be distinguished in a CCD based to the level of illumination: read noise, shot noise and fixed pattern noise [152]. Read noise does not depend on the illumination conditions and is generated by so-called dark currents as a result of thermal charge generation. Shot noise, on the other hand, depends on the random time of photon arrival at the photosensitive element and follows a $N_p^{1/2}$ scaling, where

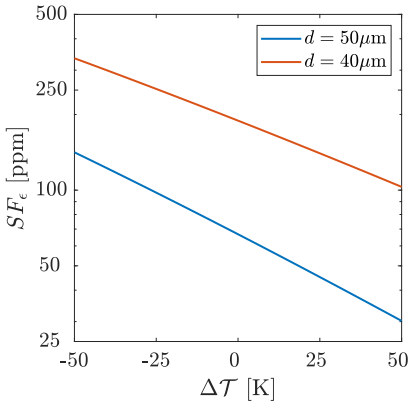

FIGURE 8.8: Effect of temperature variation on gyroscope scale-factor error due to pixel cross-talk in front-illuminated CCD for two values of the depletion depth d. Simulation parameters: cloud size $\sigma_f = 3$mm, laser wave-length $\lambda = 780$nm, diffusion length $L_0 = 100\mu$m.

N_p represents the average number of photons, due to Poisson statistics. As the illumination levels increase, fixed pattern noise becomes the dominant noise source. This noise is associated with variations in pixel sensitivity caused by fabrication defects and exhibits a linear dependency on N_p.

Chapter 9

Performance analysis

In the previous chapters, we identified and analyzed some of the error sources that affect cold-atom inertial sensors. In this chapter, we are interested in providing a *summa*, linking the various error sources to sensor performance.

When it comes to inertial sensor performance, different metrics are available. Sensor performance can be grouped into two macro-categories: short-term sensitivity and long-term stability. Short-term sensitivity is related to high-frequency noise and is mostly quantified by the noise power density. In the context of inertial sensors, it primarily impacts short-term navigation errors and initial alignment. In contrast, long-term stability pertains to the low-frequency drifts affecting medium and long-term navigation, predominantly expressed in terms of scale-factor and bias instability [1]. Long-term stability is particularly critical in inertial sensing, directly influencing position accuracy and thus determining the grade and application scenarios of inertial navigation systems [156, 6].

The performance of a cold-atom inertial sensor generally depends on system parameters, environmental conditions, and architecture. In this chapter, we will focus on the performance of a cold-atom inertial sensor based on point-source interferometry (PSI). This choice is due to the fact that the PSI configuration facilitates the automatic discrimination of the interferometric phase shift induced by angular rates (rotational signal) from the phase shift induced by specific forces (acceleration signal).

The inherent capability of PSI to detect the spatial phase distribution rather than an 'integrated' phase, and the fundamentally different nature of the rotational signal (embedded in the phase gradient) and the acceleration signal (embedded in the phase offset), pose two challenges. The first challenge lies in the requirement of an *ad hoc* error modeling for PSI, which often differs from conventional cold-atom sensors. The second challenge is to understand how an error source affects both the rotational and acceleration signals.

A comprehensive and detailed assessment of the performance of a cold-atom inertial sensor strongly depends on the operating conditions and the particular choice of

system parameters. In the same manner, the detailed evaluation of navigation performance strongly depends on the application scenario, the type of adopted inertial mechanization and the particular inertial sensor configuration. Extensive Monte Carlo simulations are usually adopted and include a trajectory simulator, an inertial navigation system implementation and a sensor block error model [4]. Therefore, conducting a detailed analysis relative to a specific case is beyond the scope of this chapter, as our focus is on establishing general trends, limitations, and trade-offs.

In this chapter we limit our quantitative analysis to the performance of a cold-atom inertial sensor using ^{85}Rb as the designated atomic species. The projected sensor performance is computed by means of a simple analytical model that summarizes the results in previous chapters. Although interesting, we do not translate the sensor performance to the navigation performance as we reserve this type of analysis for future investigations.

9.1 Inertial sensor performance

9.1.1 Short-term sensitivity

As reported in Chapter 8, the ultimate sensitivity of a cold-atom inertial sensor operating with thermally uncorrelated atoms is represented by the atom shot noise. Therefore, we derive the expressions for the ultimate short-term sensitivity of the rotational and acceleration signals.
The derivation of the shot-term sensitivity for the acceleration signal is straightforward. From Eq. (8.55) we obtain

$$STS_a = \frac{\sigma_{pix}}{\sqrt{N_{pix}}} \frac{\sqrt{T_c}}{SF_a}, \tag{9.1}$$

where T_c is the sensor cycling period and $SF_a = k_{\text{eff}}\, T^2$ is the accelerometer scale-factor. The derivation of the short-term sensitivity for the rotational signal involves a bit more work. Starting from Eq. (8.56) we derive the single-axis sensitivity as

$$STS_\omega = \frac{\sigma_{pix}}{\sqrt{N_{pix}}} \frac{\sqrt{12}}{L} \frac{\sqrt{T_c}}{SF_g}, \tag{9.2}$$

with $SF_g = 2\, k_{\text{eff}}\, T^2 / T_{ex}$ the cold-atom gyroscope scale-factor. Assuming that the detection area includes 99.9% of the atoms, i.e. $L = 6\, \sigma_f \approx 6\, \sigma_v\, T_{ex}$, we get

$$STS_\omega = \frac{\sqrt{3}}{3} \frac{\sigma_{pix}}{\sqrt{N_{pix}}} \frac{\sqrt{T_c}}{2\, k_{\text{eff}}\, \sigma_v\, T^2}. \tag{9.3}$$

The quantity σ_{pix} represents the phase map noise at the pixel level and can be expressed as a function of the interferometric signal uncertainty: $\sigma_{pix} = 2\,\sigma_{P_j}/C$, where C is the fringe contrast [157]. For the atom shot noise, the uncertainty σ_{P_j} depends on the number of detected atoms per pixel. Assuming for simplicity that the interferometric signal is equal to the average value $P_j \approx 1/2$, we obtain the ultimate short-term sensitivity for the acceleration signal

$$STS_a = \frac{1}{C\sqrt{N_A}}\,\frac{\sqrt{T_c}}{k_{\text{eff}}\,T^2} \tag{9.4}$$

and for the rotational signal

$$STS_\omega = \frac{\sqrt{3}}{3\,C\sqrt{N_A}}\,\frac{\sqrt{T_c}}{2\,k_{\text{eff}}\,\sigma_v\,T^2}\,, \tag{9.5}$$

with N_A number of total detected atoms.
As expected, the short-term sensitivity of the PSI acceleration signal is equal to that of cold-atom inertial sensors operating with cloud-averaging detection, since in both cases the acceleration signal is determined by a phase offset [158].
Modulo a numeric factor of $\sqrt{3}/3$, the PSI rotational short-term sensitivity is similar to that of cloud-launched gyroscopes, with the launch velocity being replaced by the atomic velocity width. This reflects the inherent feature of the PSI scheme to exploit the thermal expansion of the atomic cloud to infer rotations. We note that the dependence on the atomic thermal velocity constitutes a fundamental limit for PSI gyroscopes. For cloud temperatures a few micro-Kelvin, the velocity width is one to two orders of magnitude lower than the launch velocity in cloud-launched gyroscopes [50, 15]. Therefore, the ultimate short-term sensitivity of a PSI gyroscope is lower than that of atomic gyroscopes using conventional read-out schemes. Increasing the width of the thermal velocity distribution or the free-evolution time to improve the short-term sensitivity leads to rapid loss of contrast and consequent worsening of gyroscope performance. For these reasons, the use of optimal control to design large momentum transfer pulse sequences appears as a possible solution to improve the rotational short-term sensitivity [159].

The noise sources affecting short-term sensitivity can be categorized into two main groups: those dependent on the free-evolution time and those independent of it. Noise sources dependent on the free-evolution time are associated with the phase accumulated by the atomic wave-function during the interferometric sequence. Examples include linear vibrations, pointing jitter, and magnetic field noise. Noise sources independent of the free-evolution time arise during state detection and imaging, or are limited to the duration of the Raman pulses. Examples of these include Raman intensity, phase and frequency noise, as well as detection laser intensity and frequency fluctuations.

TABLE 9.1: Raman and imaging laser noise requirements to achieve accelerometer performance at the atom shot noise level. Simulation parameters: Raman pulse duration $\tau = 5\mu$s, Raman mirror distance 10cm, resonant imaging pulse with saturation parameter $s_0 = 0.1$.

Error source	Requirement
Raman phase noise	$S_\phi^0 < -116\text{dB rad}^2/\text{Hz}$
Raman frequency noise	$S_f^0 < 2.3 \times 10^5 \text{Hz}^2/\text{Hz}$
Raman intensity noise	$(S_I^0/I^2) < -109\text{dB/Hz}$
Imaging frequency noise	$(\sigma_\Delta)_{\text{Abs. Im.}} < 100\text{kHz}$
Imaging intensity noise	$(\sigma_I/I)_{\text{Abs. Im.}} < 1.1\%$

We first present an analysis of noise sources independent of free-evolution period. In Table 9.1, we outline the requirements that the Raman and imaging lasers must meet to achieve performance at the atom shot noise level ($N_A = 10^6$). The high-frequency noise of the Raman laser is limited by the pulse duration and thus remains independent of the interferometer's free-evolution period. We utilize the sensitivity function formalism to assess the requirements for Raman phase, frequency, and intensity noise (see Chapter 4). To evaluate the frequency requirement, we consider the case of a time delay between the two Raman lines due to retro-reflection [64], assuming that the mirror is positioned 10cm from the atomic cloud. For the intensity noise, we consider the effect of one-photon light-shift for circularly polarized beams, with a single photon detuning of $\Delta = 3$ GHz and pulse duration of $\tau = 5\mu$s. Finally, we assess the imaging laser requirements in terms of frequency and intensity noise for absorption imaging operating with weak resonant pulses (see Chapter 8). Modern Raman and detection laser systems allow for the realization of noise performance close to the shot noise limit [32, 61].

Figure 9.1 presents the computed short-term sensitivity for the PSI rotational and acceleration signals relative to several noise sources dependent on the free-evolution time, assumed to be white for simplicity. We employ the sensitivity function formalism to assess the short-term sensitivity of the rotational and acceleration signals, respectively, in terms of angle random walk and noise spectral density (see Chapters 4 and 6). As a benchmark, we include the atom shot noise limit corresponding to a number of atoms $N_A = 10^6$, cloud temperature $\mathcal{T} = 10\mu$K, and cycling period $T_c = 300$ms, based on experimental conditions outlined in Refs. [14, 116].

For the rotational short-term sensitivity, we evaluated the impact of pointing jitter on the Raman axis and the coupling between wavefront distortions and vibrations transverse to the Raman axis. The yellow shaded area corresponds to pointing noise in the range $0.5 - 5\text{nrad}/\sqrt{Hz}$, while the green shaded area pertains to vibrational noise in the range $10 - 100\mu\text{g}/\sqrt{Hz}$ coupled with a quadratic phase distortion characterized by a peak-to-valley amplitude of $\lambda/10$. As expected, pointing jitter represents a critical noise source for rotational short-term sensitivity as it directly affects the estimation of phase

gradient. However, the short-term sensitivity decreases as the free-evolution time increases due to the fact that the sensor bandwidth decreases with the free-evolution time, thereby leading to the rejection of high-frequency noise. In contrast, the noise induced by the coupling of transverse vibrations with phase distortions increases with the free-evolution time because it manifests as a time-varying acceleration on the atomic trajectories.

For short-term acceleration sensitivity, we assess the impact of transverse and longitudinal vibrations, pointing jitter, magnetic noise, and gravity gradient. Longitudinal vibrations and magnetic noise directly affect the acceleration signal, while pointing jitter and gravity gradient contribute indirectly by coupling with the initial atomic position. The shaded areas represent different contributions: grey and blue denote sensitivity due to longitudinal vibrations ($0.1 - 1\mu g/\sqrt{\text{Hz}}$) and magnetic noise ($0.01 - 0.1\text{mG}/\sqrt{\text{Hz}}$) respectively.
The contribution resulting from the coupling between quadratic phase distortion and transverse vibrations, for the same system parameters as in the rotational case, is negligible with respect to the other noise sources. The yellow shaded area represents the contribution of pointing jitter, with the same angular noise levels as in the rotational case, along with a transverse offset of $\ell_\perp = 100\mu$m. The red shaded area portrays the influence of gravity gradient on acceleration sensitivity via longitudinal position coupling. Our simulations incorporate the Earth's mean field for gravity gradient calculation [160], alongside longitudinal position noise ranging $10 - 100\mu\text{m}/\sqrt{Hz}$.
The most critical noise source arises from longitudinal vibrations. Its mitigation necessitates a closed-loop compensation scheme that leverages correlations between measured vibrations and random phase noise [30]. Magnetic noise and pointing jitter represent other critical noise sources. While the former can be rejected adopting alternative pulse schemes [76] or limited using better shielding [161], the latter can be mitigated by ensuring better alignment between the atomic cloud and the rotation axis of the Raman mirror [162].

Figure 9.1 highlights a well-known trend in cold-atom inertial sensors based on light-pulse atom interferometry: in an open-loop configuration, achieving navigation-grade performance, represented by the dashed blue lines indicating upper and lower bounds, requires free-evolution times exceeding 10ms and relatively benign environments. Therefore, the free-evolution time represents a critical parameter that is a compromise between sensor signal-to-noise ratio and bandwidth. The presence of noise sources in hostile environments effectively prevents the attainment of short-term performance levels close to the lower boundary of the navigation-grade band [17, 39].

In our analysis we did not include the effect of the phase offset noise on rotational signal. As shown in Chapter 7, phase offset noise affects phase gradient estimation when using multiple images to reconstruct the interferometric phase map. However, evaluating the effect of phase offset noise on PSI rotational signal strongly depends on

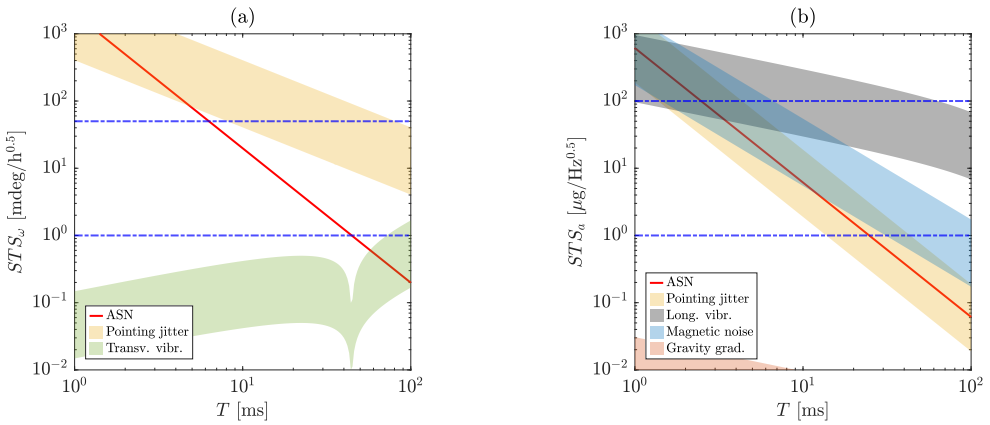

FIGURE 9.1: Variation of the short-term sensitivity with the free-evolution time. Panel (a): PSI rotational signal. Panel (b): PSI acceleration signal. The blue dashed lines represent the upper and lower bounds for navigation-grade sensors.

the adopted read-out method and requires numerical simulations. Since longitudinal vibrations represent the main source of phase offset noise, we expect that for a given vibration noise amplitude, the impact of the phase offset upon the rotational signal performance increases with the free-evolution time.

9.1.2 Accuracy

The accuracy of a cold-atom inertial sensor can be expressed in terms of bias and scale-factor errors. A more accurate evaluation of the performance level would require complex Monte Carlo simulations, in which the understanding of the impact of system parameters on a single performance can only be assessed through a lengthy exploration of the parameter space. In contrast, we develop a simple analytical model that includes some of the main error sources. This model, based on a combination of theoretical tools such as the sensitivity function formalism and convolution integrals, allows for the rapid estimation of the projected accuracy performance, highlighting the effect of system parameters in a clear manner.

Table 9.2 reports the analytical error model for a Mach-Zehnder interferometer operating with conventional rectangular pulses and with flat wavefronts. We distinguish the errors affecting the phase gradient from the errors affecting the phase offset. The terms in the Table are obtained computing the atomic trajectories relative to the body frame and their couplings with external error sources. The one- and two-photon light-shifts terms are computed assuming that the waist of the Gaussian Raman beam is

TABLE 9.2: Error model for Mach-Zehnder interferometer operating with conventional rectangular pulses and flat wavefronts. The z-axis coincides with the Raman propagation axis.

Error source	Phase gradient	Phase offset
Cross-axis	$\frac{3\,T^3}{T_{ex}}\,\left(\mathbf{k}^b \times \boldsymbol{\omega}^b_{ib} \times \boldsymbol{\omega}^b_{ib}\right)$	$-T^2\,\mathbf{k}^b \cdot \left(\boldsymbol{\omega}^b_{ib} \times \boldsymbol{\omega}^b_{ib} \times \boldsymbol{\ell}^b\right)$ $-T^3\,\mathbf{k}^b \cdot \left[(2\,\boldsymbol{\omega}^b_{ib} + \boldsymbol{\omega}^b_{nb}) \times \mathbf{f}^b_{ib}\right]$ $+2\,T^3\,\mathbf{k}^b \cdot \left(\boldsymbol{\omega}^b_{ib} \times \boldsymbol{\omega}^b_{ib} \times \boldsymbol{\omega}^b_{ib} \times \boldsymbol{\ell}^b\right)$
Maneuvering	$-\frac{3\,T^3}{T_{ex}}\left(\mathbf{k}^b \times \dot{\boldsymbol{\omega}}^b_{ib}\right)$ $-\frac{14\,T^4}{12\,T_{ex}}\left[\mathbf{k}^b \times \left(\boldsymbol{\omega}^b_{ib,0} \times \dot{\boldsymbol{\omega}}^b_{ib}\right)\right]$	$-T^2\,\mathbf{k}^b \cdot \left(\dot{\boldsymbol{\omega}}^b_{ib} \times \boldsymbol{\ell}^b\right) - T^3\,\mathbf{k}^b \cdot \dot{\mathbf{f}}^b_{ib}$
Magnetic gradient	$-\frac{2\,K_{mg}\,T^3}{T_{ex}}\,\boldsymbol{\omega}^b_{ib,\perp}$	$K_{mg}\,T^2\,\left(v_{z,0} + \frac{v_{\text{rec}}}{2} - f_z\,T\right)$
Magnetic force	$-\frac{4\,K_{mf}\,T^4}{3\,T_{ex}}\,(\mathbf{k}^b \times \boldsymbol{\omega}^b_{ib})$	$\frac{2}{3}\,k_z\,K_{mf}\,T^3\,\left(v_{z,0} + \frac{v_{\text{rec}}}{2} - f_z\,T\right)$
Gravity gradient	$-\frac{7\,\Gamma_{zz}\,T^4}{6\,T_{ex}}\,(\mathbf{k}^b \times \boldsymbol{\omega}^b_{ib})$	$k_z\,\Gamma_{zz}\,T^2\,\left[\ell_z + (v_{z,0} + \frac{v_{\text{rec}}}{2})\,T - \frac{7}{12}\,f_z\,T^2\right]$
Refractive index	$\frac{8\,T^2\,\delta n}{T_{ex}}(\mathbf{k}^b \times \boldsymbol{\omega}^b_{ib})$	$-2\,T\,\delta n\,k_z\,(v_{z,0} + v_{\text{rec}} - 2\,f_z\,T)$
Atomic collisions	$-$	$2\,T\,K_{col}\,\left(\frac{1}{\sigma(2T)} - \frac{1}{\sigma(T)}\right)$
One-photon light-shift	$-\frac{K_{\text{OPLS}}}{w_L^2}\,\boldsymbol{\ell}^b_{\perp}$	$-\frac{K_{\text{OPLS}}}{w_L^2}\,F\,\sigma_0^2$
Two-photon light-shift	$K_{\text{TPLS}}\,\frac{4\,\beta_3}{w_L^2}\,\boldsymbol{\ell}^b_{\perp}$	$K_{\text{TPLS}}\,\left(\beta_1 - \beta_3 + \frac{\beta_3}{w_L^2}\,4\,F\,\sigma_0^2\right)$

(1) $K_{mg} = 4\,\pi\,K_{QZ}\,B_0\,\frac{\partial B}{\partial z}$
(2) $K_{mf} = \frac{h\,K_{QZ}}{m}\,\left(\frac{\partial B}{\partial z}\right)^2$
(3) $K_{col} = (K_{ee} + K_{gg})\,\frac{N}{2\,(2\,\pi)^{3/2}\sigma_0^2}$
(3) $K_{\text{OPLS}} = a_1\,\delta I\,\frac{(1 - I_1^0/I_2^0)}{\Omega_0}\,\exp\left(-2\,|\boldsymbol{\ell}^b|^2/w_L^2\right)$
(4) $K_{\text{TPLS}} = \Omega_0\,\exp\left(-4\,|\boldsymbol{\ell}^b|^2/w_L^2\right)$

much larger than the atomic cloud. Error modeling for Raman wavefront and imaging distortions can be found in Chapters 6 and 8, respectively.

Each error source contributes in a manner dependent on multiple parameters. Since the free-evolution time stands as one of the most crucial system parameters of a cold-atom inertial sensor, we opt to examine how accuracy varies with the free-evolution time.

9.1.2.1 Bias

Figure 9.2 shows the bias for both the rotational and acceleration signals. For the chosen working conditions [1], the dominant error terms are represented by the cross-axis and maneuvering. Their contribution typically increases with the free-evolution time as they are the result of high-order inertial terms. The gravity gradient term is negligible with respect the other error sources.
Regarding the contribution of the wavefront distortions, we adopt the model reported

[1]Relative to a single sensitive axis we assume: $\omega^b_{ib} = 1\text{deg/s}$, $\dot{\omega}^b_{ib} = 0.01\text{deg/s}^2$, $f^b_{ib} = 1\text{g}$, $\dot{f}^b_{ib} = 0.01\text{g/s}$, $\ell^b = 100\mu\text{m}$, $T_{ex} = 4\,T$.

in Table 6.2, with a peak-to-valley wavefront amplitude corresponding to $\lambda/10$ over a radius of 1cm. In our analysis we only consider the terms directly affecting the phase gradient and offset, without including high-order spatial terms that have an indirect effect and, therefore, depend on the specific read-out protocol (e.g., maximum likelihood estimation, least square fitting, Kalman filtering, machine learning, etc.). The wavefront term exhibits complex behavior due to the coupling between phase distortions and the initial atomic phase-space distribution, which is nontrivial. As a general trend, the longer the expansion time, the less the effect of the initial distribution on the error term.
Two-photon light-shift (TPLS) represents a significant bias source affecting the acceleration signal. For its evaluation, we assume a Raman beam characterized by a Gaussian intensity distribution with a waist of $w_L = 10$mm and a pulse duration of $\tau = 5\mu$s. Moreover, we assume that the Raman transition is Doppler-detuned by the free fall motion due to gravity acceleration. The longer the free-evolution period, the lower the bias, as TPLS primarily depends on the Doppler detuning induced by the initial pulse, which is determined solely by its timing (we assume that the first pulse occurs 5ms after the release of the cloud from the MOT).
A spatial variation of the magnetic field along the Raman axis determines a bias on the acceleration signal due to the coupling with the atomic trajectories. The error induced by the magnetic gradient, for which we assume a bias field $B_0 = 100$mG and a gradient $\partial B/\partial z = 1.2$mG/mm, is almost constant with the free-evolution time as it mainly depends on the T^2 term due to the initial and recoil velocity.
The atomic density affects the acceleration signal's bias through two mechanisms: atomic collisions and variations in the momentum imparted to the atomic wavepackets due to the cloud's refractive index. The bias decreases with the free-evolution time as a consequence of the reduced atomic density resulting from the cloud's expansion. In the calculations, we assume a cloud of 10^6 atoms characterized by an initial size of $\sigma_0 = 0.5$mm and a temperature of $\mathcal{T} = 10\mu$K.
Finally, we assess the impact of motion blur on the acceleration bias. This error source arises from the displacement of the atomic cloud in a direction transverse to the imaging axis during the detection pulse. In our calculations, we assume that the imaging beam illuminates the atomic cloud for 200μs and that the relative velocity between the center of mass of the atomic cloud and the CCD is 1mm/s. Since this error source is independent of the free-evolution time, the induced bias decreases with T.

9.1.2.2 Scale-factor error

Figure 9.3 shows the scale-factor error for different error sources for both the acceleration and rotational signals. As expected, the dominant error source affecting the rotational signal is the finite size of the initial atomic cloud. As the expansion time increases, the scale-factor tends toward the point-source limit, and the error decreases.

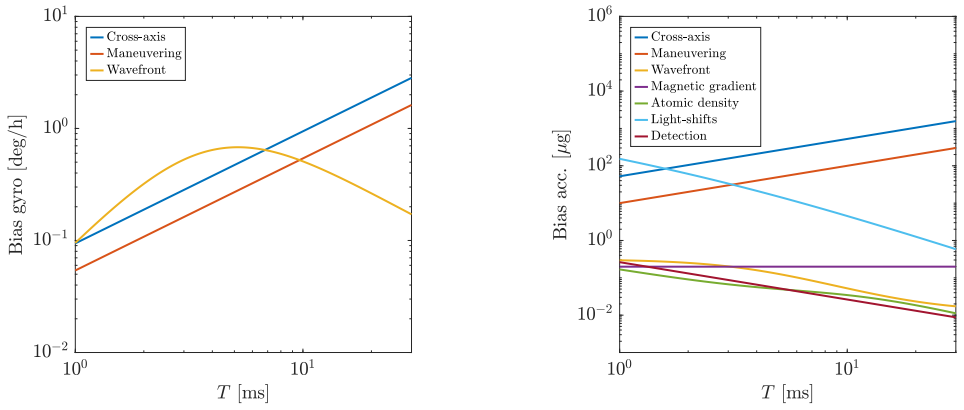

(A) Bias gyro (B) Bias accelerometer

FIGURE 9.2: Calculation of the fixed bias parameterized with respect to the free-evolution time.

Nevertheless, even for high expansion times, the scale-factor error remains sufficiently high to preclude the use of a PSI gyroscope as a sensor for inertial navigation. Therefore, calibration of the rotational scale-factor is necessary.
Another important error source affecting the rotational scale-factor is represented by the detection process, which includes optical distortions, misalignments, motion blur induced by the relative displacement of the atomic cloud with respect to the CCD system during the imaging process, and finite pixel size. Dominant error sources in the detection process include blurring due to recoil heating and free-expansion, as well as the sampling process operated by the discrete configuration of the CCD. Generally, the scale-factor error decreases with the free-evolution time, as the detection process is independent of it.
Variation of the refractive index due to atomic density and misalignment of the effective Raman wave-vector [2] induce scale-factor errors below the 1ppm level.
In contrast, magnetic field gradients and wavefront distortions induce scale-factor errors that increase with the free-evolution time. While k-reversal protocols can reject the magnetic field gradient term [50], the wavefront term still persists. Specifically, the phase distortions, such as coma and trefoil, induce a coupling between the initial cloud size and the rotational phase gradient, resulting in scale-factor non-linearity.

9.1.3 Long-term stability

9.1.3.1 Bias instability

Figure 9.4 shows the bias instability in both the acceleration and rotational signals.
Light-shift errors, in the form of one-photon light-shift (OPLS) and two-photon light-shift (TPLS), are significant error sources. OPLS is typically mitigated by adjusting

[2] In the calculation we assume a misalignment of 100μrad.

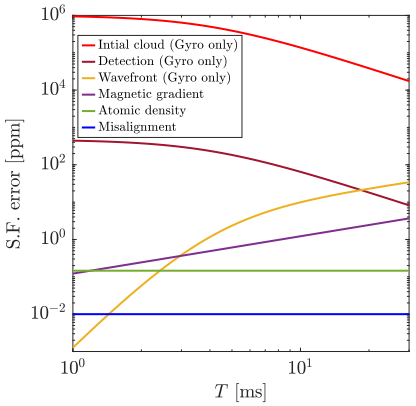

FIGURE 9.3: Calculation of the scale-factor error parameterized with respect to the free- evolution time.

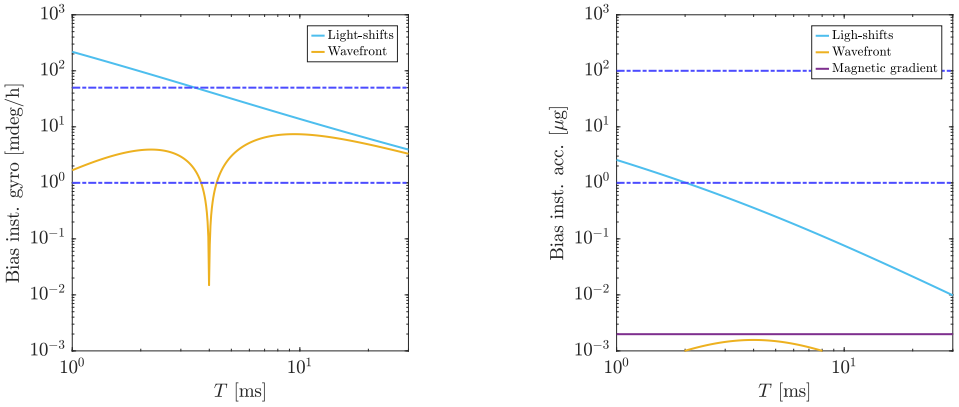

(A) Bias instability gyro

(B) Bias instability accelerometer

FIGURE 9.4: Calculation of the bias instability parameterized with respect to the free-evolution time. The dashed blue lines indicate the upper and lower performance bounds for navigation-grade sensors.

the intensities of the Raman beams. However, long-term intensity drifts contribute to instability. We observe that displacements of the center of mass of the atomic cloud relative to the centroid of the Raman beam lead to errors in the rotational signal. For the light-shift calculations, we assume a 1% relative intensity drift, circular polarization, and a displacement of 100μm between the center of the atomic cloud and the centroid of the Raman beam. Achieving strategic-grade performance is possible with long free-evolution times.

Long-term drifts in the bias magnetic field and variations in the size of the initial cloud (coupled with wavefront distortions) can lead to bias instability in the acceleration signal. Fluctuations in the initial cloud size at a 1% level and in the bias field of 1mG result in an instability of a few nano-g.

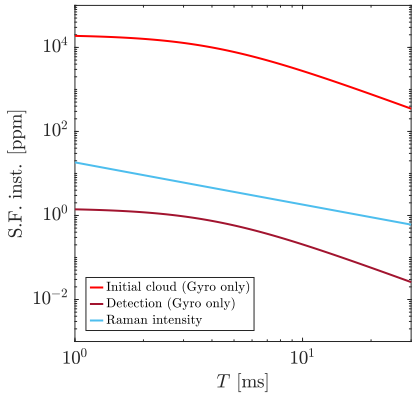

FIGURE 9.5: Calculation of the scale-factor instability parameterized with respect to the free-evolution time.

9.1.3.2 Scale-factor instability

Figure 9.5 shows the effect of different error sources on scale-factor instability.
The most dominant source of instability in the rotational scale-factor is due to fluctuations in the size and shape of the initial atomic cloud. Even fluctuations at the 1% level could lead to scale-factor instability of hundreds of ppm. Therefore, stabilization of the rotational scale-factor is necessary for inertial navigation.
Long-term drifts in the intensity of the Raman beam determine a variation in the area spanned by the atomic wave-packets during the interferometric sequence, and thus, a change in the sensor scale-factor. However, since the scale-factor error, to the first order, is proportional to the ratio between pulse duration and the free-evolution time, long free-evolution times are required to achieve scale-factor instability below the 1 ppm level for 1% intensity fluctuations.
Recoil heating during the detection process induces blurring in the imaging of the atomic cloud and scale-factor errors. Therefore, long-term drifts in the intensity of the imaging beam determine scale-factor instability. For a pulse duration of 200μm, a 1% intensity drift induces scale-factor instability below the 1 ppm level for long free-evolution times.
Scale-factor instability due to fluctuations of the bias magnetic field and wavefront distortions is below the 1ppb level.

Chapter 10

Conclusions and outlook

In this thesis, we conducted a theoretical analysis of some of the main error sources in cold-atom inertial (CAI) sensors for navigation applications. Additional error sources not considered in this thesis, mainly due to a lack of time, include, for instance, the effects introduced by the response of Doppler and vibration compensation loops, the impact of phase and frequency modulation schemes on sensor sensitivity, timing errors in the interferometric and optical read-out, the finite spatial response of the imaging laser, and the non-optimality of the algorithmic solution used to extract the inertial phase from the interferometric signal under dynamic conditions.

Overall, the analysis aimed to establish relationships between system parameters and sensor performance using a combination of methodologies and theoretical tools.

From this perspective, the sensitivity function formalism represents a powerful theoretical tool that can describe the response of an atom interferometer to both deterministic and stochastic inputs, in a manner understandable by system and navigation engineers. We utilized this formalism, along with additional modeling, to provide, when possible, closed-form expressions linking each specific error source to its corresponding performance. We particularly focused on error sources arising from the laser-atom interaction during the Raman pulse sequence and state detection and imaging, providing further insights into CAI sensors based on point-source interferometry (PSI).

Our findings reveal that the projected performance of CAI sensors strongly depends on its configuration and, in several cases, achieving a certain performance level is a trade-off between opposite driving forces. For instance, a longer duration of the free-evolution period improves short-term sensitivity for many error sources, but induces loss in signal's visibility; or, a longer Raman pulse enhances suppression of high-frequency phase noise but leads to a higher velocity selectivity with reduced efficiency of the Raman diffraction process. Moreover, the environment in which the CAI sensor operates constitute another important element: vibrations, stray magnetic fields,

signal's loss and systematic errors due to the couplings between laser-atom interaction and vehicle's dynamics are all non-negligible error sources that require careful evaluation.

The field deployment of CAI sensors in challenging and uncontrolled environments often necessitates significant engineering efforts. Implementing complex control and stabilization mechanisms is necessary to mitigate the impact of various error sources on sensor performance. Hybridization and/or integration with aiding sensors, such as conventional inertial measurement units, are frequently required. Moreover, despite their reputation for providing absolute and accurate measurements, CAI sensors still require error modelling and initial calibration [14, 16].
In this thesis, we presented several examples of these engineering efforts. For instance, we demonstrated the use of optimal control to enhance stability and reduce systematic errors in CAI sensors due to inter-pulse laser intensity variations. Additionally, we implemented a read-out scheme based on nonlinear Kalman filtering to efficiently extract phase information from interferograms of atomic populations. Furthermore, we designed a protocol for stabilizing the rotational scale-factor of a CAI sensor based on PSI, making it suitable for real-time applications.

Future works may involve assessing overall navigation performance by developing a complex simulator that accurately models the interaction between vehicle and sensor dynamics. A more refined error model, calibrated on experimental data, could be adopted to effectively predict real-world scenarios. Additionally, the analysis could be extended to include a comparative study of sensor performance using different diffraction schemes (e.g., Raman double-diffraction, Bragg, single-photon transitions) or atomic sources (e.g., Bose-Einstein condensates).
Another intriguing route could be the utilization of multi-objective optimization for the design of CAI sensors. This approach is particularly appealing for systems where opposing driving forces necessitate a trade-off optimum [163]. Therefore, integrating quantum optimal control with the navigation requirements of CAI sensors for specific mission profiles could offer an alternative approach to implementing quantum sensors for navigation applications.
Finally, an open and intriguing question concerns how CAI sensors are used for navigation applications. These sensors not only provide specific force and angular rate measurements but also offer additional information, such as the orientation of gravity and angular rate vectors with respect to the vehicle's body frame. How can this additional information be used to enhance free-inertial navigation? What navigation mechanization is required? Are there any benefits with respect to conventional navigation schemes?

However, after all these considerations and questions, we arrive at the million-dollar question: are CAI sensors suitable for high-accuracy autonomous navigation? The

simple answer is: it depends. While CAI sensors have demonstrated exceptional accuracy and stability in lab-based experiments, achieving the same level of performance in real-world scenarios depends on various factors such as sensor architecture and configuration, application type, and engineering efforts to mitigate technical and fundamental error sources. What is certain is that over the last decade, efforts and progress toward realizing CAI sensors suitable for navigation applications have exponentially increased. From hybridization with conventional sensors [16] to the use of optimal control [77] and the design of exotic and novel sensor configurations [164, 165], research groups worldwide have been pushing the frontiers of quantum inertial sensing, seeking solutions to both old and new challenges and striving to bring the much-desired quantum advantage out of the lab. In our opinion, this opens up interesting and exciting prospects for the future, as the realization of the quantum technology breakthrough appears increasingly tangible.

Appendix A

Response of Mach-Zehnder interferometer

A.1 Phase sensitivity function

In this Appendix we show how to practically compute the phase response of a Mach-Zehnder atom interferometer operating with rectangular Raman pulses.
The phase sensitivity function is defined as

$$g_\phi(t) \coloneqq \lim_{\delta\phi\to 0} \frac{\Delta\Phi(t)}{\delta\phi} = \frac{2}{C\sin(\Delta\Phi_0)} g(t)\,, \tag{A.1}$$

where $\Delta\Phi_0$ is the offset laser phase indicating the interferometer's working point, C is the fringe contrast and $g(t)$ is the sensitivity function

$$g(t) \coloneqq \lim_{\delta\phi\to 0} \frac{\delta P_j(t)}{\delta\phi}\,. \tag{A.2}$$

The quantity δP_j is the perturbation of the $|j\rangle$ state population at the output port of the interferometer and it is defined as

$$\delta P_j(t) = P_j(t) - P_{j,u}\,, \tag{A.3}$$

where $P_j(t)$ is the perturbed interferometric signal at the output port of the interferometer computed for a step phase perturbation $\delta\phi(t) = \delta\phi\,\Theta(t' - t)$, and $P_{j.u}$ is the unperturbed interferometric signal computed for zero phase perturbation.

In the calculation of the phase sensitivity function we assume:

- Flat wavefronts. We neglect phase aberrations introduced by optical elements or due to the laser intensity inhomogeneity.
- Mono-kinetic atom. The sensitivity function formalism is not generalized to the case of an atomic ensemble.
- Pulse-length errors. We neglect detuning errors introduced, for example, by the atomic velocity distribution. Therefore, the sensitivity function describes the response of a near-resonant atom.
- Interferometer operating at the maximum sensitivity point, i.e. $\Delta\Phi_0 = \pi/2$.

A.1.1 Unperturbed interferometric signal

Let us compute the interferometric signal for a mono-kinetic atom subject to pulse-length errors. Following [71], we can apply the Raman propagator to the atomic wave-packets traveling along the arms of the interferometer.
Referring to Figure A.1, ABD and ACF represent spurious paths that do not contribute to the interferometer signal. Indeed, the atomic wave-packets propagating along these two paths accumulate a velocity-dependent phase that gives rise to a highly oscillatory signal, which is suppressed when averaging over the thermal velocity distribution [1]. Therefore, only ABE and ACE paths contribute to interference and the interferometric signal P_e is given by

$$\begin{aligned} P_e &= |c_{e,\mathrm{ABE}}(t_f) + c_{e,\mathrm{ACE}}(t_f)|^2 \\ &= |c_{e,\mathrm{ABE}}(t_f)|^2 + |c_{e,\mathrm{ACE}}(t_f)|^2 + 2\,\mathrm{Re}\{c_{e,\mathrm{ABE}}(t_f)^*\, c_{e,\mathrm{ACE}}(t_f)\}\,, \end{aligned} \tag{A.4}$$

where $c_{e,\mathrm{xxx}}(t_f)$ is the amplitude to the upper hyperfine ground state evolving along the path xxx at the end of the pulse sequence $t_f = 2\,T + 4\,\tau$.
The Raman propagator describing the evolution of the atomic wavefunction in the near-resonant case is given by [166]

$$\begin{pmatrix} c_e(t_0+\tau) \\ c_g(t_0+\tau) \end{pmatrix} = \begin{bmatrix} C^* & -i\,S^* \\ -i\,S & C \end{bmatrix} \begin{pmatrix} c_e(t_0) \\ c_g(t_0) \end{pmatrix}, \tag{A.5}$$

with $C = \cos(\theta/2)$ and $S = \sin(\theta/2)\,e^{i\,\phi}$, $\theta = \Omega\,\tau$ pulse area, and ϕ Raman phase.
Starting from the initial condition $c_e(0) = 0$, $c_g(0) = 1$ leads to

$$c_{e,\mathrm{ABE}}(t_f) = -i\,S_1^*\,(-i\,S_2)\,(-i\,S_3^*)\,, \tag{A.6}$$

[1] Strictly speaking, this is true for thermal atomic ensembles. When dealing with Bose-Einstein condensates characterized by high de Broglie wavelengths extra care should be payed especially in the case of short free-evolution times.

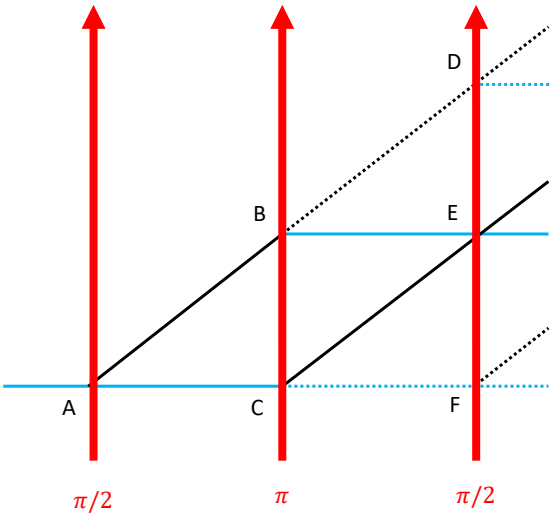

FIGURE A.1: Recoil diagram of a Mach-Zehnder interferometer. The continuous and dotted lines indicate, respectively, the main and spurious paths.

$$c_{e,\mathrm{ACE}}(t_f) = -C_1\,(-i\,S_2^*)\,C_3^*\,, \tag{A.7}$$

where C_j and S_j are the Raman propagator elements for the j-th pulse.
Inserting this two expressions in Eq. (A.4) we obtain the unperturbed interferometric signal

$$P_e = P_0 - \frac{C}{2}\cos\left(\Delta\Phi_0\right), \tag{A.8}$$

with P_0, C and $\Delta\Phi_0$, respectively, fringe offset, contrast and phase offset

$$P_0 = \frac{1}{2}\left[1 - \cos\left(\theta_1\right)\,\cos\left(\theta_2\right)\,\cos\left(\theta_3\right)\right], \tag{A.9}$$

$$C = \sin\left(\theta_1\right)\,\sin^2\left(\frac{\theta_2}{2}\right)\,\sin\left(\theta_3\right), \tag{A.10}$$

$$\Delta\Phi_0 = \phi_1 - 2\,\phi_2 + \phi_3\,. \tag{A.11}$$

If we choose $\Delta\Phi_0 = \pi/2$ we obtain

$$P_{e,u} = P_0\,. \tag{A.12}$$

A.1.2 Perturbed interferometric signal

As a further step, we need to compute the perturbed interferometric signal due to an infinitesimal laser phase step perturbation.

A.1.2.1 First Raman pulse

The phase step perturbation occurs during the first Raman pulse. In this case, we need to split the Raman propagator into two parts: one before the phase jump and one after the phase jump. Hence, the amplitude of the atomic upper state is given by

$$c_{e,\mathrm{ABE}}(t_f) = U_{eg}\,(-i\,S_2)\,(-i\,S_3^*)\,, \tag{A.13}$$

$$c_{e,\mathrm{ACE}}(t_f) = U_{ee}\,(-i\,S_2^*)\,C_3^*\,, \tag{A.14}$$

where U_{eg} and U_{ee} are the elements of the matrix

$$\begin{aligned}\mathbf{U}_1 &= \begin{bmatrix} U_{ee} & U_{eg} \\ U_{ge} & U_{gg} \end{bmatrix} \\ &= \underbrace{\begin{bmatrix} \cos\left(\frac{\Omega_1\,(t-\tau)}{2}\right) & -i\,e^{-i\,\delta\phi}\,\sin\left(\frac{\Omega_1\,(t-\tau)}{2}\right) \\ -i\,e^{i\,\delta\phi}\,\sin\left(\frac{\Omega_1\,(t-\tau)}{2}\right) & \cos\left(\frac{\Omega_1\,(t-\tau)}{2}\right) \end{bmatrix}}_{\text{After phase jump}} \underbrace{\begin{bmatrix} \cos\left(\frac{\Omega_1\,t}{2}\right) & -i\,\sin\left(\frac{\Omega_1\,t}{2}\right) \\ -i\,\sin\left(\frac{\Omega_1\,t}{2}\right) & \cos\left(\frac{\Omega_1\,t}{2}\right) \end{bmatrix}}_{\text{Before phase jump}},\end{aligned} \tag{A.15}$$

and $-i\,S_3^* = -i\,e^{-i\,(\delta\phi+\pi/2)}\sin\theta_3 = -e^{-i\,\delta\phi}\sin\theta_3$.
At this point we can compute the perturbed interferometric signal perturbation and the perturbation

$$\delta P_e(t) = -\frac{1}{2}\,\sin^2\left(\frac{\theta_2}{2}\right)\,\sin\left(\theta_3\right)\,\sin\left(\Omega_1\,t\right)\,\delta\phi\,, \tag{A.16}$$

and the phase sensitivity function

$$g_\phi(t) = -\frac{\sin\left(\Omega_1\,t\right)}{\sin\theta_1}\,. \tag{A.17}$$

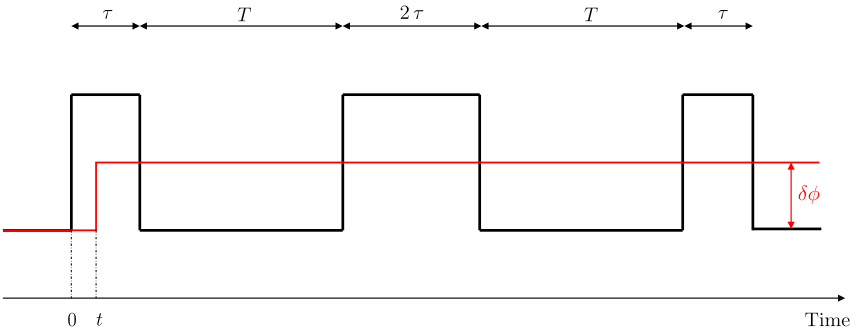

FIGURE A.2: Mach-Zehnder pulse sequence with phase step perturbation occurring during the first beam-splitter pulse.

A.1.2.2 Free evolution periods

The calculation of the phase sensitivity function during free evolution periods is easy. Assuming that the phase jump occurs during the first free evolution period we write the perturbed interferometric signal as

$$P_e = P_0 + \frac{C}{2}\sin\left(0 - 2\,\delta\phi + \delta\phi\right), \tag{A.18}$$

where the sin function is due to $\Delta\Phi_0 = \pi/2$. For an infinitesimal phase perturbation

$$P_e \approx P0 - \frac{C}{2}\,\delta\phi \tag{A.19}$$

and, therefore,

$$g_\phi(t) = -1\,. \tag{A.20}$$

The same reasoning applies to the case of phase jump arising during the second free evolution period. The perturbed interferometric signal is

$$P_e = P_0 + \frac{C}{2}\sin\left(0 - 2\,0 + \delta\phi\right), \tag{A.21}$$

and the phase sensitivity function is

$$g_\phi(t) = 1\,. \tag{A.22}$$

A.1.2.3 Other Raman pulses

In the same fashion we can compute the interferometric signal perturbation when the phase jump occurs during the second pulse

$$\delta P_e(t) = \frac{1}{2} \sin(\theta_1) \sin\left(\frac{\theta_2}{2}\right) \sin(\theta_3) \sin\left[\Omega_2 (t - T - 2\tau)\right] \delta\phi \,, \tag{A.23}$$

and the third pulse

$$\delta P_e(t) = -\frac{1}{2} \sin(\theta_1) \sin^2\left(\frac{\theta_2}{2}\right) \sin\left[\Omega_3 (t - 2T - 4\tau)\right] \delta\phi \,. \tag{A.24}$$

Applying the definition of phase sensitivity function we finally obtain the expression for the second

$$g_\phi(t) = \frac{\sin\left[\Omega_2 (t - T - 2\tau)\right]}{\sin(\theta_2/2)} \,, \tag{A.25}$$

and third pulse

$$g_\phi(t) = -\frac{\sin\left[\Omega_3 (t - 2T - 4\tau)\right]}{\sin(\theta_3)} \,. \tag{A.26}$$

A.2 Response to white noise

The response of the interferometer to a stochastic perturbation is given by the infinite sum

$$AVAR_{\Delta\Phi}(\tau_c) = \frac{1}{\tau_c} \sum_{n=1}^{+\infty} |H_\xi(2\pi n f_c)|^2 S_\xi(2\pi n f_c) \,. \tag{A.27}$$

where $AVAR_{\Delta\Phi}$ is the Allan variance of the interferometric phase computed at the cluster time τ_c, $H_\xi(2\pi n f_c)$ and $S_\xi(2\pi n f_c)$ are, respectively, the interferometer transfer function and the perturbation power spectral density computed at an integer multiple of the sensor cycling frequency f_c.
The evaluation of the sum can be done analytically if we assume that the perturbation is characterized by a white noise spectrum, i.e. $S_\xi(2\pi n f_c) = S_\xi^0$ for all n. In this case Eq. (A.28) can be written as

$$AVAR_{\Delta\Phi}(\tau_c) = \frac{S_\xi^0}{\tau_c} \sum_{n=1}^{+\infty} |H_{\xi,n}|^2 \,, \tag{A.28}$$

where the notation $H_{\xi,n} = H_{\tilde{\xi}}(2\,\pi\,n\,f_c)$.
The sum over all the integer harmonics can be computed applying the Plancherel's theorem: given a periodic signal $h_{\tilde{\xi}}(t)$ over an interval $[-T_c/2,\, T_c/2]$, with T_c period, the following identity is valid [167]

$$T_c \int_{-T_c/2}^{T_c/2} |h_{\tilde{\xi}}(t)|^2\, dt = \sum_{n=-\infty}^{+\infty} |H_{\xi,n}|^2\,, \tag{A.29}$$

where $H_{\xi,n}$ is the Fourier transform of the periodic function $h_{\tilde{\xi}}(t)$ computed at the n-th harmonic, i.e. $H_{\tilde{\xi},n} = \mathcal{F}\{h_{\tilde{\xi}}\}_{\omega=2\,\pi\,n\,f_c}$.
We can rewrite Eq. (A.29) as

$$T_c \int_{-T_c/2}^{T_c/2} |h_{\tilde{\xi}}(t)|^2\, dt = |H_{\tilde{\xi},0}|^2 + 2\sum_{n=1}^{+\infty} |H_{\xi,n}|^2\,, \tag{A.30}$$

and get

$$\sum_{n=1}^{+\infty} |H_{\xi,n}|^2 = \frac{1}{2}\left[T_c \int_{-T_c/2}^{T_c/2} |h_{\tilde{\xi}}(t)|^2\, dt - |H_{\tilde{\xi},0}|^2\right]. \tag{A.31}$$

Recalling that the zeroth harmonic is equal to the time integral of the function $h_{\tilde{\xi}}(t)$, we finally obtain the key result

$$AVAR_{\Delta\Phi}(\tau_c) = \frac{S^0_{\tilde{\xi}}}{2\,\tau_c}\left[T_c \int_{-T_c/2}^{T_c/2} |h_{\tilde{\xi}}(t)|^2\, dt - \left|\int_{-\infty}^{+\infty} h_{\tilde{\xi}}(t)\, dt\right|^2\right]. \tag{A.32}$$

The above expression allows for the calculation of the interferometer's white noise response given the sensitivity in time domain, $h_{\tilde{\xi}}(t)$.

Appendix B

Wavefunction evolution in Wigner representation

In point-source atom interferometry (PSI), the spatial distribution of the atomic population at one of the output ports of the interferometer is measured. Therefore, simulations of the PSI signal require the reconstruction of the atomic distribution in real space. One possible solution is to adopt a particle-based Monte Carlo technique, where atoms are considered as particles with random initial positions and velocities subject to the diffraction induced by the laser grating. However, this approach is computationally expensive since the accuracy of the method is based on the number of particles. A more interesting solution is to describe the wavefunction evolution using the Wigner representation formalism.
Wigner function is a pseudo-probability density function that describes the wavefunction evolution in phase-space. therefore, marginalization of the Wigner function allows for the reconstruction of the PSI output.

Wigner function is defined as Weyl transform of the density matrix operator [69]

$$W(\mathbf{x},\,\mathbf{p}) := \frac{1}{(2\,\pi\,\hbar)^3}\int_{-\infty}^{+\infty} \exp\left(-i\,\frac{\mathbf{p}\cdot\mathbf{y}}{\hbar}\right)\,\langle \mathbf{r}_+ \,|\, \boldsymbol{\rho} \,|\, \mathbf{r}_-\rangle\; d^3\mathbf{y}\,, \tag{B.1}$$

where $\mathbf{r}_\pm = \mathbf{r} \pm \mathbf{y}/2$, and $\boldsymbol{\rho} = |\psi(\hat{\mathbf{r}})\rangle\,\langle\psi(\hat{\mathbf{r}})|$.
Since we are interested in the time-evolution of wavefunction we take the time derivative of the Eq. (B.1)

$$\frac{\partial W}{\partial t} = \frac{1}{(2\,\pi\,\hbar)^3}\left(\frac{1}{i\hbar}\right)\int_{-\infty}^{+\infty} \exp\left(-i\,\frac{\mathbf{p}\cdot\mathbf{y}}{\hbar}\right)\,\langle \mathbf{r}_+ \,|\, \mathbf{H}\,\boldsymbol{\rho} - \boldsymbol{\rho}\,\mathbf{H}^\dagger \,|\, \mathbf{r}_-\rangle\; d^3\mathbf{y}\,, \tag{B.2}$$

where $\mathbf{H}$ is the Hamiltonian operator that in general can be time-dependent.
Readjusting the bra-ket term in Eq. (B.2) leads to

$$\frac{\partial W}{\partial t} = \frac{1}{(2\,\pi\,\hbar)^3}\,\left(\frac{1}{i\hbar}\right)\int_{-\infty}^{+\infty}\exp\left(-i\,\frac{\mathbf{p}\cdot\mathbf{y}}{\hbar}\right)\,\left(\mathbf{H}(\mathbf{r}_+)-\mathbf{H}^\dagger(\mathbf{r}_-)\right)\,\langle\,\mathbf{r}_+\,|\,\boldsymbol{\rho}\,|\,\mathbf{r}_-\,\rangle\,d^3\mathbf{y}\,. \tag{B.3}$$

Eq. (B.3) has a general validity and provides the time-evolution of the Wigner function in phase space for a given Hamiltonian.

B.1 Free-evolution

The free-evolution Hamiltonian is given by

$$\begin{aligned}\mathbf{H} =& \frac{\hat{\mathbf{p}}^2}{2\,m} + \hat{\mathbf{p}}\cdot(\hat{\mathbf{r}}\times\boldsymbol{\omega}) + V(\hat{\mathbf{r}}) \\ & -\frac{\hbar^2}{2m}\,\frac{\partial^2}{\partial\mathbf{r}^2} - i\hbar\,\frac{\partial}{\partial\mathbf{r}}\cdot(\mathbf{r}\times\boldsymbol{\omega}) + V(\mathbf{r})\end{aligned} \tag{B.4}$$

where $V(\hat{\mathbf{r}})$ is the potential and the kinetic energy term accounts for both translational and rotational motion.
Now

$$\begin{aligned}\frac{\partial}{\partial\mathbf{r}_+} =& \frac{\partial\mathbf{r}}{\partial\mathbf{r}_+}\frac{\partial}{\partial\mathbf{r}} + \frac{\partial\mathbf{y}}{\partial\mathbf{r}_+}\frac{\partial}{\partial\mathbf{y}} = \frac{1}{2}\frac{\partial}{\partial\mathbf{r}} + \frac{\partial}{\partial\mathbf{y}} \\ \frac{\partial}{\partial\mathbf{r}_-} =& \frac{\partial\mathbf{r}}{\partial\mathbf{r}_-}\frac{\partial}{\partial\mathbf{r}} + \frac{\partial\mathbf{y}}{\partial\mathbf{r}_-}\frac{\partial}{\partial\mathbf{y}} = \frac{1}{2}\frac{\partial}{\partial\mathbf{r}} - \frac{\partial}{\partial\mathbf{y}}\,,\end{aligned} \tag{B.5}$$

and, therefore

$$\begin{aligned}\frac{\partial^2}{\partial\mathbf{r}_+^2} =& \left(\frac{1}{2}\frac{\partial}{\partial\mathbf{r}} + \frac{\partial}{\partial\mathbf{y}}\right)^2 \\ \frac{\partial^2}{\partial\mathbf{r}_-^2} =& \left(\frac{1}{2}\frac{\partial}{\partial\mathbf{r}} - \frac{\partial}{\partial\mathbf{y}}\right)^2\,,\end{aligned} \tag{B.6}$$

from which we finally obtain,

$$\frac{\partial^2}{\partial\mathbf{r}_-^2} - \frac{\partial^2}{\partial\mathbf{r}_+^2} = -2\,\frac{\partial^2}{\partial\mathbf{r}\partial\mathbf{y}}\,. \tag{B.7}$$

Inserting the free-evolution Hamiltonian in Eq. (B.3) and using the previous relations gives

$$\frac{\partial W}{\partial t} = \frac{1}{(2\,\pi\,\hbar)^3}\left(\frac{1}{i\hbar}\right)\int_{-\infty}^{+\infty}\exp\left(-i\,\frac{\mathbf{p}\cdot\mathbf{y}}{\hbar}\right)\Big[-\frac{\hbar^2}{m}\frac{\partial^2}{\partial\mathbf{r}\partial\mathbf{y}}+\dots \\ -i\hbar\frac{\partial}{\partial\mathbf{r}_+}\cdot(\mathbf{r}_+\times\boldsymbol{\omega})-i\hbar\frac{\partial}{\partial\mathbf{r}_-}\cdot(\mathbf{r}_-\times\boldsymbol{\omega})+\dots \\ +V(\mathbf{r}_+)-V(\mathbf{r}_-)\Big]\,\langle\mathbf{r}_+\,|\,\boldsymbol{\rho}\,|\,\mathbf{r}_-\rangle\,d^3\mathbf{y}\,. \tag{B.8}$$

The integral term that depends on the second derivative term can be rewritten as

$$A = -\frac{\hbar^2}{2\,m}\frac{\partial}{\partial\mathbf{r}}\int_{-\infty}^{+\infty}\exp\left(-i\,\frac{\mathbf{p}\cdot\mathbf{y}}{\hbar}\right)\frac{\partial}{\partial\mathbf{y}}\,\langle\mathbf{r}+\mathbf{y}/2\,|\,\boldsymbol{\rho}\,|\,\mathbf{r}-\mathbf{y}/2\rangle\,d^3\mathbf{y}\,. \tag{B.9}$$

Integrating by parts and noting that the projection operator acting on the density matrix is null at $\mathbf{y}=\pm\infty$ leads to the following result

$$A = -\frac{\hbar^2}{m}\frac{\partial}{\partial\mathbf{r}}\left[i\,(2\pi\hbar)^3\,(\mathbf{p}/\hbar)\,W(\mathbf{x},\mathbf{p})\right]\,. \tag{B.10}$$

The integral term that depends on the angular rate can be rewritten as

$$B = \int_{-\infty}^{+\infty}\exp\left(-i\,\frac{\mathbf{p}\cdot\mathbf{y}}{\hbar}\right)(-i\hbar)\left[\frac{\partial}{\partial\mathbf{r}}\cdot(\mathbf{r}\times\boldsymbol{\omega})+\frac{\partial}{\partial\mathbf{y}}\cdot(\mathbf{y}\times\boldsymbol{\omega})\right]\langle\mathbf{r}+\mathbf{y}/2\,|\,\boldsymbol{\rho}\,|\,\mathbf{r}-\mathbf{y}/2\rangle\,d^3\mathbf{y}\,. \tag{B.11}$$

Integration by parts leads to

$$B = (-i\hbar)\,(2\pi\hbar)^3\,\left[(\mathbf{r}\times\boldsymbol{\omega})\frac{\partial W}{\partial\mathbf{r}}+(\mathbf{p}\times\boldsymbol{\omega})\frac{\partial W}{\partial\mathbf{p}}\right]\,, \tag{B.12}$$

where we used the relations $\partial/\partial\mathbf{y} = (i/\hbar)\mathbf{p}$ and $\mathbf{y} = (i\hbar)(\partial/\partial\mathbf{p})$. At this point we can write Eq. (B.8) as

$$\frac{\partial W}{\partial t}+\frac{\mathbf{p}}{m}\cdot\frac{\partial W}{\partial\mathbf{r}}+(\mathbf{r}\times\boldsymbol{\omega})\cdot\frac{\partial W}{\partial\mathbf{r}}+(\mathbf{p}\times\boldsymbol{\omega})\cdot\frac{\partial W}{\partial\mathbf{p}}+Q=0\,, \tag{B.13}$$

where

$$Q = \frac{1}{(2\,\pi\,\hbar)^3}\left(\frac{1}{i\hbar}\right)\int_{-\infty}^{+\infty}\exp\left(-i\,\frac{\mathbf{p}\cdot\mathbf{y}}{\hbar}\right)\,\big[V(\mathbf{r}+\mathbf{y}/2)-V(\mathbf{r}-\mathbf{y}/2)\big]\dots \\ \langle\mathbf{r}+\mathbf{y}/2\,|\,\boldsymbol{\rho}\,|\,\mathbf{r}-\mathbf{y}/2\rangle\,d^3\mathbf{y}\,, \tag{B.14}$$

is the potential dependent term.

B.1.1 Semi-classical approximation

Eq. (B.13) describes the full quantum wavefunction evolution in the Wigner representation. However, under the semi-classical approximation, the full-quantum dynamics can be simplified.
Let us start by assuming that the potential function can be expanded in Taylor series

$$V(\mathbf{r} \pm \mathbf{y}/2) = \sum_{n=0}^{+\infty} \frac{1}{n!} \frac{\partial^n V(\mathbf{r})}{\partial \mathbf{r}^n} (\pm \mathbf{y}/2)^n \tag{B.15}$$

and then

$$V(\mathbf{r} + \mathbf{y}/2) - V(\mathbf{r} + \mathbf{y}/2) = \sum_{n=0}^{+\infty} \frac{1}{n!} \frac{\partial^n V(\mathbf{r})}{\partial \mathbf{r}^n} (\mathbf{y}/2 - \mathbf{y}/2)^n \,. \tag{B.16}$$

The previous term is non zero only if n is odd, and we can set $n = 2\,\ell + 1$. Therefore

$$V(\mathbf{r} + \mathbf{y}/2) - V(\mathbf{r} + \mathbf{y}/2) = \sum_{\ell=0}^{+\infty} \frac{1}{(2\,\ell+1)!} \frac{\partial^{2\,\ell+1} V(\mathbf{r})}{\partial \mathbf{r}^{2\,\ell+1}} \frac{1}{2^{2\,\ell}} \mathbf{y}^{2\,\ell+1} \tag{B.17}$$

and substitution in the term Q leads to

$$Q = \sum_{\ell=0}^{+\infty} \frac{1}{(2\,\ell+1)!} \left(-\frac{\hbar}{2}\right)^{2\,\ell} \frac{\partial^{2\,\ell+1} V(\mathbf{r})}{\partial \mathbf{r}^{2\,\ell+1}} \frac{\partial^{2\,\ell+1} W}{\partial \mathbf{p}^{2\,\ell+1}} \,. \tag{B.18}$$

Note that for a potential at most quadratic in space($\ell = 0$), the term Q becomes

$$Q = \frac{\partial V}{\partial \mathbf{r}} \frac{\partial W}{\partial \mathbf{p}} \tag{B.19}$$

and Eq. (B.13) reduces to the Liouville's equation that describes the time-evolution of a classical probability density function in phase-space. This is equivalent to say that centre of mass of the atomic wavepacket follows classical trajectories as predicted by the Ehrenfest theorem.
However, even if the potential is not a quadratic function of space, we can still neglect the full quantum dynamics and assume that the time evolution of the center of mass of the atomic wavepacket is governed by the classical equation of motion. This assumption, known as the semi-classical approximation, is valid when the contribution of the higher-order terms in the Taylor expansion of the potential are negligible compared to that of the quadratic term.
The ratio between the potential's third and second-order term is given by

$$R = \frac{\frac{1}{3!}\left(-\frac{\hbar}{2}\right)^2 \frac{\partial^3 V(\mathbf{r})}{\partial \mathbf{r}^3} \frac{\partial^3 W}{\partial \mathbf{p}^3}}{\frac{\partial V}{\partial \mathbf{r}} \frac{\partial W}{\partial \mathbf{p}}} . \tag{B.20}$$

Assuming that the space and momentum variables can be normalized with respect to characteristic quantities, i.e. $\mathbf{r}^* = \mathbf{r}/L_c$ and $\mathbf{p}^* = \mathbf{p}/p_c$, we obtain

$$R \sim \frac{\hbar^2}{24} \frac{1}{p_c^2 L_c^2} , \tag{B.21}$$

where p_c is the characteristic momentum associated to the atomic wavefunction evolution and L_c is the characteristic length associated to the spatial variations of the potential. The quantity $\hbar/p_c$ has the dimensions of a length, and indicates the characteristic length associated to the wavefunction evolution. Therefore we can set $\hbar/p_c \sim v_{\text{rec}}\, T$, with v_{rec} recoil velocity and T free-evolution time. If the spatial variations of the potential are induced only by the inhomogeneity of the Earth's gravitational field, we can assume that $L_c \sim 3$km [168]. Hence, for a free-evolution time of 10ms and ^{85}Rb atoms, we obtain $R \sim 1$ppb. The third-order term is approximately nine orders of magnitude lower than the second-order term. Therefore, for inertial navigation applications with relatively short free-evolution times, it is reasonable to assume that the motion of the center of mass of the atomic wavepackets is governed by classical equations of motion.

B.1.2 Liouville equation

Neglecting the high-order terms in the potential expansion leads to the Liouville equation

$$\frac{\partial W}{\partial t} + \frac{\mathbf{p}}{m} \cdot \frac{\partial W}{\partial \mathbf{r}} + (\mathbf{r} \times \boldsymbol{\omega}) \cdot \frac{\partial W}{\partial \mathbf{r}} + (\mathbf{p} \times \boldsymbol{\omega}) \cdot \frac{\partial W}{\partial \mathbf{p}} + \frac{\partial V}{\partial \mathbf{r}} \frac{\partial W}{\partial \mathbf{p}} = 0 , \tag{B.22}$$

and noting that

$$\begin{aligned} \dot{\mathbf{r}} &= \frac{\mathbf{p}}{m} + \mathbf{r} \times \boldsymbol{\omega} \\ \dot{\mathbf{p}} &= \mathbf{p} \times \boldsymbol{\omega} - \frac{\partial V}{\partial \mathbf{r}} , \end{aligned} \tag{B.23}$$

we obtain the Liouville equation in compact form

$$\frac{\partial W}{\partial t} + \frac{\partial H}{\partial \mathbf{p}} \frac{\partial W}{\partial \mathbf{r}} - \frac{\partial H}{\partial \mathbf{r}} \frac{\partial W}{\partial \mathbf{p}} = 0 , \tag{B.24}$$

where we used the classical Hamilton equations $\dot{\mathbf{r}} = \partial H/\partial \mathbf{p}$ and $\dot{\mathbf{p}} = -\partial H/\partial \mathbf{r}$. Starting from a known initial distribution in phase-space, $W(\mathbf{r},\, \mathbf{p},\, t_0)$, Eq. (B.24) can be solved analytically

$$W(\mathbf{r},\, \mathbf{p},\, t) = W(\mathbf{R}(\mathbf{r},\, \mathbf{p},\, t_0 - t),\, \mathbf{P}(\mathbf{r},\, \mathbf{p},\, t_0 - t),\, t_0)\,, \tag{B.25}$$

where $\mathbf{R}(\mathbf{r},\, \mathbf{p},\, t)$ and $\mathbf{P}(\mathbf{r},\, \mathbf{p},\, t)$ represent the solution of the equations of motion at time t with initial conditions $\mathbf{R}(t_0) = \mathbf{r}$ and $\mathbf{P}(t_0) = \mathbf{p}$.
Eq. (B.25) allows for the time propagation of the atomic distribution in phase-space space during the interferometer's free-evolution periods.

B.2 Raman diffraction

We need now to derive the time-evolution of the Wigner distribution inside the Raman pulse. Under the rotating-wave approximation and adiabatic elimination, the two-photon Raman diffraction is described by a two-level system [166]

$$\begin{pmatrix} c(e,\, \mathbf{p} + \hbar\mathbf{k}_{\text{eff}},\, t_0 + \Delta t) \\ c(g,\, \mathbf{p},\, t_0 + \Delta t) \end{pmatrix} = e^{-i\,\frac{\Sigma_{AC}\,\Delta t}{2}} \begin{bmatrix} e^{-i\,\frac{\delta_{12}\,\Delta t}{2}}\, C^* & -i\, e^{-i\,\frac{\delta_{12}\,\Delta t}{2}}\, S^* \\ -i\, e^{i\,\frac{\delta_{12}\,\Delta t}{2}}\, S & e^{i\,\frac{\delta_{12}\,\Delta t}{2}}\, C \end{bmatrix} \begin{pmatrix} c(e,\, \mathbf{p} + \hbar\mathbf{k}_{\text{eff}},\, t_0) \\ c(g,\, \mathbf{p},\, t_0) \end{pmatrix}, \tag{B.26}$$

with $|e\rangle$ and $|g\rangle$, respectively, upper and lower hyperfine ground states, and

$$\begin{aligned} C &= \cos(\Omega_R\, \Delta t/2) + i\, \cos\theta\, \sin(\Omega_R\, \Delta t/2) \\ S &= \sin\theta\, \sin(\Omega_R\, \Delta t/2)\, e^{i(\delta_{12}\, t_0 +\, \phi_{\text{eff}})} \\ \Omega_R &= \sqrt{\Omega_{\text{eff}}^2 + (\delta_{12} - \delta_{AC})^2} \\ \sin\theta &= \Omega_{\text{eff}}/\Omega_R \\ \cos\theta &= -(\delta_{12} - \delta_{AC})/\Omega_R \\ \Sigma_{AC} &= \Omega_e^{AC} + \Omega_g^{AC}\,, \end{aligned} \tag{B.27}$$

where Ω_{eff} is the effective Rabi frequency, ϕ_{eff} is the effective laser phase, δ_{AC} is the differential AC Stark shift (or one-photon light-shift). $\Sigma_{AC}/2$ is the average AC Stark shift and δ_{12} is the two-photon detuning.

The Weyl transform of the density matrix is given by [69]

$$W_{\alpha\beta} = \frac{1}{(2\,\pi)^3} \int_{-\infty}^{+\infty} \exp(i\mathbf{q}\cdot\mathbf{r})\, c(\alpha,\, \mathbf{p}_+)\, c^*(\beta, \mathbf{p}_-)\, d^3\mathbf{q} \tag{B.28}$$

where this time the shift has been operated on the momentum operator and $\mathbf{p}_{\pm} = \mathbf{p} \pm \hbar\mathbf{q}/2$.
Substituting Eq. (B.26) in (B.28), we obtain the time-evolution for the populations

$$\begin{aligned} W_{ee}(\mathbf{r},\, \mathbf{p},\, t_0 + \Delta t) = C^* C\, W_{ee}(\mathbf{r},\, \mathbf{p},\, t_0) + S^* S\, W_{gg}(\mathbf{r},\, \mathbf{p} - \hbar\, \mathbf{k}_{\text{eff}},\, t_0) + \dots \\ + 2\,\text{Re}\{i\, C^* S\, e^{-i\, \mathbf{k}_{\text{eff}} \cdot \mathbf{r}}\, W_{eg}(\mathbf{r},\, \mathbf{p} - \hbar\, \mathbf{k}_{\text{eff}}/2,\, t_0)\}\,, \end{aligned} \tag{B.29}$$

$$\begin{aligned} W_{gg}(\mathbf{r},\, \mathbf{p},\, t_0 + \Delta t) = S^* S\, W_{ee}(\mathbf{r},\, \mathbf{p} + \hbar\, \mathbf{k}_{\text{eff}},\, t_0) + C^* C\, W_{gg}(\mathbf{r},\, \mathbf{p},\, t_0) + \dots \\ - 2\,\text{Re}\{i\, C^* S\, e^{-i\, \mathbf{k}_{\text{eff}} \cdot \mathbf{r}}\, W_{eg}(\mathbf{r},\, \mathbf{p} + \hbar\, \mathbf{k}_{\text{eff}}/2,\, t_0)\}\,, \end{aligned} \tag{B.30}$$

and the coherence terms

$$\begin{aligned} W_{eg}(\mathbf{r},\, \mathbf{p},\, t_0 + \Delta t) = i\, C^* S^* e^{-i\, \delta_{12}\, \Delta t}\, e^{i\, \mathbf{k}_{\text{eff}} \cdot \mathbf{r}} \dots \\ \left[W_{ee}(\mathbf{r},\, \mathbf{p} + \hbar\, \mathbf{k}_{\text{eff}}/2,\, t_0) - W_{gg}(\mathbf{r},\, \mathbf{p} - \hbar\, \mathbf{k}_{\text{eff}}/2,\, t_0)\right] + \dots \\ + S^* S^* e^{-i\, \delta_{12}\, \Delta t}\, e^{2\, i\, \mathbf{k}_{\text{eff}} \cdot \mathbf{r}}\, W_{ge}(\mathbf{r},\, \mathbf{p},\, t_0) + C^* C^* e^{-i\, \delta_{12}\, \Delta t} W_{eg}(\mathbf{r},\, \mathbf{p},\, t_0)\,, \end{aligned} \tag{B.31}$$

$$W_{ge} = W_{eg}^* \tag{B.32}$$

The equations above describe the time-evolution of the Wigner functions associated to the upper and lower hyperfine ground states undergoing Raman transitions. They generalize the expression presented in Ref. [69], including both off-resonance and pulse-length errors.
We explicitly note that the presented computational model could be used to study the evolution of an atomic ensemble in phase-space, not only for rectangular pulses but also for tailored pulses with piecewise laser phase and intensity control laws.

B.3 Interferometer simulation model

The Liouville equation and the Wigner function' time-evolution during the Raman pulses are the building blocks of our simulation model. The simulation of the evolution of the atomic populations in phase-space during the interferometer sequence is based on the following steps

1. The model receives in input an initial arbitrary distribution in phase-space. For instance, we assume as initial condition $W_{gg}(\mathbf{r},\, \mathbf{p},\, t_0) = W_0$, and $W_{ee} = W_{eg} = W_{ge} = 0$.

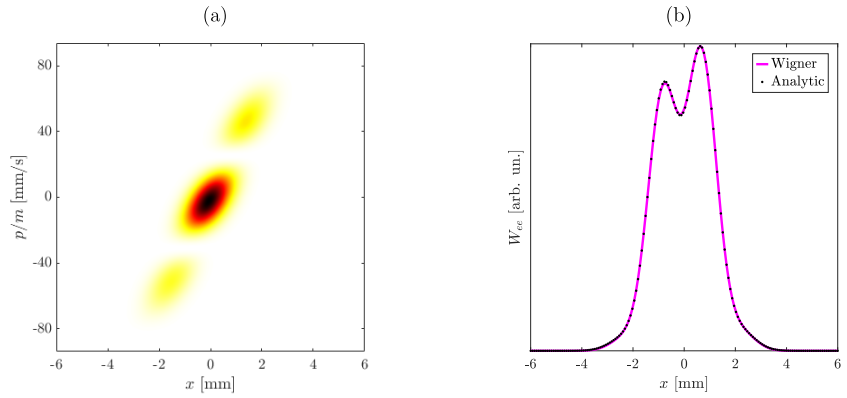

FIGURE B.1: Atomic population at the output port of the interferometer. Panel (a): phase-space distribution. Panel (b): real-space marginal distribution. The continuous line represents the full numeric solution of the Wigner model, while the black dots represents the analytic solution. We assume initial Gaussian phase-space distribution, resonant pulses, and constant angular rate and acceleration.

2. For assigned initial conditions and dynamics, we compute the classical trajectories $\mathbf{R}(\mathbf{r}, \mathbf{p}, t)$ and $\mathbf{P}(\mathbf{r}, \mathbf{p}, t)$. Therefore, the initial distribution is propagated in time solving the Liouville equation.

3. The phase-space distribution undergoes the interferometer's pulse sequence. The model accounts for both pulse-length and off-resonance errors and accepts in input an arbitrary laser intensity profile.

4. After a final free evolution period, the Wigner function is marginalized and the spatial atomic distribution is obtained. This signal represents the output of a PSI sensor.

In order to validate the interferometer model we compare the full numeric solution with an analytic model developed by Hoth *et al.*, [44], assuming an initial Gaussian phase-space distribution, resonant pulses, constant angular rate and acceleration. The Wigner model marginal agrees with the analytic solution as are reported in figure B.1.

Appendix C

Electric field propagation

For a monochromatic light beam with wave-number $k = 0 = 2\,\pi/\lambda$, the electric field evolution is governed by the Helmholtz equation [169]

$$\nabla^2\,\mathcal{E}_i(\mathbf{r}) + k_0^2\,[1+\chi(\mathbf{r})]\;\mathcal{E}_i(\mathbf{r}) = 0\,, \tag{C.1}$$

with $\mathcal{E}_i$ i-th polarization component of the electric field, and $\chi(\mathbf{r})$ susceptibility of the medium through which the light propagates.
The previous equation can be rewritten separating the axial from transverse variables as

$$-\frac{\partial^2\mathcal{E}_i}{\partial z^2} = \left[\nabla_\perp^2 + k_0^2\;(1+\chi(\mathbf{r}))\right]\;\mathcal{E}_i\,, \tag{C.2}$$

where z is the propagation axis of the electric field.
Assuming that the electric field propagates as a plane wave along the z axis, i.e. $\mathcal{E}_i(\mathbf{r}) = E(\mathbf{r}_\perp,\,z)\,\exp\left(i\,k_0\,z\right)$, we get

$$-\left[\frac{\partial^2 E(\mathbf{r}_\perp,\,z)}{\partial z^2} + 2\,i\,k_0\,\frac{\partial E(\mathbf{r}_\perp,\,z)}{\partial z} - k_0^2\,E(\mathbf{r}_\perp,\,z)\right] = \left[\nabla_\perp^2 + k_0^2\;(1+\chi(\mathbf{r}_\perp,\,z))\right]E(\mathbf{r}_\perp,\,z)\,. \tag{C.3}$$

For low divergent laser beams, the paraxial approximation ($\partial^2/\partial z^2 \ll \partial/\partial z$) is typically valid. Therefore, the Helmholtz equation simplifies in

$$-2\,i\,k_0\,\frac{\partial E(\mathbf{r}_\perp,\,z)}{\partial z} = \left[\nabla_\perp^2 + k_0^2\,\chi(\mathbf{r}_\perp,\,z)\right]E(\mathbf{r}_\perp,\,z)\,. \tag{C.4}$$

C.1 Free-space propagation

For an electric field that propagates in vacuum ($\chi(\mathbf{r}_\perp, z) = 0$), we can find a general solution of the Helmholtz equation in Fourier domain. By taking the Fourier transform of Eq. (C.4) with respect to the transverse variables we obtain

$$\frac{\partial \widehat{E}(\mathbf{k}_\perp, z)}{\partial z} = \frac{i}{2\,k_0}\left(-\mathbf{k}_\perp^2\,\widehat{E}(\mathbf{k}_\perp, z)\right), \tag{C.5}$$

and integrating the equation between z and $z + \Delta z$ we obtain

$$\widehat{E}(\mathbf{k}_\perp, z + \Delta z) = \underbrace{\exp\left(-\frac{i\,\mathbf{k}_\perp^2\,\Delta z}{2\,k_0}\right)}_{\widehat{H}_f(\mathbf{k}_\perp, \Delta z)}\,\widehat{E}(\mathbf{k}_\perp, z)\,. \tag{C.6}$$

The exponential operator, denoted as $\widehat{H}_f$, propagates the electric field in free space and is responsible for the emergence of a quadratic phase term.

C.2 Propagation through a medium

For an electric field propagating through a medium ($\chi(\mathbf{r}_\perp, z) \neq 0$), Eq. (C.4) has no general solution. However, if we assume that the distance through which the electric field propagates within the medium is small enough we can neglected the Laplacian-dependent term and obtain

$$-2\,i\,k_0\,\frac{\partial E(\mathbf{r}_\perp, z)}{\partial z} = k_0^2\,\chi(\mathbf{r}_\perp, z)\,E(\mathbf{r}_\perp, z)\,. \tag{C.7}$$

Integrating between z and Δz we get a general solution in the form

$$E(\mathbf{r}_\perp, z + \Delta z) = \underbrace{\exp\left(\int_z^{z+\Delta z} \frac{i\,k_0}{2}\,\chi(\mathbf{r}_\perp, z)\,dz'\right)}_{H_m(\mathbf{r}_\perp, \Delta z)}\,E(\mathbf{r}_\perp, z)\,, \tag{C.8}$$

where the exponential operator H_m is analogous to the free space propagator introduced in frequency domain.

Eq. (C.8) holds if the free space propagation is negligible, or, in other words, if the phase factor $k_\perp^2\,\Delta z/(2\,k_0) \ll 1$. Therefore, the physical extension of the medium must be smaller than a quantity, known as depth-of-field, that depends on the maximum transverse frequency, i.e. $\Delta z \ll 2\,k_0/k_{max}^2$. The depth-of-field practically limits the

maximum size of the object that can be imaged by a monochromatic light beam. In particular, the maximum transverse frequency could depend on

- The resolution of the imaging system (e.g. numerical aperture).
- The maximum significant frequency in the imaging plane (e.g. spatial modulation induced by rotation in atomic distribution).
- The electric field wave-number k_0 [1] .

C.2.1 The Beer-Lambert law

Imaging systems detects light scattered or absorbed by atoms in the form of intensity. Therefore, it is more useful to write the equation that describes the propagation of the light radiation through the atomic medium in terms of intensity.
Given the relation between intensity and electric field $I \propto |E|^2 = E^* E$, we can compute the rate of change of the intensity as

$$\frac{\partial I}{\partial z} \propto E^* \frac{\partial E}{\partial z} + \frac{\partial E^*}{\partial z} E \,, \tag{C.9}$$

and using Eq. (C.7) we get

$$E^* \frac{\partial E}{\partial z} + \frac{\partial E^*}{\partial z} E = \left(\frac{i\, k_0}{2} \chi - \frac{i\, k_0}{2} \chi^* \right) E\, E^* \,. \tag{C.10}$$

Remembering that for a generic complex number c it is valid the following relation $\mathrm{Im}\{c\} = (c - c^*)/(2\, i)$, we finally obtain the so-called Beer-Lambert law

$$\frac{\partial I(\mathbf{r}_\perp, z)}{\partial z} = -k_0\, \mathrm{Im}\{\chi(\mathbf{r}_\perp, z)\}\, I(\mathbf{r}_\perp, z) \,, \tag{C.11}$$

that describes the intensity attenuation of a light beam passing through a medium characterized by a susceptibility χ.

[1] This provides the ultimate limit for the maximum transverse frequency.

Appendix D

Blue-fluorescence modelling

D.1 Optical Bloch equations

In this Appendix, we present the set of equations that describe the atomic dynamics in a multi-level system. This forms the basis for the blue-fluorescence modelling, the results of which are presented in Chapter 8.
The optical Bloch equations (OBE) for an atomic multi-level system can be written in general form [170]

$$\frac{\partial \boldsymbol{\rho}}{\partial t} = \underbrace{\frac{1}{i\,\hbar}\left[\mathbf{H},\, \boldsymbol{\rho}\right]}_{\text{Laser-atom}} + \underbrace{\sum_{j,k} \Gamma_{kj} \left[\mathbf{L}_{jk}\, \boldsymbol{\rho}\, \mathbf{L}_{jk}^{\dagger} - \frac{1}{2}\left(\mathbf{L}_{jk}^{\dagger}\, \mathbf{L}_{jk}\, \boldsymbol{\rho} + \boldsymbol{\rho}\, \mathbf{L}_{jk}^{\dagger}\, \mathbf{L}_{jk}\right)\right]}_{\text{Spontaneous emissions}}, \tag{D.1}$$

where $\boldsymbol{\rho}$ is the density matrix operator, $\mathbf{H}$ is the Hamiltonian describing the laser-atom interaction, Γ_{kj} is the decay rate for the generic transition $|j\rangle \rightarrow |k\rangle$, and $\mathbf{L}_{jk} = |k\rangle \langle j|$ is the jump operator [1].
The Hamiltonian in the rotating frame is given by [171]

$$\mathbf{H} = \sum_{j,k} \hbar\, \Delta_{jk} \left|k\right\rangle \left\langle k\right| + \frac{\hbar}{2}\left(\Omega_{jk} \left|j\right\rangle \left\langle k\right| + \Omega_{kj} \left|k\right\rangle \left\langle j\right|\right) \tag{D.2}$$

,

where $\Delta_{jk} = \omega_{jk} - \omega_{jk}^{0}$ is the detuning from the resonant $|j\rangle \rightarrow |k\rangle$ transition, and Ω_{jk} is the Rabi frequency expressing the coupling between the two states.
The spontaneous emission part can be simplified expanding the jump operators

[1] Clearly, it is valid the relation $\mathbf{L}_{jk}^{\dagger} = |j\rangle \langle k|$

$$\sum_{jk} \Gamma_{kj} \left[|j\rangle \langle k| \boldsymbol{\rho} |k\rangle \langle j| - \frac{1}{2} \left(|k\rangle \langle j| |j\rangle \langle k| \boldsymbol{\rho} + \boldsymbol{\rho} |k\rangle \langle j| |j\rangle \langle k| \right) \right] , \tag{D.3}$$

and noting that $\langle k| \boldsymbol{\rho} |k\rangle = \rho_{kk}$, and $\langle j| |j\rangle = 1$, we obtain

$$\sum_{jk} \Gamma_{kj} \left[|j\rangle \rho_{kk} \langle j| - \frac{1}{2} \left(|k\rangle \langle k| \boldsymbol{\rho} + \boldsymbol{\rho} |k\rangle \langle k| \right) \right] . \tag{D.4}$$

For an atomic multi-level structure the term $\Gamma_{kj} = b_{jk}\,\Gamma$, where Γ is the fine structure linewidth and b_{jk} is the branching ratio that accounts for the hyperfine structure. The branching ratio of the spontaneous decay associate to the transition $|F\rangle \rightarrow |F'\rangle$ is given by [170]

$$b_{FF'} = \frac{C_{FF'}^2}{\sum\limits_{F} C_{FF'}^2} \tag{D.5}$$

where the coupling strength $C_{FF'}$ is related to the Clebsch–Gordan coefficients, $\mu(\ldots)$ via the relation

$$C_{FF'}^2 = \sum_{m_F} \mu(F,\, m_F;\, F',\, m'_F)^2 \,. \tag{D.6}$$

The absolute value of the Clebsch–Gordan coefficient associated to the transition $|F,\, m_F\rangle \rightarrow |F', m'_F\rangle$ is given by

$$\mu(F,\, m_F;\, F',\, m'_F) = \sqrt{(2\,F'+1)(2\,F+1)(2\,J+1)} \begin{pmatrix} F' & 1 & F \\ m'_F & q & -m_F \end{pmatrix} \begin{Bmatrix} J & J' & 1 \\ F' & F & I \end{Bmatrix} \tag{D.7}$$

where round and curly brackets denote, respectively, the Wigner 3-j and 6-j symbol. The total nuclear angular momentum number within a single fine structure level is given by $I = \max\{F\} - J$. The upper state magnetic sub-level $m'_F = m_F + q$, where $q = 0, \pm 1$ indicates the polarization of the laser field. We observe that the sum of the square of the Clebsch–Gordan coefficients over all the m_F sub-levels does not depend on the polarization parameter q: indeed, the term $C_{FF'}^2$ has the same value for every q. For this reason, we can compute the terms $C_{FF'}^2$ setting $q = 0$.

Similarly, the Rabi frequency Ω_{jk} for a multi-level system depends on the hyperfine structure coupling via the coupling strengths. For the transition $|F\rangle \rightarrow |F\rangle$, the Rabi frequency is [170]

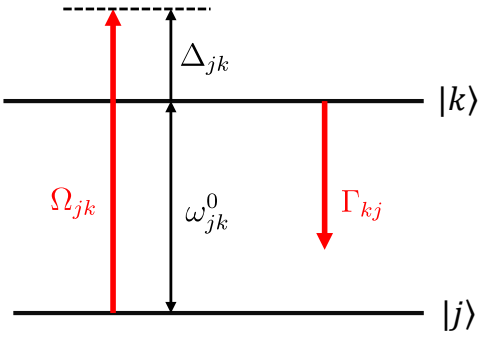

FIGURE D.1: Generic two-level system.

$$\Omega_{FF'} = \sqrt{\frac{C^2_{FF'}\, s}{2}}\,\Gamma\,, \tag{D.8}$$

where $s = I/I_s$ is the saturation parameter and is given by the ratio between the laser intensity and the saturation intensity. The saturation intensity for the circularly-polarized cycling transition is given by [170]

$$I_s = \frac{\pi}{3}\frac{\hbar\,\omega}{\lambda^2}\,\Gamma\,. \tag{D.9}$$

D.2 Blue-fluorescence for ^{85}Rb

Background-free detection can be achieved in ^{85}Rb via a two-photon ladder transition. The $5S_{1/2}$ state is coupled with the $5D_{5/2}$ state via the intermediate $5P_{3/2}$ state using 780nm and 776nm lasers. From the $5D_{5/2}$ state, a fraction of atoms decays back to the $5S_{1/2}$ state via the $5P_{3/2}$ level, emitting 'red' photons. Another fraction of atoms decays to the $5S_{1/2}$ state via the $6P_{3/2}$ level, emitting 'blue' photons at 420nm. Figure D.2 shows the fine structure of ^{85}Rb [172].

Table D.1 reports the fine structure parameters of the atomic transitions required for achieving background-free imaging in ^{85}Rb [173]. It is observed that the linewidth of the 776nm transition is approximately 14 times smaller than that of the 780nm transition. Consequently, the 776nm transition is more susceptible to Doppler broadening and necessitates a laser system with high spectral purity.

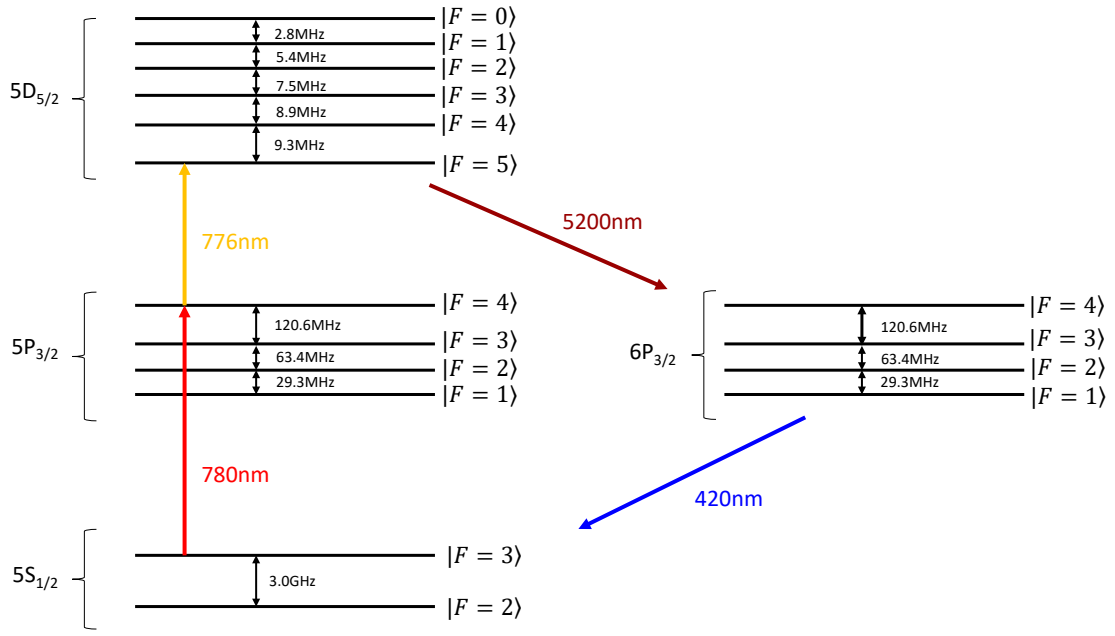

FIGURE D.2: Two-photon ladder system used to generate background-free imaging in ^{85}Rb. Energy levels are not to scale.

TABLE D.1: Fine-structure parameters of the ^{85}Rb ladder system. The indicated saturation intensity corresponds to the circularly-polarized cycling transition.

Transition	**Wavelength** [nm]	**Saturation intensity** [W/m^2]	**Linewidth** (Γ)
$5S_{1/2} \rightarrow 5P_{3/2}$	780	16.48	$2\pi \times 6.066$MHz
$5P_{3/2} \rightarrow 5D_{5/2}$	776	1.2	$2\pi \times 0.431$MHz
$5D_{5/2} \rightarrow 6P_{3/2}$	5200	0.0021	$2\pi \times 0.233$MHz
$6P_{3/2} \rightarrow 5S_{1/2}$	420	10.3	$2\pi \times 0.583$MHz

Tables D.2 and D.3 reports the coupling strengths and the branching ratios that characterize the hyperfine structure of the involved transitions. We observe that the $5P_{3/2}$ and the $6P_{3/2}$ states have the same hyperfine structure.

The blue-fluorescence modelling is based on the numerical resolution of the OBE, that is written in the matrix form

$$\dot{\boldsymbol{\rho}}_v = \mathbf{A}\,\boldsymbol{\rho}_v\,, \tag{D.10}$$

where the $\boldsymbol{\rho}_v$ is a column vector obtained reshaping each row of the density matrix, i.e. $\boldsymbol{\rho}_v = \left[\boldsymbol{\rho}(1,:), \boldsymbol{\rho}(2,:), \ldots \boldsymbol{\rho}(n,:)\right]^T$, and the notation $\boldsymbol{\rho}(i,:)$ indicates the i-th row of the density matrix.
The coupling matrix $\mathbf{A}$ depends on the saturation parameters of the 780nm and 776nm transitions, s_{780} and s_{776}, and on the detunings Δ_{780} and Δ_{776}.

TABLE D.2: Branching ratios and coupling strengths of the $5S_{1/2} \rightarrow 5P_{3/2}$ ($\lambda = 780$nm) and $6P_{3/2} \rightarrow 5S_{1/2}$ ($\lambda = 420$nm) transitions in ^{85}Rb. Here, F' (F) denotes the hyperfine structure level of the upper (lower) state.

F	F'	$C^2_{FF'}$	$b_{FF'}$
2	1	1/2	1
	2	35/54	7/9
	3	14/27	4/9
3	2	5/27	2/9
	3	35/54	5/9
	4	3/2	1

TABLE D.3: Branching ratios and coupling strengths of the $5P_{3/2} \rightarrow 5D_{5/2}$ ($\lambda = 776$nm) and $5D_{5/2} \rightarrow 6P_{3/2}$ ($\lambda = 5200$nm) transitions in ^{85}Rb. Here, F' (F) denotes the hyperfine structure level of the upper (lower) state.

F	F'	$C^2_{FF'}$	$b_{FF'}$
1	0	2/9	1
	1	7/15	7/10
	2	14/45	7/25
2	1	1/5	3/10
	2	2/3	3/5
	3	4/5	18/35
3	2	2/15	3/25
	3	7/10	9/20
	4	3/2	3/4
4	3	1/18	1/28
	4	1/2	1/4
	5	22/9	1

We solve the OBE using the matrix exponential method by dividing the integration domain in equal intervals of length Δt, and computing at each time-step the quantity

$$\boldsymbol{\rho}_v(t + \Delta t) = \exp(\mathbf{A}\,\Delta t)\,\boldsymbol{\rho}_v(t)\,. \tag{D.11}$$

The method can also be applied to the case of a time-variant system, where the saturation and detuning parameters are described by piece-wise control laws.
Unlike rate equations, OBE account for possible coherent processes and can be used in the strong coupling regime. However, this comes at the price of an increased number of variables. The density matrix has dimensions of NxN, where N is the number of considered states. For the ^{85}Rb case, we consider all the $N = 16$ hyperfine states involved in the generation of the blue-fluorescence signal to account for losses in dark states.
Figure D.3 shows the results of the OBE solution in terms of the number of scattered red and blue photons per atom. We compare the complete 16-state model with a simple

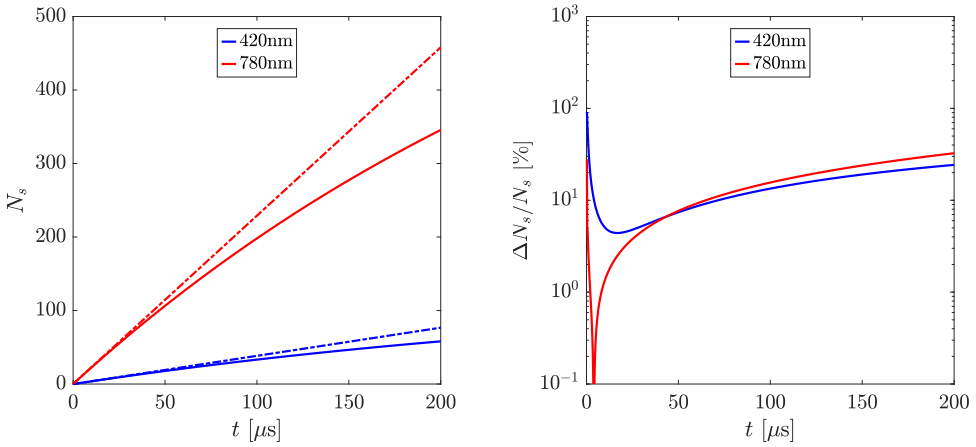

(A) Scattered photons (B) Relative error

FIGURE D.3: Result of the multi-level atomic dynamics. Panel (A): Number of red and blue scattered photons per atom. The continuous lines are the solutions of the complete 16-level model, while the dashed lines are the steady-state solution of a simple 4-level model that does not account for losses in the dark states. Panel (B): relative error in the number of scattered atoms when using the simple 4-level model. Simulation parameters: laser intensity parameters $s_{780} = 0.1$, $s_{776} = 10$, laser frequency parameters $\Delta_{780} = \Delta_{776} = 0$.

4-states model that does not take into account losses in dark states due to the hyperfine structure. The error in the number of scattered red and blue photons is, respectively, $\sim 32\%$ and $\sim 24\%$ for relatively modest laser intensity parameters ($s_{780} = 0.1$, $s_{776} = 10$) and on-resonance ($\Delta_{780} = \Delta_{776} = 0$). Therefore, the losses are not negligible, and we need to consider the entire hyperfine structure.

References

[1] D. Titterton and J. Weston, *Strapdown inertial navigation technology*. The Institution of Electrical Engineering, 2004.

[2] R. C. Duncan and A. S. Gunnersen, "Inertial guidance, navigation, and control systems," *Journal of Spacecraft and Rockets*, vol. 1, no. 6, pp. 577–587, 1964.

[3] P. D. Groves, *Principles of GNSS, inertial, and multisensor integrated navigation systems*. Artech House, 2013.

[4] P. G. Savage, *Strapdown Analytics*. Strapdown Associates, 2000.

[5] C. Jekeli, "Gravity on precise, short-term, 3-D free-inertial navigation," *Navigation*, vol. 44, no. 3, pp. 347–357, 1997.

[6] N. El-Sheimy and A. Youssef, "Inertial sensors technologies for navigation applications: state of the art and future trends," *Satellite Navigation*, vol. 1, no. 2, pp. 2662–1363, 2020.

[7] X. Ru, N. Gu, H. Shang, and H. Zhang, "MEMS inertial sensor calibration technology: current status and future trends," *Micromachines*, vol. 13, no. 6, 2022.

[8] A. Helfrick, "The centennial of avionics: Our 100-year trek to performance-based navigation," *IEEE Aerospace and Electronic Systems Magazine*, vol. 30, no. 9, pp. 36–45, 2015.

[9] M. Kasevich and S. Chu, "Measurement of the gravitational acceleration of an atom with a light-pulse atom interferometer," *Applied Physics B*, vol. 54, pp. 321–332, 1992.

[10] C. Jekeli, "Navigation error analysis of atom interferometer inertial sensor," *Navigation*, vol. 52, no. 1, pp. 1–14, 2005.

[11] R. Geiger, A. Landragin, S. Merlet, and F. Pereira Dos Santos, "High-accuracy inertial measurements with cold-atom sensors," *AVS Quantum Science*, vol. 2, no. 2, 2020.

[12] A. V. Rakholia, H. J. McGuinness, and G. W. Biedermann, "Dual-axis high-data-rate atom interferometer via cold ensemble exchange," *Physical Review Applied*, vol. 2, p. 054012, 2014.

[13] D. Savoie, M. Altorio, B. Fang, L. A. Sidorenkov, R. Geiger, and A. Landragin, "Interleaved atom interferometry for high-sensitivity inertial measurements," *Science Advances*, vol. 4, no. 12, p. eaau7948, 2018.

[14] C. Avinadav, D. Yankelev, M. Shuker, O. Firstenberg, and N. Davidson, "Rotation sensing with improved stability using point-source atom interferometry," *Physical Review A*, vol. 102, p. 013326, 2020.

[15] Z.-W. Yao, H.-H. Chen, S.-B. Lu, R.-B. Li, Z.-X. Lu, X.-L. Chen, G.-H. Yu, M. Jiang, C. Sun, W.-T. Ni, J. Wang, and M.-S. Zhan, "Self-alignment of a large-area dual-atom-interferometer gyroscope using parameter-decoupled phase-seeking calibrations," *Physical Review A*, vol. 103, p. 023319, 2021.

[16] S. Templier, P. Cheiney, Q. d'Armagnac de Castanet, B. Gouraud, H. Porte, F. Napolitano, P. Bouyer, B. Battelier, and B. Barrett, "Tracking the vector acceleration with a hybrid quantum accelerometer triad," *Science Advances*, vol. 8, no. 45, p. eadd3854, 2022.

[17] R. Geiger, V. Ménoret, G. Stern, N. Zahzam, P. Cheinet, B. Battelier, A. Villing, F. Moron, M. Lours, Y. Bidel, A. Bresson, A. Landragin, and P. Bouyer, "Detecting inertial effects with airborne matter-wave interferometry," *Nature Communications*, vol. 2, p. 474, 2011.

[18] J. M. Hogan, D. M. S. Johnson, and M. A. Kasevich, "Light-pulse atom interferometry," 2008.

[19] M. Dupont-Nivet, C. I. Westbrook, and S. Schwartz, "Contrast and phase-shift of a trapped atom interferometer using a thermal ensemble with internal state labelling," *New Journal of Physics*, vol. 18, no. 11, p. 113012, 2016.

[20] A. Gauguet, B. Canuel, T. Lévèque, W. Chaibi, and A. Landragin, "Characterization and limits of a cold-atom Sagnac interferometer," *Physical Review A*, vol. 80, p. 063604, 2009.

[21] M. Kasevich and S. Chu, "Atomic interferometry using stimulated Raman transitions," *Physical Review Letters*, vol. 67, pp. 181–184, 1991.

[22] S. Hartmann, J. Jenewein, E. Giese, S. Abend, A. Roura, E. M. Rasel, and W. P. Schleich, "Regimes of atomic diffraction: Raman versus Bragg diffraction in retroreflective geometries," *Physical Review A*, vol. 101, p. 053610, 2020.

[23] L. Hu, N. Poli, L. Salvi, and G. M. Tino, "Atom interferometry with the Sr optical clock transition," *Physical Review Letters*, vol. 119, p. 263601, 2017.

[24] J. Rudolph, T. Wilkason, M. Nantel, H. Swan, C. M. Holland, Y. Jiang, B. E. Garber, S. P. Carman, and J. M. Hogan, "Large momentum transfer clock atom interferometry on the 689 nm ontercombination line of strontium," *Physical Review Letters*, vol. 124, p. 083604, 2020.

[25] J. N. Tinsley, S. Bandarupally, M. Chiarotti, S. Manzoor, L. Salvi, and N. Poli, "Prospects for a simultaneous atom interferometer with ultracold cadmium and strontium for fundamental physics tests," in *Optical and Quantum Sensing and Precision Metrology II* (J. Scheuer and S. M. Shahriar, eds.), vol. 12016 of *Society of Photo-Optical Instrumentation Engineers (SPIE) Conference Series*, p. 1201602, 2022.

[26] F. Theron, O. Carraz, G. Renon, N. Zahzam, Y. Bidel, M. Cadoret, and A. Bresson, "Narrow linewidth single laser source system for onboard atom interferometry," *Applied Physics B*, vol. 118, pp. 1–5, 2015.

[27] M. A. Kasevich and M. Y. Shverdin, "Zero dead-time gravimeter," U.S. Patent 10 371 856 B1, Aug. 2019.

[28] J. M. Kwolek and A. T. Black, "Continuous Sub-Doppler-Cooled Atomic Beam Interferometer for Inertial Sensing," *Physical Review Applied*, vol. 17, p. 024061, 2022.

[29] G. Tackmann, P. Berg, C. Schubert, S. Abend, M. Gilowski, W. Ertmer, and E. M. Rasel, "Self-alignment of a compact large-area atomic Sagnac interferometer," *New Journal of Physics*, vol. 14, no. 1, p. 015002, 2012.

[30] J. Lautier, L. Volodimer, T. Hardin, S. Merlet, M. Lours, F. Pereira Dos Santos, and A. Landragin, "Hybridizing matter-wave and classical accelerometers," *Applied Physics Letters*, vol. 105, no. 14, p. 144102, 2014.

[31] P. Cheiney, L. Fouché, S. Templier, F. Napolitano, B. Battelier, P. Bouyer, and B. Barrett, "Navigation-compatible hybrid quantum accelerometer using a Kalman filter," *Physical Review Applied*, vol. 10, p. 034030, 2018.

[32] C. Janvier, V. Ménoret, B. Desruelle, S. Merlet, A. Landragin, and F. Pereira dos Santos, "Compact differential gravimeter at the quantum projection-noise limit," *Physical Review A*, vol. 105, p. 022801, 2022.

[33] H. F. Rice and V. Benischek, "Submarine navigation applications of atom interferometry," in *2008 IEEE/ION Position, Location and Navigation Symposium*, pp. 933–939, 2008.

[34] D. Brown, L. Mauser, B. Young, M. Kasevich, H. F. Rice, and V. Benischek, "Atom interferometric gravity sensor system," in *Proceedings of the 2012 IEEE/ION Position, Location and Navigation Symposium*, pp. 30–37, 2012.

[35] A. M. Phillips, M. J. Wright, I. Riou, S. Maddox, S. Maskell, and J. F. Ralph, "Position fixing with cold atom gravity gradiometers," *AVS Quantum Science*, vol. 4, no. 2, p. 024404, 2022.

[36] T. C. Welker, M. Pachter, and R. E. Huffman, "Gravity gradiometer integrated inertial navigation," in *2013 European Control Conference (ECC)*, pp. 846–851, 2013.

[37] B. Dubetsky, "Local positioning system as a classic alternative to atomic navigation," *Journal of Navigation*, vol. 75, no. 2, p. 273–298, 2022.

[38] M. A. Kasevich and B. Dubetsky, "Kinematic sensors employing atom interferometer phases," U.S. Patent US 7 317 184 B2, Jan. 2008.

[39] Y. Bidel, N. Zahzam, C. Blanchard, A. Bonnin, M. Cadoret, A. Bresson, D. Rouxel, and M. F. Lequentrec-Lalancette, "Absolute marine gravimetry with matter-wave interferometry," *Nature Communications*, vol. 9, p. 627, 2018.

[40] S. M. Dickerson, J. M. Hogan, A. Sugarbaker, D. M. S. Johnson, and M. A. Kasevich, "Multiaxis inertial sensing with long-time point source atom interferometry," *Physical Review Letters*, vol. 111, p. 083001, 2013.

[41] A. Peters, K. Y. Chung, and S. Chu, "High-precision gravity measurements using atom interferometry," *Metrologia*, vol. 38, no. 1, pp. 25–61, 2001.

[42] A. Roura, W. Zeller, and W. P. Schleich, "Overcoming loss of contrast in atom interferometry due to gravity gradients," *New Journal of Physics*, vol. 16, p. 123012, dec 2014.

[43] S.-Y. Lan, P.-C. Kuan, B. Estey, P. Haslinger, and H. Müller, "Influence of the Coriolis force in atom interferometry," *Physical Review Letters*, vol. 108, p. 090402, 2012.

[44] G. W. Hoth, B. Pelle, S. Riedl, J. Kitching, and E. A. Donley, "Point source atom interferometry with a cloud of finite size," *Applied Physics Letters*, vol. 109, no. 7, 2016.

[45] S.-w. Chiow, T. Kovachy, H.-C. Chien, and M. A. Kasevich, "102$\hbar k$ Large Area Atom Interferometers," *Physical Review Letters*, vol. 107, p. 130403, Sep 2011.

[46] Y. Luo, S. Yan, Q. Hu, A. Jia, C. Wei, and J. Yang, "Contrast enhancement via shaped Raman pulses for thermal cold atom cloud interferometry," *European Physical Journal D*, vol. 70, no. 12, p. 262, 2016.

[47] K. Bongs, R. Launay, and M. Kasevich, "High-order inertial phase shifts for time-domain atom interferometers," *Applied Physics B*, vol. 84, p. 599–602, 2006.

[48] B. Barrett, G. Condon, L. Chichet, L. Antoni-Micollier, R. Arguel, M. Rabault, C. Pelluet, V. Jarlaud, A. Landragin, P. Bouyer, and B. Battelier, "Testing the universality of free fall using correlated ^{39}K-^{87}Rb atom interferometers," *AVS Quantum Science*, vol. 4, no. 1, p. 014401, 2022.

[49] D. S. Weiss, B. C. Young, and S. Chu, "Precision measurement of $\hbar/m_{Cs}$ based on photon recoil using laser-cooled atoms and atomic interferometry," *Applied Physics B*, vol. 59, pp. 217–256, 1994.

[50] B. Canuel, F. Leduc, D. Holleville, A. Gauguet, J. Fils, A. Virdis, A. Clairon, N. Dimarcq, C. J. Bordé, A. Landragin, and P. Bouyer, "Six-axis inertial sensor using cold-atom interferometry," *Physical Review Letters*, vol. 97, p. 010402, 2006.

[51] I. Perrin, J. Bernard, Y. Bidel, A. Bonnin, N. Zahzam, C. Blanchard, A. Bresson, and M. Cadoret, "Zero-velocity atom interferometry using a retroreflected frequency-chirped laser," *Physical Review A*, vol. 100, p. 053618, 2019.

[52] A. Gauguet, T. E. Mehlstäubler, T. Lévèque, J. Le Gouët, W. Chaibi, B. Canuel, A. Clairon, F. Pereira Dos Santos, and A. Landragin, "Off-resonant Raman transition impact in an atom interferometer," *Physical Review A*, vol. 78, p. 043615, 2008.

[53] V. Schkolnik, B. Leykauf, M. Hauth, C. Freier, and A. Peters, "The effect of wavefront aberrations in atom interferometry," *Applied Physics B*, vol. 120, pp. 311–316, 2015.

[54] P. Gillot, B. Cheng, S. Merlet, and F. Pereira Dos Santos, "Limits to the symmetry of a Mach-Zehnder-type atom interferometer," *Physical Review A*, vol. 93, p. 013609, Jan 2016.

[55] G. K. Campbell, A. E. Leanhardt, J. Mun, M. Boyd, E. W. Streed, W. Ketterle, and D. E. Pritchard, "Photon recoil momentum in dispersive media," *Physical Review Letters*, vol. 94, p. 170403, 2005.

[56] R. A. McCutcheon and S. F. Yelin, "Limits and possibilities of refractive index in atomic systems," *Optics Communications*, vol. 505, p. 127583, 2022.

[57] Y. Sortais, S. Bize, C. Nicolas, A. Clairon, C. Salomon, and C. Williams, "Cold collision frequency shifts in a ^{87}Rb atomic fountain," *Physical Review Letters*, vol. 85, pp. 3117–3120, 2000.

[58] C. Antoine, "Rotating matter-wave beam splitters and consequences for atom gyrometers," *Physical Review A*, vol. 76, p. 033609, 2007.

[59] B. Cheng, P. Gillot, S. Merlet, and F. Pereira Dos Santos, "Coherent population trapping in a Raman atom interferometer," *Physical Review A*, vol. 93, p. 063621, 2016.

[60] O. Carraz, R. Charrière, M. Cadoret, N. Zahzam, Y. Bidel, and A. Bresson, "Phase shift in an atom interferometer induced by the additional laser lines of a Raman laser generated by modulation," *Physical Review A*, vol. 86, p. 033605, 2012.

[61] C. Rammeloo, L. Zhu, Y.-H. Lien, K. Bongs, and M. Holynski, "Performance of an optical single-sideband laser system for atom interferometry," *Journal of the Optical Society of America B*, vol. 37, no. 5, pp. 1485–1493, 2020.

[62] T. Farah, P. Gillot, B. Cheng, A. Landragin, S. Merlet, and F. Pereira Dos Santos, "Effective velocity distribution in an atom gravimeter: Effect of the convolution with the response of the detection," *Physical Review A*, vol. 90, p. 023606, 2014.

[63] B. Fang, N. Mielec, D. Savoie, M. Altorio, A. Landragin, and R. Geiger, "Improving the phase response of an atom interferometer by means of temporal pulse shaping," *New Journal of Physics*, vol. 20, no. 2, p. 023020, 2018.

[64] J. Le Gouët, P. Cheinet, J. Kim, D. Holleville, A. Clairon, A. Landragin, and F. Pereira Dos Santos, "Influence of lasers propagation delay on the sensitivity of atom interferometers," *The European Physical Journal D*, vol. 44, no. 5, pp. 419–425, 2007.

[65] S. Bade, L. Djadaojee, M. Andia, P. Cladé, and S. Guellati-Khelifa, "Observation of extra photon recoil in a distorted optical field," *Physical Review Letters*, vol. 121, p. 073603, 2018.

[66] J. M. Hogan, D. M. S. Johnson, S. Dickerson, T. Kovachy, A. Sugarbaker, S. wey Chiow, P. W. Graham, M. A. Kasevich, B. Saif, S. Rajendran, P. Bouyer, B. D. Seery, L. Feinberg, and R. Keski-Kuha, "An atomic gravitational wave interferometric sensor in low earth orbit (AGIS-LEO)," *General Relativity and Gravitation*, vol. 43, no. 7, pp. 1953–2009, 2011.

[67] P. Cheinet, B. Canuel, F. Pereira Dos Santos, A. Gauguet, F. Yver-Leduc, and A. Landragin, "Measurement of the Sensitivity Function in a Time-Domain Atomic Interferometer," *IEEE Transactions on Instrumentation and Measurement*, vol. 57, no. 6, pp. 1141–1148, 2008.

[68] W. M. Itano, J. C. Bergquist, J. J. Bollinger, J. M. Gilligan, D. J. Heinzen, F. L. Moore, M. G. Raizen, and D. J. Wineland, "Quantum projection noise: Population fluctuations in two-level systems," *Physical Review A*, vol. 47, pp. 3554–3570, 1993.

[69] B. Dubetsky and M. A. Kasevich, "Atom interferometer as a selective sensor of rotation or gravity," *Physical Review A*, vol. 74, p. 023615, Aug 2006.

[70] C. Antoine, "Matter wave beam splitters in gravito-inertial and trapping potentials: generalized ttt scheme for atom interferometry," *Applied Physics B*, vol. 84, p. 585–597, 2006.

[71] R. Stoner, D. Butts, J. Kinast, and B. Timmons, "Analytical framework for dynamic light pulse atom interferometry at short interrogation times," *Journal of the Optical Society of America B*, vol. 28, no. 10, pp. 2418–2429, 2011.

[72] A. Bonnin, N. Zahzam, Y. Bidel, and A. Bresson, "Characterization of a simultaneous dual-species atom interferometer for a quantum test of the weak equivalence principle," *Physical Review A*, vol. 92, p. 023626, 2015.

[73] N. Dedes, J. Saywell, M. Carey, I. Kuprov, and T. Freegarde, "Optimizing beamsplitter pulses for atom interferometry: A geometric approach," *Physical Review A*, vol. 108, p. 053319, 2023.

[74] G. J. Dick, "Local oscillator induced instabilities in trapped ion frequency standards," in *Proceedings of the 19th Annual Precise Time and Time Interval Systems and Applications Meeting*, (Redondo Beach, California), pp. 133–147, December 1987.

[75] C. Overstreet, P. Asenbaum, and M. A. Kasevich, "Physically significant phase shifts in matter-wave interferometry," *American Journal of Physics*, vol. 89, no. 3, pp. 324–332, 2021.

[76] P. Berg, S. Abend, G. Tackmann, C. Schubert, E. Giese, W. P. Schleich, F. A. Narducci, W. Ertmer, and E. M. Rasel, "Composite-light-pulse technique for high-precision atom interferometry," *Physical Review Letters*, vol. 114, p. 063002, 2015.

[77] J. C. Saywell, M. S. Carey, P. S. Light, S. S. Szigeti, A. R. Milne, K. Gill, M. L. Goh, V. S. Perunicic, N. M. Wilson, C. D. Macrae, A. Rischka, P. J. Everitt, N. P. Robins, R. P. Anderson, M. R. Hush, and M. J. Biercuk, "Enhancing the sensitivity of atom-interferometric inertial sensors in dynamic environments using robust control," *arXiv:2303.03683 [quant-ph]*, 2023.

[78] T. Lévèque, A. Gauguet, F. Michaud, F. Pereira Dos Santos, and A. Landragin, "Enhancing the area of a Raman atom interferometer using a versatile double-diffraction technique," *Physical Review Letters*, vol. 103, p. 080405, 2009.

[79] L. Morel, Z. Yao, P. Cladé, and S. Guellati-Khélifa, "Velocity-dependent phase shift in a light-pulse atom interferometer," *arXiv:2006.14354 [physics.atom-ph]*, 2020.

[80] A. Makdissi, F. Vernotte, and E. De Clercq, "Stability variances: a filter approach," *IEEE Transactions on Ultrasonics, Ferroelectrics, and Frequency Control*, vol. 57, no. 5, pp. 1011–1028, 2010.

[81] K. Takase, *Precision rotation rate measurements with a mobile atom interferometer*. PhD thesis, Stanford University, 2008.

[82] N. Malossi, Q. Bodart, S. Merlet, T. Lévèque, A. Landragin, and F. P. D. Santos, "Double diffraction in an atomic gravimeter," *Physical Review A*, vol. 81, p. 013617, 2010.

[83] B. Barrett, L. Antoni-Micollier, L. Chichet, B. Battelier, T. Lévèque, A. Landragin, and P. Bouyer, "Dual matter-wave inertial sensors in weightlessness," *Nature Communications*, vol. 7, no. 1, p. 13786, 2016.

[84] R.-B. Li, L. Zhou, J. Wang, and M.-S. Zhan, "Measurement of the quadratic Zeeman shift of ^{85}Rb hyperfine sublevels using stimulated Raman transitions," *Optics Communications*, vol. 282, no. 7, pp. 1340–1344, 2009.

[85] S. Dimopoulos, P. W. Graham, J. M. Hogan, and M. A. Kasevich, "General relativistic effects in atom interferometry," *Physical Review D*, vol. 78, p. 042003, 2008.

[86] B. J. Kokkelmans, S. J. .and Verhaar, K. Gibble, and D. J. Heinzen, "Predictions for laser-cooled Rb clocks," *Physical Review A*, vol. 56, pp. R4389–R4392, 1997.

[87] J. McGuirk, G. Foster, J. Fixler, M. Snadden, and M. Kasevich, "Sensitive absolute-gravity gradiometry using atom interferometry," *Physical Review A*, vol. 65, p. 033608, 2002.

[88] D. Butts, K. Kotru, J. Kinast, A. Radojevic, B. Timmons, and R. Stoner, "Efficient broadband Raman pulses for large-area atom interferometry," *Journal of the Optical Society of America B*, vol. 30, no. 4, pp. 922–927, 2013.

[89] T. Wilkason, M. Nantel, J. Rudolph, Y. Jiang, B. Garber, H. Swan, S. Carman, M. Abe, and J. Hogan, "Atom interferometry with Floquet atom optics," *Physical Review Letters*, vol. 129, p. 183202, 2022.

[90] J. Saywell, I. Kuprov, D. Goodwin, M. Carey, and T. Freegarde, "Optimal control of mirror pulses for cold-atom interferometry," *Physical Review A*, vol. 98, p. 023625, 2018.

[91] J. Saywell, M. Carey, M. Belal, I. Kuprov, and T. Freegarde, "Optimal control of Raman pulse sequences for atom interferometry," *Journal of Physics B: Atomic and Molecular Physics*, vol. 53, no. 8, p. 085006, 2020.

[92] J. Saywell, M. Carey, N. Dedes, I. Kuprov, and T. Freegarde, "Can optimised pulses improve the sensitivity of atom interferometers?," in *Quantum Technology: Driving Commercialisation of an Enabling Science II* (M. Padgett, K. Bongs, A. Fedrizzi, and A. Politi, eds.), SPIE, 2021.

[93] A. Peters, *High precision gravity measurements using atom interferometry*. PhD thesis, Stanford University, 1998.

[94] W. Magnus, "On the exponential solution of differential equations for a linear operator," *Communications on Pure and Applied Mathematics*, vol. 7, pp. 649–673, 1954.

[95] F. Dyson, "The radiation theories of Tomonaga, Schwinger, and Feynman," *Physical Review*, vol. 75, pp. 486–502, 1949.

[96] S. Blanes, F. Casas, J. Oteo, and J. Ros, "The Magnus expansion and some of its applications," *Physics Reports*, vol. 470, no. 5, pp. 151–238, 2009.

[97] M. Carey, M. Belal, M. Himsworth, J. Bateman, and T. Freegarde, "Matterwave interferometric velocimetry of cold Rb atoms," *Journal of Modern Optics*, vol. 65, no. 5-6, pp. 657–666, 2018.

[98] J. Saywell, M. Carey, N. Dedes, I. Kuprov, and T. Freegarde, "Efficient state-symmetric beamsplitters and mirrors for atom interferometers using optimized pulses," *Journal of Physics B: Atomic, Molecular and Optical Physics*, vol. 55, no. 20, p. 205501, 2022.

[99] I. Kuprov, *Spin: From basic symmetries to quantum optimal control*. Springer Cham, 2023.

[100] M. Goerz, D. Basilewitsch, F. Gago-Encinas, M. Krauss, K. Horn, D. Reich, and C. Koch, "Krotov: A Python implementation of Krotov's method for quantum optimal control," *SciPost Physics*, vol. 7, p. 80, 2019.

[101] R. Tycko, "Broadband population inversion," *Physical Review Letters*, vol. 51, pp. 775–777, 1983.

[102] J. Saywell, *Optimal control of cold atoms for ultra-precise quantum sensors*. Phd thesis, University of Southampton, 2020.

[103] I. Kuprov, "Spin system trajectory analysis under optimal control pulses," *Journal of Magnetic Resonance*, vol. 233, pp. 107–112, 2013.

[104] Brimrose, *Acousto-optic modulator TEM-85-10*.

[105] R. Karcher, A. Imanaliev, S. Merlet, and F. Pereira Dos Santos, "Improving the accuracy of atom interferometers with ultracold sources," *New Journal of Physics*, vol. 20, p. 113041, nov 2018.

[106] A. Louchet-Chauvet, T. Farah, Q. Bodart, A. Clairon, A. Landragin, S. Merlet, and F. Pereira Dos Santos, "The influence of transverse motion within an atomic gravimeter," *New Journal of Physics*, vol. 13, no. 6, p. 065025, 2011.

[107] S. Feng and H. G. Winful, "Physical origin of the Gouy phase shift," *Optics Letters*, vol. 26, no. 8, pp. 485–487, 2001.

[108] X. Wu, Z. Pagel, B. S. Malek, T. H. Nguyen, F. Zi, D. S. Scheirer, and H. Müller, "Gravity surveys using a mobile atom interferometer," *Science Advances*, vol. 5, no. 9, p. eaax0800, 2019.

[109] P. A. Bélanger and C. Paré, "Optical resonators using graded-phase mirrors," *Optics Letters*, vol. 16, no. 14, pp. 1057–1059, 1991.

[110] Y.-L. Chung and Z.-H. Lin, "Analytical thermal analysis of radially functionally graded circular plates with coating or undercoating under transverse and radial temperature distributions," *Applied Sciences*, vol. 13, no. 12, 2023.

[111] H. Wang, C. Blair, M. D. Álvarez, A. Brooks, M. F. Kasprzack, J. Ramette, P. M. Meyers, S. Kaufer, B. O'Reilly, C. M. Mow-Lowry, and A. Freise, "Thermal modelling of Advanced LIGO test masses," *Classical and Quantum Gravity*, vol. 34, no. 11, p. 115001, 2017.

[112] A. Leissa, "Vibration of plates," *NASA SP-160*, 1969.

[113] K. Numata, K. Yamamoto, H. Ishimoto, S. Otsuka, K. Kawabe, M. Ando, and K. Tsubono, "Systematic measurement of the intrinsic losses in various kinds of bulk fused silica," *Physics Letters A*, vol. 327, no. 4, pp. 263–271, 2004.

[114] V. Lakshminarayanan and A. Fleck, "Zernike polynomials: a guide," *Journal of Modern Optics*, vol. 58, no. 7, pp. 545–561, 2011.

[115] A. Trimeche, M. Langlois, S. Merlet, and F. Pereira Dos Santos, "**??**Active Control of Laser Wavefronts in Atom Interferometers," *Physical Review Applied*, vol. 7, p. 034016, 2017.

[116] Y.-J. Chen, A. Hansen, M. Shuker, R. Boudot, J. Kitching, and E. A. Donley, "Robust inertial sensing with point-source atom interferometry for interferograms spanning a partial period," *Optics Express*, vol. 28, no. 23, pp. 34516–34529, 2020.

[117] Y.-J. Chen, A. Hansen, G. W. Hoth, E. Ivanov, B. Pelle, J. Kitching, and E. A. Donley, "Single-Source Multiaxis Cold-Atom Interferometer in a Centimeter-Scale Cell," *Physical Review Applied*, vol. 12, p. 014019, 2019.

[118] A. Dytso, R. Bustin, H. V. Poor, and S. Shamai, "Analytical properties of generalized Gaussian distributions," *Journal of Statistical Distributions and Applications*, vol. 5, p. 6, 2018.

[119] H. Al-Jlailaty and M. M. Mansour, "Efficient attitude estimators: A tutorial and survey," *Journal of Signal Processing Systems*, vol. 94, p. 1309–1343, 2022.

[120] A. Sugarbaker, S. M. Dickerson, J. M. Hogan, D. M. S. Johnson, and M. A. Kasevich, "Enhanced atom interferometer readout through the application of phase shear," *Physical Review Letters*, vol. 111, p. 113002, 2013.

[121] X. Xu, G. Lu, G. Han, F. Gao, Z. Jiao, and D. Li, "Phase stitching and error correction in aperture synthesis for generalized phase-shifting interferometry," *Applied Optics*, vol. 52, no. 20, pp. 4864–4870, 2013.

[122] J. J. Martinez-Espla, T. Martinez-Marin, J. D. Ballester-Berman, and J. M. Lopez-Sanchez, "InSAR phase unwrapping by means of a particle filter," in *IGARSS*

2008 - 2008 IEEE International Geoscience and Remote Sensing Symposium, vol. 4, pp. IV – 1217–IV – 1220, 2008.

[123] Z. Cheng, D. Liu, Y. Yang, T. Ling, X. Chen, L. Zhang, J. Bai, Y. Shen, L. Miao, and W. Huang, "Practical phase unwrapping of interferometric fringes based on unscented Kalman filter technique," *Optics Express*, vol. 23, no. 25, pp. 32337–32349, 2015.

[124] R. G. Waghmare, P. R. Sukumar, G. R. K. S. Subrahmanyam, R. K. Singh, and D. Mishra, "Particle-filter-based phase estimation in digital holographic interferometry," *Journal of the Optical Society of America A*, vol. 33, no. 3, pp. 326–332, 2016.

[125] J. A. Farrell, F. O. Silva, F. Rahman, and J. Wendel, "Inertial measurement unit error modeling tutorial: Inertial navigation system state estimation with real-time sensor calibration," *IEEE Control Systems Magazine*, vol. 42, no. 6, pp. 40–66, 2022.

[126] E. Rocco, R. Palmer, T. Valenzuela, V. Boyer, A. Freise, and K. Bongs, "Fluorescence detection at the atom shot noise limit for atom interferometry," *New Journal of Physics*, vol. 16, no. 9, p. 093046, 2014.

[127] M. Pappa, P. C. Condylis, G. O. Konstantinidis, V. Bolpasi, A. Lazoudis, O. Morizot, D. Sahagun, M. Baker, and W. von Klitzing, "Ultra-sensitive atom imaging for matter-wave optics," *New Journal of Physics*, vol. 13, no. 11, p. 115012, 2011.

[128] W. Ketterle, D. S. Durfee, and D. M. Stamper-Kurn, "Making, probing and understanding Bose-Einstein condensates," *arXiv:cond-mat/9904034v2*, 1999.

[129] P. B. Wigley, P. J. Everitt, K. S. Hardman, M. R. Hush, C. H. Wei, M. A. Sooriyabandara, P. Manju, J. D. Close, N. P. Robins, and C. C. N. Kuhn, "Non-destructive shadowgraph imaging of ultra-cold atoms," *Optic Letters*, vol. 41, no. 20, pp. 4795–4798, 2016.

[130] G. P. Greve, C. Luo, B. Wu, and J. K. Thompson, "Entanglement-enhanced matter-wave interferometry in a high-finesse cavity," *Nature*, vol. 610, p. 472–477, 2022.

[131] G. Reinaudi, T. Lahaye, Z. Wang, and D. Guéry-Odelin, "Strong saturation absorption imaging of dense clouds of ultracold atoms," *Optics Letters*, vol. 32, no. 21, pp. 3143–3145, 2007.

[132] W. Muessel, H. Strobel, M. Joos, E. Nicklas, I. Stroescu, J. Tomkovič, D. B. Hume, and M. K. Oberthaler, "Optimized absorption imaging of mesoscopic atomic clouds," *Applied Physics B*, pp. 69–73, 2013.

[133] G. E. Marti, R. B. Hutson, A. Goban, S. L. Campbell, N. Poli, and J. Ye, "Imaging optical frequencies with 100 μHz precision and 1.1 μm resolution," *Physical Review Letters*, vol. 120, p. 103201, 2018.

[134] E. W. Packel and D. S. Yuen, "Projectile motion with resistance and the Lambert W function," *The College Mathematics Journal*, vol. 35, no. 5, pp. 337–350, 2004.

[135] V. Ménoret, P. Vermeulen, N. Le Moigne, S. Bonvalot, P. Bouyer, A. Landragin, and B. Desruelle, "Gravity measurements below 10^{-9} g with a transportable absolute quantum gravimeter," *Scientific Reports*, vol. 8, p. 12300, 2018.

[136] R. Veyron, V. Mancois, J. B. Gerent, G. Baclet, P. Bouyer, and S. Bernon, "Quantitative absorption imaging: The role of incoherent multiple scattering in the saturating regime," *Physical Review Research*, vol. 4, p. 033033, 2022.

[137] R. Veyron, V. Mancois, J. B. Gerent, G. Baclet, P. Bouyer, and S. Bernon, "Effective two-level approximation of a multilevel system driven by coherent and incoherent fields," *Physical Review A*, vol. 105, p. 043105, 2022.

[138] G. W. Biedermann, X. Wu, L. Deslauriers, K. Takase, and M. A. Kasevich, "Low-noise simultaneous fluorescence detection of two atomic states," *Optics Letters*, vol. 34, pp. 347–349, Feb 2009.

[139] J. P. McGilligan, K. R. Moore, A. Dellis, G. D. Martinez, E. de Clercq, P. F. Griffin, A. S. Arnold, E. Riis, R. Boudot, and J. Kitching, "Laser cooling in a chip-scale platform," *Applied Physics Letters*, vol. 117, no. 5, p. 054001, 2020.

[140] H. Ohadi, M. Himsworth, A. Xuereb, and T. Freegarde, "Magneto-optical trapping and background-free imaging for atoms near nanostructured surfaces," *Optics Express*, vol. 17, no. 25, pp. 23003–23009, 2009.

[141] J. Shamir, "Teaching Fourier optics for engineers," in *1995 International Conference on Education in Optics*, vol. 2525, pp. 689–698, International Society for Optics and Photonics, SPIE, 1995.

[142] M. Nazarathy and J. Shamir, "Fourier optics described by operator algebra," *Journal of the Optical Society of America*, vol. 70, no. 2, pp. 150–159, 1980.

[143] M. Gu, *Advanced Optical Imaging Theory*. Springer Berlin Heidelberg, 2013.

[144] J. W. Goodman, *Introduction to Fourier optics*. Roberts & Co. Publishers, 2005.

[145] C. Ricolfe-Viala and A. J. Sanchez-Salmeron, "Lens distortion models evaluation," *Applied Optics*, vol. 49, no. 30, pp. 5914–5928, 2010.

[146] M. A. Joffe, W. Ketterle, A. Martin, and D. E. Pritchard, "Transverse cooling and deflection of an atomic beam inside a Zeeman slower," *Journal of the Optical Society of America B*, vol. 10, no. 12, pp. 2257–2262, 1993.

[147] A. Stern and N. S. Kopeika, "Analytical method to calculate optical transfer functions for image motion and vibrations using moments," *Journal of the Optical Society of America A*, vol. 14, no. 2, pp. 388–396, 1997.

[148] C. F. Ockeloen, A. F. Tauschinsky, R. J. C. Spreeuw, and S. Whitlock, "Detection of small atom numbers through image processing," *Physical Review A*, vol. 82, p. 061606, 2010.

[149] F. Xiong, Y. Long, and C. V. Parker, "Enhanced principle component method for fringe removal in cold atom images," *Journal of the Optical Society of America B*, vol. 37, no. 7, pp. 2041–2044, 2020.

[150] O. Yadid-Pecht, "Geometrical modulation transfer function for different pixel active area shapes," *Optical Engineering*, vol. 39, no. 4, pp. 859–865, 2000.

[151] P. H. Richter, "Estimating errors in least-squares fitting," *Telecommunications and Data Acquisition Progress Report*, vol. 122, pp. 107–137, 1995.

[152] J. R. Janesick, *Scientific Charge-Coupled Devices*. SPIE Press Monograph PM83, 2001.

[153] D. Seib, "Carrier diffusion degradation of modulation transfer function in charge coupled imagers," *IEEE Transactions on Electron Devices*, vol. 21, no. 3, pp. 210–217, 1974.

[154] M. Blouke and D. Robinson, "A method for improving the spatial resolution of frontside-illuminated CCD's," *IEEE Transactions on Electron Devices*, vol. 28, no. 3, pp. 251–256, 1981.

[155] M. A. Green, "Self-consistent optical parameters of intrinsic silicon at 300K including temperature coefficients," *Solar Energy Materials and Solar Cells*, vol. 92, no. 11, pp. 1305–1310, 2008.

[156] N. Barbour and G. Schmidt, "Inertial sensor technology trends," *IEEE Sensors Journal*, vol. 1, no. 4, pp. 332–339, 2001.

[157] J. Le Gouët, T. Mehlstäubler, J. Kim, S. Merlet, A. Clairon, A. Landragin, and F. Pereira Dos Santos, "Limits to the sensitivity of a low noise compact atomic gravimeter," *Applied Physics B*, vol. 92, pp. 133–144, 2008.

[158] T. Hensel, S. Loriani, C. Schubert, F. Fitzek, S. Abend, H. Ahlers, J.-N. Siemß, K. Hammerer, E. M. Rasel, and N. Gaaloul, "Inertial sensing with quantum gases: a comparative performance study of condensed versus thermal sources for atom interferometry," *The European Physical Journal D*, vol. 75, p. 108, 2021.

[159] J. Li, G. R. M. da Silva, W. C. Huang, M. Fouda, J. Bonacum, T. Kovachy, and S. M. Shahriar, "High sensitivity multi-axes rotation sensing using large momentum transfer point source atom interferometry," *Atoms*, vol. 9, no. 3, 2021.

[160] A. M. Nobili, A. Anselmi, and R. Pegna, "Systematic errors in high-precision gravity measurements by light-pulse atom interferometry on the ground and in space," *Physical Review Research*, vol. 2, p. 012036, 2020.

[161] P. J. Hobson, J. Vovrosh, B. Stray, M. Packer, J. Winch, N. Holmes, F. Hayati, K. McGovern, R. Bowtell, M. J. Brookes, K. Bongs, T. M. Fromhold, and M. Holynski, "Bespoke magnetic field design for a magnetically shielded cold atom interferometer," *Scientific Reports*, vol. 12, p. 10520, 2022.

[162] S.-T. Yan, J.-J. Jiang, L. Zhou, Y.-H. Ji, C. He, Z. Hou, B. Tang, X. Chen, J. Wang, and M.-S. Zhan, "Absolute-phase-shift measurement in a phase-shear-readout atom interferometer," *Physical Review A*, vol. 108, p. 063313, 2023.

[163] E. Zitzler, M. Laumanns, and S. Bleuler, "A tutorial on evolutionary multiobjective optimization," in *Metaheuristics for Multiobjective Optimisation* (X. Gandibleux, M. Sevaux, K. Sörensen, and V. T'kindt, eds.), (Berlin, Heidelberg), pp. 3–37, Springer Berlin Heidelberg, 2004.

[164] C. A. Weidner and D. Z. Anderson, "Experimental demonstration of shaken-lattice unterferometry," *Physical Review Letters*, vol. 120, p. 263201, 2018.

[165] G. Raithel, A. Duspayev, B. Dash, S. C. Carrasco, M. H. Goerz, V. Vuletić, and V. S. Malinovsky, "Principles of tractor atom interferometry," *Quantum Science and Technology*, vol. 8, no. 1, p. 014001, 2022.

[166] P. Berman, *Atom interferometry*. Academic Press, 1997.

[167] Y. Katznelson, *An introduction to harmonic analysis*. Cambridge University Press, 2004.

[168] Y. M. Wang, "GSFC00 mean sea surface, gravity anomaly, and vertical gravity gradient from satellite altimeter data," *Journal of Geophysical Research: Oceans*, vol. 106, no. C12, pp. 31167–31174, 2001.

[169] J. D. Jackson, *Electrodynamics, Classical*. John Wiley & Sons, 2003.

[170] D. A. Steck, "Quantum and atom optics," 2012.

[171] G. Morigi, S. Franke-Arnold, and G.-L. Oppo, "Phase-dependent interaction in a four-level atomic configuration," *Physical Review A*, vol. 66, p. 053409, 2002.

[172] N. Vujičić, T. Ban, G. Kregar, D. Aumiler, and G. Pichler, "Velocity-selective double resonance in Doppler-broadened rubidium vapor," *Physical Review A*, vol. 87, p. 013438, 2013.

[173] A. Vernier, S. Franke-Arnold, E. Riis, and A. S. Arnold, "Enhanced frequency up-conversion in Rb vapor," *Optics Express*, vol. 18, no. 16, pp. 17020–17026, 2010.